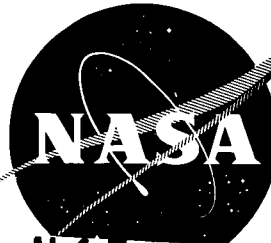


0074

NASA CR-54136



N65 32548

FACILITY FORM 802

(ACCESSION NUMBER)
287
(PAGES)
(NASA CR OR TMX OR AD NUMBER)

(THRU)
1
(CODE)
22
(CATEGORY)

ION ROCKET ENGINE DEVELOPMENT

by

Members of the Staff
Ion Propulsion Department
G. R. Brewer, Manager

prepared for

NATIONAL AERONAUTICS AND SPACE ADMINISTRATION

CONTRACT NAS 3-4109

GPO PRICE \$ _____

CSFTI PRICE(S) \$ _____

Hard copy (HC) 6.00

Microfiche (MF) 1.50

ff 653 July 65

HUGHES

HUGHES AIRCRAFT COMPANY

RESEARCH LABORATORIES

NOTICE

This report was prepared as an account of Government sponsored work. Neither the United States, nor the National Aeronautics and Space Administration (NASA), nor any person acting on behalf of NASA:

- A.) Makes any warranty or representation, expressed or implied, with respect to the accuracy, completeness, or usefulness of the information contained in this report, or that the use of any information, apparatus, method, or process disclosed in this report may not infringe privately owned rights; or
- B.) Assumes any liabilities with respect to the use of, or for damages resulting from the use of any information, apparatus, method or process disclosed in this report.

As used above, "person acting on behalf of NASA" includes any employee or contractor of NASA, or employee of such contractor, to the extent that such employee or contractor of NASA, or employee of such contractor prepares, disseminates, or provides access to, any information pursuant to his employment or contract with NASA, or his employment with such contractor.

Requests for copies of this report should be referred to

National Aeronautics and Space Administration
Office of Scientific and Technical Information
Attention: AFSS-A
Washington, D.C. 20546

SUMMARY REPORT

ION ROCKET ENGINE DEVELOPMENT

by

Members of the Staff
Ion Propulsion Department
G. R. Brewer, Manager

prepared for

NATIONAL AERONAUTICS AND SPACE ADMINISTRATION

August 1965

CONTRACT NAS 3-4109

Technical Management
NASA Lewis Research Center
Cleveland, Ohio
Spacecraft Technology Division
David L. Lockwood

HUGHES RESEARCH LABORATORIES
A Division of Hughes Aircraft Company
Malibu, California

TABLE OF CONTENTS

	LIST OF ILLUSTRATIONS	v
	SUMMARY	1
I.	INTRODUCTION	3
II.	DEVELOPMENT OF THE 15 to 23 mlb STRIP ION ENGINE	9
III.	ENGINE TESTS	27
	A. Three-Strip Engine Program Summary	27
	B. Engine 32-150-3	33
	C. Engine 32-150-4	57
IV.	ENGINE DEVELOPMENT STUDIES	89
	A. Ionizer Manifold Fabrication and Evaluation	89
	B. Ionizer Heater Thermodynamics and Life Analysis	130
	C. Focus Electrode Heat Load and Tempera- ture Distribution.	142
	D. Electrode Simulation Studies.	164
	E. Accel Drain Currents	188
	F. Ionizer Manifold Pressure Distribution	199
	G. Test Environment and Apparatus	211
V.	OPTICS CONSIDERATIONS FOR AN INTEGRAL FOCUS ENGINE	267
VI.	CONTRIBUTORS	277
	REFERENCES	279
	DISTRIBUTION LIST	281

LIST OF ILLUSTRATIONS

Fig. I-1.	Expected engine life as a function of beam current density and neutral fraction	4
Fig. II-1.	(a) Focus electrode heat rejection path	15
	(b) Cutaway sketch of engine electrode structure	15
Fig. II-2.	Effect of electrode width and heat drain impedance on peak electrode temperature	16
Fig. II-3.	Peak focus temperature, power to be rejected by the focus electrode, power to thrust ratio, and total ionizer power for the 20-strip engine	18
Fig. II-4.	Side view of 20-strip engine design	20
Fig. II-5.	Photograph of 20-strip ion engine	22
Fig. II-6.	Back view of engine showing double shielded insulators and base plates	23
Fig. II-7.	(a) Ionizer side of manifold	24
	(b) Heater side of manifold	24
	(c) Ten 2-strip ionizer fastened to tungsten manifold	24
Fig. III-1.	Three-strip engine 32-150-3	28
Fig. III-2.	(a) Photomicrograph of Mod A ionizer material	30
	(b) Photomicrograph of Mod E ionizer material	30
Fig. III-3.	Beam current and accel drain data from long duration tests of multistrip engines	32
Fig. III-4.	Engine 32-150-3 mounted for test	36
Fig. III-5.	Front view of engine 32-150-3 showing the electrodes as well as the position of the neutral detector	37

Fig. III-6.	Principal parameter time history for engine 32-150-3, phases 2, 3, and 4	41
Fig. III-7.	Critical temperature curves for engine 32-150-3	43
Fig. III-8.	Critical temperature curves for engine 32-150-3	44
Fig. III-9.	Critical temperature curves for engine 32-150-3	45
Fig. III-10.	ΔF versus temperature for hydrogen and oxygen, tungsten and oxygen, and cesium and oxygen	47
Fig. III-11.	Neutral fraction versus ionizer temperature for engine 32-150-3	49
Fig. III-12.	Front view of engine 32-150-3 showing the open accel electrodes	51
Fig. III-13.	Critical temperature plots showing operating points for engine 32-150-3, test phases 3 and 4	52
Fig. III-14.	Partial history of test phase 4 for engine 32-150-3 showing the effects of accel electrode power on the accel drains	54
Fig. III-15.	Engine 32-150-3 after the phase 4 test	56
Fig. III-16.	(a) Beam current profile for 260 hour test of engine 32-150-4	60
	(b) Accel drain profile for 260 hour test of engine 32-150-4	61
Fig. III-17.	Ionizer temperature-heater power charac- teristics for engine 32-150-4	64
Fig. III-18.	Accel end temperatures for engine 32-150-4	65
Fig. III-19.	Focus electrode end temperatures for engine 32-150-4	66

Fig. III-20.	Typical critical temperature data from engine 32-150-4 during the first 55 hours of the 260 hour test	69
Fig. III-21.	Ionizer temperature profile of engine 32-150-4 during the 260 hour test	71
Fig. III-22.	Photograph of neutral detector as positioned during the 260-hour test of engine 32-150-4	73
Fig. III-23.	Bottom view of neutral detector showing the erosion from the edge trajectories of the beam that occurred during the 260 hour test of engine 32-150-4	74
Fig. III-24.	Graph showing the work function of a tungsten surface with various arrival rates of copper and other elements onto the tungsten surface	75
Fig. III-25.	Front view of engine 32-150-4 with superimposed outline of erosion on a molybdenum cage which was part of the engine structure	76
Fig. III-26.	Angle at which neutralized trajectories would have to leave the decel region of the engine to strike the molybdenum cage	77
Fig. III-27.	Neutral percent, neutral detector sensitivity, and average beam current during the first 96 hours of the 260 hour test of engine 32-150-4	79
Fig. III-28.	View of accel electrodes after test of engine 32-150-4	81
Fig. III-29.	View of portion of accel No. 4 from engine 32-150-4 after 260 hour test	81
Fig. III-30.	Cross sections of accels from engine 32-150-4, showing original dimensions, coatings, and erosion patterns	82
Fig. III-31.	Perveance profile of engine 32-150-4	85

Fig. IV-1.	Relative permeability data for 0.050 in. and 0.085 in. thick Mod E ionizer material as a function of ionizer density	91
Fig. IV-2.	Nitrogen decay time versus percent theoretical density for slabs made from different sizes of spherical tungsten powder	92
Fig. IV-3.	HRL permeability test fixture	93
Fig. IV-4.	Philips Metalonics permeability data sheet for the ionizers intended for use in the first 20-strip engine	94
Fig. IV-5.	Philips Metalonics permeability data sheet for the ionizers intended for use in the first 20-strip engine	95
Fig. IV-6.	HRL flow rate- ΔP measurements for the Philips Metalonics ionizers intended for use in the first 20-strip engine	96
Fig. IV-7.	HRL flow rate- ΔP measurements for the Philips Metalonics ionizers intended for use in the first 20-strip engine	97
Fig. IV-8.	Schematic of the flow rate measurement apparatus used at HRL	98
Fig. IV-9.	Twenty-strip ionizer doublet process — flow chart	101
Fig. IV-10.	Records of inspections performed on 20-strip engine ionizers after welding some of the ionizer segments to the manifold	103
Fig. IV-11.	Records of inspections performed on 20-strip engine ionizers after welding some of the ionizer segments to the manifold	104
Fig. IV-12.	Photomicrograph of typical electric discharge machined tungsten surface (100x)	105
Fig. IV-13.	Grain and pore characteristics of a metallographically polished and copper evaporated sample of porous tungsten	105

Fig. IV-14.	Smeared surface, prior to copper evaporation, of a 50% HNO ₃ etched surface of a ground ionizer	107
Fig. IV-15.	Smeared surface, prior to copper evaporation, of a 50% HNO ₃ etched surface of a machined ionizer	108
Fig. IV-16.	Fifty percent HNO ₃ etched surface of a ground ionizer after evaporation	108
Fig. IV-17.	Fifty percent HNO ₃ etched surface of a machined ionizer after evaporation	109
Fig. IV-18.	Effects of concentrated HF-HNO ₃ etch on ground surface of ionizer	109
Fig. IV-19.	Effect of dilute HF-HNO ₃ etch on ground surface of ionizer	110
Fig. IV-20.	Effect of Murakami etch on ground surface of ionizer	110
Fig. IV-21.	Photomicrograph of electron beam weld — manifold to emitter, left side	112
Fig. IV-22.	Photomicrograph of electron beam weld — manifold to emitter, right side	112
Fig. IV-23.	Photomicrograph of electron beam weld — tungsten tube to manifold nipple	113
Fig. IV-24.	Photomicrograph of electron beam weld — 98% tungsten-2% molybdenum sleeve to tungsten tube	113
Fig. IV-25.	Photomicrograph of electron beam weld — 98% tungsten-2% molybdenum sleeve to molybdenum tube	114
Fig. IV-26.	Photomicrograph of electron beam weld — nickel bellows to nickel sleeve	114
Fig. IV-27.	Tooling used for sealing the porous material between each emitting strip of the multistrip ionizer	116
Fig. IV-28.	Fixtures for welding 14-strip emitter to manifold thermal conductance legs	118

Fig. IV-29.	Ionizer (14-strip) electron beam weld distortion study	121
Fig. IV-30.	Polished and etched tungsten manifold showing surface defects	124
Fig. IV-31.	Photograph of two 10-strip ionizers	124
Fig. IV-32.	Graph showing the variation in center to center spacing for two 10-strip ionizers	125
Fig. IV-33.	Illustration of possible thermal stress if ionizer and manifold are not maintained at same temperature	131
Fig. IV-34.	Heater temperature versus units of heat transfer from heating element to ionizer manifold	133
Fig. IV-35.	Ionizer heating configurations	135
Fig. IV-36.	Ceramic installation into the ionizer-manifold assembly	143
Fig. IV-37.	Heater ceramics used in engine 2018-150-1	144
Fig. IV-38.	Focus heat drain structure	150
Fig. IV-39.	Focus electrode temperature differential	151
Fig. IV-40.	Focus heat load per unit length versus spring end temperature	153
Fig. IV-41.	Spring end focus temperature versus ionizer temperature	154
Fig. IV-42.	Focus electrode temperature profile obtained during operational test of engine 32-40-8	158
Fig. IV-43.	Focus electrode end temperature versus ionizer temperature	160
Fig. IV-44.	Focus electrode and structure temperature distribution during an electrode heat load of 2.4 W/cm	161
Fig. IV-45.	Focus electrode temperature profile	163

Fig. IV-46.	Accel temperature profiles for various ionizer temperatures 32-150-1 thermal test	165
Fig. IV-47.	Schematic of electrode simulation experiment tube arrangement	167
Fig. IV-48.	Surface ionization characteristics for tungsten . . .	169
Fig. IV-49.	Surface ionization characteristics for molybdenum	170
Fig. IV-50.	Surface ionization characteristics for platinum or platinum-10% iridium	172
Fig. IV-51.	Electron and ion emission characteristics for molybdenum disilicide	174
Fig. IV-52.	Electron and ion emission characteristics for thoriated tungsten	176
Fig. IV-53.	Circuit for observing electron and ion emission characteristics of cylindrical Al_2O_3 sample	177
Fig. IV-54.	Ion and electron emission characteristics of Al_2O_3 . Ionization characteristics of tungsten are shown for comparison	179
Fig. IV-55.	Cesium ion emission data for Al_2O_3	180
Fig. IV-56.	Ion and electron emission characteristics of flat Al_2O_3 sample brazed to tungsten electrode	181
Fig. IV-57.	Electron and ion emission characteristics for copper	184
Fig. IV-58.	Ion and electron emission characteristics for titanium	186
Fig. IV-59.	Combination of electron and ion currents in heated accel electrode simulation	187
Fig. IV-60.	Accel-focus electrode used in phases 3 and 4 of engine 32-150-3	190
Fig. IV-61.	Accel-focus electrode used in engine 32-150-4 . . .	191

Fig. IV-62.	Ionizer temperature-accel electron drain characteristic showing the methods of heat rejection required to maintain the focus electrode at 900 to 1000°K	193
Fig. IV-63.	Isometric view of double optics system	194
Fig. IV-64.	Conformal map showing the potential distribution between the accel and focus electrodes for both the conventional electrode shapes as well as for a form of the double optics system	195
Fig. IV-65.	Electric field effect on the thermionic emission for field between zero and 10^5 V/cm	196
Fig. IV-66.	Section A-A (see Fig. IV-63) of double optics system showing the arrival rate of particles from the ionizer surface to the focus and accel electrodes	198
Fig. IV-67.	Linear plot of clean copper current density versus temperature	200
Fig. IV-68.	Ionizer manifold pressure deviation as a function of transmission coefficient and current density	202
Fig. IV-69.	Ionizer manifold pressure requirement for various current densities	203
Fig. IV-70.	Ionizer manifold pressure deviation for 2018-150-1 engine at design current density of 15 mA/cm ² (or 10^{-3} g/sec)	204
Fig. IV-71.	Engine 2018-150-1 manifold	206
Fig. IV-72.	Illustration of terms used in expression for view factor	213
Fig. IV-73.	Illustrations of how beam is distributed on the collector due to beam spread	214
Fig. IV-74.	View factors for various collector configurations	216
Fig. IV-75.	Sketch of various collector geometries	218

Fig. IV-76.	Calculated depression of ionizer work function due to adsorbed film of material sputtered from the accel electrode	220
Fig. IV-77.	Collector erosion pattern resulting from the extended test of engine 32-150-4	221
Fig. IV-78.	Contour of collector erosion calculated for two operating conditions of a 20-strip engine	222
Fig. IV-79.	Schematic of decelerating collector	224
Fig. IV-80.	Time constant for diffusion of carbon through solid tungsten	229
Fig. IV-81.	Normalized carbon concentration profiles at various times after start of cleanup	231
Fig. IV-82.	Normalized carbon concentration profiles at various times after start of engine operation	233
Fig. IV-83.	Normalized carbon concentration versus time after start of engine operation	235
Fig. IV-84.	Ratio of operating time to cleanup time	237
Fig. IV-85.	Diffusion constant: carbon in tungsten	239
Fig. IV-86.	Physical significance of the time constant τ	240
Fig. IV-87.	Mass flow rate (atoms/cm ² -sec) of carbon diffusing from the surface of a grain and into the bulk volume of the grain	243
Fig. IV-88.	Equilibrium surface coverage on tungsten versus carbon sticking rate for 5 μ grain at 1600°K	245
Fig. IV-89.	Work function (based on Wilson's work function versus surface coverage plot)	250
Fig. IV-90.	Ion engine life test console	253
Fig. IV-91.	Traces showing (a) voltage and (b) current response of ionizer supply to a 10 μ sec wide short circuit load (simulated arc)	255

Fig. IV-92.	Traces showing (a) voltage and (b) current response of the ionizer supply to a 10 μ sec wide short circuit load (simulated arc)	256
Fig. IV-93.	Traces showing (a) voltage and (b) current response of the accel supply to a 10 μ sec wide short circuit load (simulated arc)	257
Fig. V-1.	Model 70 ion optics shown with reduced space charge	268
Fig. V-2.	Ion trajectory plots for integral-focus optics (cusp type ionizer)	270
Fig. V-3.	Current density distribution from cusp-type integral focus ionizer	271
Fig. V-4.	Ion trajectory plots (electrolytic tank) for integral focus optics with rectangular focusing structure	272
Fig. V-5.	Current density plot (digital computer solution) for integral focus optics with rectangular focusing structure	274
Fig. V-6.	Ion trajectory plots (electrolytic tank) for integral focus optics with knife-edge focusing structure	275

SUMMARY

The objective of this program has been the development of a cesium contact ion rocket engine exhibiting a thrust of 15 mlb at a specific impulse of between 6000 and 9000 sec, and of such a configuration that it can be used as the basis for higher thrust engines by clustering. The principal elements of this program were the design and fabrication of the development engines, the development and life tests of the engines, and the supporting research necessary to understand and solve various performance and life limiting problems.

The engine design developed to satisfy the contract requirement of 15 mlb thrust was a multiple strip "cold" focus electrode type having 20 linear strips with a total active ionizer area of 54.6 cm^2 . Concurrent with the engineering of the 20-strip engine, a development and test program was conducted using three-strip engines. The three-strip engines duplicated the optics and engineering facets of the 20-strip engine and thus provided a test device that saved considerable time and expense. Five three-strip engines were built and evaluated up to the contract requirement of 15 mA/cm^2 current density. The maximum life attained from the last engine was 260 hours. During this test the neutral fraction increased to 17% because the ionizer became coated with molybdenum sputtered from a shield at the side of the engine.

The three-strip engine tests confirmed our belief that an engine could be designed with sufficient reliability that charge exchange erosion of the accel electrodes becomes the principal inhibitor of engine life. Solutions to the problem of charge exchange erosion are, in order of their potential effectiveness: decreasing the number of charge exchange ions with improved ionizer materials, reducing the erosion rate by the use of accel electrode materials which have lower sputtering yields, and diverting the charge exchange ions from the accel electrode by the addition of a separate electrode which will not influence the engine optics as it is eroded.

Engine development supporting studies have resulted in techniques for (1) evaluating ionizers by surface scanning the permeability of a porous tungsten slab, (2) fabricating the tungsten manifold with conventional machine tools instead of electrosark machining, and (3) electron beam welding large multiple strip ionizers to manifolds without distortion.

Analysis of the ionizer heater design indicated a calculated life time of this element of 50 years, which greatly exceeds any expected mission duration. Based on studies of the electron emission from copper surfaces it was determined that an accel electrode temperature of 800 to 900°K prevented the accel drains from increasing without limit as a function of test time. Thermal analysis provided data for an engine design which would ensure operation of the accel electrodes at the desired temperature as well as operation of the focus electrode at a temperature low enough to prevent ion formation at its surface.

Problems associated with long duration engine testing were studied. The ionizer critical temperature and neutral fraction approached the values for clean tungsten after the vacuum chamber pump oil was changed to D.C. 705 and the O rings were changed to Viton. The problem of sputtering from the copper collector in the vacuum chamber was also studied. It was concluded that the multilouvered collector which was designed and is now being used will not sputter enough to affect the ionizer work function seriously, but that extended tests should utilize a larger tank and/or a decelerating collector structure.

A longer term objective of this program has been to develop a higher performance simpler configuration than the present "cold" focus engine. Preliminary optics studies have shown that it is feasible to make an engine with the focusing element attached as an integral part of the ionizer. Future studies will be necessary to determine if ion emission from the tip of the integral focus cusp is a serious life limiting problem.

I. INTRODUCTION

This summary report presents the accomplishments of Hughes Research Laboratories on National Aeronautics and Space Administration Contract NAS 3-4109. The principal goal of the program has been to develop a 15-23 mlb cesium contact ion engine. The current density and life test requirements for the engine were 15 mA/cm^2 and 500 hours, respectively, during this contract period.

The effort in execution of this contract was directed to the design of a multiple strip ion engine with an active ionizer area of 54.6 cm^2 . The class of cesium contact engine was a cold focus type which was prescribed by state-of-the-art ionizer material as well as a 10,000 hour life design goal.

The engine development was pursued by using analysis and experiments in various associated technical disciplines which together constituted the knowledge necessary to make an engine.

In addition, a vigorous program was undertaken to evaluate experimentally the development engines. This program used three-strip ion engines which were similar, except for the total number of ionizer strips, to the 15-23 mlb device. A series of five three-strip engines were evaluated up to the contract required current density. The maximum life attained from the last engine tested was 260 hours. Sputtering from a shield at the engine side caused molybdenum to coat the ionizer. This resulted in an increase in neutral fraction from 1 to 17%, and thereby, in excessive erosion.

These engine tests, especially the last, confirmed our belief that an engine could be designed with charge exchange erosion as the principal limit of engine life. Figure I-1 shows the expected engine life as a function of beam current density. The ionizer neutral fraction is the parameter on this curve. The band outlined on the curve is for currently available ionizer material. Engine life will be enhanced further by advances in ionizer materials which provide

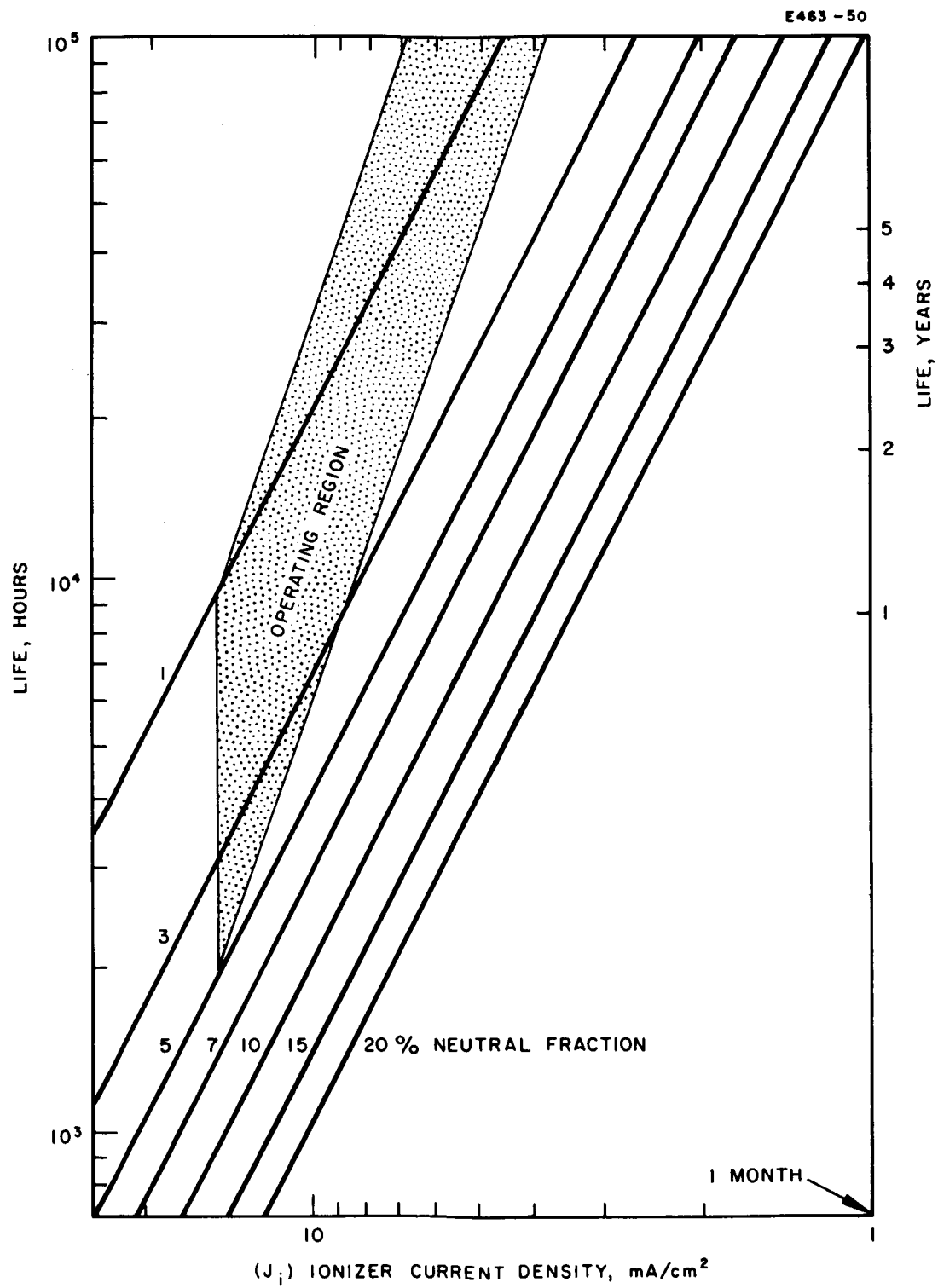


Fig. 1-1. Expected engine life as a function of beam current density and neutral fraction.

markedly lower neutral efflux at high current densities, the use of accel electrode materials which have lower sputtering yields than copper, and the application of a special electrode to prevent ions formed by charge exchange from impinging onto the accel electrode. The use of the diverter electrode can provide an increase in life by a factor of 2 to 3. The improved accel electrode material can improve engine life by a factor of 5 to 7. Improved ionizers, however, can markedly enhance engine life by a factor of 3 to hundreds.

The support work described in this report includes techniques for evaluation of the ionizer by scanning the surface permeability of a porous tungsten slab. Methods were developed for fabricating the tungsten manifold with conventional machine tools. It was determined that the use of electro-spark machining methods caused microcracks to develop in the manifold surface. The tungsten parts were hot machined at 450°C without developing cracks — sources of cesium leaks — in the manifold. In addition, electron beam welding techniques were developed for fastening large ionizers to manifolds without incurring distortions.

Heater design was rigorously examined to confirm our approach toward making this part of the engine failure proof. Analysis of the heater life indicated that operation for periods very much greater than any anticipated mission could be expected. The calculated lifetime was 50 years.

Analysis was continued to determine the heat load on the electrodes as well as to establish the configuration of the thermal paths to ensure "cold focus" operation of the engine. A principal contributor of heat to the focus electrode was the electron drains from the accel electrode. Measurements were made of the electron emission from copper surfaces. Also studied were the ion emission properties of copper since, with a cold focus engine, the focus electrode would be copper coated. It was determined that an 800 to 900°K accel electrode eliminated the increase of accel drains with test time.

A longer term objective was to develop means for making a higher performance, simpler engine than the cold focus configuration. In support of this objective, preliminary work was performed on optics for an integral focus engine. Also examined were the ion emission properties of an alumina surface. The preliminary optics studies showed that it was feasible to make an engine without a separate focus electrode. However, the initial studies indicated that ions would emit from a 0.010 in. region of the sharp tip and impinge onto the accel electrode. This emission could be a life limiting factor unless the emission region or the neutral fraction were reduced or the tip of the integral focus cusp made non-ion-emitting.

Future ionizer material and optic studies will determine the benefits of pursuing these technical avenues. Non-emitting surfaces were studied, however. Emission from alumina was not conclusively shown to be reduced from that of tungsten and copper at higher temperatures. Initial data from a heated alumina tube showed an emission reduction of 10^3 to 10^4 at 1400°K . However, evaluation of a brazed alumina sample on a substrate showed negligible reduction in ion emission at higher temperatures.

Problems associated with long duration testing were also studied. The diffusion pump oil, O rings, and baffles were changed. It was found that the ionizer critical temperature and neutral fraction approach those of clean tungsten when more stable pump oil, D.C. 705, and Viton O rings were substituted for the Convoil 20 and Buna materials.

The tank collector was also studied with the objective of minimizing the rate of sputtered copper arriving at the ionizer. Two factors were of major concern: one was the possibility of copper scaling from the electrodes and causing an engine short, the second, the reduction of ionizer work function resulting from excessive surface coverage of copper on tungsten. The solution of the final problem can be achieved only by using a larger tank or by deceleration of the ion beam. The multilouvered collector described in this report, with the present tank, does not sputter sufficient copper to affect the ionizer work function seriously. The detailed results of engine tests and supporting analysis are presented.

The draft of this report was submitted November 25, 1964.
The approval was received April 26, 1965.

II. DEVELOPMENT OF THE 15 to 23 mlb STRIP ION ENGINE

The design of the 20-strip cesium contact ion engine is based primarily on the principle that an approach to controlling life-limiting erosion of the accel electrode from focus originated ions is to cool the focus electrode. Earlier ion engines, as reported in the final report for NAS 5-517, showed conclusively that the focus electrode must be limited in its ability to produce ions. To attain an engine life of 10,000 hours, the focus ion current must not exceed 2.8×10^{-6} A/cm for a cold focus class of engine or 1.2×10^{-6} A/cm for integral focus ion engines wherein a narrow focus electrode is permitted.

This level of focus current is computed on the basis of an allowed erosion of the accel material of 30% of its initial mass. The expression for the allowable linear current density from the focus electrode, based on accel electrode life, is:

$$I_F = \frac{Z C e A}{\gamma M t} \text{ A/cm} \quad . \quad (\text{II-1})$$

where

- $Z \equiv$ (ρwh) the mass per unit length of the accel electrode
1.8 g/cm for a 0.6 cm wide copper electrode
- $C \equiv$ fraction of the accel electrode which is permitted to be eroded
- $e \equiv$ electron charge
- $A \equiv$ Avogadro number
- $M \equiv$ atomic mass
- $\gamma \equiv$ sputtering yield factor for the accel material
(γ for copper = 8)
- $t \equiv$ required accel electrode life, seconds.

A focus ion current density of 7.4×10^{-6} A/cm², corresponding to 2.8×10^{-6} A/cm for an engine with a focus electrode width of 0.150 in., could only be attained from an ionizer material which has a neutral fraction of 0.02%. For this neutral flux limited case, the focus temperature could be greater than 1000°K without causing an increase in the focus ion current. However, the neutral fraction can be a higher value such as 5% for a focus temperature less than or equal to 1000°K. In the latter case, the focus ion current density will still be equal to or less than 7.4×10^{-6} A/cm². An examination of the ion emission characteristics of copper as a function of temperature indicates the origin of the stated temperatures and current densities presented.

An alternative means for limiting the focus ion current is to minimize the focus electrode ion emitting width and/or cover the focus electrode surface with a non-ion-emitting material. The minimum width focus electrode approach to the design of an integral focus engine permits operation for 10,000 hours at a current density of 15 mA/cm² only when the ionizer neutral fraction is less than 1%. The life of an ion engine with an ion emitting focus electrode is determined by the following expression:

$$t = \frac{CZ \times 1.5 \times 10^5}{\gamma M J (NF) A_F} \text{ sec.} \quad (\text{II-2})$$

where

$Z \equiv$ mass per unit length of the accel electrode -
0.62 g/cm for a 0.28 cm wide copper electrode

$J \equiv$ current density, A/cm²

$NF \equiv$ neutral fraction

$A_F \equiv$ ion emitting region of the focus electrode, cm².

The remaining quantities are the same as used in (II-1). A 0.010 in. region where ions originate which impinge onto the accel electrode would limit the engine life to a maximum of 4000 hours. The current

density and neutral fraction for this case are 15 mA/cm^2 and 1%. Only a neutral fraction less than 1.0% or emission from the tip region of the integral focus which is less than 0.010 in. wide could permit the attainment of an engine life of 10,000 hours for this high temperature or integral focus configuration ion engine.* However, a program was undertaken to establish a focus electrode coating to inhibit ion emission to a level such as 10^{-5} A/cm^2 for ionizers which have neutral fractions less than 10%. A description of this program is presented in Section IV-D of this report. It is also important to realize that it could be possible to obtain ionizers with neutral fractions which are orders of magnitude less than the presently evaluated porous tungsten ionizers. This could be done by using high pore count ionizer materials, such as those with 6×10^6 pores/cm², in conjunction with such high work function ionizer materials as iridium or rhenium.

Utilizing the present technology with respect to the neutral fraction-current density characteristics of porous tungsten permits attainment of engine life, as determined by focus originated ions, of 10,000 hours. This can be attained by using the technology developed under Contract NAS 3-4109 in conjunction with future work directed toward producing better ionizers and/or lower sputter yield accel materials. The improvements in ionizers and accel materials will make possible an increase in engine life reducing the effects of focus and charge exchange ion erosion. Improved ionizers also permit simplicity of engine design; the accommodation of the higher neutral fractions and the associated increased accel drain currents would require complicated means for ensuring a cold focus electrode.

The effects of charge exchange ions were examined and reported under Contract NAS 5-517. The results of the electrolytic tank-analog computer analysis indicated the regions of erosion

*Preliminary charge exchange analysis indicates that the life of the integral focus type engine would be limited to 2500 hours for the same neutral fraction and current density.

and the relative levels of erosion from five regions of the accel electrode surface. A recent long duration test of a three-strip ion engine proved the accuracy of the original charge exchange analysis. The volume of material eroded from the accel electrode was within 8% of the computed value. The tradeoff between engine life, current density, and neutral fraction can therefore be made with reasonable assurance of the validity of the results.

The life of this cold focus cesium contact ion engine, using the model 70 optics, can be expressed by the following relationship:

$$t = \frac{CV}{7.2 \times 10^3 v} \left(\frac{7}{NF} \right) \left(\frac{15}{J} \right)^2 \quad (\text{II-3})$$

where

$t \equiv$ life of the engine (hours)

$C \equiv$ fraction of the accel electrode which is permitted to be eroded

$V \equiv$ volume of the accel electrode per centimeter of length, cm^3/cm

$v \equiv$ volume of accel eroded per centimeter side for a neutral fraction of 7% and a current density of $15 \text{ mA}/\text{cm}^2$

NF and $J \equiv$ neutral fraction and current density, % and mA/cm^2 , respectively.

The values for v as determined by the electrolytic tank-analog computer study for various values of accel-decel ratio V_A/V_F are:

$\frac{V_A}{V_F}$	\underline{v}
1.25	$6.68 \times 10^{-9} \text{ cm}^3/\text{sec-cm side}$
1.6	7.7
2.0	8.25
4.0	10.1
6.0	10.2

A graph of this life relationship is presented in Fig. I-1. The result of a long duration test confirming the charge exchange results is presented in Section III-C-4. Figure II-2 shows that the limitation on engine life resulting from charge exchange erosion would be 1900 hours at a current density of 15 mA/cm^2 . The neutral fraction has been assumed to be 5%.

The utilization of the decel electrode as a charge exchange diverter electrode can improve the life by a factor of 2 to 3. Changing the accel material to one with a low sputter yield, such as titanium, could further improve the engine life by an additional factor of 7. On this basis, at a current density of 15 mA/cm^2 and with a neutral fraction of 5%, a 4000 hour life could be attained without changing the accel electrode material and a 28,000 hour life could be attained with an improved accel electrode material.

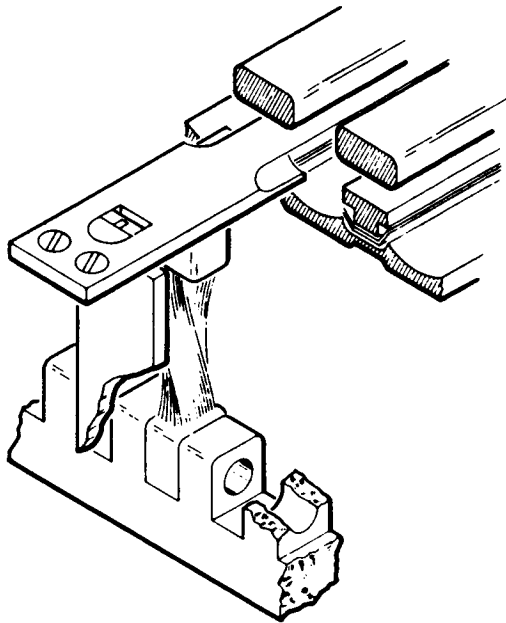
The ion engine developed under this contract has been designed such that its lifetime is limited only by charge exchange erosion. The characteristics of the engine are as follows:

Thrust, lb	0.015	0.023
Beam current, A	0.825	0.825
Specific impulse, sec	6000	9000

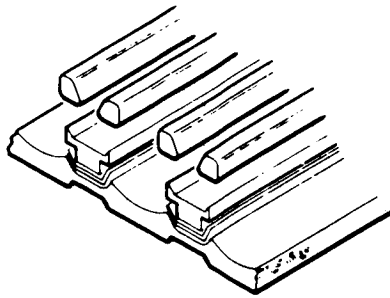
The present life objective for the engine is 1000 hours. The minimum engine life requirement is 500 hours. It is believed, considering the major life inhibitors previously described, that these life requirements can be attained with this engine.

The 15 to 23 mlb ion engine uses an active ionizer area of 54.7 cm^2 . The electrode strip length, and thus the ionizer width, for this cooled focus type engine is prescribed by thermal considerations, i. e., the peak focus temperature. This requires an electrode length of 1.846 in. An analysis supplementary to that presented in the NAS 5-517 final report and the experimental data of the temperature of the focus electrode as they relate to the heat load are presented in Section IV-C of this report. This information has been used as a part of the thermal design of the 20-strip engine. The requirement to operate the engine with a focus electrode operating at a temperature less than $900 \text{ to } 1000^\circ\text{K}$ necessitates careful consideration of (1) thermal power radiated to the focus electrode, (2) electron bombardment power which is received from the accel electrode, and (3) the means for rejecting this power to the engine mounting structure for subsequent radiation to space. Figure II-1(a) shows the conduction method for rejection of focus electrode heat. Figure II-1(b) shows the heat shield between the ionizer and focus electrode. The copper braids brazed to the focus electrode ends serve as the heat path to the engine structure. The heat load is rejected by the engine structure acting as a radiator. The choice of the focus electrode width is dependent on a tradeoff between the decrease in thermal impedance of the electrode as the width increases and the increased thermal load from the nonemitting region of the ionizer as well as increases in electron bombardment power. Figure II-2 shows how this tradeoff was made under the previous contract. The heavy lines represent the peak focus temperature as a function of the width of the electrode. For a fixed ionizer temperature, the electrode width also determines the electrode impedance Z_o as well as the electrode heat load. The dashed line represents the physically allowable heat conduction impedance which can be used with a

E429-6



(a) The "cool" focus electrode showing flexible heat conduction straps and solid accel electrode.



(b) Cool focus electrode showing accel electrode slotted to reduce electron current to the focus electrode and to reduce impingement onto accel electrode of any ions which are formed on the focus electrode.

Fig. II-1.

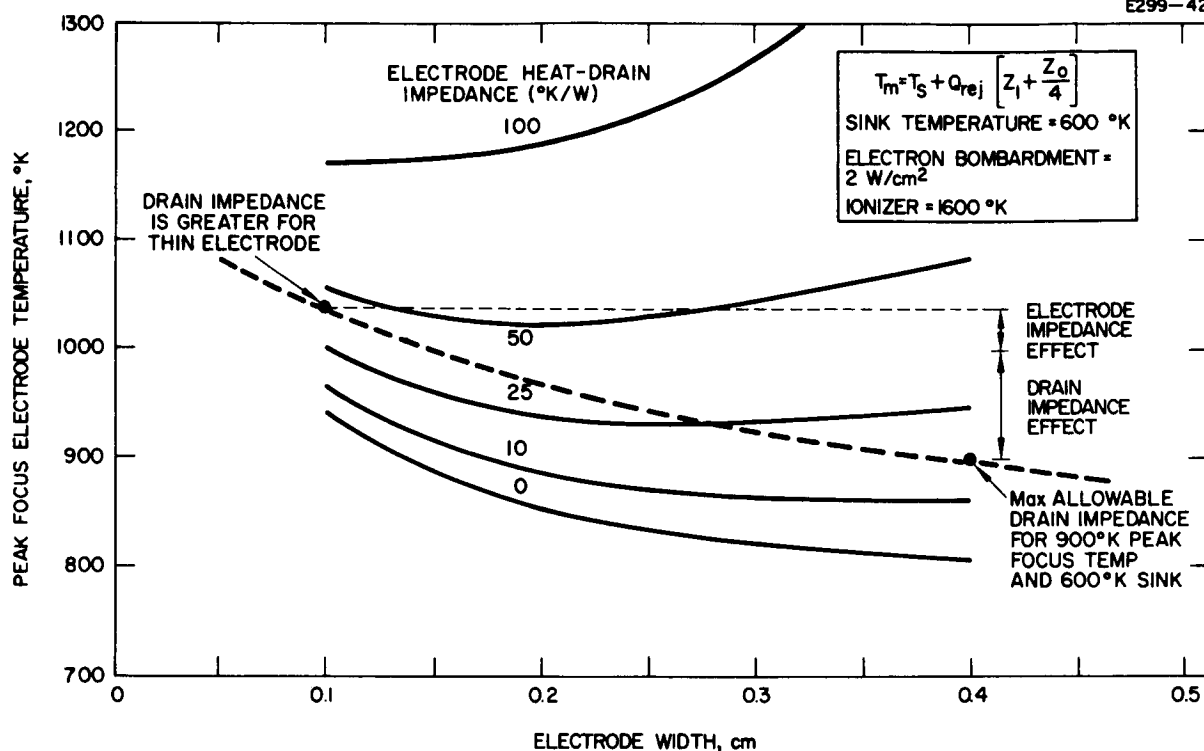


Fig. II-2. Effect of electrode width and heat drain impedance on peak electrode temperature.

electrode width. For low heat drain impedance values Z_1 , the peak temperature falls as the electrode width increases. This is a result of the lowering of electrode impedance Z_o . With high Z_1 , the peak temperature rises because the Q_{rej} increase is dominant. Only impedances above the dashed line are attainable.

The 20-strip engine is designed with a 0.4 cm focus width. The total impedance from the electrode end to the mounting structure ranges from 15 to 20°K/W.

The 20-strip engine uses an ionizer strip which is slightly shorter than that used in the three-strip engines. The reduction in the emitter and focus electrode lengths results in a reduced peak focus temperature for the equivalent linear heat load to the engine. The emitter length was changed early in the design from 2.00 to 1.845 in. This 7% length reduction results in a 15% ΔT reduction.

The peak focus temperature, the power to be rejected by the focus electrode, the power to thrust ratio, and the total ionizer power have been determined for this 20-strip engine. This information is presented in Fig. II-3. The 1.3 W/cm thermal load (non-beam) to the focus electrode used in the calculations was obtained from three-strip engine tests. The focus electrode temperature can be maintained below 1000°K (500°K sink) even for accel electrode drains up to 6%.

The last two three-strip engine tests showed conclusively that the control of the accel drains required the accel electrode to operate near 950°K. The power-to-thrust data represent two cases:

1. accel electrode operating without a heater
2. accel electrode requiring a heater to operate near 950°K.

It is possible that the need for a heater can be alleviated after a better understanding of the nature of the accel drains is obtained. Our present understanding is given in Section IV-E.

The electrode configuration is composed of 20 (each) focus, accel, and decel electrodes. A side view of the 20-strip engine, with the ionizer and electrodes perpendicular to the plane of the paper, is shown in

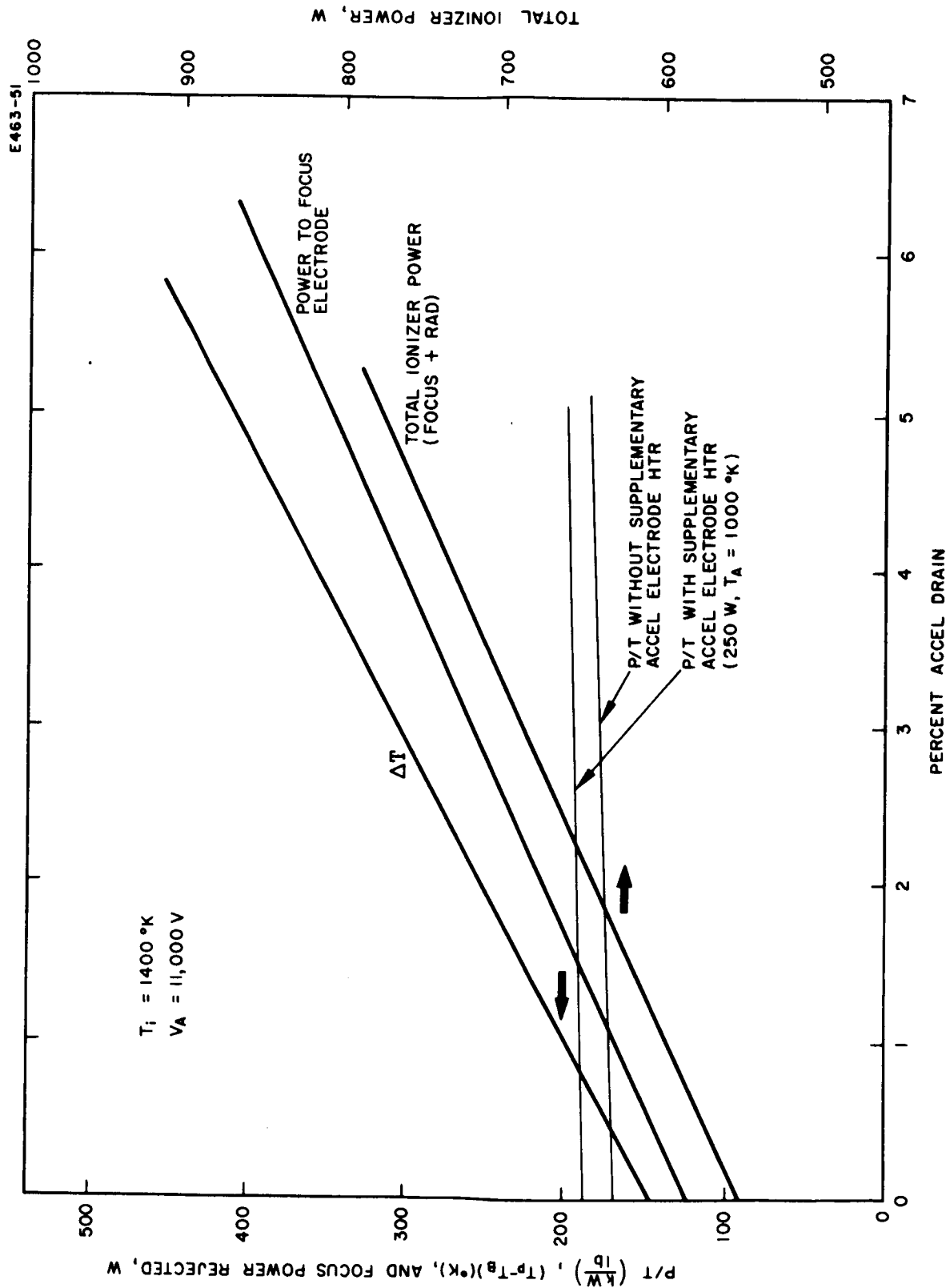


Fig. II-3. Peak focus temperature, power to be rejected by the focus electrode, power to thrust ratio, and total ionizer power for the 20-strip engine.

Fig. II-4. This view shows the structure for the ionizer and electrode support. Included are two of the six insulator stacks employed between the electrode mounting plates. The electrical isolation between these plates through the insulators is from the focus mounting plate to the decel mounting plate and from the decel to the accel mounting plate. This insulator arrangement results in a longer length and a lower electrical potential across any given insulator and thus provides maximum insurance against insulator failure. All of the insulators are protected by double reentry shielding to minimize particles impinging on the insulator surface; these particles would produce a conducting layer. The ionizer assembly is also isolated from the focus mounting plates (even though the two are at the same electrical potential) for performance evaluation purposes as well as to facilitate measurement of the performance of the cold focus engines when operating in parallel.

The primary design requirement is to maintain the engine optics as well as the prescribed limit of focus electrode temperature under engine operating conditions. The ionizer and manifold assembly operates at a temperature of 1500°K with a resultant structure temperature of 700 to 900°K . To maintain the engine optics, the thermal expansion of the electrode support must match the thermal expansion of the ionizer, in addition to meeting the structural requirement of electrode support under tension. The titanium alloy 6Al-4V was used for this application because its thermal expansion at 600°K matched the expansion of the 1500°K tungsten ionizer.

Positioning of the ionizer assembly with respect to the electrode mounting plate structure is maintained through the geometric center of the ionizer. The ionizer mounting plate is indexed to the focus mounting plate through an insulated bushing and sleeve assembly. In addition, the ionizer assembly is mounted to the ionizer mounting plate through two grooves located on each of the orthogonal center lines of the ionizer. Tungsten carbide balls in the ionizer grooves and in corresponding grooves on posts on the mounting plate permit the ionizer to expand or

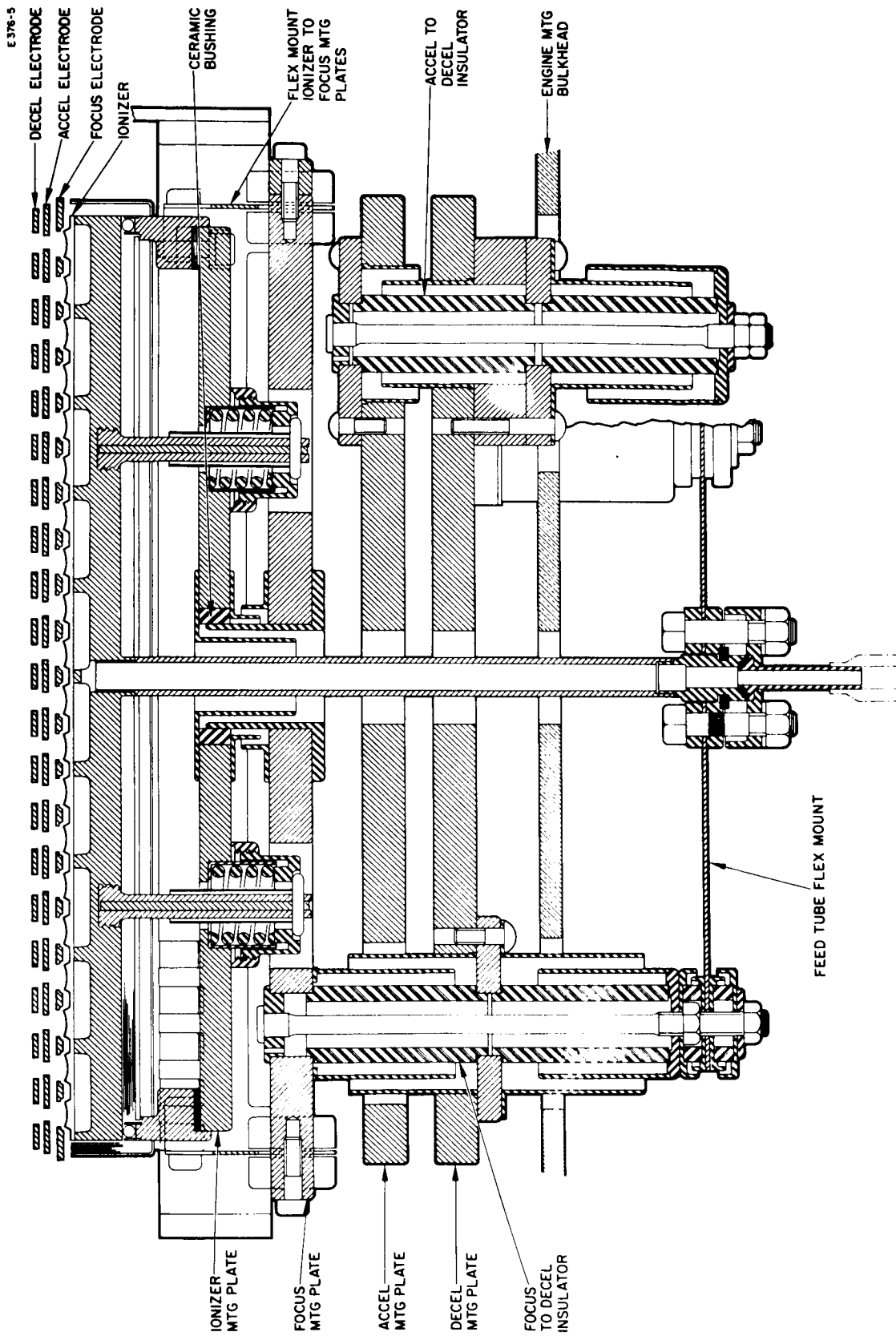


Fig. II-4. Side view of 20-strip engine design, with ionizer strips and electrodes perpendicular to the plane of the paper, showing the ionizer and electrode support structure.

contract. The ionizer is held to the mounting plate by two spring loaded bars. The spacing between the focus mounting plate and the ionizer mounting plate is maintained by the two insulated flex mountings on the extreme end of the two plates.

The electrodes are fastened to the structure by a pair of knife edge supporting "fingers." One finger is a fixed support, the other, a leaf spring support. The leaf spring support is necessary to maintain a tension load on the electrode as the electrode heats and expands. The knife edge support is necessary to prevent the angular deflection of the leaf spring from applying a bending moment on the electrode.

A photograph of a 20-strip engine (Fig. II-5) shows the ionizer manifold, electrodes, and ionizer installed onto the engine frame. The focus electrode has copper braids brazed to the electrode end which serve as a heat path to the engine base. The focus electrode in this design is maintained below 900°K to 1000°K with a normal heat load to the focus electrode. A back view of the engine (Fig. II-6) shows the reentry shield insulator structure, feed tube, and base plates.

One of the major technical areas has been the fabrication of the ionizer-manifold assembly. The manifold which holds the ionizers and distributes cesium uniformly to their back side is machined from solid tungsten. This brittle material is machined, using conventional machine tools and carbide cutters, with the work maintained at 450°C . A photograph of the ionizer and heater side of the manifold is shown in Fig. II-7(a) and (b). The porous tungsten ionizer is fastened to the manifold by electron beam welding techniques. The ionizers are made in two-strip sections; these 10 sets of ionizers are used to make a 20-strip ionizer manifold assembly. A special technique of electron beam welding followed by periodic stress relieving is used in joining each ionizer to the manifold. The parts are uniformly heated before and after welding. The multiple welds of the ionizer to the manifold are accomplished with negligible distortion of the assembly. A photograph of the ionizer manifold assembly is shown in Fig. II-7(c). Additional details relating to all aspects of the ionizers are found in Section IV-A of this report.

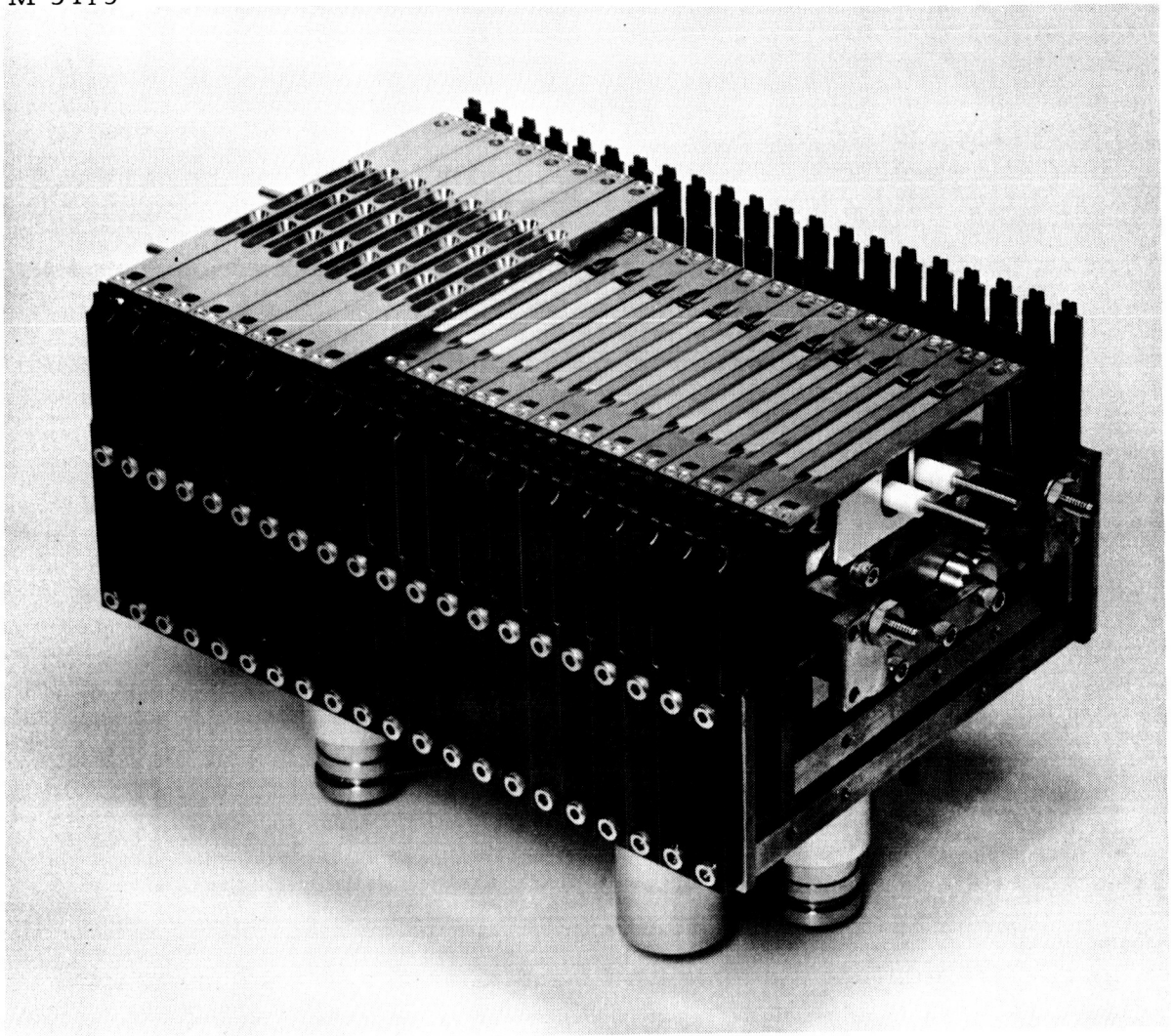


Fig. II-5. Photograph of 20-strip ion engine. This current engine includes both a cooler focus electrode and a decel electrode. Considerable simplification can result from elimination of either or both electrodes. This same basic structure can be used with any of the several modifications discussed in this report.

M 3414

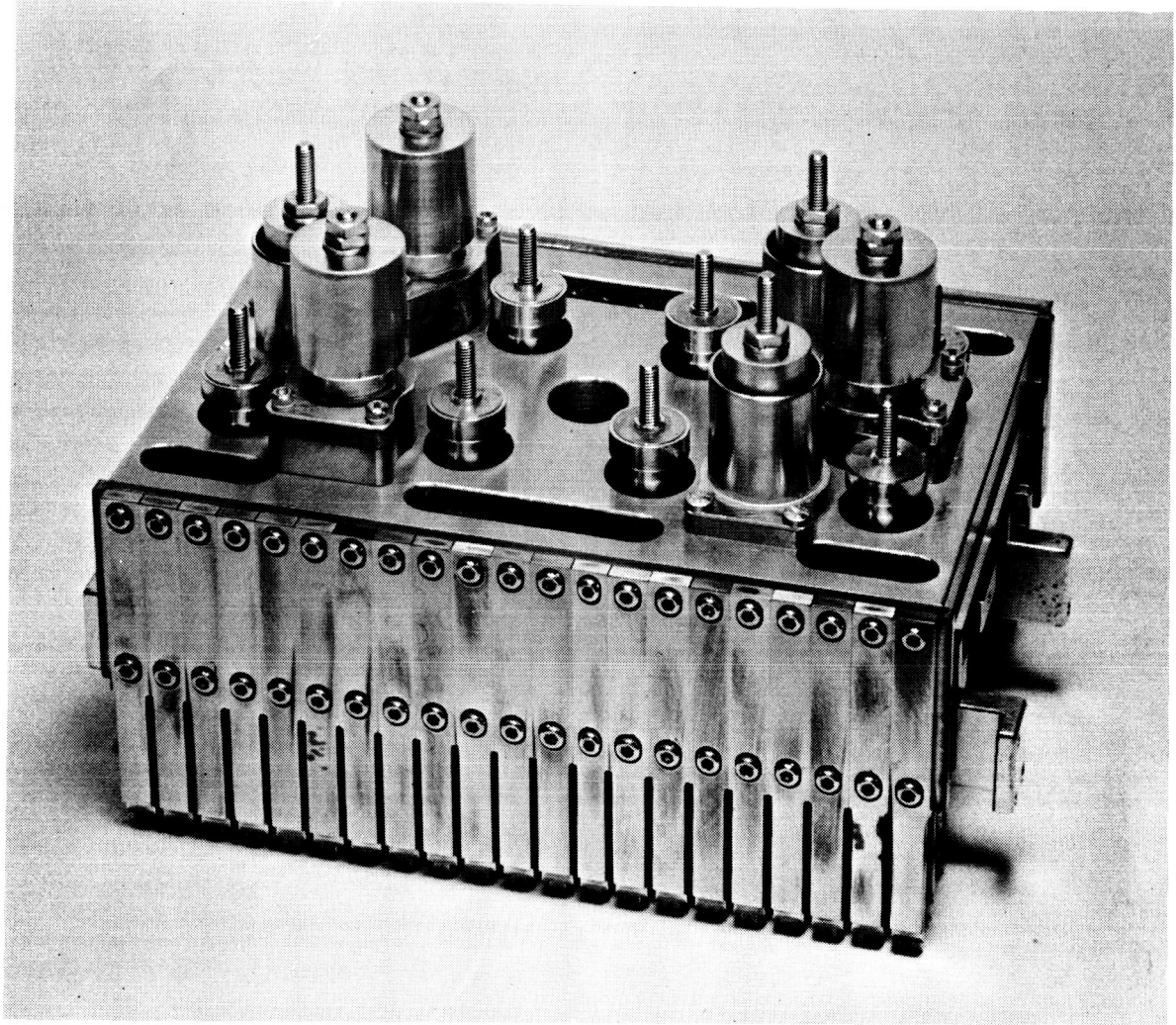
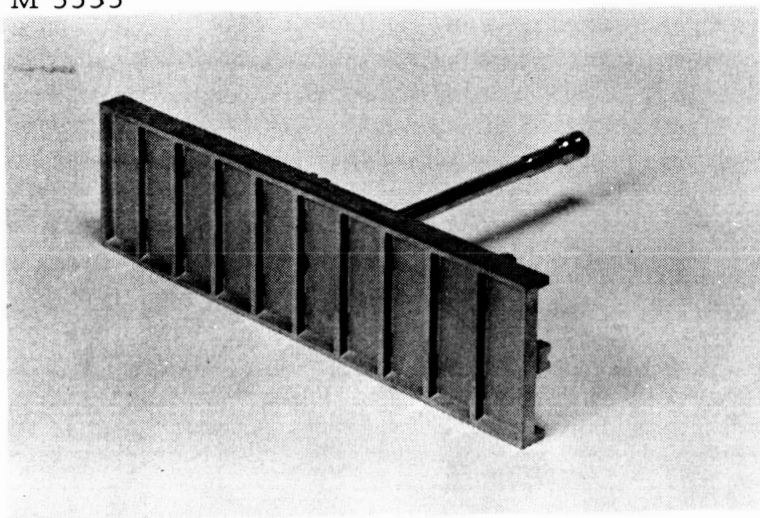


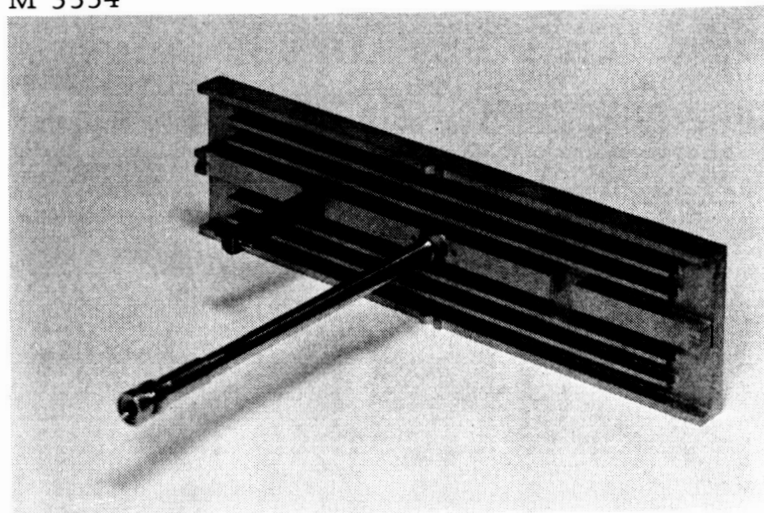
Fig. II-6. Back view of engine showing double shielded insulators and base plates.

M 3333



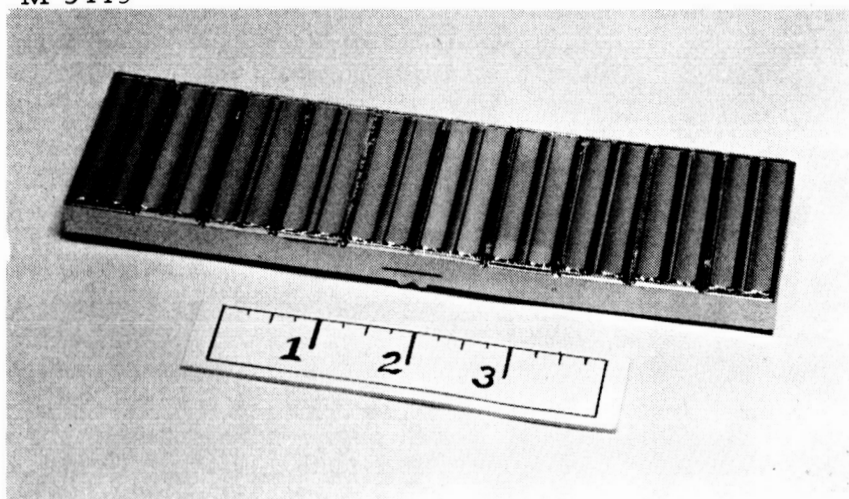
(a) Ionizer side of manifold.

M 3334



(b) Heater side of manifold.

M 3415



(c) Ten two-strip ionizers fastened to tungsten manifold.

Fig. II-7

The back side of the manifold contains the spiral tungsten heater. This heater is insulated from the manifold by shaped sections of alumina which support the tungsten wire with minimum impedance in the transfer of heat from the 1800°K tungsten wire to the manifold. Efficient transfer of heat from the wire to the manifold allows the heater wire temperature to be reduced and thus ensures against a heater failure.

Figure IV-34 in Section IV-B shows the reduction of wire temperature as the heat transfer from the wire to the manifold is increased. The relative heat transfer from the wire to the manifold is shown in Fig. IV-35 of the same section.

The heat transfer number (see Section IV-B-1) on the 20-strip design lies between six and eight versus one to two for earlier engines. More details are presented in Section IV-B of this report.

A recent space test showed that beam neutralization was effective without the explicit use of the decelerating electrode for an engine operating with a low accel-decel ratio. The 20-strip engine design allows easy removal or reassignment of the decel electrodes. It is planned to use the reconnected decel electrode as a charge exchange diverter electrode. In this operating mode the electrode will be connected so that its potential will be 5000 V more negative than the accel electrode. Charge exchange erosion would thus be shared by both the accel and diverter electrode. The more negative potential of this diverter electrode should result in more erosion of this electrode than the accel electrode. The optic dependent accel electrode should thus have an enhanced life.

This engine was designed as a conservative vehicle for the determination of long life effects in ion engines. Actual tests to date of this engine design have been carried out using scaled down three-strip versions, which are otherwise essentially identical to the 20-strip engine. The results of the three-strip engine tests are found in Sections III and V of this report.

The first 20-strip cooled focus ion engine will enter a test phase in the early part of December 1964. The engine will be provided with 12.5 lb of cesium. The engine will be tested for 500 to 1000 hours at a current density of 15 mA/cm^2 . The engine incorporates a diverter electrode.

III. ENGINE TESTS

A. Three-Strip Engine Program Summary

A series of five three-strip ion engines was designed and evaluated during the contract period. These engines were designed to prove or establish the technical approach required for the design of the 15 to 23 mlb engine described. The first engine (32-40-8) used a 0.040 in. wide focus electrode; the latter four engines (32-150-1, -2, -3, and -4) incorporated an improved thermal design and used a 0.150 in. wide focus electrode. A photograph of engine 32-150-3 is shown in Fig. III-1. Engine 32-40-8 was evaluated primarily to prove the thermal analysis that had been made during the latter phase of Contract NAS 5-517. The referenced analysis showed that a practical engine could not be designed using the 0.040 in. wide focus electrode. The electrode as well as other thermal conduction paths could not be made to have a thermal impedance sufficiently low to satisfy both the lower limit of sink temperature and peak electrode temperature established for the program. The engine used a basic design that required a minimum of rework; it served only as an expedient to confirm the theories that had been developed.

The first two engines in which the 0.150 in. wide focus electrode was used also were employed as thermal test vehicles. These engines provided us with information on the heat load to the focus electrode, the temperature distribution of the focus electrode, the effects of ionizer temperature on these heat loads, and the temperature distribution of the accel electrode. The details of these tests are reported in Section IV-C of this report.

In addition to the electrode thermal data, it should be noted that the first engine tested, 32-150-1, operated for a total test time of 100 hours. Twenty percent of the time was at the contract required current density of 15 mA/cm^2 . This engine was still undergoing improvement in its thermal design. It required, in contrast to the succeeding engines, artificial cooling to keep the peak focus temperature less than 1000°K .

M 3144

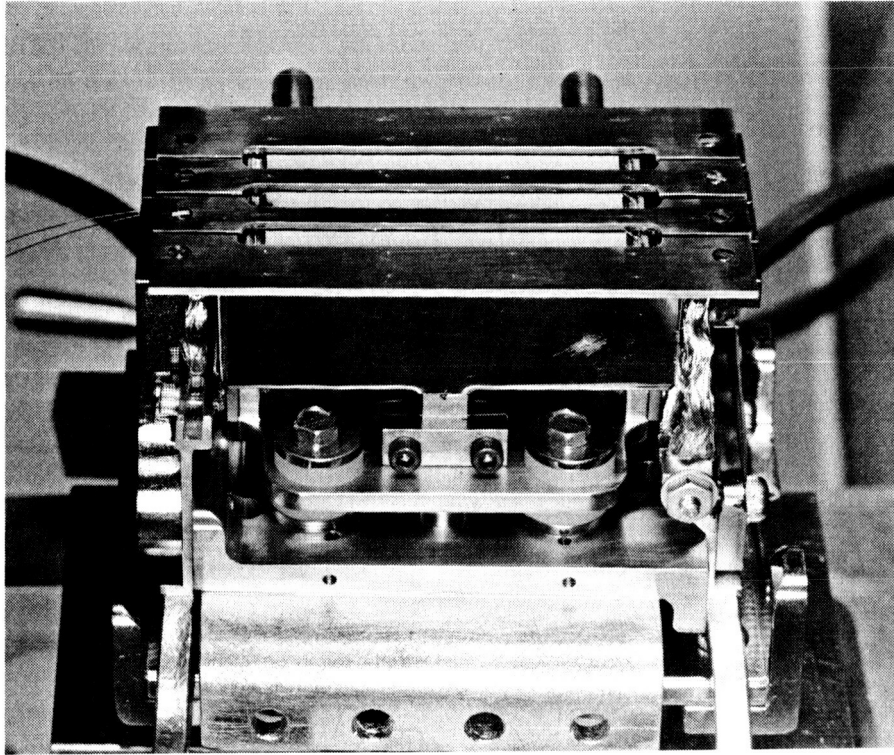


Fig. III-1. Three-strip engine 32-150-3.

In addition to the need for continued thermal design improvement, engine 32-150-1 alerted us to the need for (1) careful processing of the ionizer surface, (2) maintaining all exposed surfaces at the engine rear at low temperatures to avoid surface ionization, (3) improving the insulator design so that the electrode potential was supported with respect to ground rather than the full accel potential being supported across a 5/8 in. long ceramic, and (4) double shielding all insulators.

The first two engines used the Philips Mod A ionizer material. In comparison with our current standards, this material was extremely poor. The pore count was 10^5 pores/cm² versus 10^6 pores/cm² for the Mod E material used on the latter two engines. Photomicrographs of these two materials are shown in Fig. III-2(a) and (b). Although careful processing techniques were applied to the ionizers during the entire program, it should be pointed out the factors affecting the ionizer surface are only now beginning to be understood. The NAS 3-4110 Summary Report presents recent data on contamination of ionizers from processing in a vacuum furnace; it was shown that furnace temperature in excess of 1900°C resulted in 1500 ppm of molybdenum on the ionizer. Further increases in furnace temperature to 2300°C resulted in 3.2% molybdenum and 6.4% tantalum on the part. In addition, our carbon analysis and cleanup experiments showed the effectiveness of wet hydrogen firing to remove surface carbon as well as to lower the bulk carbon in porous tungsten. In addition, we experimentally observed improvements in engine performance by substituting D.C. 705 for Octoil 20 diffusion pump oil.

Improvements were continually made in the engine test facilities. The discussion on the test of engine 32-150-3 describes the use of a cold finger to cover the diffusion pump outlet and a cryowall to surround the engine. These items helped to keep the engine free of cesium as well as pump products during the test.

M 3193

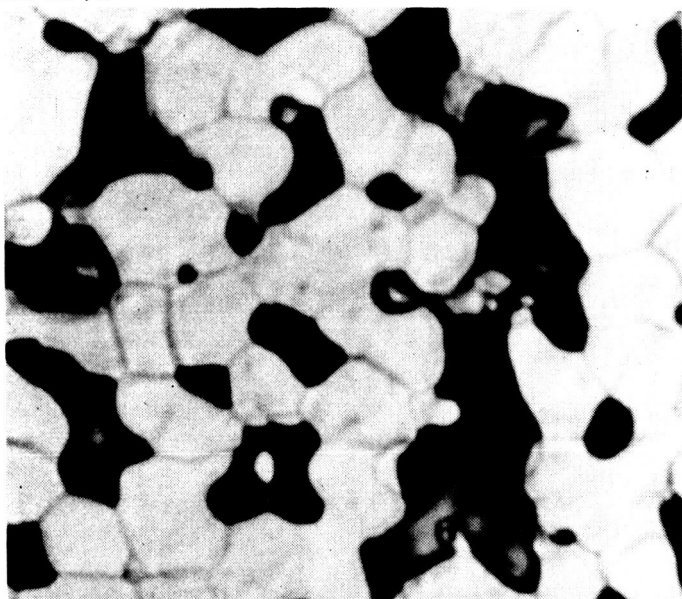


Fig. III-2(a).
Photomicrograph of Mod A
ionizer material (2000x).

M 761

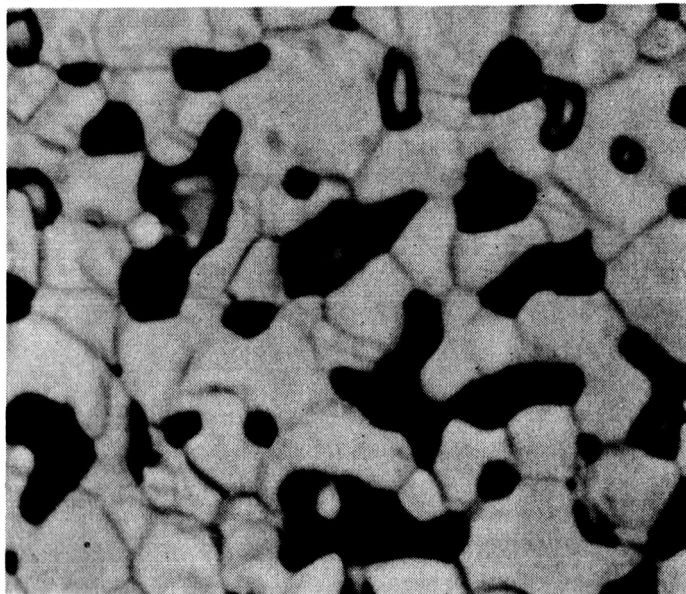


Fig. III-2(b).
Photomicrograph of Mod E
ionizer material (2000x).

Although considerable effort was applied to each separate engine test in an attempt to correct all known problems, it was observed that one major fault reappeared in each test of engines 32-40-8 through 32-150-3. This problem was the accel electrode drain current which was time dependent and always limited the engine test to less than 100 hours of operation. It is possible that this problem plagued previous engine tests over the past years but was obscured by other engine design problems which limited engine life to a few hours. The best way to show the accel drain problem is to examine the time current characteristics of the engines tested. Figure III-3 shows a comparison of engines 32-150-1, -2, -3, and -4. It is observed that only engine 32-150-4 showed no signs of increasing accel drains up to the 232nd hour of test. An experimental program, part of the test on engine 32-150-3, had indicated that the accel drains were controllable by operating the electrode at 900 to 1000°K rather than 500°K, the normal temperature for a 1400°K ionizer. This significant discovery was a major factor in making this cold focus type of contact engine into a workable device. An analysis of the accel drain problems with respect to electric field and temperature effects is presented in Section IV-E. An exact understanding of the changes in the electrode surface with time has not been attained.

The ionizer heater presented another problem in earlier engines. It was determined that heater failures were occurring because of chemical reactions of tungsten with melted alumina heater insulators. A concept was originated to reduce the heater wire and alumina temperature such that these parts operated only a few hundred degrees above the ionizer temperature. The concept was simple. It was only necessary to increase the area to which the filament radiated and surround the filament and alumina with manifold structure at ionizer temperature. This concept was subsequently analyzed and used in recent engine tests. The present heaters show no signs of degradation with time.

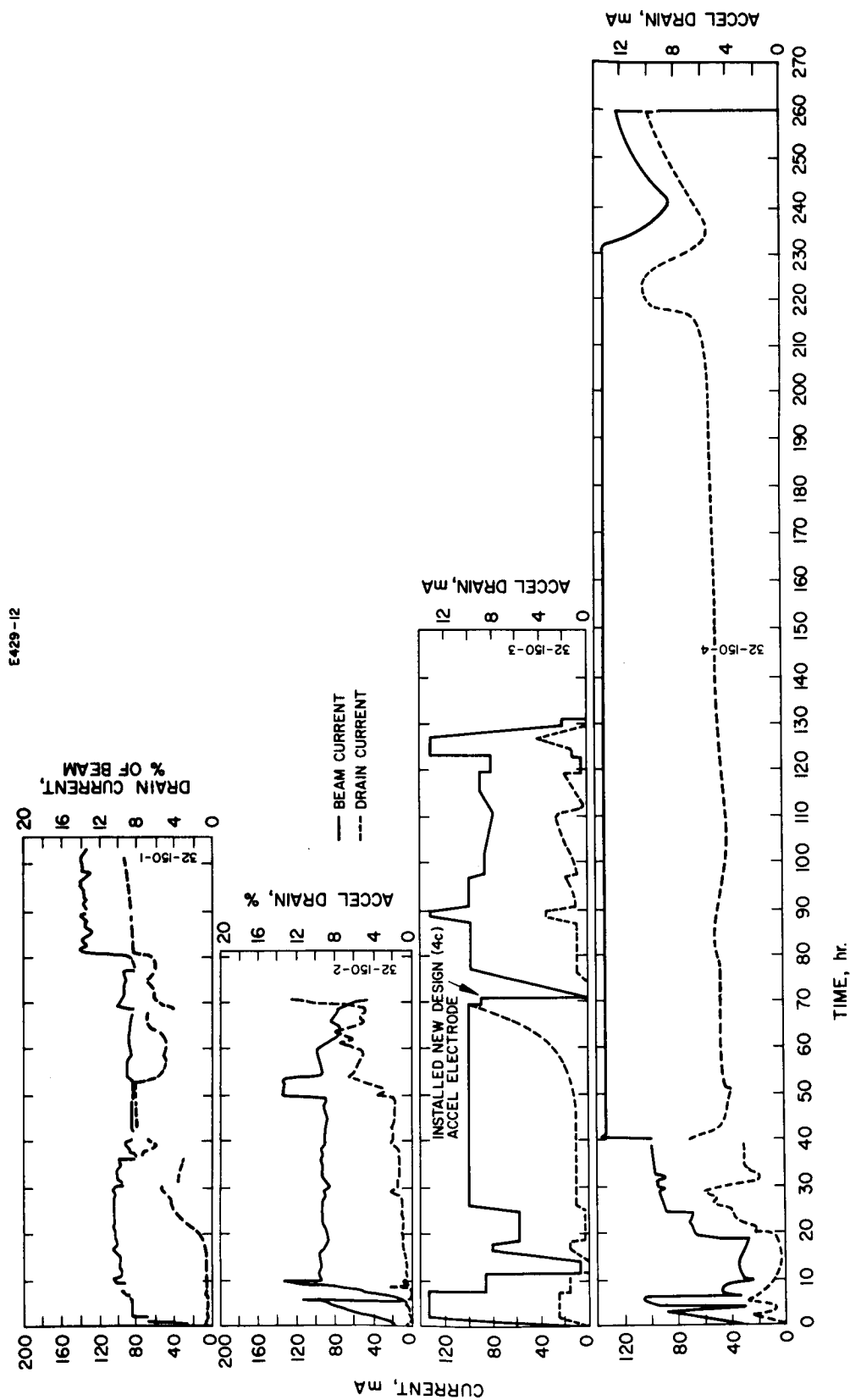


Fig. III-3. Beam current and accel drain data from long duration tests of multistrip engines 32-150-1, 32-150-2, 32-150-3, and 32-150-4.

Ionizer neutral fraction measurements have been a part of recent engine tests. A new neutral detector was designed which uses a liquid nitrogen cooled collimating tube and collector. The collector is isolated from ground. The device was designed to look at a narrow $1/8 \times 1-1/8$ in. section of an ionizer strip. The positioning of the device allows neutrals from only the surface of the ionizer to enter the detector; the device cannot see neutrals evaporated from other parts of the engine. Saha plots and neutral fraction measurements have been made on engines 32-150-3 and -4. The 32-150-4 measurements are of doubtful value because of incorrect initial positioning of the detector. The 32-150-3 data indicate that 1% of neutrals originate from Mod E material at 11 mA/cm^2 .

The most significant result of the three-strip engine tests was the comparatively long life attained by engine 32-150-4. This engine operated for a total test time of 260 hours. It ran 70% of this time at a current density of 15 mA/cm^2 . The remaining test period was at a current density of 10 mA/cm^2 . The limitation of the test life resulted only from back sputtering of a molybdenum structure onto the ionizer. The tests produced charge exchange erosion data which corresponded within 8% to the theoretically derived values for this engine system.

The test details for engines 32-150-3 and 32-150-4 are presented in the following sections. The previously tested engines served mostly to provide insight into general engine problems. Analyses and data relating to these tests are found in Section IV.

B. Engine 32-150-3

1. Summary

This engine was tested during the period 19 April 1964 to 8 July 1964. This engine, in contrast to the previous three-strip ion engines, incorporated the following features.

- a. A high pore count ionizer material, Philips Metalonics Mod E was used. This material has a pore density of 2×10^6 pores/cm² and an average pore size of 3.5 to 4 μ .
- b. The engine insulators, as in 32-150-2, were shielded. The insulators supported the accel and ionizer structure with respect to the decel structure. Hot surfaces such as the feed tube and heater leads were radiation shielded to prevent the formation of ions at the rear of the engine. With unshielded insulators the sputtering from the spurious ions results in coating of the insulators and eventually causes engine failure.
- c. The engine assembly included a helical shroud around the engine structure. The shroud acted as a local cryotrap in the vicinity of the engine and thus served to trap reflected cesium and minimize cesium deposits near the engine.
- d. In addition to the helical cold wall, the engine system also included a cold finger to pass in front of the diffusion pump port. The pump port is within a few feet of the engine face. The cold finger serves to ensure that pump oil does not deposit onto the ionizer.
- e. A neutral detector designed to interrogate a narrow (0.125 x 1.125 in.) strip of ionizer was also included as a part of the engine assembly.

- f. The engine optics were identical to previous engines (Model 70 optics). The first two phases of the test used conventional rectangular accel and decel electrodes. The third and fourth phase of the test included an accel electrode with the center section removed. The modified electrode system, designated the "double optics system," reduced the accel electrode current to the focus electrode and ejected focus generated ions through the center of the accel electrodes. Other advantages are described later in this report.
- g. In the fourth phase of the test, the accel electrodes were radiant heated by a tungsten wire-molybdenum reflector heater placed at the front of the engine.
- h. The facilities were also changed prior to commencing the third phase of test. Dow Corning 705 was used in the latter tests whereas Octoil 20 had been used in the 4' and 5' vacuum systems during all previous engine tests. The wedge collector was replaced by a flat copper plate at the engine rear.

A photograph of the engine, helical cryowall, cold finger, and neutral detector prior to the start of test is shown in Fig. III-4. Figure III-5 shows the electrode assembly which was used for the first two phases of test. The collimating tube on the liquid nitrogen cooled neutral detector is directed to see a portion of the ionizer surface without receiving neutral particles evaporated from the electrode surfaces. The collector is floating and connected to a micromicroammeter. The background noise from this detector is two to three orders of magnitude below the signal level.

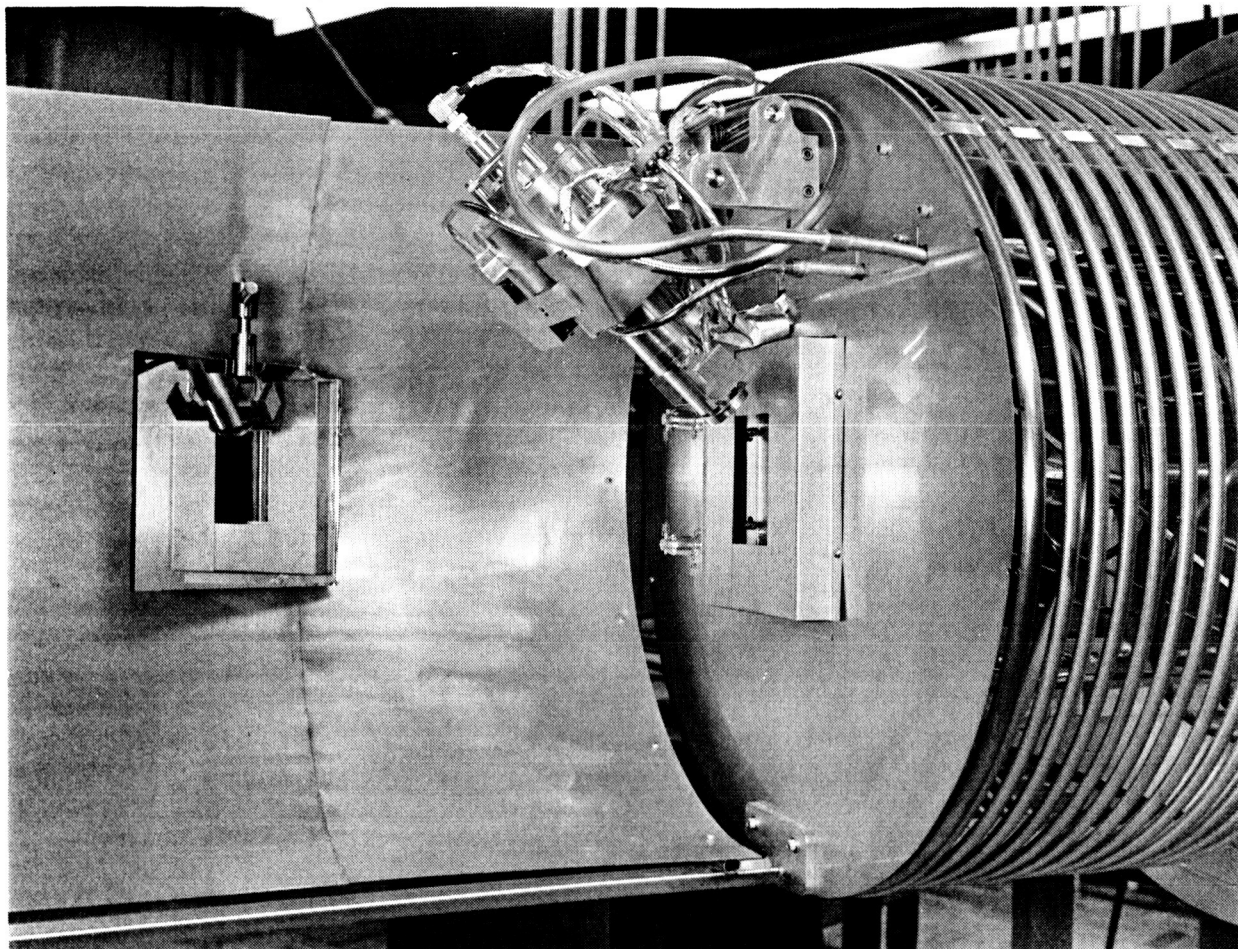


Fig. III-4. Engine 32-150-3 mounted for test. The ionizer reflection can be seen in the mirror. The cryowall helical shroud is used to trap reflected cesium. The cold surface prevents the pump opening from seeing the engine ionizer. The neutral detector is positioned to see a portion of a single strip of the ionizer.

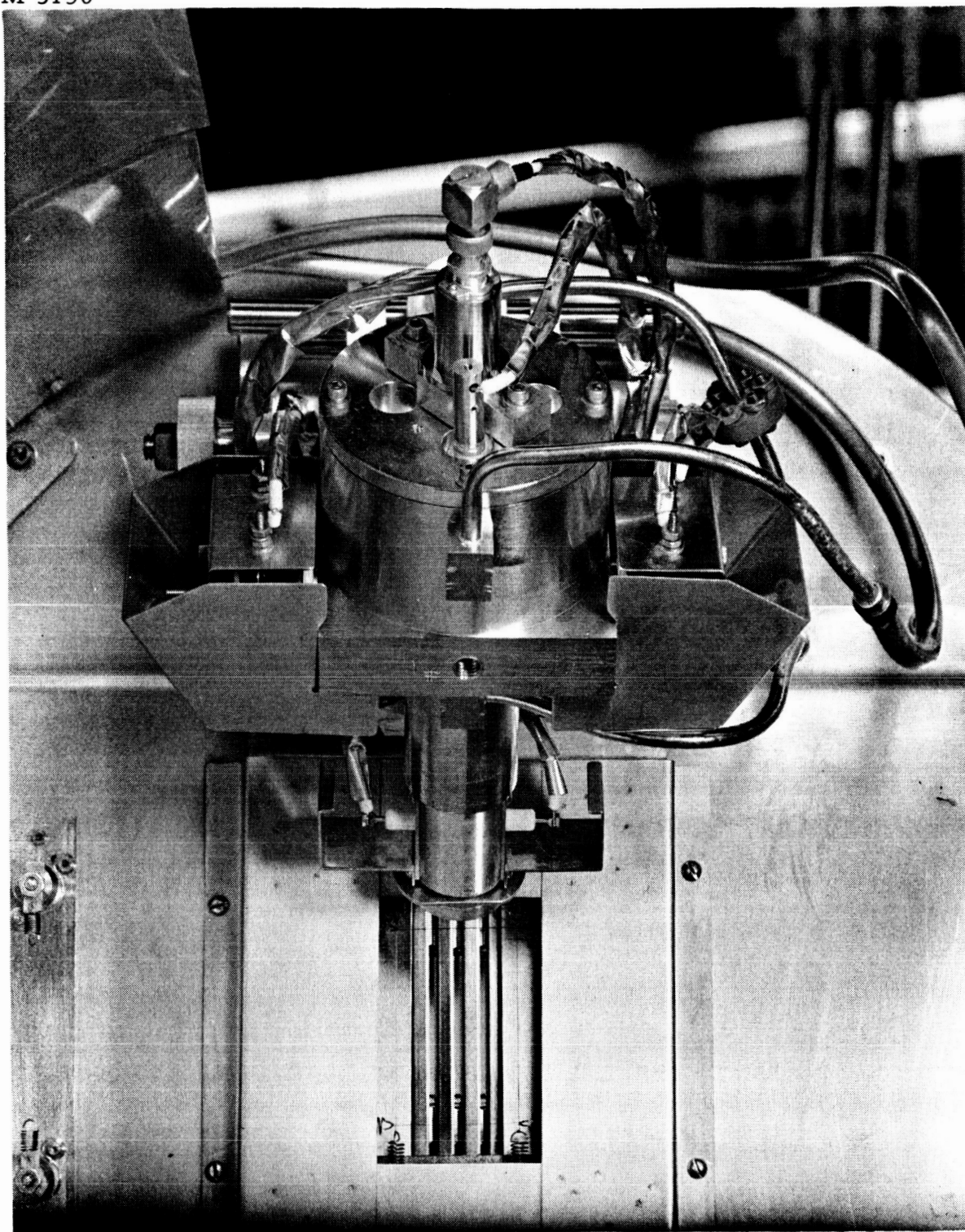


Fig. III-5. Front view of engine 32-150-3 showing the electrodes as well as the position of the neutral detector.

The engine was operated for 160 hours. During the last 130 hours, the engine provided a beam current density between 9 and 15 mA/cm². The average current was 10 mA/cm²; the drains averaged 2.18%. The 160 hours of test were divided into four test phases. The first phase involved ionizer cleanup. Critical temperature data showed that the characteristics were rounded and were shifted to the right of the oxygenated tungsten line. It was apparent that a contaminant was on the surface of the tungsten. The test involved operation at low current density (~ 1 mA/cm²) with the addition of oxygen into the vacuum system to remove carbon from the ionizer surface. It was determined that the surface could be cleaned by subjecting it to a partial pressure of 10^{-5} Torr oxygen for a period of 7 hours.

In the second phase of the test only the engine electrodes were replaced since scales had appeared on the electrodes as a result of the in situ oxygen cleanup of the ionizer. During this phase of the test, the engine operated for 70 hours at current densities ranging from 10 to 15 mA/cm². The drain current started at 1%; after 50 hours of operation it increased to about 8% with no upper limit in sight. The ionizer seemed to show that an operating temperature between the clean porous tungsten and oxidized tungsten was possible.

The time dependent drain was similar to the characteristic observed on engines 32-150-1 and 32-150-2. Previous erosion data of the accel electrode as well as the ability to suppress accel erosion by control of the focus temperature indicated clearly that the problem was not from focus ions. In addition, drain separation experiments as well as engine tests with the electrodes removed showed that the drains, as previously suspected, were not in the insulator structure. The drains were thus considered to be electrons derived from the accel electrode. The diffusion pump oil and the collector were changed prior to the third test phase. The pump oil was changed from Octoil 20 to D.C. 705. A comparison of the pump oils, presented in another part of the report, indicated that the D.C. 705 produces few contaminants and thus is not likely to contaminate the ionizer.

The large wedge collector which was positioned within 2 ft of the front of the engine was removed and a flat plate collector was installed at the end of the tank. It was first thought that the arrival rate of sputtered copper from the collector to the engine was causing a reduction in tungsten surface work function and therefore required a higher ionizer temperature. Subsequent analysis, presented elsewhere in this report, shows that the collector change was not necessary.

The third phase of the test consisted of an experiment to determine whether the drains could be reduced by removing a nonessential portion of the accel electrode. It was believed that an open accel structure would reduce the rates of arrival of cesium and contaminants to the accel and that it could therefore be possible to lower the drains and eliminate the time dependent drain increase. The test showed that the time dependent phenomenon was not eliminated. However, the engine's sensitivity to accel temperature was greatly lowered. The engine was able to operate at an ionizer temperature lowered by 100°K . The ionizer power was also lower by 100 W. It was apparent that partial success was attained. The next step was to limit the drains by modifying the operating temperature of the accel electrodes. Two approaches existed for limiting the drains. One was to cool the accel electrodes; the second approach was to heat the accel electrodes. The accel emission did not seem to follow the characteristics of clean copper.

Previous attempts to collect S curve data always indicated that the drain current increased as the accel temperature was decreased. Control of the accel temperature during the previous experiments was indirect and was accomplished by varying the ionizer temperature. The apparent work function of the accel electrodes at 500°K was 1.05 eV with measured accel current densities of 1 mA/cm^2 . It was believed that reducing the electrode temperatures to inhibit accel electrons, probably would result in further reduction in the apparent work function of the surface; this would worsen the situation before a gain could be

observed. In addition, it was difficult to reduce the accel temperature on the engine. Thus, in phase 4 the accel temperature was raised by indirect heat radiation from the front of the engine to the electrodes. It was believed that a temperature approaching 1000°K would sufficiently reduce the cesium surface coverage on this complex surface as well as evaporate coatings which were lowering the work function. Accel temperature measurements were not made during this experiment. Heating the accel electrodes at the beginning of phase 4 did reduce the accel electron drain substantially. With the engine beam current density at 10 mA/cm^2 , the drains were reduced from 2.7% to 0.45%. The accel drain was 0.9% at 15 mA/cm^2 . The effects of the heated accel on the time dependent drains could not be observed because of experimental setup problems. The engine beam intercepted the molybdenum accel heater reflectors and sputtered material back to the ionizer.

A principal parameter time history for phases 2, 3, and 4 is presented in Fig. III-6. Photomicrographic examination of the phase 3 and 4 accel electrodes after test showed no charge exchange erosions. The total operating time for these electrodes was only 60 hours. The details of the 32-150-3 test are presented in the following sections.

2. Detailed Test Results

a. Phase 1 — The first test phase involved ionizer evaluation. Critical temperature and work function measurements were made. The critical temperature measurement seems to be more applicable from an engine point of view since the measurement is made in an engine environment, i. e., with cesium. In general, it is difficult to attain the electron work function of clean tungsten in typical engine test chambers with a pressure of 10^{-6} to 10^{-7} Torr; however, it seems possible (but difficult) to measure ion work function and critical temperature characteristics of clean tungsten in the engine chamber environment with cesium in the system.

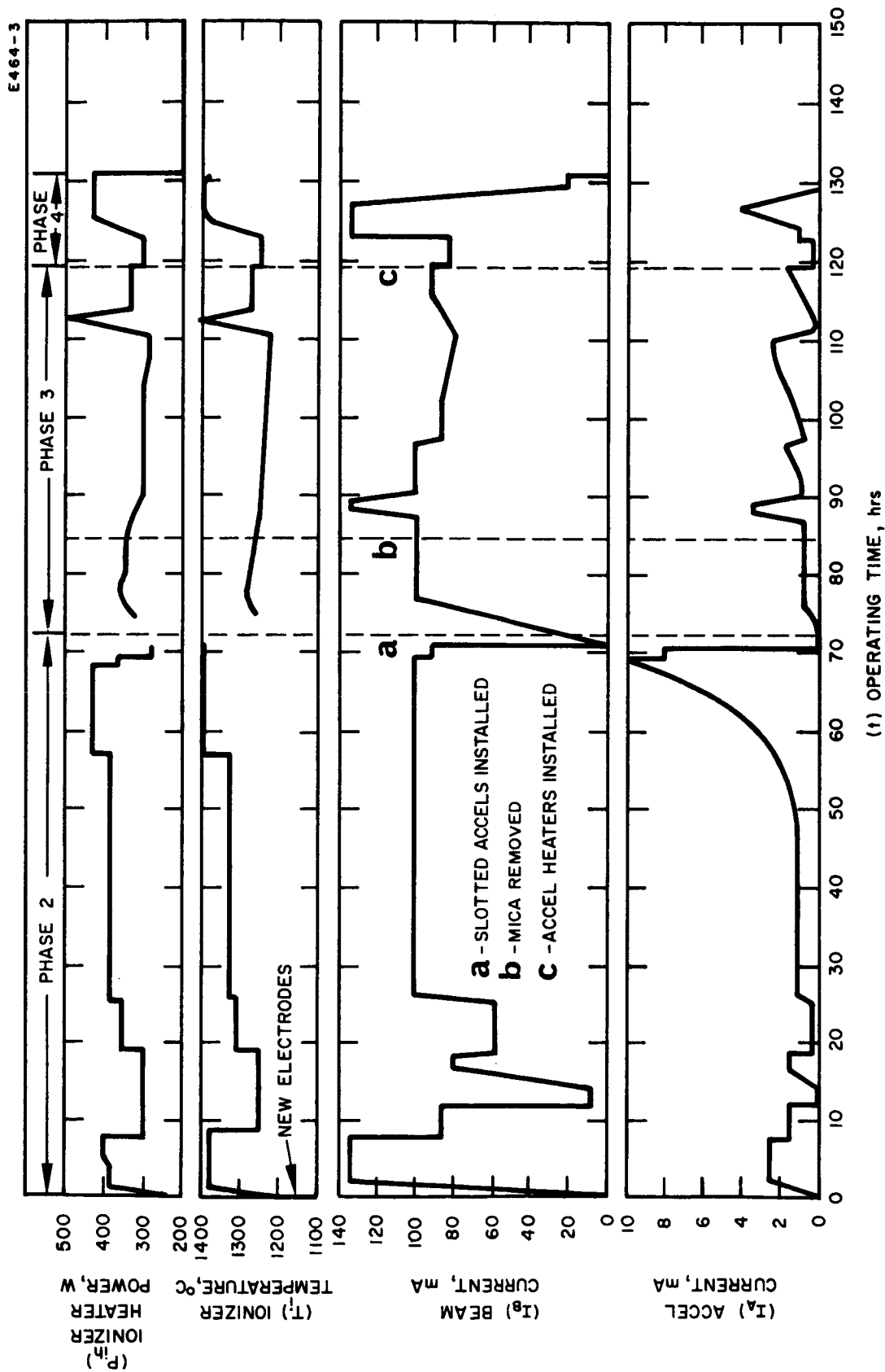


Fig. III-6. Principal parameter time history for engine 32-150-3, phases 2, 3, and 4.

Initial critical temperature characteristics are shown in Fig. III-7. The first curve shows a typical oxygenated surface characteristic whereas the subsequent curves seem to indicate a reduced ability to ionize the cesium. The chamber pressure during the tests was increased from 3×10^{-7} to 6×10^{-7} Torr. Approximately 50% of the chamber pressure was oxygen.

Increasing the ionizer temperature to 1330°C resulted in a rise of 30% in the mass 28 peaks. This was accompanied by a reduction in mass 32 peak. The oxygen was probably reacting with the carbon monoxide on the ionizer surface. However, the oxygen arrival rate was not sufficient to "clean" the ionizer surface (see curves 4 and 5 in Fig. III-7).

Figure III-8 shows the effects of continued treatment with oxygen. Curve 6 shows the critical temperature characteristic after 24 hours at a partial pressure of 3×10^{-6} Torr. This curve is essentially the same as the previous curves 4 and 5 in Fig. III-7. Curve 7 shows the results of 2 hours of oxygen environment at 10^{-6} Torr while curve 8 shows an improvement when the surface was exposed to a partial pressure of 10^{-5} Torr for 7 hours. The current density was increased to 6 mA/cm^2 as shown in Fig. III-8, curve 9. This test was terminated because of arcing caused by a loose thermocouple and tungsten scale deposits on the accel electrode.

The engine was removed from the chamber to make the thermocouple repairs as well as to repair a loose neutral detector shutter and mass spectrometer filament; the electrodes were not changed. Additional critical temperature data were taken upon return to the chamber. Figure III-9 shows subsequent test results which indicate continued clean-up of the ionizer surface. However, the scale deposits on the electrodes limited the engine operating voltage.

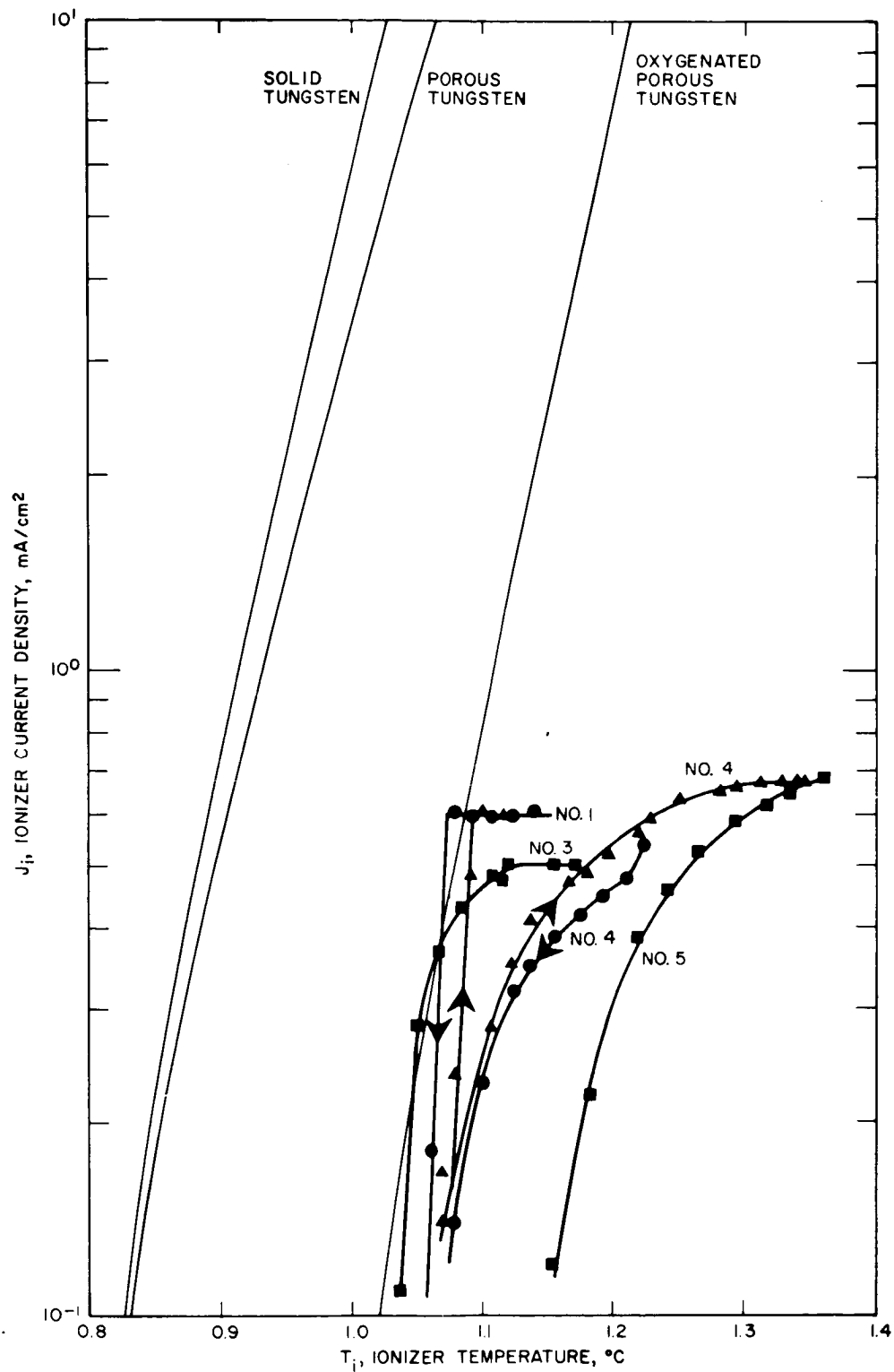


Fig. III-7. Critical temperature curves for engine 32-150-3. Curve 1 is the initial curve taken on this engine. Curve 3 was taken before oxygen treatment. Curves 4 and 5 were obtained after initial oxygen treatment.

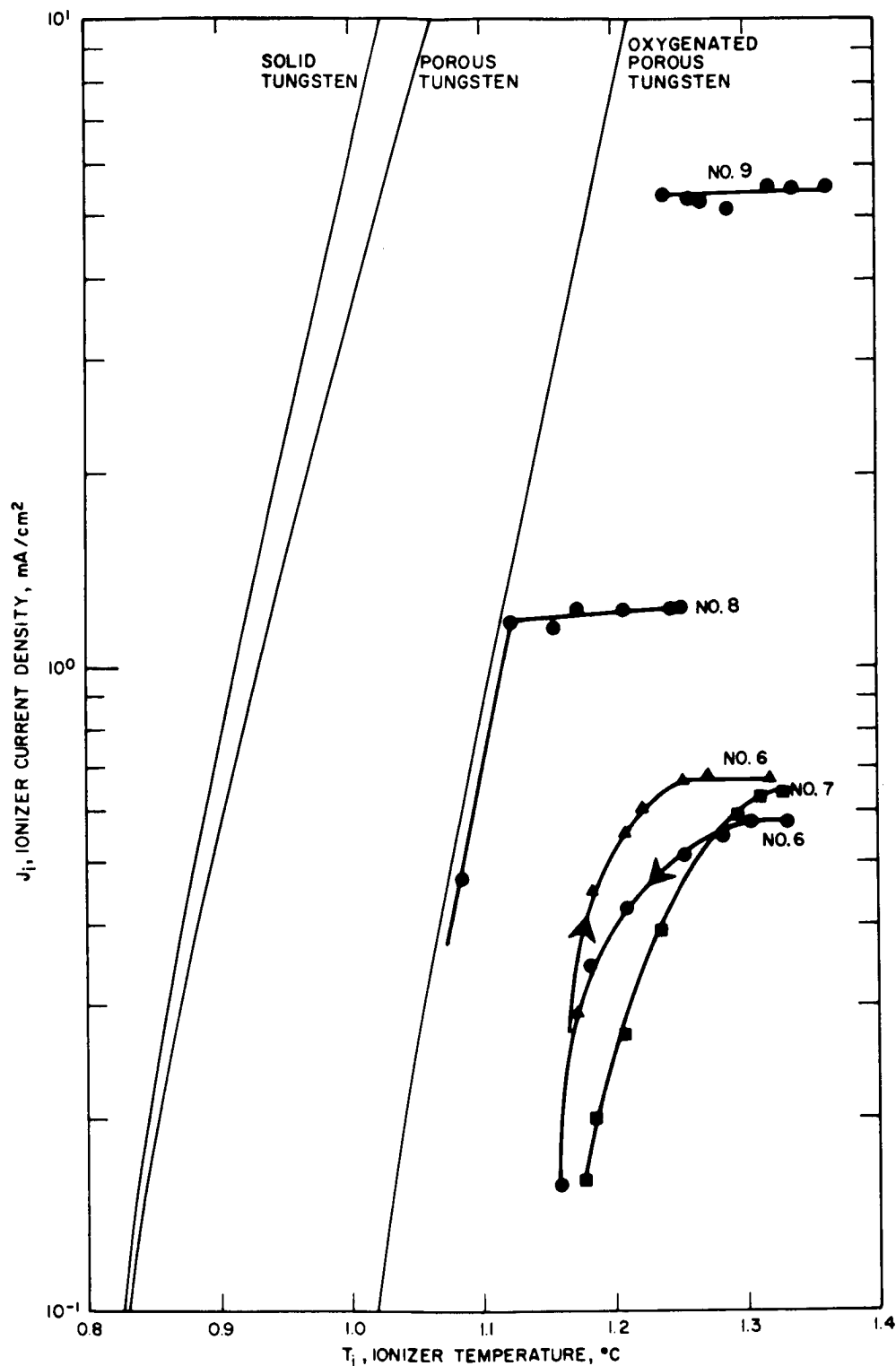


Fig. III-8. Critical temperature curves for engine 32-150-3. Curves 6 and 7 show the inability to clean the surface after 2 hours with a partial pressure of oxygen from 3×10^{-6} Torr, respectively. Curve 8 shows the apparent ionizer surface cleanup after 7 hours at a partial oxygen pressure of 1×10^{-5} Torr. Curve 9 shows a partial critical temperature curve for a current density of 6 mA/cm².

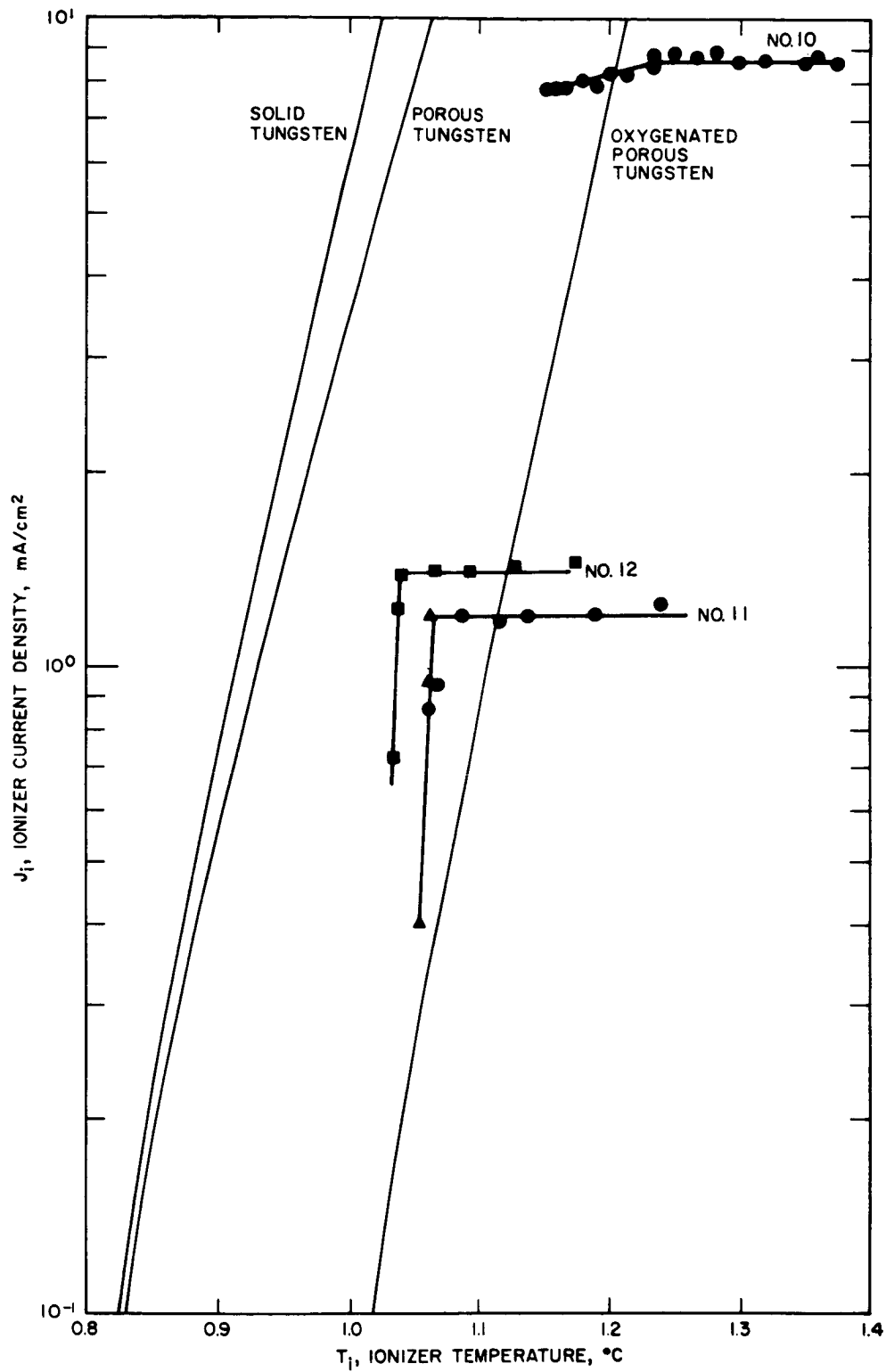


Fig. III-9. Critical temperature curves for engine 32-150-3. The curves show the ionizer improvement as engine operation continued.

The cleanup process had caused tungsten oxide scales to be deposited onto the accel electrode. The scales flaked off the electrode and caused an electrode short. The in situ cleanup of the ionizer was believed to be the cause of the scaling problem. However, considering the critical condition of the ionizer, the application of oxygen at this time was practically unavoidable. Figure III-10, from the final report of NAS 5-517, shows the reduction of tungsten oxide by cesium as a function of accel temperature. The reduction will take place below 475°K . When the accel is above this temperature, the tungsten oxide will evaporate. The accumulated test time during the phase 1 test was 34 hours.

b. Phase 2 — Phase 2 began with 4 hours of testing at current densities between 15 and 16 mA/cm^2 and drain percentages in the 1.5% region. The critical temperature was still near that of oxidized porous tungsten and a work function of 4.9 eV was measured. Rising drain currents and focus electrode temperatures dictated operation at a reduced current density. The ionizer temperature was maintained near 1325 to 1390 $^{\circ}\text{C}$ to minimize the accel drain.

Tests at an average current density of 11 mA/cm^2 were undertaken for several days. The purpose of these tests was to see whether the ionizer would be cleaned up with operating time. If the oxygen could be removed from the ionizer surface, a reduction in ionizer temperature could be achieved and operation at 15 mA/cm^2 could be resumed. A reduction in ionizer temperature, however, caused the accel drains to increase and this resulted in increased focus temperatures.

During test periods of 6 to 8 hours per day, the indicated oxidized surface remained on the ionizer. The drain currents and neutral fractions remained low. After the engine ran for several hours in a day, the drains tended to increase slightly. The engine would be shut down and restarted the next day, at which time the original operating point of about 1% drains at 11 mA/cm^2 would be achieved. Over several hours, the drains would creep up to about 1.5%.

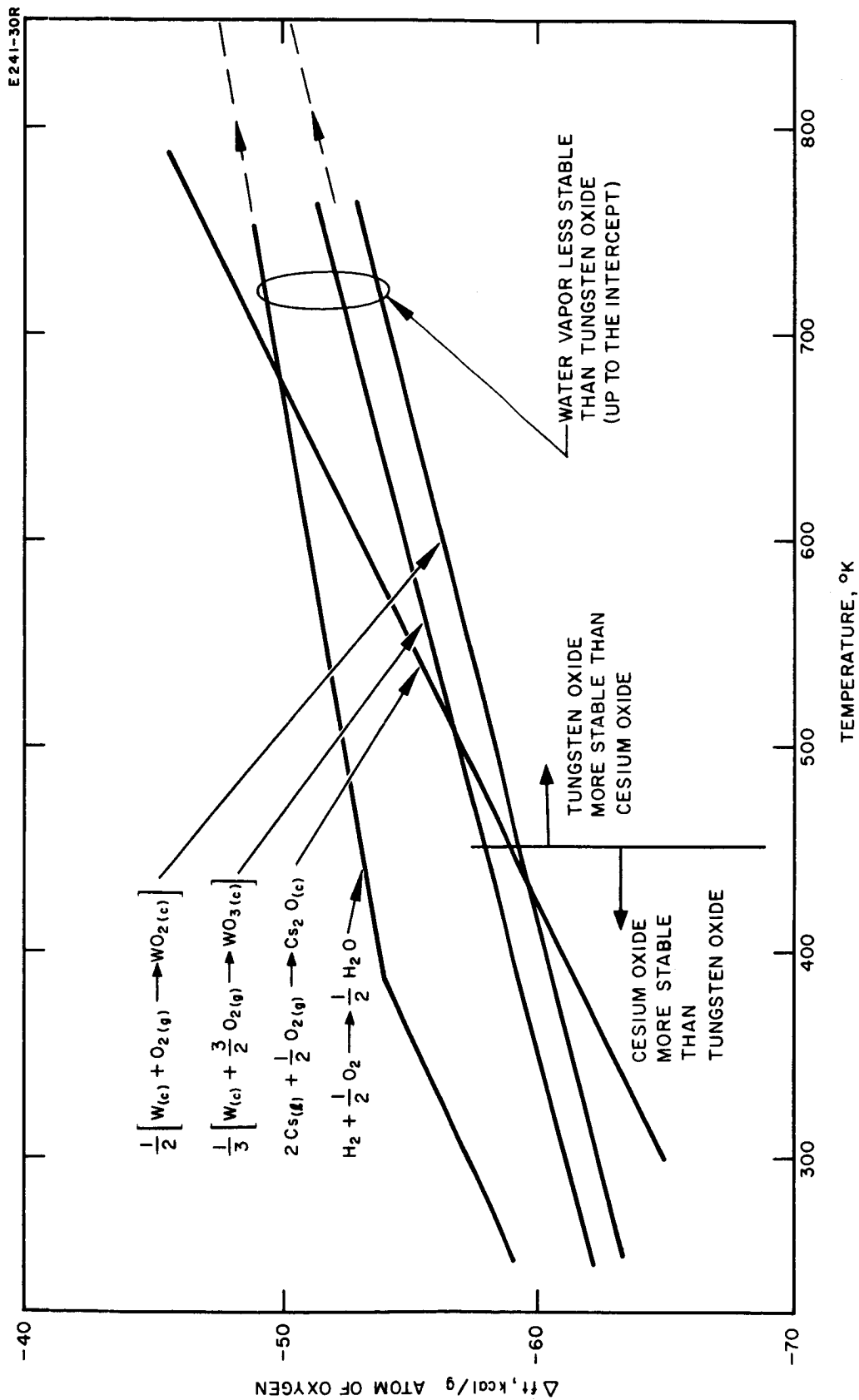


Fig. III-10. ΔF versus temperature for hydrogen and oxygen, tungsten and oxygen, and cesium and oxygen. Tungsten oxide forms below 1500°K , and tungsten oxide deposits as tungsten (when reduced by cesium) below 475°K .

After 40 hours of this type of testing, no changes in ionizer performance were evident; it was therefore decided to attempt an extended run at 11 mA/cm^2 . The critical temperature was 100°C higher than that of clean porous tungsten.

Changes in ionizer characteristics became evident within 10 hours after starting the extended run. The critical temperature began to drop slowly while the neutral fraction and drain currents rose. After a day of continuous running, the drain currents were at 6% and the neutral fraction had risen from about 0.2% to 1%.

Recorded neutral fraction is compared with the Saha equation in Fig. III-11. This figure shows the ion work function for the ionizer surface as well as the critical temperature.

Curve 1 in Fig. III-11 was taken at the start of the one-day run at 11 mA/cm^2 ionizer current density; it shows a work function of 4.83 eV and a critical temperature of 1265°C . The neutral fraction was 0.2%. The critical temperature falls on the oxygenated porous tungsten line (if plotted on a chart showing the oxidized porous tungsten critical temperature envelope). Curve 2 in Fig. III-11 shows the 24-hour test data. The work function had dropped to about 4.6 eV and the neutral fraction had risen to about 1%. The critical temperature dropped 80° to 1185°C . Curve 3 in Fig. III-11 is a later plot of ionizer performance which indicated a continued decrease in critical temperature. The ionizer temperature and power savings, which lower the neutral fraction and direct thermal power to the focus electrode, are countered by high drain currents at the optimum ionizer temperature. (See curve 3A in Fig. III-11.)

Continued testing of the engine with high drain current resulted in an interelectrode short. The time dependent drains heated the focus electrode beyond the safe temperature point and caused excessive sputtering and accel electrode heating. The electrodes were removed from the engine to permit a high voltage recheck of the engine at temperature and in vacuum. The engine drains without electrodes were nil. This high voltage test, with and without cesium leaving the front of the engine, thus indicates that none of the drains occurred across the insulators.

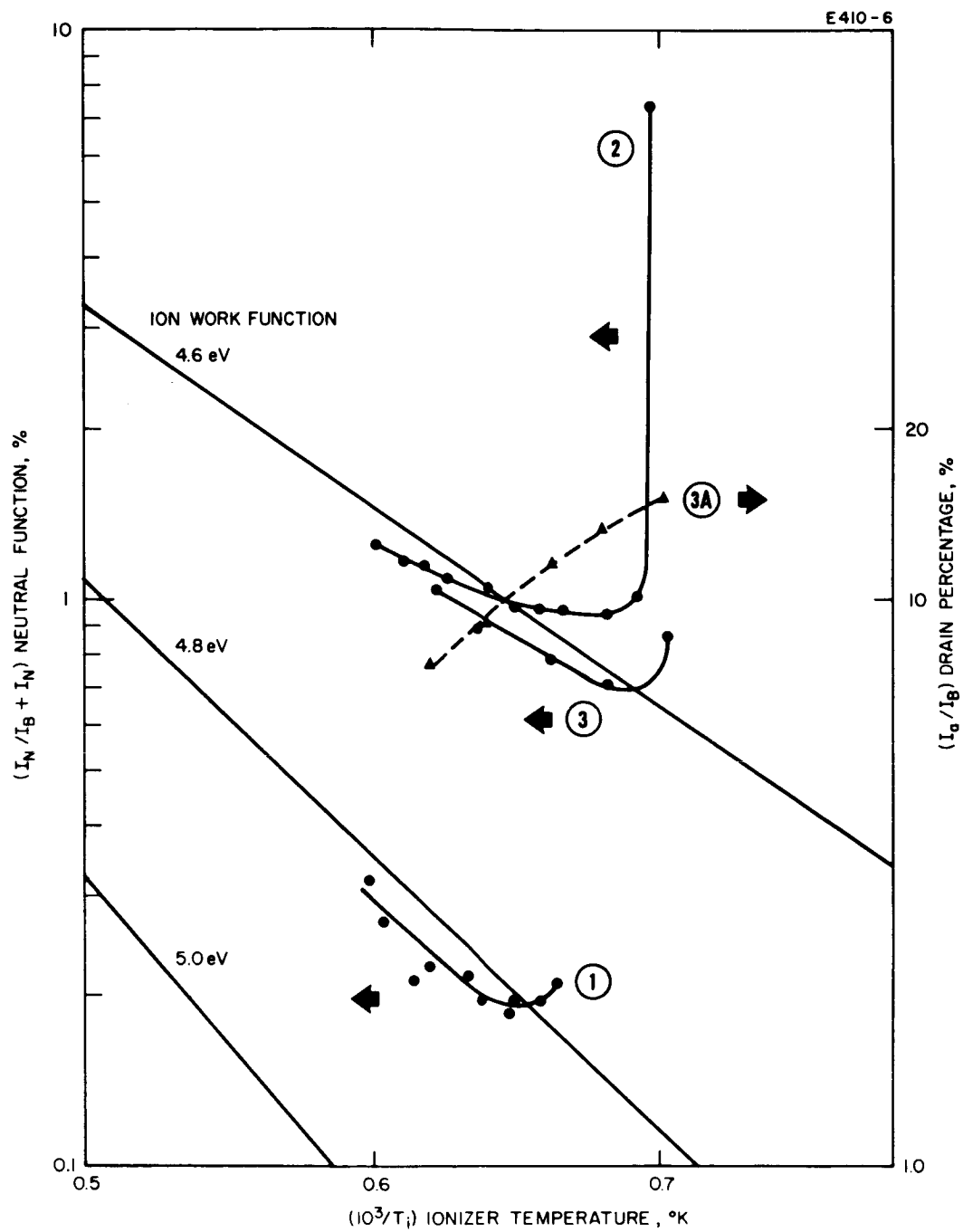


Fig. III-11. Neutral fraction versus ionizer temperature for engine 32-150-3.

c. Phase 3 — The engine accel and focus electrodes were changed to the open accel configuration as described in Section IV-E of this report. The purpose of this test was to determine the feasibility of controlling or reducing the time dependent drains by reducing the electric field and arrival rate of cesium to the inter-accel-focus region of the engine. Figure III-12 shows the open accel configuration which was used in test phases 3 and 4 of engine 32-150-3.

Initial operating conditions were favorable. At a current density of 9.4 mA/cm^2 , an ionizer temperature of 1155°C was recorded as shown by point No. 1 in Fig. III-13. At 11 mA/cm^2 drains were less than 1% with an ionizer temperature of 1173°C (point No. 2 in Fig. III-13).

A critical temperature of 1131°C was attained at 11.2 mA/cm^2 (point No. 3 in Fig. III-13). The drain currents at 11 mA/cm^2 were typically 0.5%.

Engine current density was raised to 15 mA/cm^2 and it was found that the ionizer was capable of operating at temperatures below that for oxidized porous tungsten at 2.5% drains (point 4 in Fig. III-13). Focus temperatures were high, however, and any significant reduction in ionizer temperature was offset by a rise in drain current which supplied enough power to the focus electrodes to raise their temperature. Current density was reduced to 11 mA/cm^2 in order to preserve low focus electrode temperatures at lower ionizer temperatures.

Another critical temperature plot was taken at 11.3 mA/cm^2 and an ionizer temperature of 1072°C was achieved before high drain currents prohibited further testing (point 5 in Fig. III-13). The ionizer operated on the clean porous tungsten line, indicating that a clean ionizer surface had been achieved. The remaining problem was the increasing time dependent drain currents.

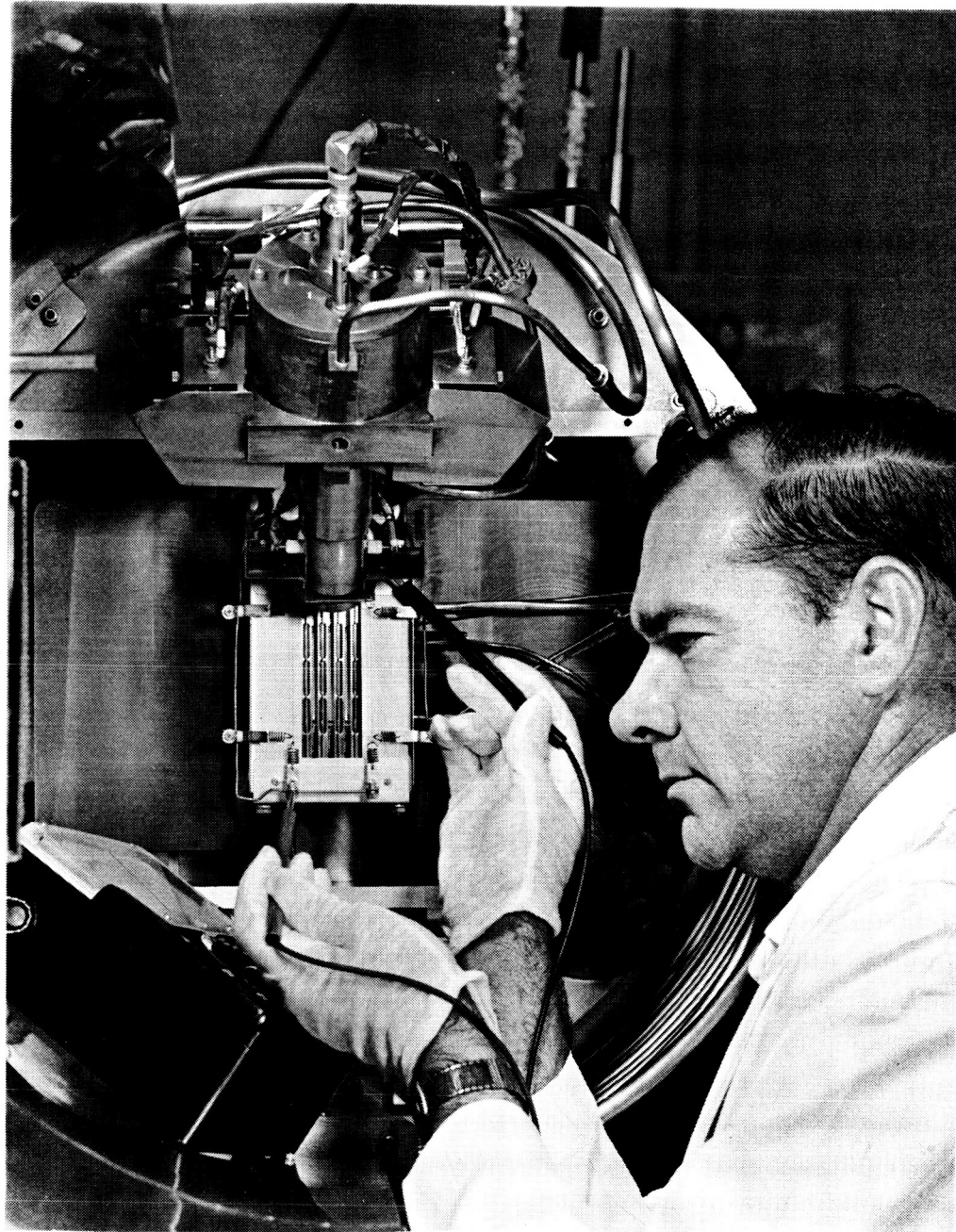


Fig. III-12. Front view of engine 32-150-3 showing the open accel electrodes. This engine configuration was used in phase 3 and phase 4 tests.

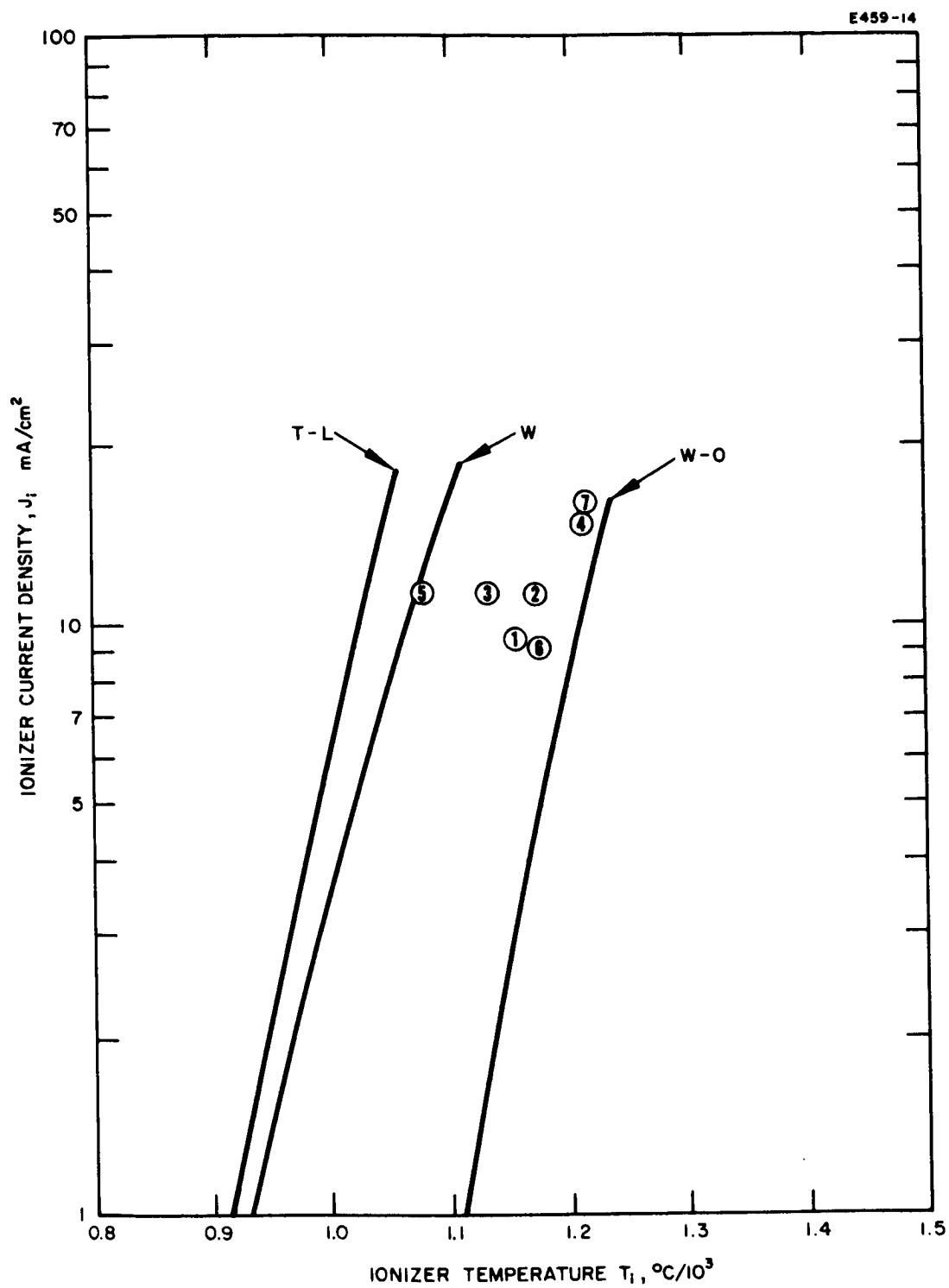


Fig. III-13. Critical temperature plots showing operating points for engine 32-150-3, test phases 3 and 4.

The reduced accel to focus drain current, before the time dependent effect became prominent, seemed to indicate that operation at lower ionizer power and at lower ionizer temperature was feasible. It also should be emphasized that higher ionizer temperatures were necessitated by the need for controlling the drain current by indirectly increasing the accel electrode temperature.

Drains of less than 1% could still be maintained with high ionizer temperatures. The new accel design did not appear to retard the increase of drains. The engine was operated continuously between hours 112 and 139. Past that time focus center line temperatures could be kept below 970°C only by reducing current density to 9 mA/cm^2 at an ionizer temperature of 1175°C and a drain of 3.2% (point 6 in Fig. III-13). By raising the ionizer temperature to 1400°C , the drain current at 10 mA/cm^2 could be reduced to 0.5%. At this time, it was decided to perform an experiment to determine the qualitative effect of higher accel temperature on drain currents.

d. Phase 4 — The observed low critical temperature as well as previous measurements of low neutrals indicated that the principal cause of drains resulted from the accel temperature's dependence on ionizer temperature. A heated accel would serve to reduce cesium coverage on the accel and thus help to raise the effective work function of its surface. The engine was removed from the chamber and heating elements (coils of tungsten wire for radiative heating) were installed in front of the accel electrodes. They were placed parallel to the ionizer strips and to each side of the engine. Each one was backed by a molybdenum radiation shield.

Figure III-14 shows the history of phase 4. On 7 July, from 1850 to 2110 hours, the engine was operated at about 9 mA/cm^2 . The effect of the accel heaters can be seen at 1920 hours. The heaters were turned on and the drain current dropped from 1 to 0.4 mA. The drains rose again to 1.3 mA, but a further increase in power dropped them back to 0.7 mA. When the accel heaters were turned off the drain current rose to 2.5 mA.

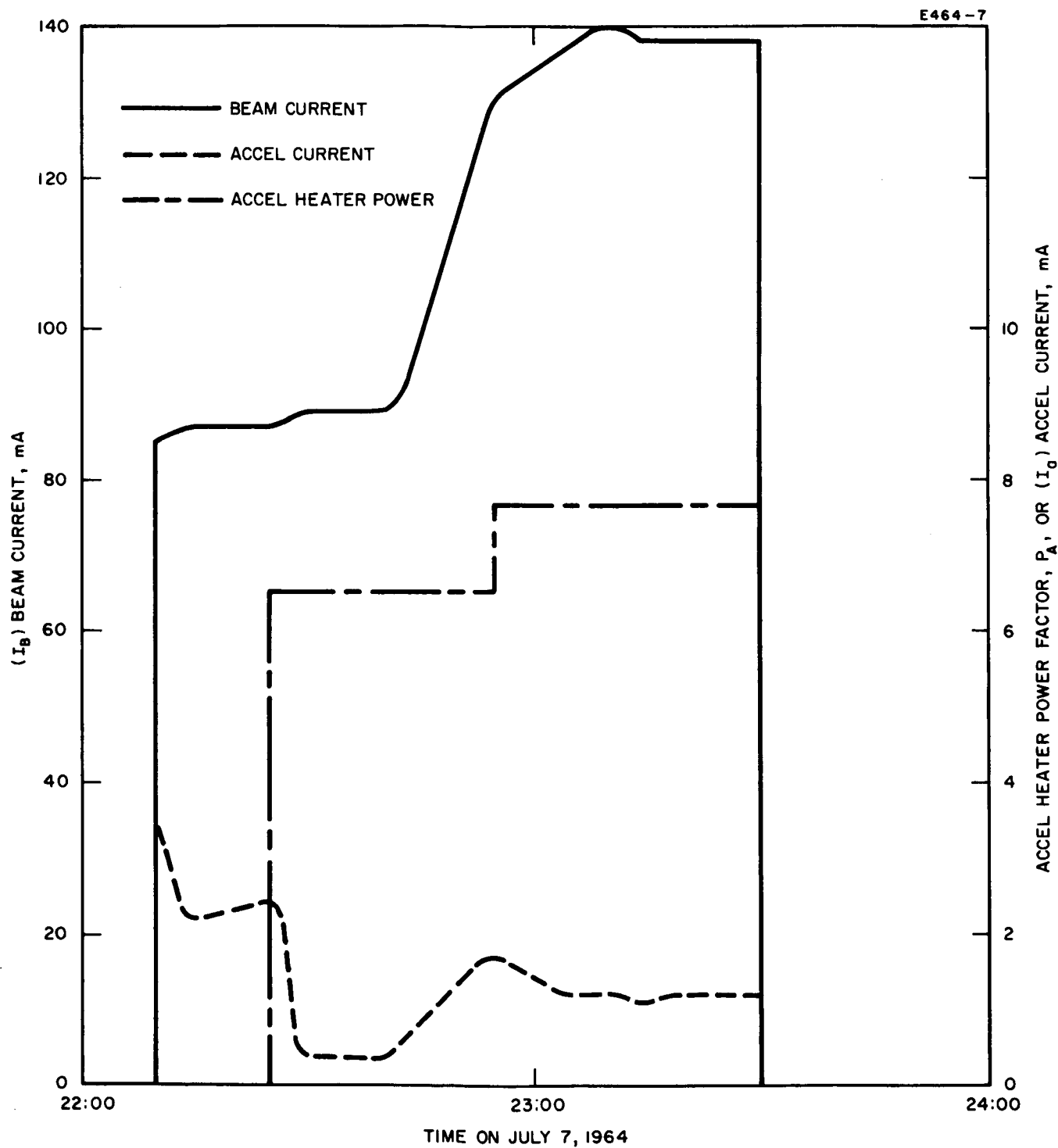


Fig. III-14. Partial history of test phase 4 for engine 32-150-3 showing the effects of accel electrode power on the accel drains.

From 2210 to 2220 hours, the engine was operated at 10 mA/cm^2 and drains were stable at 2.4 mA or 2.7% before the accel heaters were turned on. The drains were reduced to 0.4 mA or 0.45% with the accel heaters on. Beam current was then raised to 15.5 mA/cm^2 and accel heater power was raised slightly. Drain currents stabilized at 1.2 mA or 0.9%. Ionizer temperature was 1215°C . No attempt was made to reduce ionizer temperature (point 7 in Fig. III-13). The accel temperature was not measured but is estimated to be between 900 and 1000°K . Testing for the day was concluded at 2330 hours.

On 8 July, the engine current density was set at 15 mA/cm^2 ; the drain currents started out as during the previous day. In a short time they began to rise and were over 4 mA at 1100 hours. Neutral flux was also rising sharply during this time. At 1110 hours beam current was reduced and drains dropped. They immediately began to rise again and from that point on continued to rise. Neutrals also rose during this time. It was discovered that a small amount of the beam was sputtering part of the improvised molybdenum accel heater radiation shield onto the electrode structure and ionizer. A photograph of the engine after the test is shown in Fig. III-15. The uneroded electrodes as well as the radiation shield are shown in the figure.

The test of engine 32-150-3 showed the following:

- The Mod E ionizer was capable of operation with a low neutral efflux (1% at 11 mA/cm^2).
- The ionizer surface could be cleaned sufficiently to permit operation on the clean porous tungsten line.
- An improvement in engine operation was attained by reducing the accel to focus drains. The ionizer power and temperature could be reduced below the levels used in engines 32-150-1 and 32-150-2.

M 3286

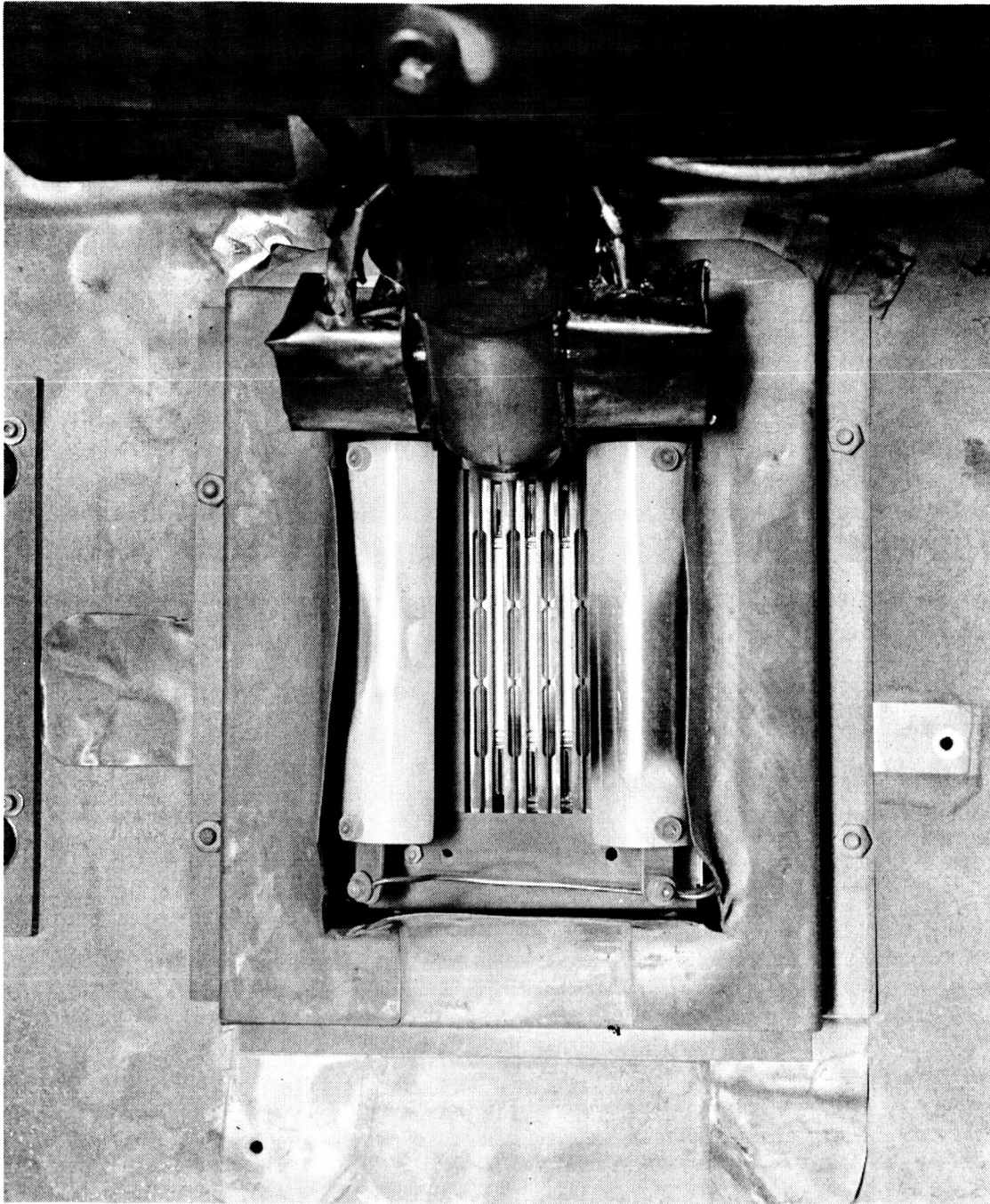


Fig. III-15. Engine 32-150-3 after the phase 4 test.

- Higher temperature accels showed promise of being able to eliminate the time dependent drain effect by either reducing the cesium coverage on the accel or by maintaining the surface in a clean condition.
- The ionizer surface should be cleaned prior to use in an engine, as shown later by test. Engine 32-150-4 incorporated the changes in design observed from the test of engine 32-150-3. Section IV-E on accel drains presents an analysis which delineates the advantages of using a shaped accel electrode as well as one operated at temperatures near 1000°K.

Engine 32-150-4 incorporates all factors relating to processes and design that were learned from the test of engine 32-150-3.

C. Engine 32-150-4

1. Summary

Engine 32-150-4 was in preparation during the third phase of the program and evaluated at the onset of the fourth quarter. The detailed results of this test are presented here. The most important of the findings is that very long duration operation of an ion engine is feasible — a confirmation of previous analyses. This will become evident in the discussion of charge exchange erosion.

Engine 32-150-4 was similar to the third phase version of engine 32-150-3 except for the following:

- a. An improved version of the double optics electrode system was incorporated into this engine to minimize the electron drain current to the focus electrode. (Refer to Section IV-E.)
- b. The accel electrode was allowed to operate at a temperature of 900 to 1000°K rather than 500 to 700°K as in previous engines.
- c. The engine incorporated a modified focus and accel electrode in order to terminate the ends of the strip engine properly.

This three-strip engine operated for a total test time of 260 hours, averaging 13.4 mA/cm² of beam current. Seventy percent of the time the engine operated at a current density of 14 mA/cm² and an average drain of 4.06%. During the remaining period, the current density was 10 mA/cm² and drains averaged 5.48%.

In contrast to all previous engines, the accel drain current in 32-150-4 was not time dependent. Elimination of time increasing drains was the result of heating the accel electrodes to end temperatures in the 1000°K range where stable operation prevailed. Toward the end of the test, drain current did rise with time, but this is attributed to very high neutral efflux which was caused by molybdenum sputtered onto the ionizer.

The test was limited as a result of accel electrode erosion caused by ions formed by charge exchange with the engine high neutral atom efflux. The erosion became severe, and an accel-to-ground short finally terminated the test.

The ionizer for this engine had been previously fired in wet hydrogen and was subsequently vacuum fired during a work function pre-engine installation process. Typical critical temperatures during operation at 15 mA/cm² deviated from the porous tungsten critical temperature by 15 to 50°C. It is believed that the pre-processing as

well as the use of the D. C. 705 pump oil helped in obtaining these low critical temperature results. In previous engines, ionizer operating temperatures as much as 300°C above critical temperature were required, and good critical temperature data were not obtainable because of (1) contamination from pump oil and (2) the prohibitive accel drains which resulted from reduced ionizer temperature (and subsequently accel temperature). The average neutral efflux, as determined by the cesium expenditure, was 17.8%. This value is three to five times greater than the normal neutral efflux for the Mod E material.

Post test analysis of the engine indicated that two factors could be responsible for the large neutral efflux: a high arrival rate of copper to the ionizer from a sputtered neutral detector or molybdenum sputtered onto the ionizer from edge trajectory ions striking a molybdenum cage which surrounded the engine. The sputtered molybdenum which induced a high neutral flux, is considered to be the primary cause for premature failure of the accel electrodes.

One of the most interesting facets of post test analysis was the correlation of charge exchange ion erosion calculations with experiment. The accel electrodes were weighed after test to determine the total copper weight as a result of charge exchange erosion. The measured loss compared within an 8% deviation to the analytically predicted loss for charge exchange. Figure II-2 presents the analytical predicted life for this engine. The ionizer neutral fraction as a function of current density is represented by a band which represents the spread in measurements of neutral efflux attained by ultrahigh vacuum and engine test techniques. The elimination of molybdenum sputtering onto the Mod E ionizer should reduce neutral efflux to at least these proportions.

The beam current and accel drains for this 260 hours test are presented in Fig. III-16(a) and (b), respectively. The erratic nature of the drain and beam current resulted principally from arc sensitivity

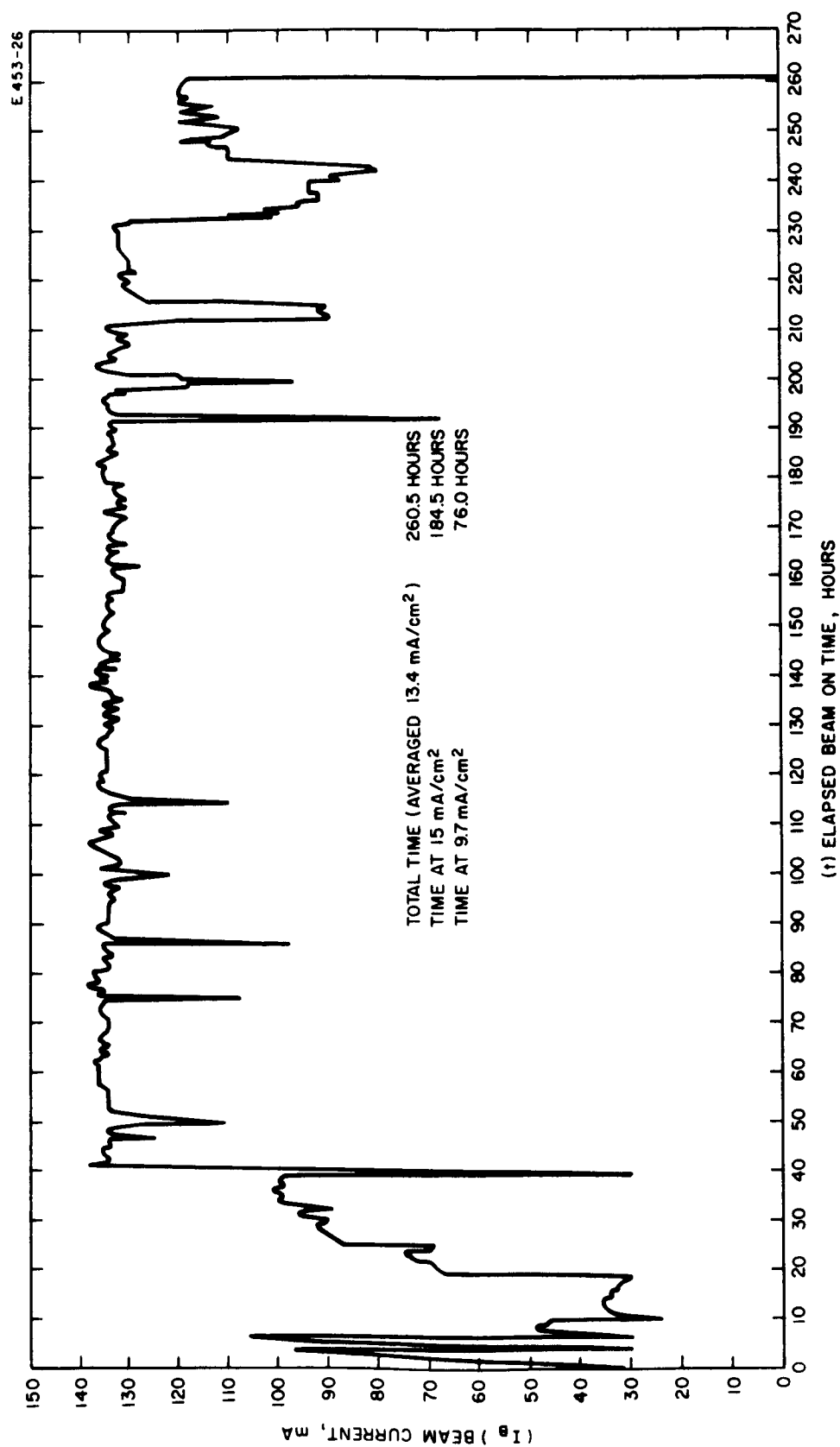


Fig. III-16(a). Beam current profile for 260 hour test of engine 32-150-4.

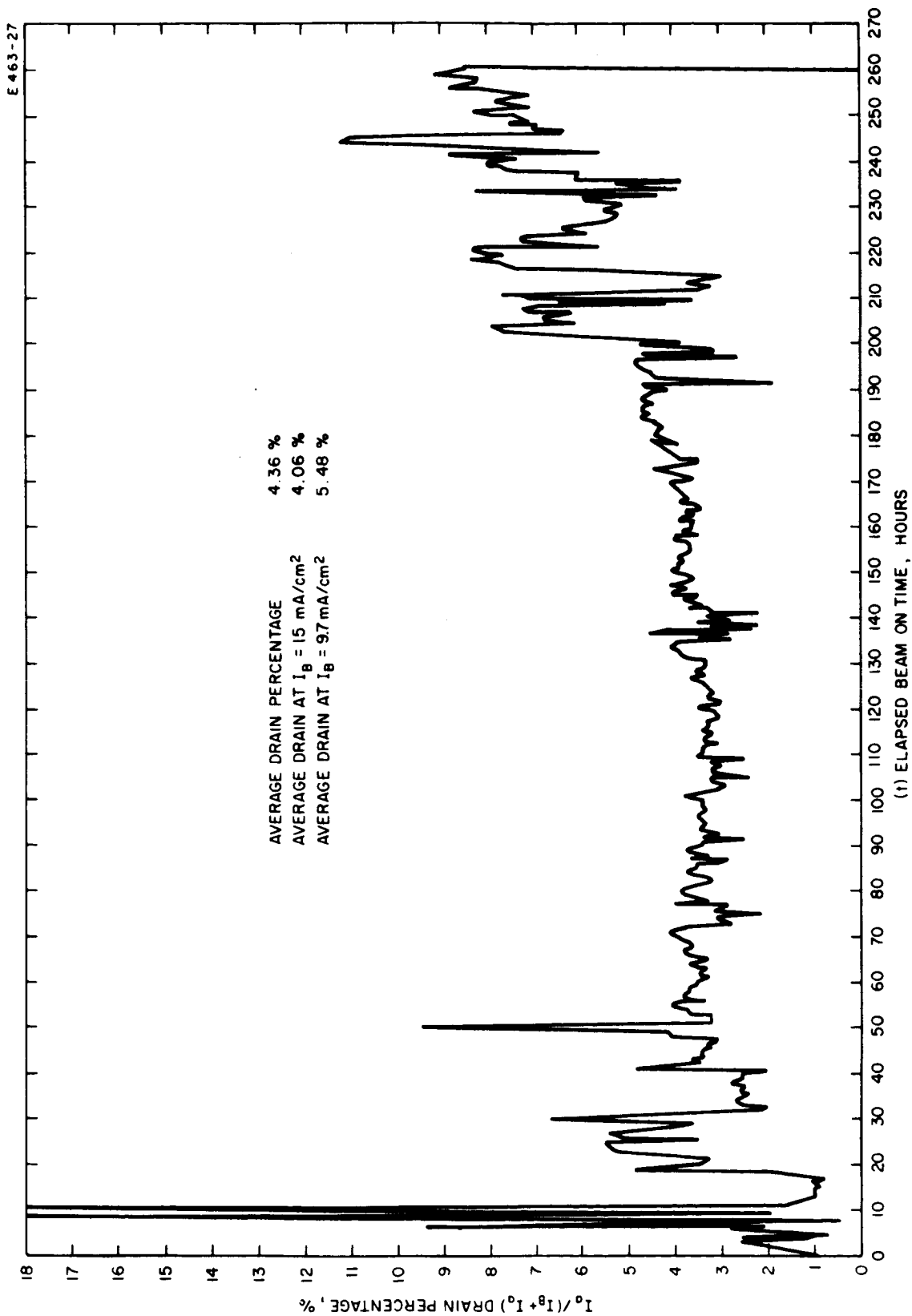


Fig. III-16(b). Accel drain profile for 260 hour test of engine 32-150-4.

and voltage breakdowns in parts of the test console which was operated for the first time during this engine test. In addition, high temperature cesium solenoid valve malfunctioned in an open condition at the beginning of the test, this permitted excessive cesium to flow, and a portion of it deposited onto the bulkhead feedthrough insulators during high voltage off periods. The characteristics of the test console have since been modified. The present performance of this device is described in Section IV-G-5.

2. Pretest Ionizer Processing

The evaluation of engine 32-150-3 as well as previous engines indicated that the ionizers were contaminated to start with. Prior to initiating the evaluation of engine 32-150-4 an investigation had been pursued to determine the impurity level of foreign elements in tungsten. Carbon was singled out since it was known that trace quantities could result in substantial tungsten work function depression. Section IV-G-4 of this report discusses the effects of cleaning up a carbon contaminated surface as well as the possibility of refilling the surface with carbon from the bulk contamination and from deposits of carbon bearing molecules on the ionizer surface. The final report of Contract NAS 3-4110 describes the results of the carbon measuring and cleanup program. The same report describes the changes in electrical characteristics of ionizers which can occur from carbon contaminated surfaces and vacuum systems. It was determined that wet hydrogen firing of porous tungsten samples for periods from 1 to 4 hours and at temperatures from 1100 to 1400°C served to reduce the bulk carbon level by at least a factor of two.

In order to avoid repeating the in situ cleanup of the ionizer, as was required for engine 32-150-3, the ionizer was wet hydrogen fired at 1250°C for 2 hours prior to assembly into an engine. The ionizer electron work function then was evaluated to establish the effectiveness of the wet hydrogen firing. The work function test also served to vacuum fire the part to remove the volatile tungsten oxide and the adsorbed oxygen from the ionizer surface. The vacuum system was back-filled with nitrogen to minimize the addition of large quantities of oxygen onto the tungsten surface prior to removal of the part from the vacuum system.

The use of the work function measurement to determine the apparent cleanliness of the ionizers was not totally effective; however, a low work function, indicative of a carburized surface, was not measured. On the other hand, a work function of 4.9 eV (indicative of a tungsten-oxygen surface) was measured. The high work function was attributed to the practical problem of executing this test in a vacuum station which can achieve a pressure of only 10^{-7} Torr.

Prior to operation of the engine, the ionizer was again desorbed of surface layers of oxygen. In this process, with the accel electrodes heated to 800°K to avoid condensation of tungsten oxide onto the electrode surface, the ionizer was heated in the engine test chamber to 1400°K for 11 hours.

Post test spectrographic analysis of the electrode surfaces as well as the ionizer indicates that the techniques for inhibiting the transportation of tungsten from the ionizer to the electrodes was ineffective. Although scales of tungsten did not appear (as in the second phase of the test of engine 32-150-3), a tungsten coating was found on the electrodes. The tungsten transport process probably occurred during the engine test period as a result of the partial pressure of oxygen within the chamber. The carbon removal process, however, did seem to work. It was feasible to operate the engine within 50°C of the Taylor-Langmuir critical temperature line. More details of engine tests and post test analyses are found in the following sections.

3. Pretest Thermal Characteristics

The thermal characteristics of engine 32-150-4 are shown in Figs. III-17, III-18, and III-19. Figure III-17 shows the ionizer heater power as a function of the ionizer temperature. The ionizer required 180 W to attain a temperature of 1350°K . Figure III-18 shows the accel power requirement as it relates to the ionizer temperature. It is observed that the accel power requirement, because of the accel power radiation loss, becomes more independent of the ionizer temperature as the accel temperature increases. The accel power requirement for

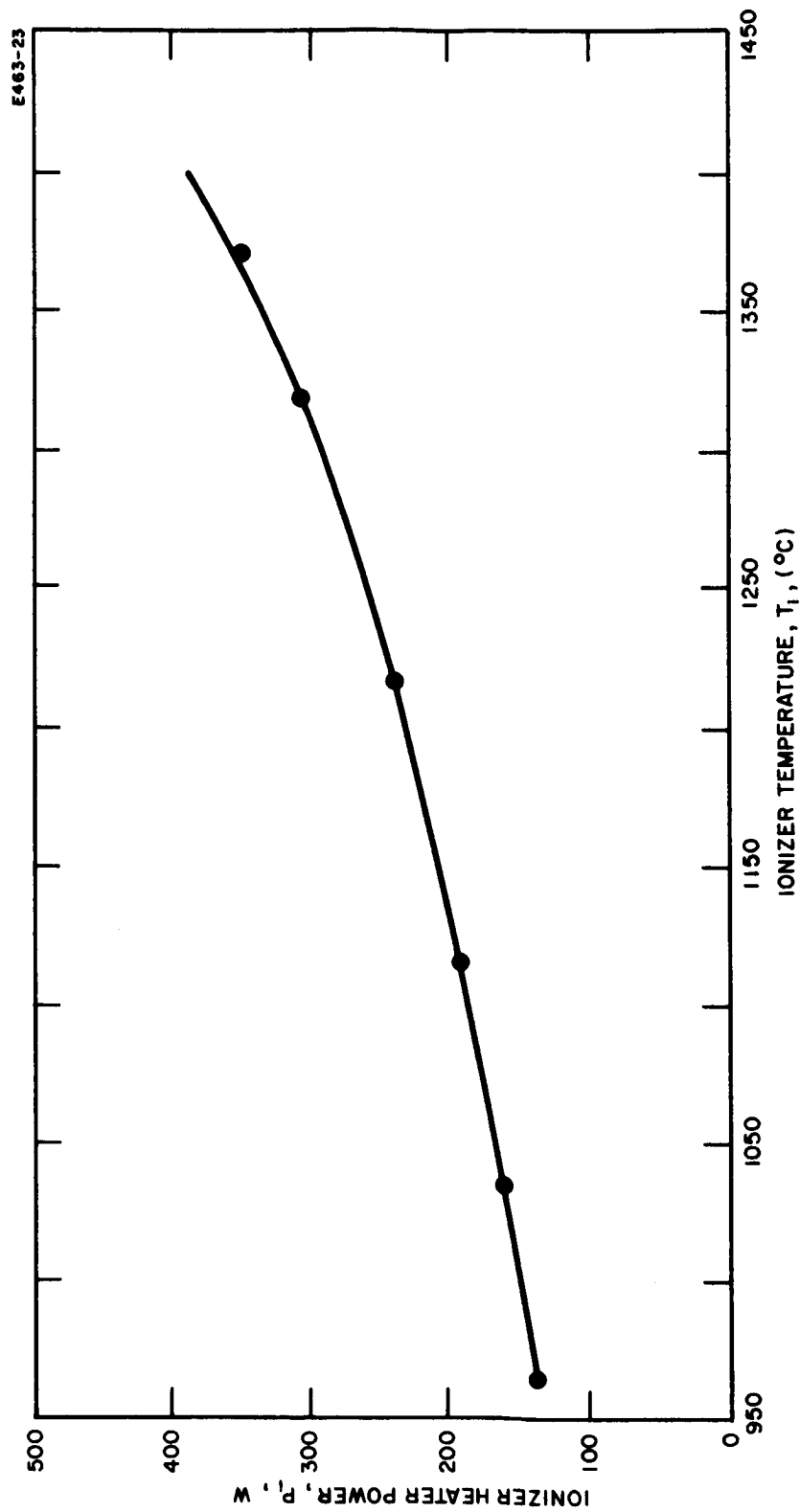


Fig. III-17. Ionizer temperature-heater power characteristics for engine 32-150-4.

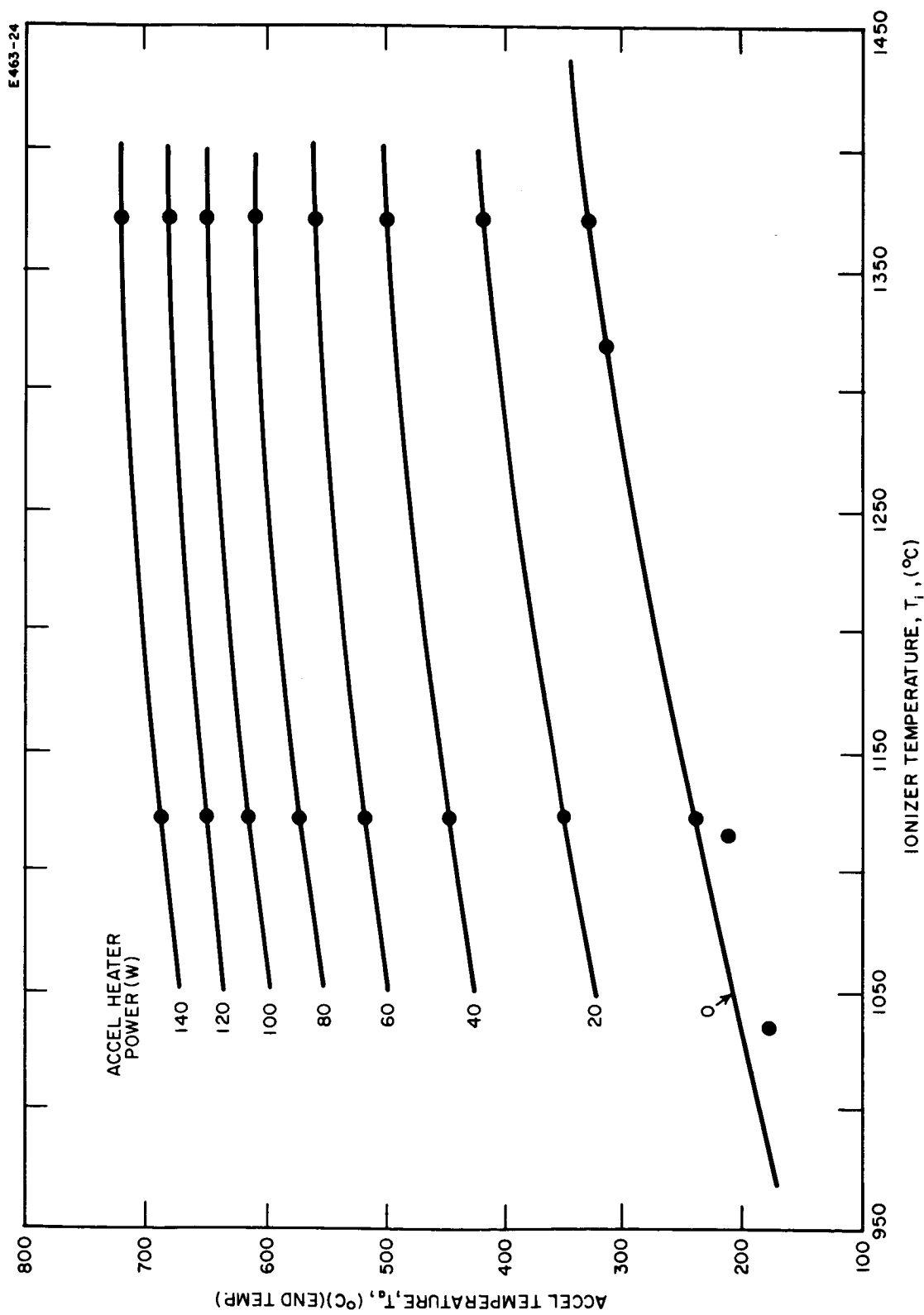


Fig. III-18. Accel end temperatures for engine 32-150-4.

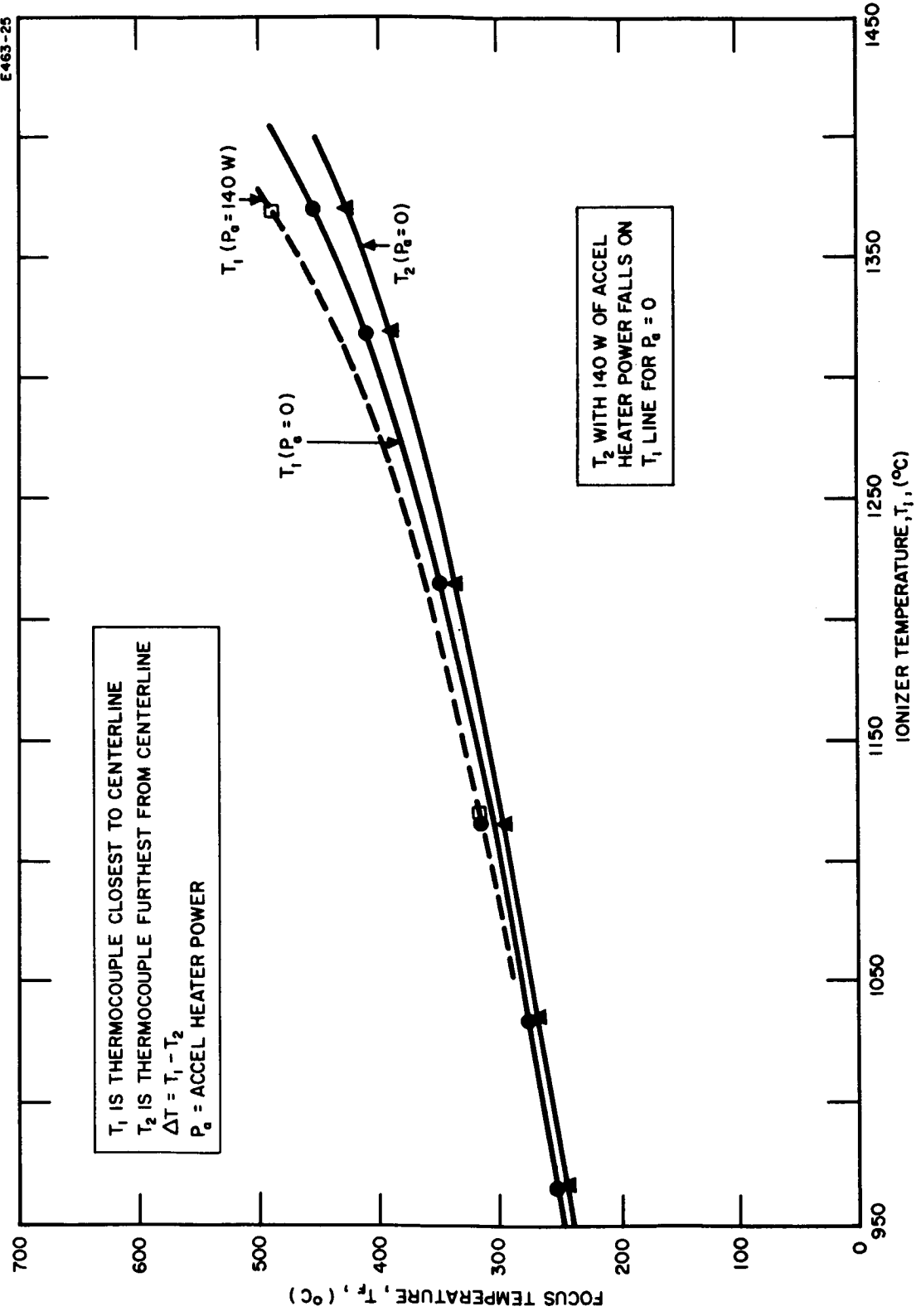


Fig. III-19. Focus electrode end temperatures for engine 32-150-4.

this engine is atypical. In this particular case, a very narrow (0.020 in.), decel electrode was positioned above the 0.245 in. wide accel electrode. Operation of the engine with either a wide decel electrode or a charge exchange diverter electrode which could also serve as a radiation shield would permit power to the accel electrode to be reduced to 40 W.

The effects of the heated accel electrode on the temperature of the focus electrode were also determined experimentally. Figure III-19 shows the focus temperature as a function of ionizer temperature for the case of zero accel electrode power as well as for an accel electrode power of 140 W. In the usual ionizer temperature range, it is observed that the focus electrode is increased by only 10°C for this 140 W accel power range.

The focus temperature characteristics provide information on the effectiveness of the electrode radiation shields as well as the emissivity of the ionizer and electrode. The ΔT measurement across a section of the electrode end is used to compute the power conducted through the heat transfer copper braids at the electrode ends. For these measurements, the maximum ΔT across the impedance is also only 10°C . The end impedance is approximately 5°K/W ; the power through each end of the focus electrode is thus 2 W. The thermal heat load for a 5 cm electrode is 0.8 W/cm; this corresponds well to measurements made on earlier engines. Section IV-C presents the thermal data for engines 32-150-1 and -2.

4. Test Results

Engine 32-150-4 operated for a total period of 260 hours. During 70% of this time, the current density was 15 mA/cm^2 . Two factors were especially significant in this test: (1) the lack of a time dependent increase in accel drain current, and (2) the excellent correlation between computed charge exchange erosion of the accel electrode and measured erosion. In addition to these factors, this test showed that engine operation near the Taylor-Langmuir critical temperature line was feasible.

The accel drain problem has been examined in Section IV-E. Figure IV-67 of that section presents typical accel drain current as a function of the accel temperature. A comparison is also made between Schottky emission from a clean copper-cesium system and the measured data from this engine. The measured data correlate with the data obtained from electrode simulation experiments only at the higher accel electrode temperatures. In the 900 to 1000°K temperature range the drains were at a minimum and stable. However, in general, the accel currents as a function of temperature were not repeatable, they tended to increase and were dependent on the immediate temperature history of the electrode. The lowest accel electrode temperature attainable is 500°K; earlier engine tests, in which the accel temperature was lowered to 500°K by reducing the ionizer temperature, also exhibited unpredictably high accel drain currents. The accel electrodes were operated at 970°K. It is necessary to maintain the accel electrode current at a prescribed level because control of the input power to the focus electrode and the consequent control of the peak focus temperature is essential. Section IV-C presents a summary of experimental and analytical data relating the total focus heat load to the peak focus temperature.

The engine ionizer as previously described, was preprocessed to remove surface carbon. It should be emphasized that the need for this had not been established but was only inferred from previous test experience. In addition to the clean ionizer, the vacuum system used D.C. 705 pump oil. The advantages are described in Section IV-G-1. This vacuum system was identical to that used for the engine 32-150-3 test described in Section III-B but differed from that used in the tests of engines 32-150-1 and -2. Figure III-20 shows typical critical temperature and operating point data up to the fiftieth hour of test. It can be seen that an operating point within 50°C of the clean tungsten line was attainable. This low ionizer temperature contrasts with data from the test of engines 32-150-1, -2, and -3. These earlier

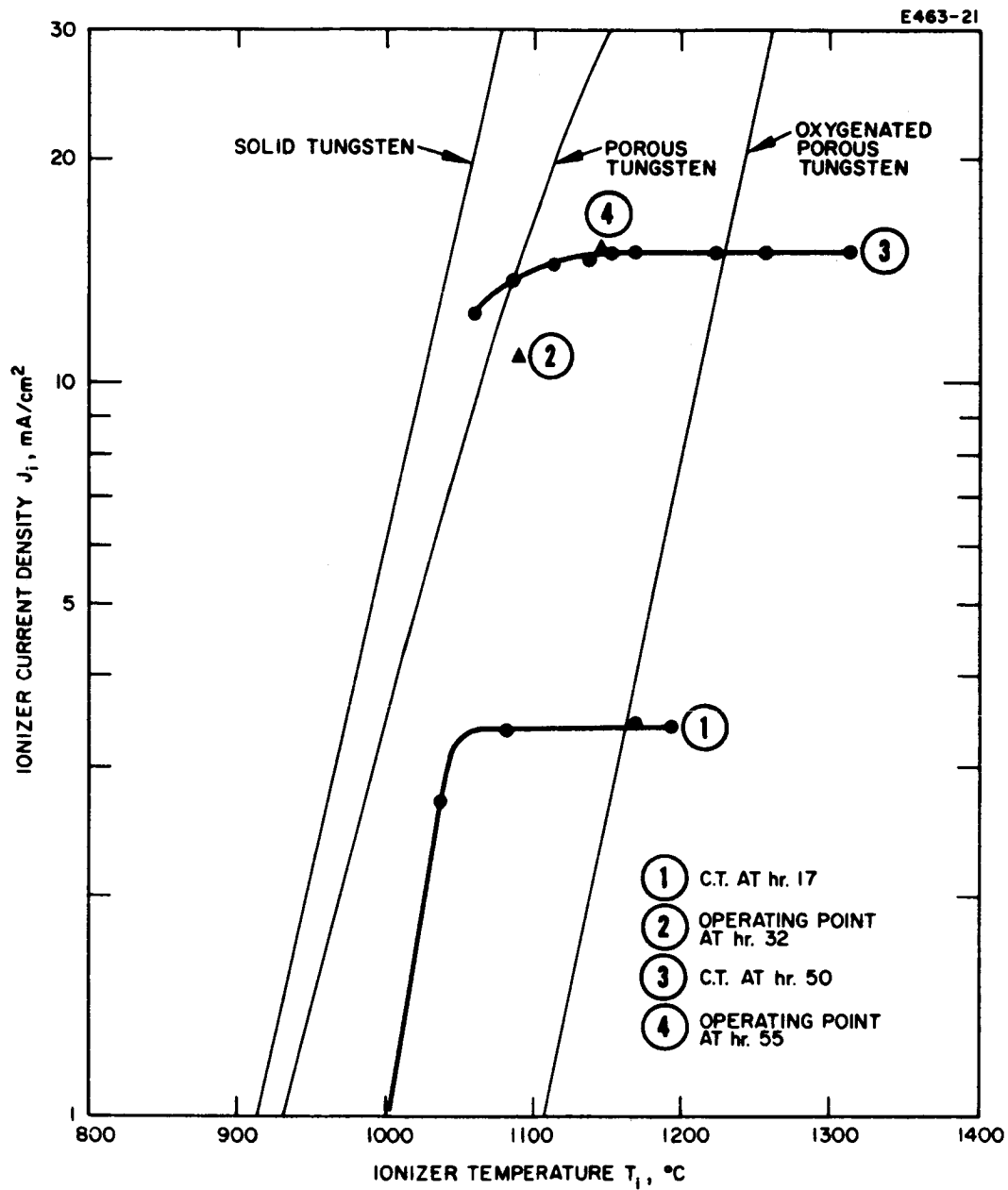


Fig. III-20. Typical critical temperature data from engine 32-150-4 during the first 55 hours of the 260 hour test.

engines required high ionizer temperatures for two reasons: (1) the contamination of the ionizer surface and (2) the reduction of accel drain current which depended on heating the accel electrode indirectly by radiation from the ionizer. The dependence of the accel electrode temperature on the ionizer temperature is shown in Section IV-C, Fig. IV-46. Similar accel temperature data are presented in Fig. III-18.

Figure III-21 shows the ionizer temperature as a function of test time. The clean porous tungsten as well as the oxygenated porous tungsten for a current density of 15 mA/cm^2 are also shown on this curve. These data are presented for information purposes only; no attempt was made to operate the engine at the lowest temperature.

As stated earlier, the engine test was limited to 260 hours as a result of a short which developed between the accel electrode and ground. Prior to this total malfunction the engine exhibited excessive arcing after the 232nd hour of test. Part of this arcing was attributed to cesium which had collected on the bulkhead insulators, the extreme sensitivity of the control console to arcs, the enhancement of arcs by the control console, and an excessive neutral efflux of cesium from the ionizer. The arc enhancement by the control console resulted from the overshooting voltage characteristics of the high voltage power supplies. Post test examination of the console indicated that transient electrode voltage increased by 50% following an engine arc which subsequently induced additional arcs. These deleterious characteristics of the console have been eliminated.

The engine was instrumented with the same neutral detector used in the engine 32-150-3 test. The neutral detector was positioned to see a 0.125×1.125 in. wide section of the center ionizer strip. For this engine installation, however, the detector was placed at a 39° angle with respect to the engine normal instead of the usual 49° . The distance from the ionizer to the filament was 10 in. The error in the placement caused the end of the copper detector to be sputtered by the beam ions. After 15 to 47 hours of engine operation, the beam

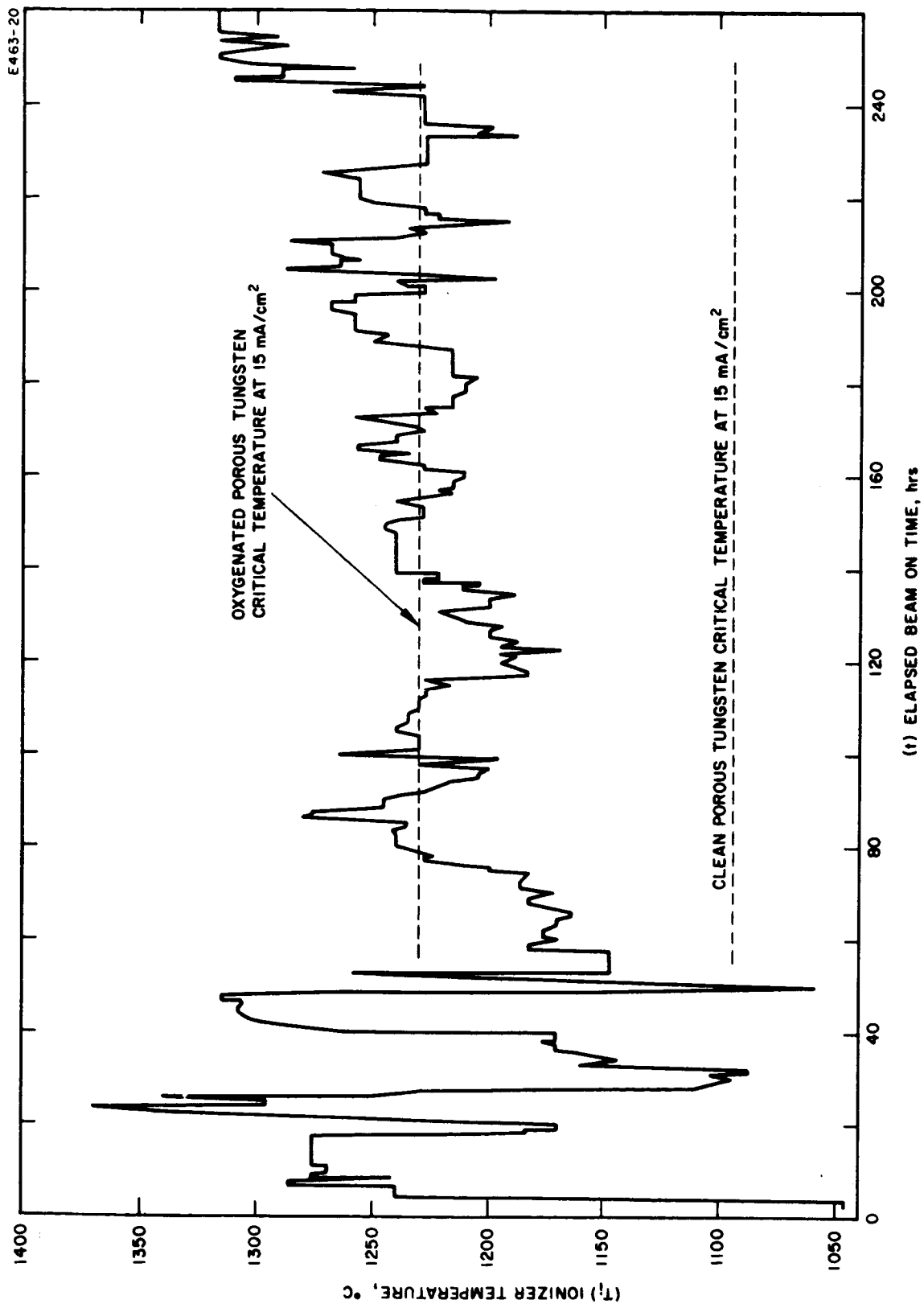


Fig. III-21. Ionizer temperature profile of engine 32-150-4 during the 260 hour test.

penetrated the copper shell of the detector. The collimating characteristics were destroyed; the beam also impinged onto the tube wall which resulted in beam ions dislodging cesium atoms from the collimating tube. The tube viewed a larger portion of the ionizer and also acted as a secondary source of cesium atoms to the neutral detector filament. It is possible, since the ion deflector system was also destroyed as a result of beam interception, that some beam ions could have penetrated to the neutral detector ion collector. All of these factors would cause the detector output to read high. Figure III-22 is a photograph of the neutral detector as it was positioned during the engine test. The pertinent dimensions are given.

A bottom view of the neutral detector showing the erosion from the edge trajectories of the beam is shown in Fig. III-23. The estimated copper arrival rate from the sputtered neutral detector is 7×10^{15} copper atoms/cm²-sec. The computed work function for the clean ionizer with this copper arrival rate could be 4.46 eV (copper) instead of 4.54 eV (tungsten) (see Fig. III-24).

Post test examination of the engine indicated that the edge trajectories of the beam also impinged onto a sheet of molybdenum which acted as a cage to protect the engine from copper sputtered from the vacuum tank beam collector. The molybdenum from the cage sputtered onto the ionizer and thus, as a function of test time, caused the portions of the ionizer surface to act as a molybdenum instead of a tungsten ionizer.

Figure III-25 shows a front view of the engine. The outline of erosion on a molybdenum cage which was a part of the engine structure is shown by a drawn line. The charge exchange eroded electrode is also shown in this figure. Molybdenum from the back side of this cage was sputtered to the ionizer. Figure III-26 shows how this could happen; it indicates the angle at which neutralized trajectories would have to leave the decel region of the engine in order to strike the molybdenum cage.

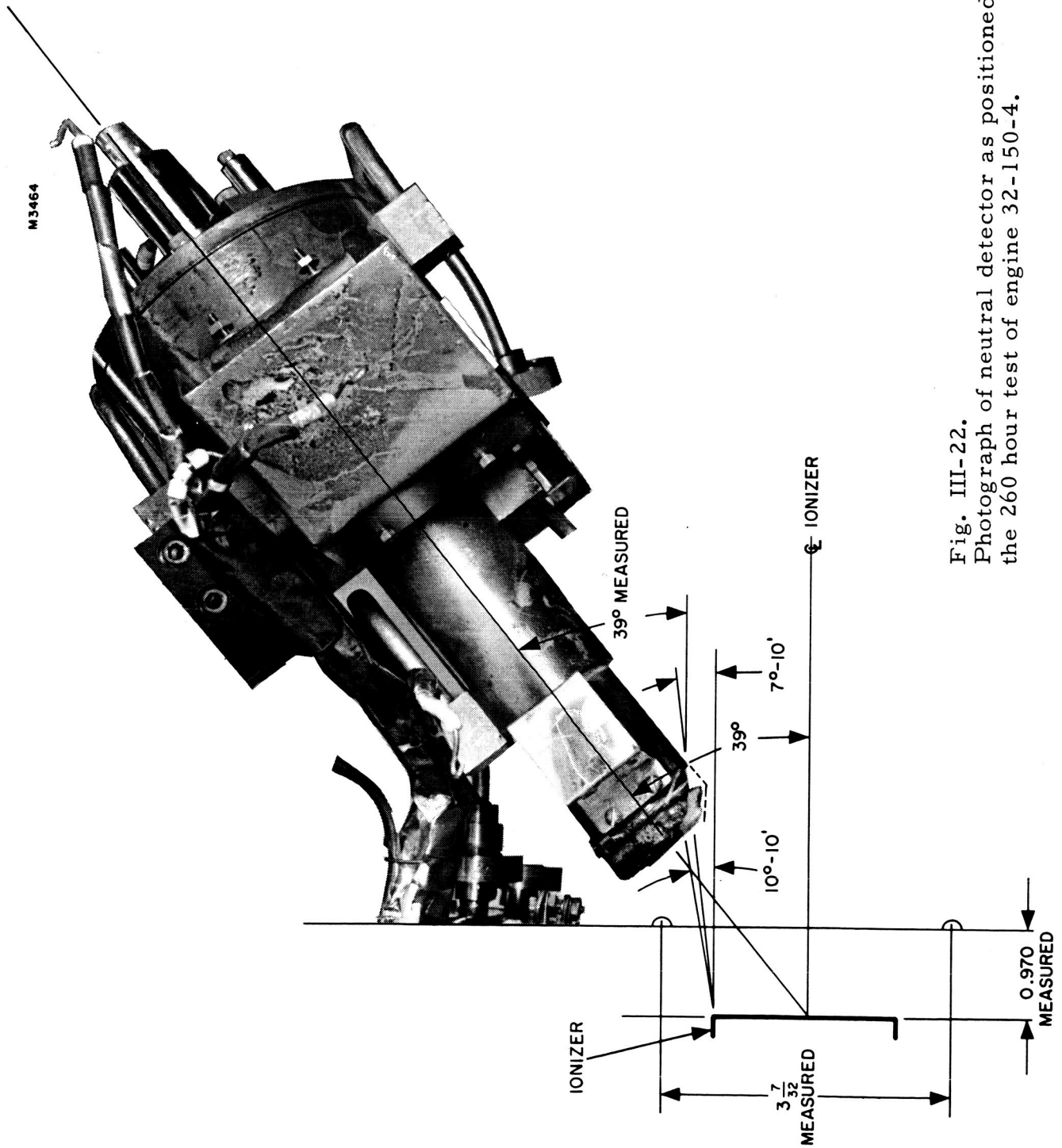


Fig. III-22.
Photograph of neutral detector as positioned during
the 260 hour test of engine 32-150-4.

M 3462

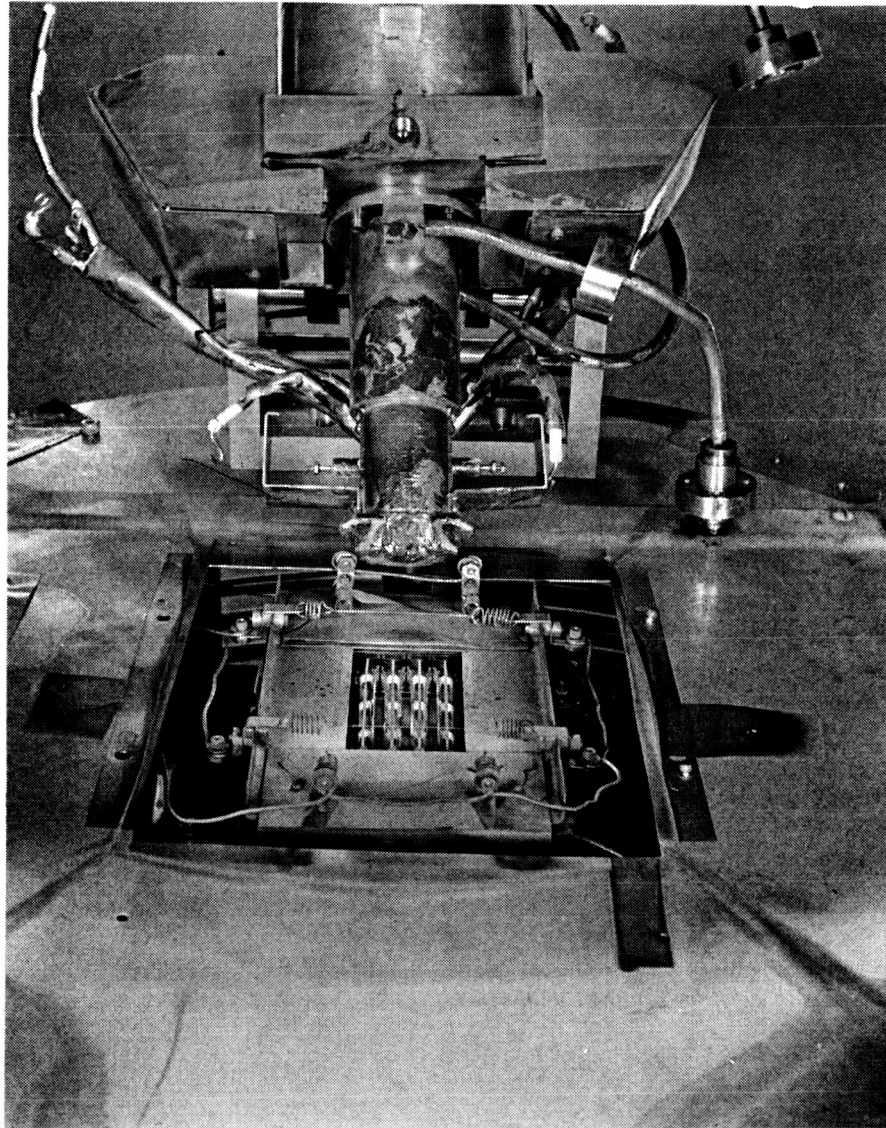


Fig. III-23. Bottom view of neutral detector showing the erosion from the edge trajectories of the beam that occurred during the 260 hour test of engine 32-150-4.

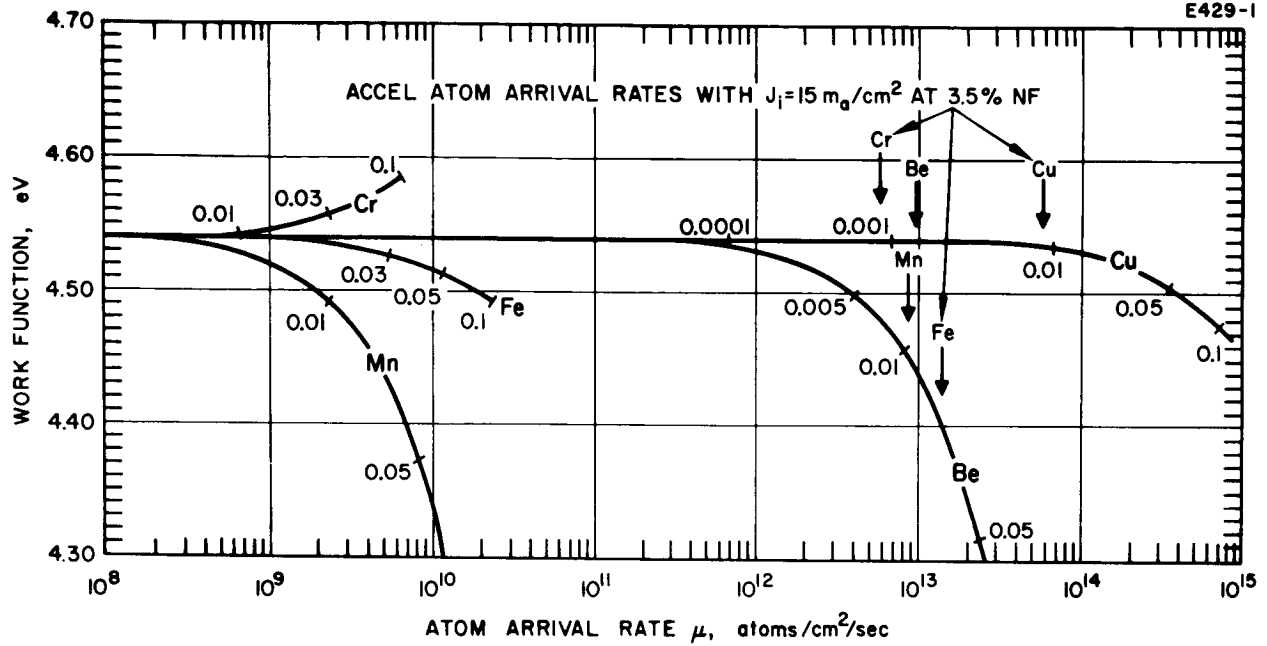


Fig. III-24. Graph showing the work function of a tungsten surface with various arrival rates of copper and other elements onto the tungsten surface.

M3461

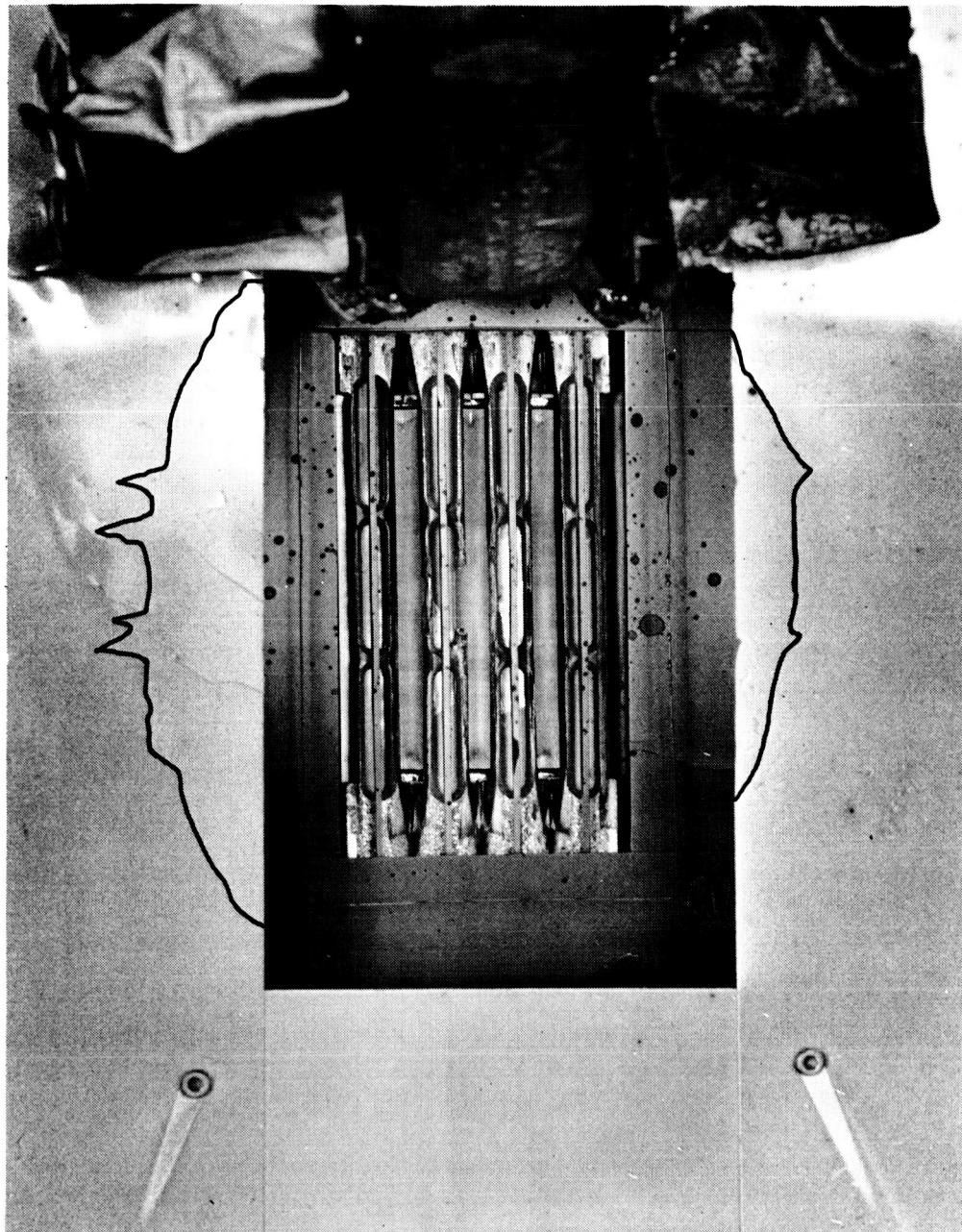


Fig. III-25. Front view of engine 32-150-4 with superimposed outline of erosion on a molybdenum cage which was part of the engine structure.

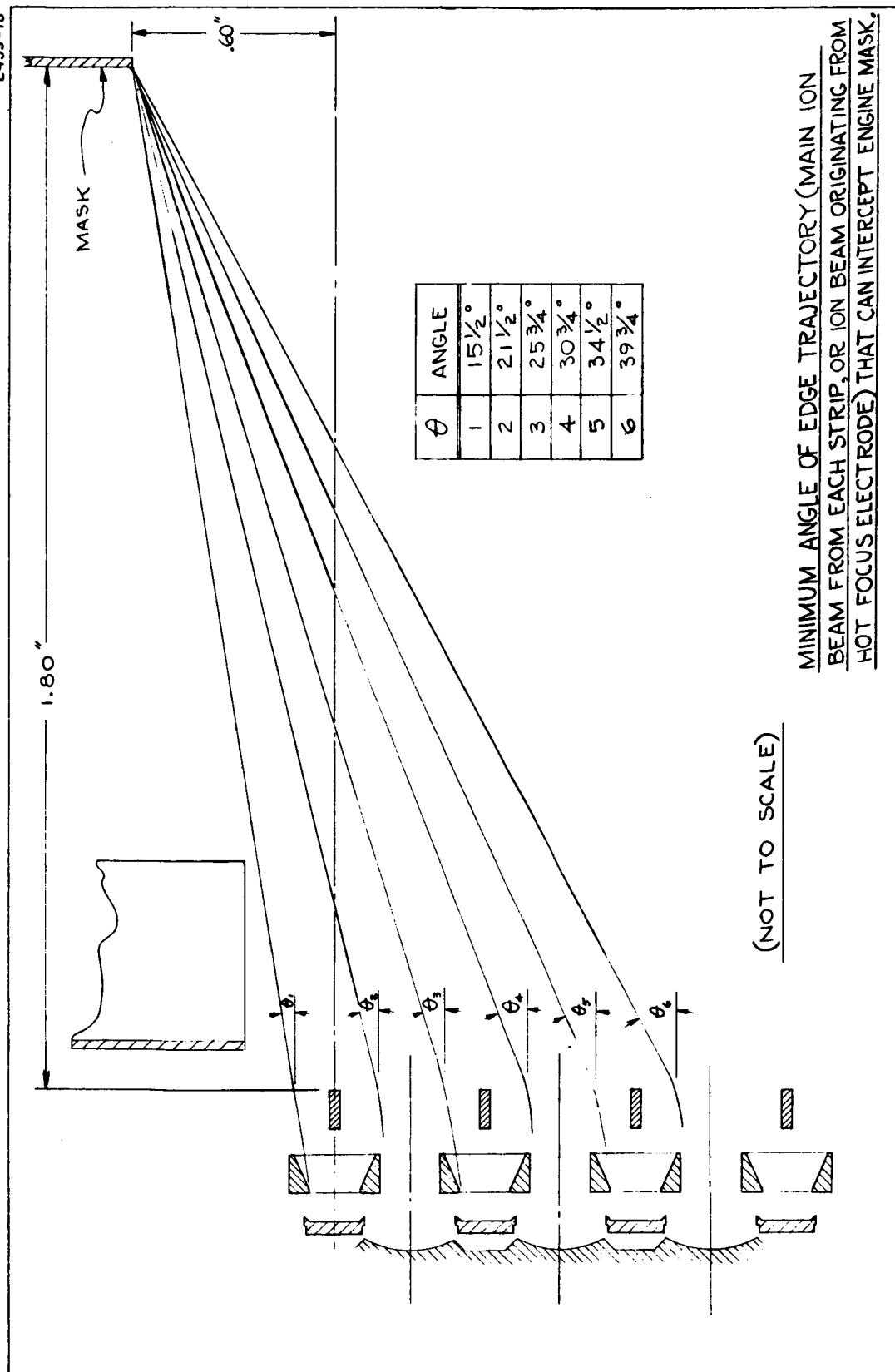


Fig. III-26. Angle at which neutralized trajectories would have to leave the decel region of the engine to strike the molybdenum cage.

Possible trajectory angles of the main beam as well as possible trajectory angles for ions leaving the top of the focus electrode are shown. It is observed that edge trajectories which have angles from 15 to 30° could strike the molybdenum cage. Engine trajectories with edge angles of 25° are possible. Measurements of the eroded cage indicate that 1.2 g of molybdenum were removed by sputtering. Computations indicate that 0.060 g of molybdenum were sputtered to the ionizer. Emission spectrographic analysis of the surface indicated a molybdenum concentration of 2200 ppm. The surface was essentially molybdenum coated.

The engine neutral fraction sensitivity and average beam current are shown in Fig. III-27. The neutral fraction continues to rise as the detector fails and as the molybdenum continues to be sputtered onto the ionizer. The triangles on the curve indicate the times when the detector sensitivity was redetermined. At the onset of the test the neutral fraction was between 0.5 and 1% at a current density of 6.2 mA/cm². The neutral fraction was between 4 and 5% for a current density of 15 mA/cm² after 20% of the test period and after approximately 12 mg of molybdenum had been deposited onto the ionizer surface. It is probable, therefore, that a neutral fraction-current density characteristic less than the measured level could be attained. Neutral fraction measurements on engine 32-150-3, which also used the Mod E ionizer material, were 1% at a current density of 11 mA/cm².

The average neutral fraction for the 260 hour test was estimated from a calculation of the integrated beam current and a measurement of the cesium expelled during the test. The average beam current was 13.4 mA/cm² for a period of 260.5 hours. The cesium expelled was 189 g. The computed average neutral efflux was 17.8%.

The engine test served as the best experiment to verify the utility of the charge exchange analysis presented in the summary report of Contract NAS 5-517. The pertinent results of the analysis are presented in Section II, Fig. II-2 of this report. Examination of

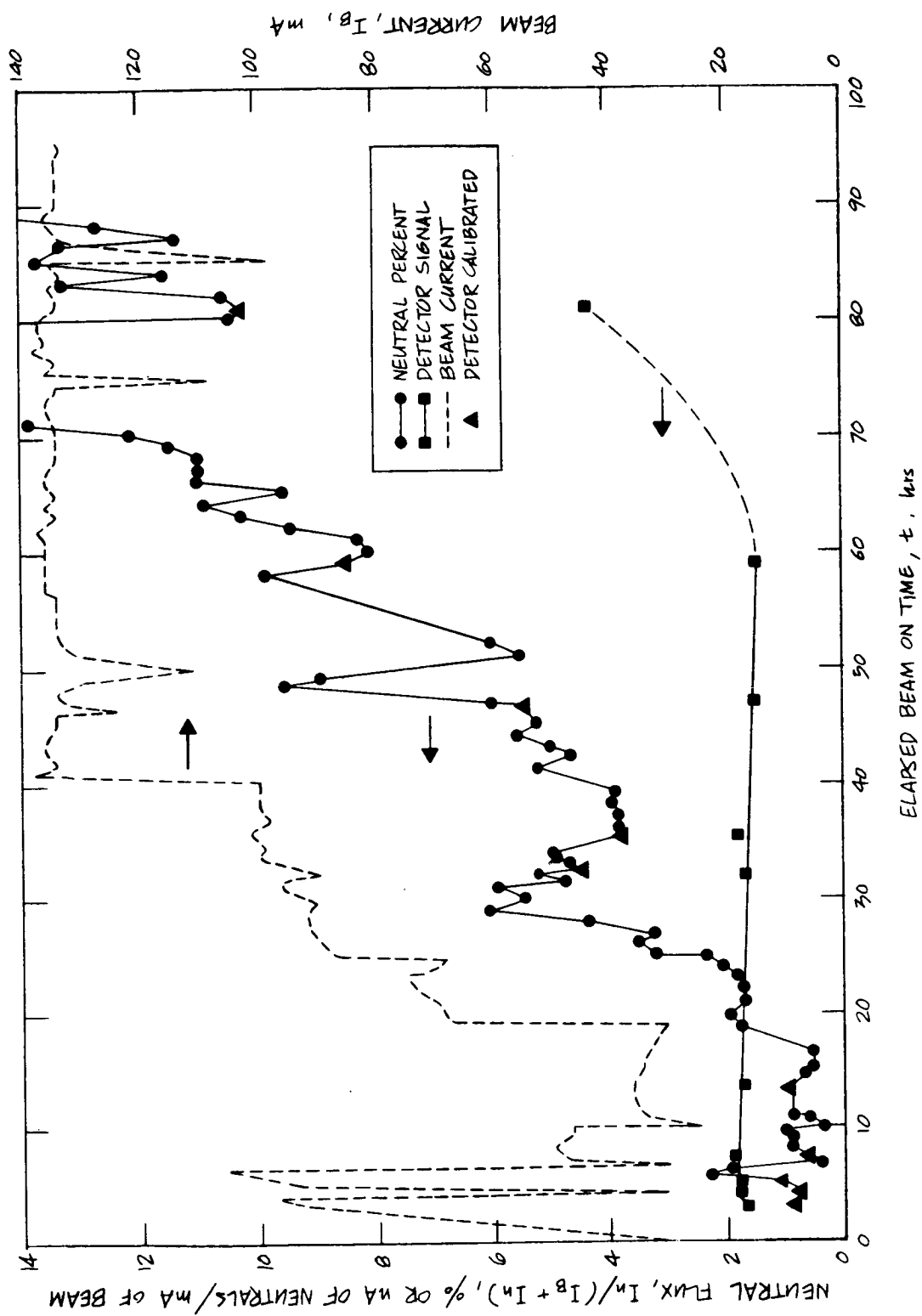


Fig. III-27. Neutral percent, neutral detector sensitivity, and average beam current during the first 96 hours of the 260 hour test of engine 32-150-4.

the accel electrodes confirmed (1) the charge exchange erosion patterns on the electrode and (2) the erosion volume for the average beam density and neutral efflux. A front view of the electrodes which were removed from this engine is shown in Fig. III-28. It can be seen that a portion of the second electrode has been completely eroded. A bottom view of the fourth electrode is shown in Fig. III-29. Note that erosion occurred from ions which originated from the focus electrode. Sections through the remaining electrodes did not show similar signs of erosion from focus originated ions. Examination of the engine after test indicated that the ionizer-manifold assembly was loose. It is possible that this part shifted so that the fourth focus electrode was in contact with ionizer, thus causing this electrode's temperature to increase to a point at which ions could form. The ionizer-manifold mount for the 20-strip engine is designed to prevent the part from shifting. The charge exchange erosion patterns were obtained from the sectioned electrodes and are shown in Fig. III-30(a), (b), and (c). Figure III-30(a) shows a section through the unwebbed portion of the electrode. Note the removal of less than 0.005 in. from the lower perveance determining portion of the electrode. The erosion at the electrode sides is typical of that which was analytically predicted.

Figure III-30(b) shows similar side erosion, slight erosion on each side of the base of the electrode, and erosion on the electrode top. The absence of erosion in the base center region confirms, for this electrode, the lack of the formation of ions from the focus electrode. The pattern on the electrode top indicates a deposit of material sputtered to the electrode from the beam collector as well as charge exchange erosion.

Figure III-30(c) again shows the typical charge exchange erosion. The base erosion of the fourth electrode resulted from ions formed on the focus electrode. The top and base erosion is approximately 20% of the total. The remaining erosion occurs at the side of the accel electrode which faces the ion beam. The volume of electrode eroded by charge exchange is determined from the following expression:

1188

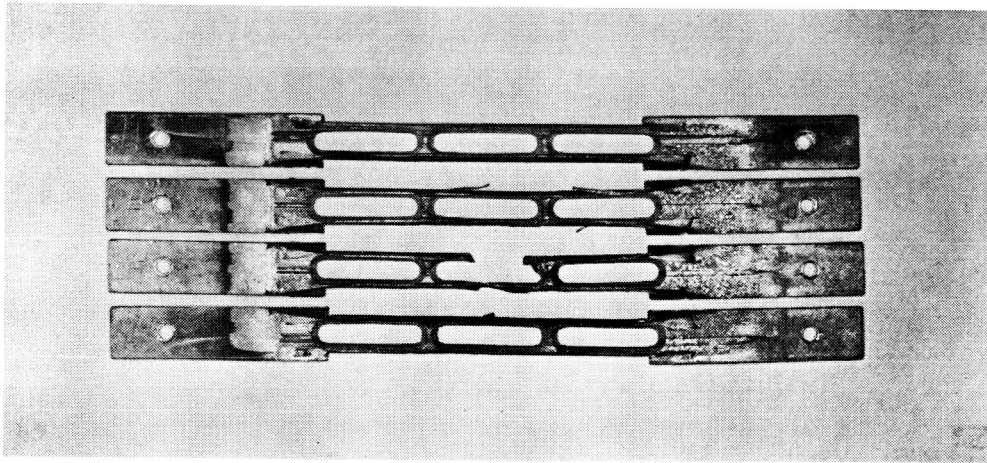


Fig. III-28.
View of accel electrodes (looking
toward ionizer) after test of engine
32-150-4.

1191

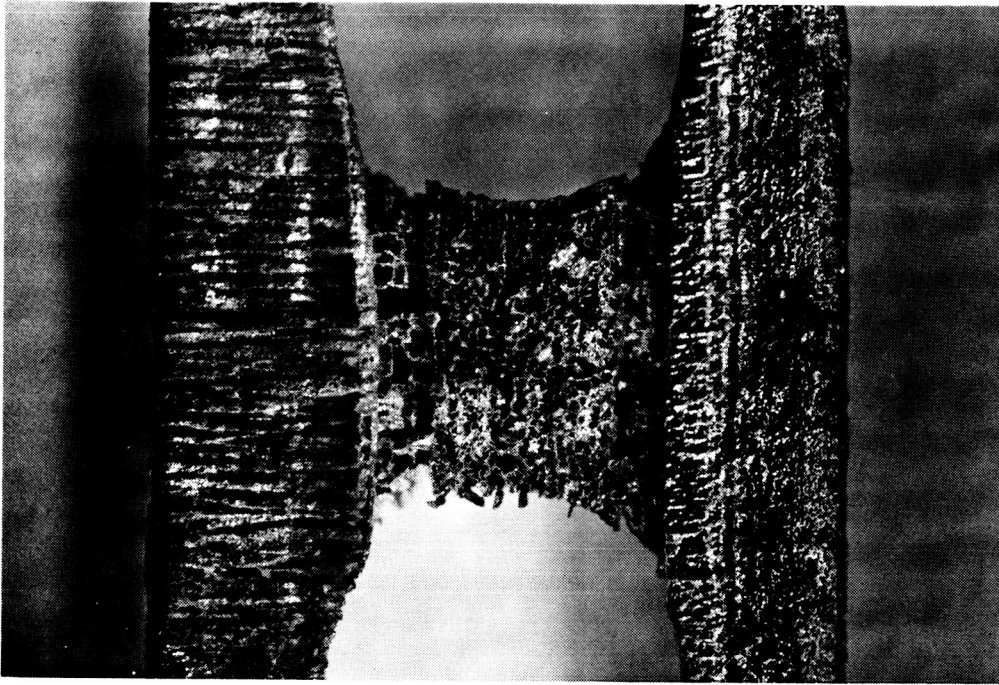
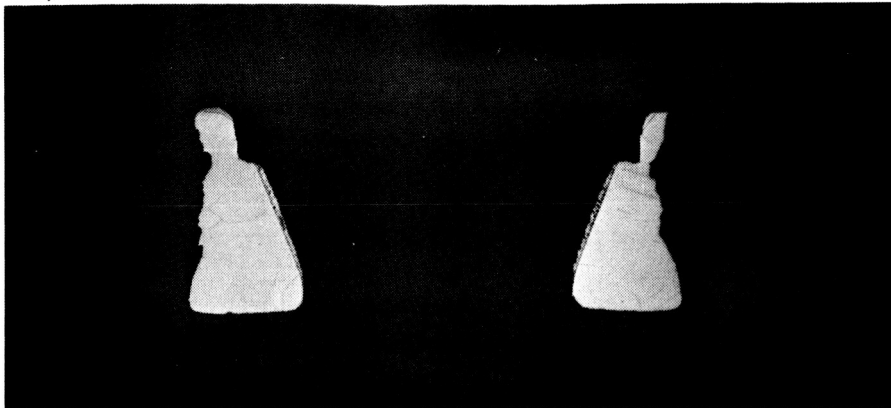


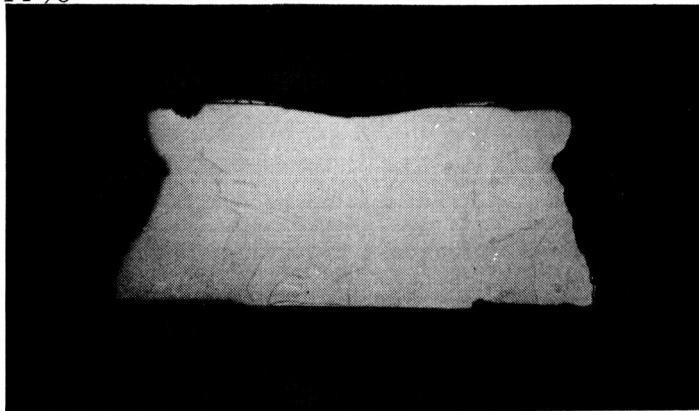
Fig. III-29.
View of portion of accel No. 4 (facing
focus electrode) from engine 32-150-4
after 260 hour test.

1195



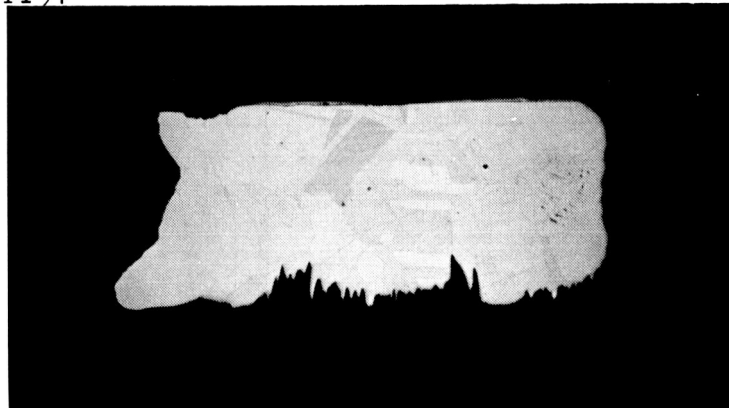
(a) Cross section of web area of accel No. 4.

1196



(b) Cross section of web area of accel No. 3.

1197



(c) Cross section of accel No. 3.

Fig. III-30. Cross sections of accels from engine 32-150-4, showing original dimensions, coatings, and erosion patterns.

$$V = v \left(\frac{NF}{7} \right) \left(\frac{J}{15} \right)^2 L \times 3.6 \times 10^3 \times 2n \times \ell, \text{ cm}^3 \quad (\text{III-1})$$

where

- $v \equiv$ sputtering volume/sec-cm electrode length
($8.25 \times 10^{-9} \text{ cm}^3/\text{sec-cm}$ for $V_a/V_f = 2$)
- $\overline{NF} \equiv$ average neutral fraction, %
- $\overline{J} \equiv$ average current density, mA/cm^2
- $L \equiv$ test duration, hours
- $n \equiv$ number of strips
- $\ell \equiv$ strip length, cm.

The volume of copper eroded from the accel electrode was 0.442 cm^3 . The experimentally determined sputtering volume per second per centimeter side, computed on the basis of an average current density of $13.4 \text{ mA}/\text{cm}^2$ and a neutral fraction of 17.8%, is $7.65 \times 10^{-9} \text{ cm}^3/\text{sec-cm}$ side. The experimentally determined coefficient is 8% lower than the computer determined coefficient of $8.25 \times 10^{-9} \text{ cm}^3/\text{sec-cm}$ side. The deviation results from test factors such as variation in accel-decel ratio, focus ion erosion, and back sputtering of material to the electrodes.

It should be emphasized that the computed engine life is dependent on uniform erosion of the electrodes. Therefore, it does not correlate with the experimentally determined life.

The computer-determined life, at $J = 13.4 \text{ mA}/\text{cm}^2$ and $NF = 17.8\%$, is 530 hours and allows a total electrode erosion of $0.04 \text{ cm}^3/\text{cm}$ length. However, the actual engine life was 260 hours. The nonuniform erosion, which probably resulted from the molybdenum sputtered onto the ionizer, is the primary cause of the deviation in this charge exchange-life experiment.

The operation of the ion engine required continuous increases in the total engine accel voltage in order to extract a flow limited beam; i. e., the engine perveance was decreasing. This trend is shown in Fig. III-31 in which the engine perveance is plotted as a function of test time.

Two factors can possibly account for the change in perveance from the rated value of $134 \times 10^{-9} \text{ A/V}^{3/2}$ to $95 \times 10^{-9} \text{ A/V}^{3/2}$. One is the charge exchange erosion of the accel electrodes. The complete disintegration of a portion of the second accel electrode must have affected the engine perveance. The eroded portion of the accel electrode is approximately 1 cm long. The maximum effect on perveance could be 2 cm out of the 30 cm electrode length, or 6%. The perveance would thus be reduced to 126 nperv. The remainder of the optically critical accel electrode edge nearest the emitter remained without being eroded; thus the remaining charge exchange erosion had no appreciable effect on engine perveance.

A second factor is the sputtering of 0.06 g of molybdenum onto the ionizer. The molybdenum ionizer coating increased monotonically with time. It is believed that pore blockage as well as nonutilization of the ionizing capability of the emitter area accounted for most of the 37% decrease in perveance.

5. Chemical Analysis of Ionizer and Electrode Surfaces

a. Emitter — During the latter portion of the 260 hour run, the neutral fraction was observed to be abnormally high. X-ray diffraction analysis of the surfaces showed possible traces of molybdenum which were probably responsible for this effect. This was confirmed by emission spectrographic analysis of a layer about 1 mil thick which was removed from the face of the ionizer for analysis. Approximately 0.2% molybdenum was present on the outer emitter surface, while only 0.04 to 0.02% — the normal amount — was found on the inner side of the emitter and in the bulk of the porous tungsten. No other significant contaminants were found except in a 1 mm^2 sintered area near the edge of one strip; this area contained 0.22% aluminum, 0.7% iron, which was probably a random sputter or arc product.

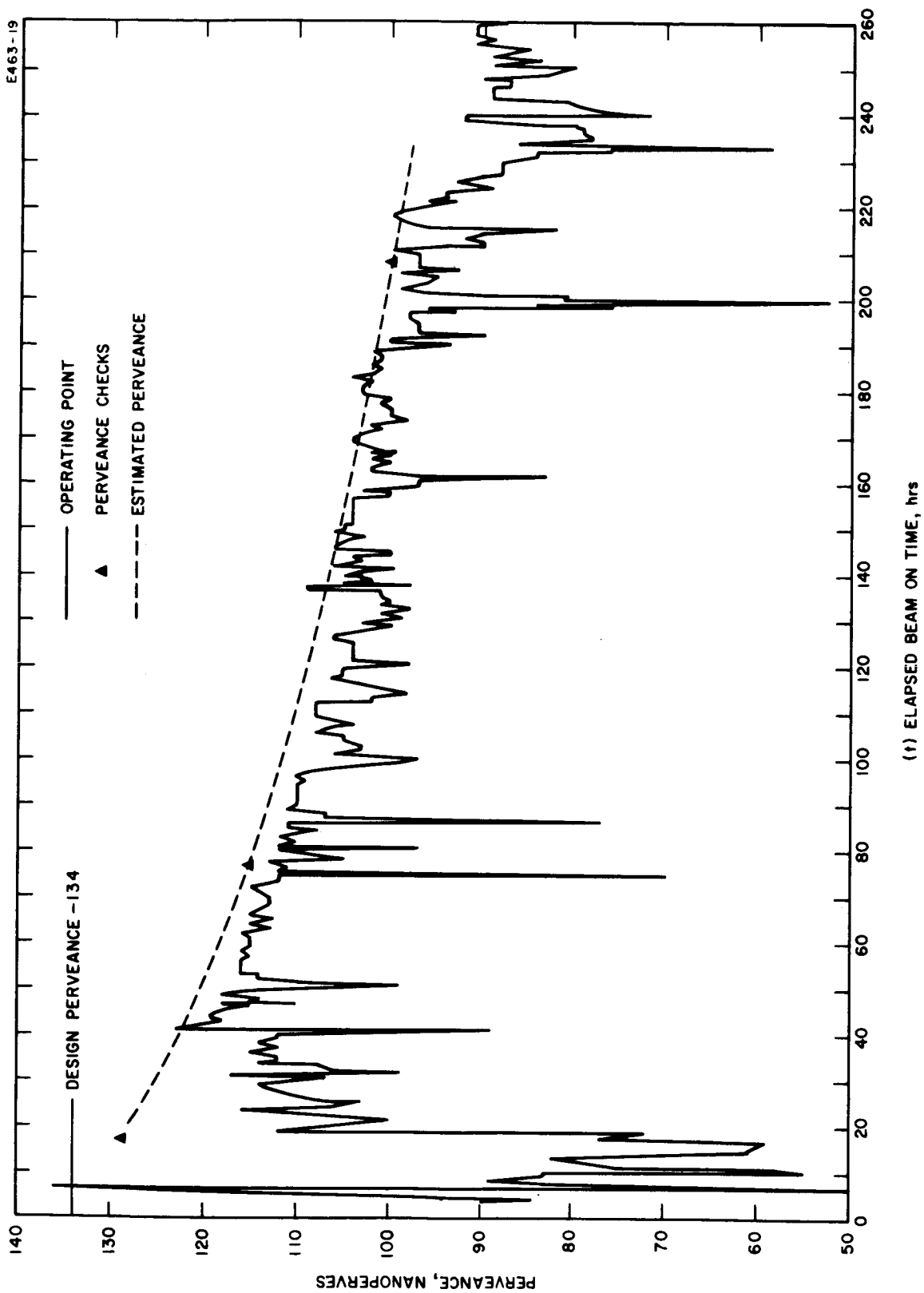


Fig. III-31. Perveance profile of engine 32-150-4.

X-ray fluorescence analysis was also used and detected the molybdenum with better sensitivity. This technique may be used to advantage for nondestructive analysis in future engine tests.

The molybdenum deposit was traced to sputtering caused by the edge of the ion beam striking the edge of the molybdenum engine cage mask. Sputtered molybdenum was also found on the manifold assembly outer shield and on the outer surfaces of the focus, accel, and decel electrodes.

Combustion carbon analysis of total carbon in the ionizer showed 28 ppm compared with the vendor's original analysis of 27 ppm. This difference is well within the expected range. As the two analyses were made by the same reputable laboratory several months apart, it is reasonable to assume that the results are reliable. The carbon content indicates that during the 260 hour operation, the ionizer did not pick up appreciable carbon from the chamber which was evacuated by a diffusion pump using D.C. 705 fluid.

b. Electrode Surfaces — The spectrographic analysis of the focus, accel, and decel electrode surfaces showed some unexpected deposits. Results of analyses of the surfaces facing the emitter (back) and facing the vacuum chamber (front) are given in Table III-1. Each set of electrodes is comprised of two outer and two inner electrodes. The side focus electrodes operate at a considerably lower temperature than the inner electrodes and thus act as a condensing site for material effusing from the hotter engine components.

Copper was the principal deposit on the electrodes because of sputtering of the copper beam collector and front of the neutral detector. Molybdenum was derived from the cage shield. Almost without exception, iron, chromium, nickel, silicon, calcium, and tungsten were found in considerably greater abundance on the back side of the electrode. Although these elements are in high percentage, they actually represent a rather small total deposit. The side focus electrodes had the heaviest deposits since they were cooler and were directly over the opening of

TABLE III-1

Contamination of Various Electrodes, percent

	Side Molybdenum Focus Electrode No. 1		Center Molybdenum Focus Electrode No. 2		Side Molybdenum Focus Electrode No. 4		Copper Accel Center No. 2		Copper Decel Center No. 3	
	front	back	front	back	front	back	front	back	front	back
Cu	remainder	15								
Mo	18		remainder				remainder			5
W	6.7	44	14	28	7	18	9.9	3.1	1.2	3.1
Si	0.12	20	0.052	0.50	0.05	5.9	5.1	18	1.0	0.26
Fe	0.20	2.1	0.10	0.24	0.19	0.87	0.09	0.08	0.10	0.29
Mg	0.008	0.59	trace	0.028	0.006	0.25	0.42	nil	0.08	0.14
Ni	trace	0.32	nil	trace	trace	0.17	0.006	0.007	0.009	nil
Ca	trace	0.07	nil	trace	trace	0.014	0.07	nil	trace	0.06
Cr	0.015	0.05	nil	trace	0.03	0.02	0.01	trace	nil	0.21
							0.08	nil		

outer edges of laminated molybdenum heat shields. All the materials vaporized from the large surface area of the multiple layers thus could deposit on the cooler part of the electrode. The shields also directed a large amount of the gaseous efflux from the heater area to the back side of the electrode. Traces of iron, chromium, and nickel were probably boiled out of the emitter or from surfaces contaminated with stainless steel during fabrication. It is unlikely, although not impossible, that some of these materials were vaporized from the cesium feed system.

Probably the most important deposit is tungsten. This could come only from the emitter or heater area of the engine. Since tungsten is on the front and the back of all electrodes (except the front of the decel), it must mean that there is tungsten atmosphere in some form in front of the emitter. The decel tungsten concentration may appear negligible merely because it is less than 1%, the limit of detection in this particular sample. The tungsten atmosphere may be composed of oxides produced by environmental oxygen striking the emitter surfaces and vaporizing as WO_2 or WO_3 . Because it is generally in higher concentration on the side facing the emitter, this seems probable. The deposits on the center focus electrodes which ran very hot showed no dark oxide deposit and were essentially clean molybdenum with a coppery tint. The fronts of the electrodes were also metallic. The oxide on the focus electrode must therefore be either reduced to metal or dissolved in the sputtered copper and molybdenum deposit. If the tungsten is a result of a negative ion sputtering of the emitter surface, it is difficult to account for its presence on the surfaces facing away from the emitter.

The silicon deposit may have boiled off the polished molybdenum heat shields, which had been wet hydrogen treated but not vacuum fired. It may also have been driven out of the alumina heater insulators. This probably has no effect on the emitter as spectrographic analysis showed it to be present in normal amounts.

3. Heater Analysis

The post test ionizer heater analysis is presented in Section IV-B-2.

IV. ENGINE DEVELOPMENT STUDIES

A. Ionizer Manifold Fabrication and Evaluation

1. Noncesium Evaluation of Ionizers

The porous tungsten ionizers intended for use on the 15 mlb ion engine are carefully evaluated for their uniformity of flow characteristic to establish their suitability for use in an ion engine. The evaluation and selection processes include the following:

- a. The relative incremental permeability (pressure decay time) of the ionizer slab intended for ionizer fabrication is measured. Measurements are made at 3/4 in. intervals over the entire slab surface.
- b. Ionizer slabs which can be matched within $\pm 10\%$ in relative permeability are reimpregnated with copper and subsequently machined into an ionizer.
- c. Flow rate- ΔP measurements are made on the finished ionizers. The finished ionizers are again matched such that their flow characteristics are within 10% of one another.
- d. The flow rate- ΔP measurements are made on the "as received" ionizer as well as after the required hot flattening subsequent to sealing the nonemitting regions.

The necessity for using the permeability test to evaluate material intended for ionizer application became apparent after nonuniform bubble patterns were observed on the large 10-strip ionizers. It was determined that the nonuniformity in flow was attributable to a variation in sintered ionizer density and thus was reflected in a variation in permeability. The manufacturer (Philips Metalonics) solved the uniformity problem by reducing the density of the material from 83 to 73%.

The characteristics of their Mod E material were evaluated to determine the relationship between density and relative permeability. The relative permeability is presented as the time (sec) for 1550 cm³ of nitrogen to drop from 12 to 10 in. Hg. The data for a 0.050 and 0.085 in. thick Mod E ionizer material are shown in Fig. IV-1 as a function of ionizer density. In this material it is observed that a density variation from 74 to 84% of theoretical results in a sixfold increase in the blow-down time. In fact, a $\pm 2\%$ density variation around a mean density of 74% results in a permeability variation of 50% from the mean value.

To show the usefulness of the relative permeability measuring apparatus, additional data are shown in Fig. IV-2. In this figure, the decay times for various densities of spherical porous tungsten are compared. The parameter is the particle size. It is observed that a $\pm 2\%$ density variation also results in a decay time spread of 2:1 for both the 3.9 and 6.9 μ tungsten particle size. The density variation will have to be held to better than $\pm 1\%$ in order to attain uniform ion emission from large engine ionizers. A photograph of the HRL permeability test apparatus used to measure the data presented in Fig. IV-2 is shown in Fig. IV-3.

The Philips Metalonics permeability data sheets supplied with the ionizers for use on the first 20-strip engine are presented in Figs. IV-4 and IV-5. Hughes Research Laboratories' flow rate- ΔP measurements for the same ionizers are presented in Figs. IV-6 and IV-7. A schematic of the flow rate measurement apparatus used at HRL is shown in Fig. IV-8.

The flow rate apparatus is used in evaluating the two-strip or larger ionizers. This apparatus, however, is not sufficiently sensitive when used to measure the flow through a small region (e.g., 1/4 in. diameter) of an ionizer. The decay time technique measures the integrated flow and is thus more useful in interrogating the small regions of the ionizer surface.

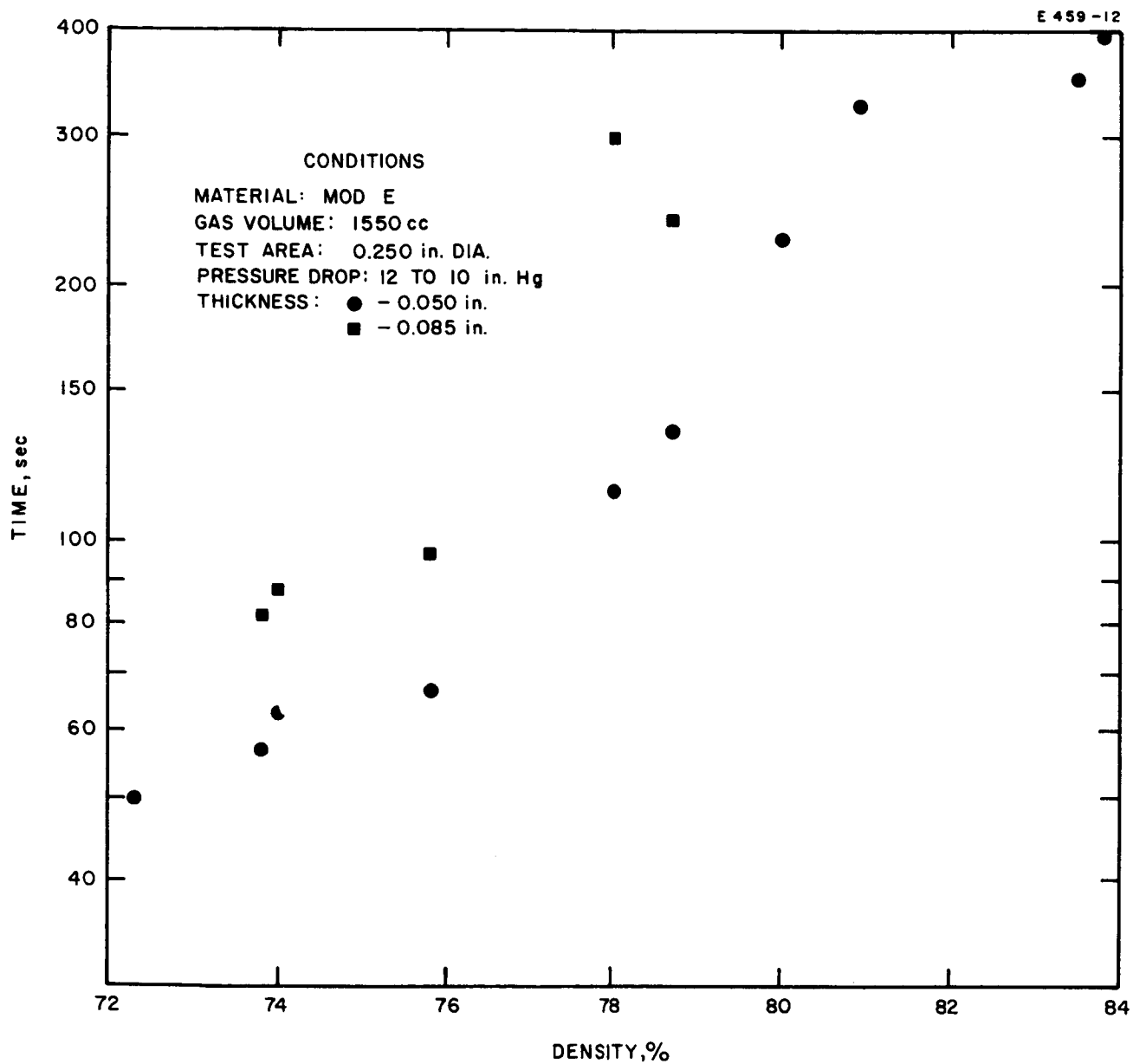


Fig. IV-1. Relative permeability data for 0.050 in. and 0.085 in. thick Mod E ionizer material as a function of ionizer density. (Data provided by Philips Metalonics.)

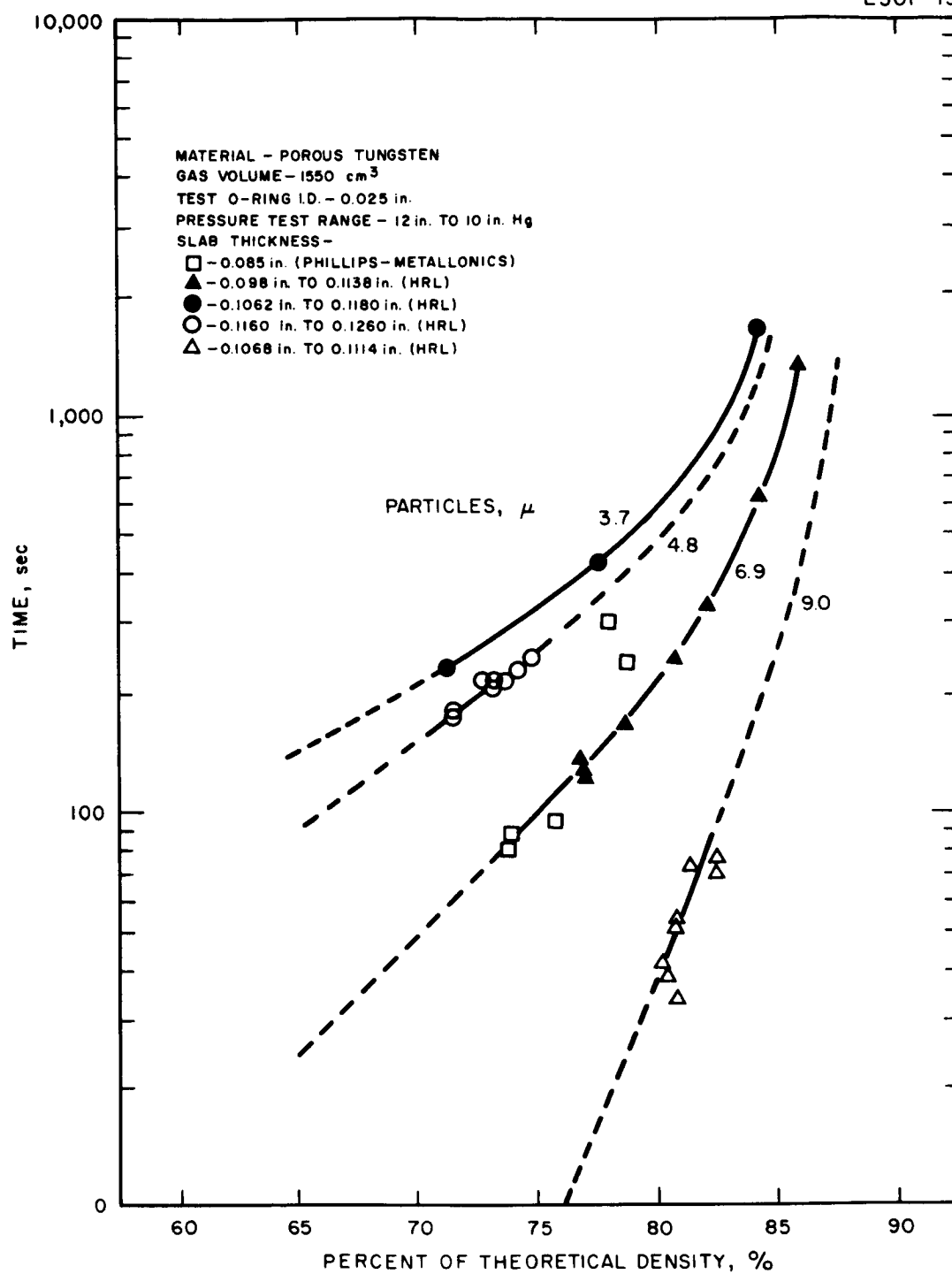


Fig. IV-2. Nitrogen decay time versus percent theoretical density for slabs made from different sizes of spherical tungsten powder.

M 3529

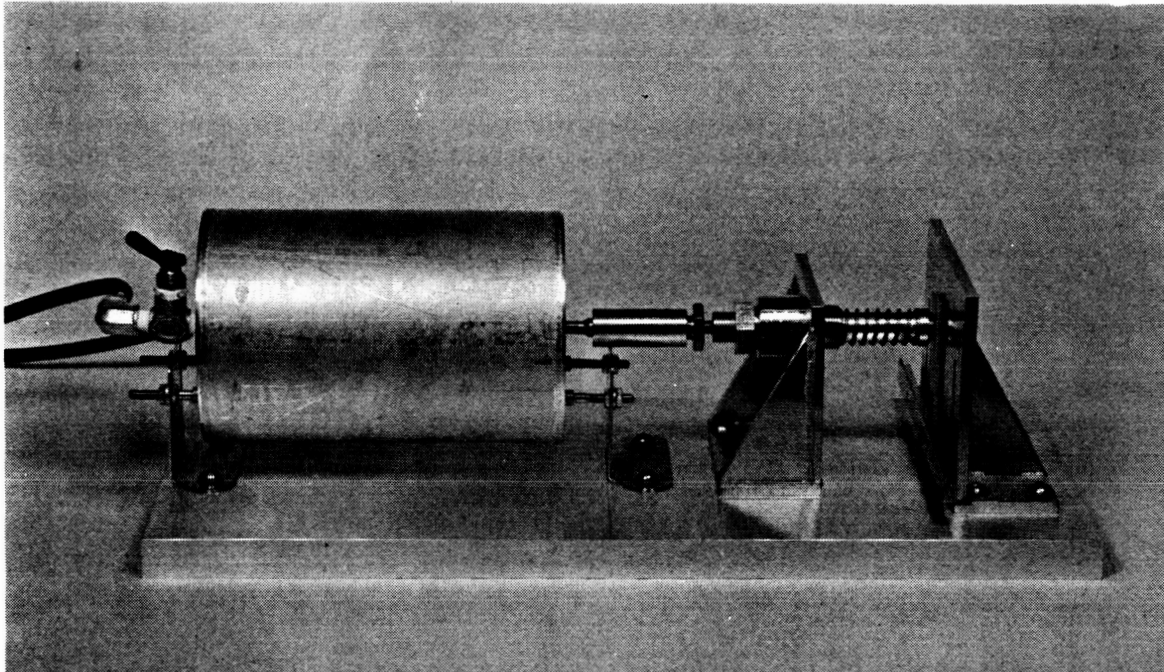


Fig. IV-3. HRL permeability test fixture.

SERIAL NO. 508 TO 511

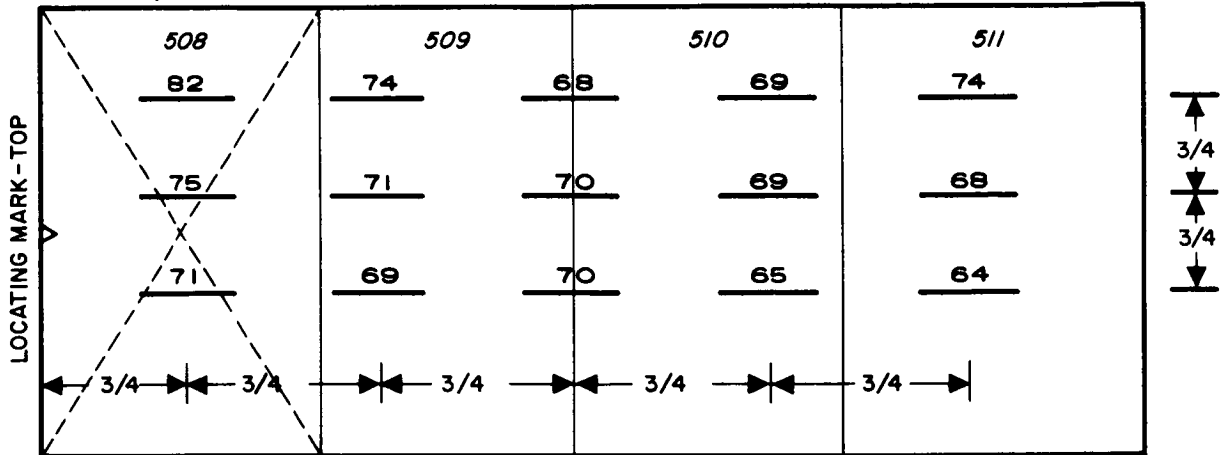
NITROGEN TRANSMISSION TEST

BILLET NO. M769

BLANK NO. 3A

DATA, sec.

E459-5



SERIAL NO. 512 TO 515

NITROGEN TRANSMISSION TEST

BILLET NO. M769

BLANK NO. 4A

DATA, sec.

E459-6

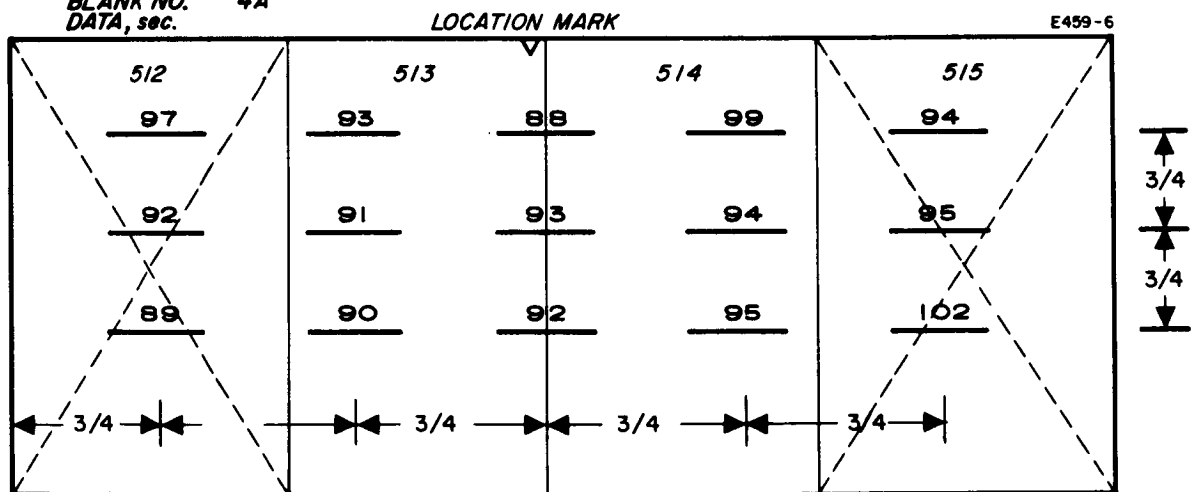


Fig. IV-4. Philips Metalonics permeability data sheet for the ionizers intended for use in the first 20-strip engine.

SERIAL NO. 504 TO 507

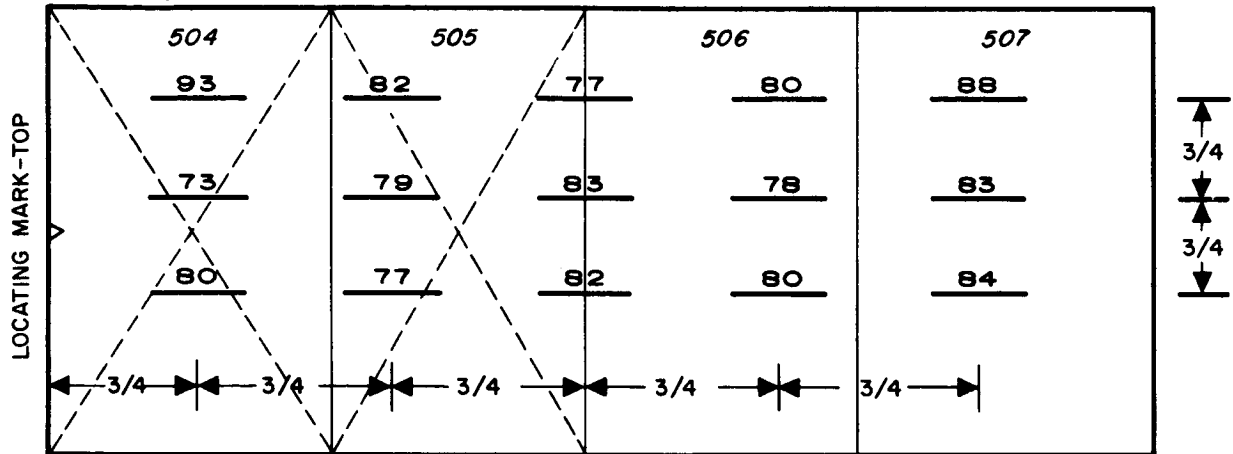
NITROGEN TRANSMISSION TEST

BILLET NO. M769

BLANK NO. 2B

DATA, sec.

E459-9



SERIAL NO. 516 TO 519

NITROGEN TRANSMISSION TEST

BILLET NO. M769

BLANK NO. 3B

DATA, sec.

E459-10

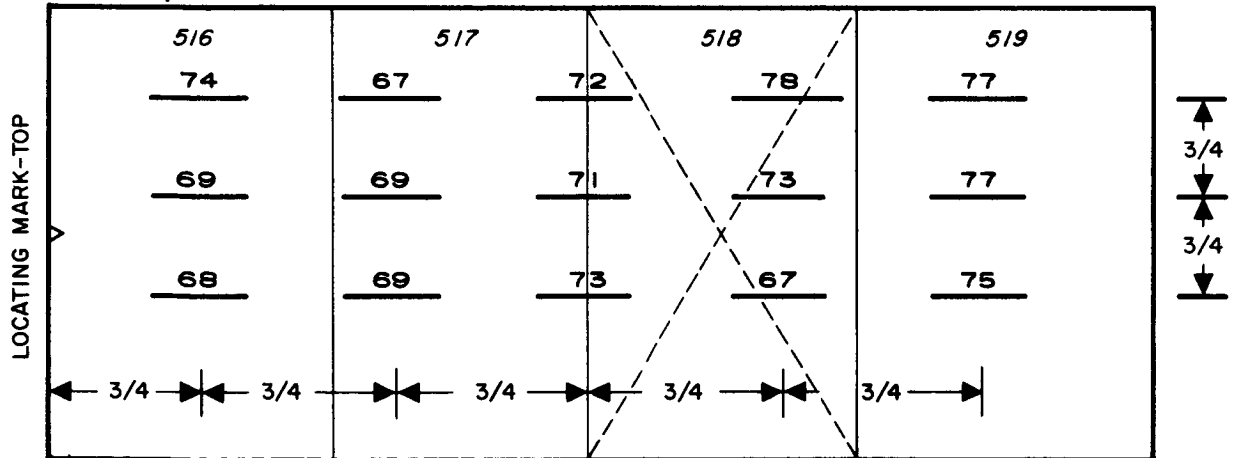


Fig. IV-5. Philips Metalonics permeability data sheet for the ionizers intended for use in the first 20-strip engine.

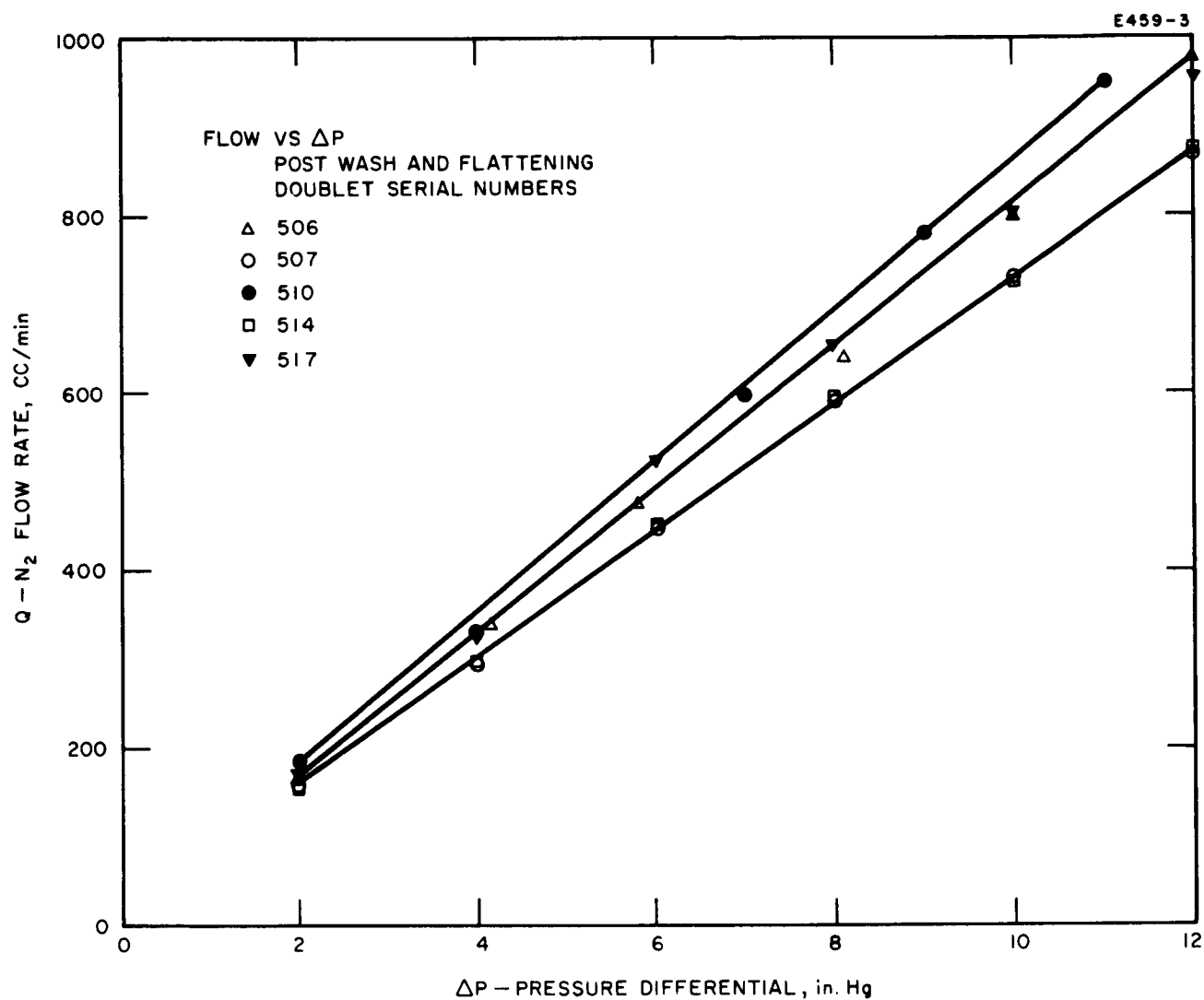


Fig. IV-6. HRL flow rate- ΔP measurements for the Philips Metalonics ionizers intended for use in the first 20-strip engine.

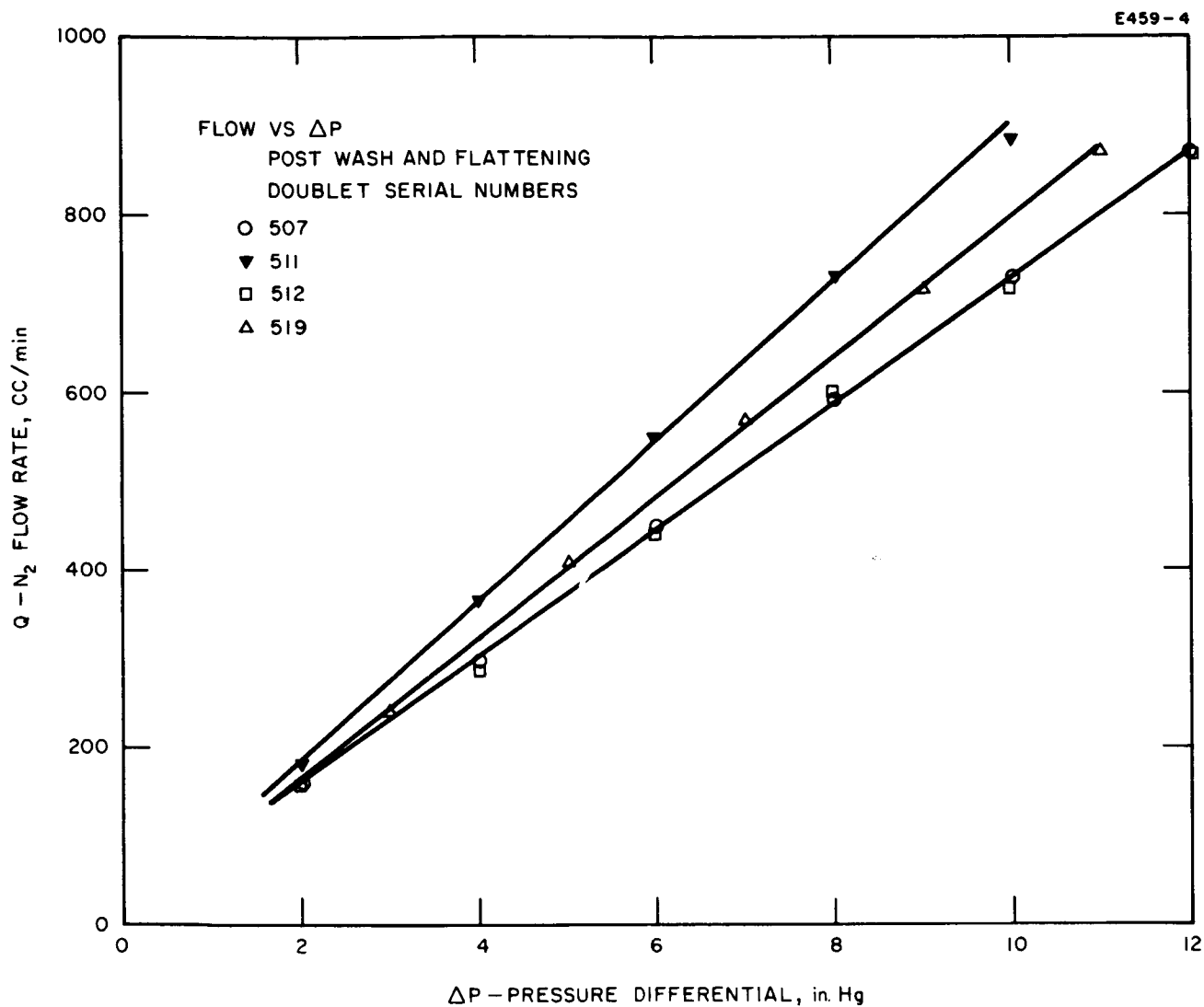
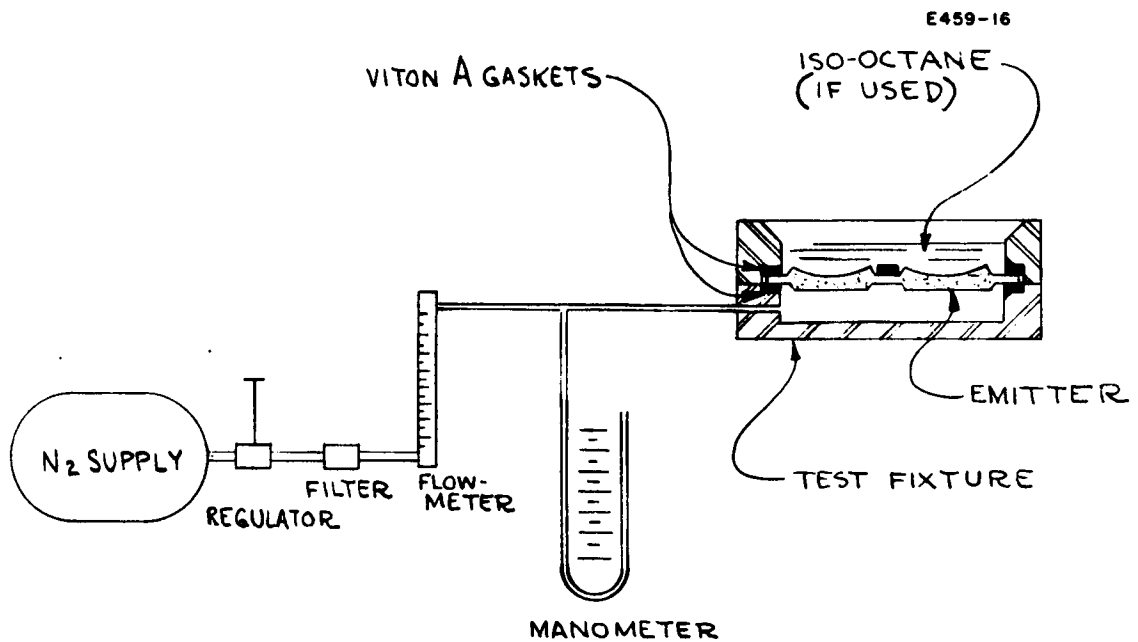


Fig. IV-7. HRL flow rate- ΔP measurements for the Philips Metalonics ionizers intended for use in the first 20-strip engine.



NITROGEN FLOW TEST

Fig. IV-8. Schematic of the flow rate measurement apparatus used at HRL.

Other records are maintained on the conditions to which each ionizer or group of ionizers is subjected before and during fastening of the ionizer to the tungsten manifold. Figure IV-9 shows a typical furnace history of the ionizers before weld to the manifold. Figures IV-10 and 11 show inspection records after welding 10 two-strip ionizers to the manifold.

2. Machining of Tungsten Manifolds

Early in the multistrip ion engine program, it was found that conventional machining techniques were not suitable for fabrication of tungsten manifolds. The electric discharge process was therefore used to perform all machining of the manifold. After weld fabrication and during leak testing of the assembly, it was found that occasional leakage occurred through the side walls of the manifold. At that time, a coarse electric discharge cut was being used. In an effort to minimize or eliminate the problem, a fine finish cut was made and the side wall thickness of the tungsten was increased. Other types of tungsten were obtained to improve the finished parts. While these precautions reduced the problem, leakage still occurred in a few instances.

A two-phase program was initiated in order to study machining techniques; their effect on end item quality was determined by metallographic studies. One segment of the program involved electric discharge machining, the other a modified conventional type machining.

The electric discharge machining investigation proved that this process was unsuitable for fabrication of tungsten, which, during subsequent welding, was subject to high stresses. Even with machining carried out at the lowest metal removal rates, examination of the parts indicated that the grain boundaries in the tungsten had been attacked and that surface cracks had resulted. The depth of the grain boundary attack varied between 0.002 and 0.007 in. for a fine to medium rate of metal removal. The higher rates of machining resulted in penetration to 0.011 in. A typical photomicrograph of an electric discharge machined surface is shown in Fig. IV-12. The fracture in this surface is very apparent.

Surface cracks have also been observed on the polished surface of weld stressed manifolds which have been machined by this process. (Figure IV-30 shows the resultant cracked surface (see Section IV-A-4).)

In order to alleviate the fracture problems resulting from discharge machining, a program was instituted to develop the forming of tungsten by hot machining methods. Photomicrographs of tungsten samples machined by this method did not show the surface cracks or grain boundary penetration observed earlier. The tungsten samples were machined at 450°C; each was mounted to the machine tool with a specially built vise which served to heat as well as hold the part. Tungsten carbide tipped tools were used. No lubricants were employed nor were any available which could function at 450°C.

The tungsten manifold used for the 20-strip engine program reflects the perfection attained in treating tungsten with this hot machining method. Photographs of the manifold, presented in Section II (Figs. II-8(a) and (b)), show the slotted back, the milled ionizer plenum, the cesium gas passage slots, and the broached "Xmas tree" slots in the rear of the tungsten manifold.

Special techniques were required to avoid breaking the edge of the tungsten as the horizontal mill tool passed through the work. In most cases, the part was backed up with a close fitting molybdenum slab to accept the runoff from the tool. Climb milling was used where applicable; the cut usually started at the center of the work and proceeded toward both ends by reversing both the table direction as well as the rotation of the tool. The depth of cut was usually 0.060 in. The tool typically would traverse the work in a few minutes.

3. Ionizer Surface Processing

Metallurgical examination of each engine ionizer is a part of the routine quality control process for this critical component. Photomicrographs of the ionizer surface which are used for pore count and general inspection for anomalies are a part of this examination.

20 STRIP IONIZER DOUBLET PROCESS - FLOW CHART

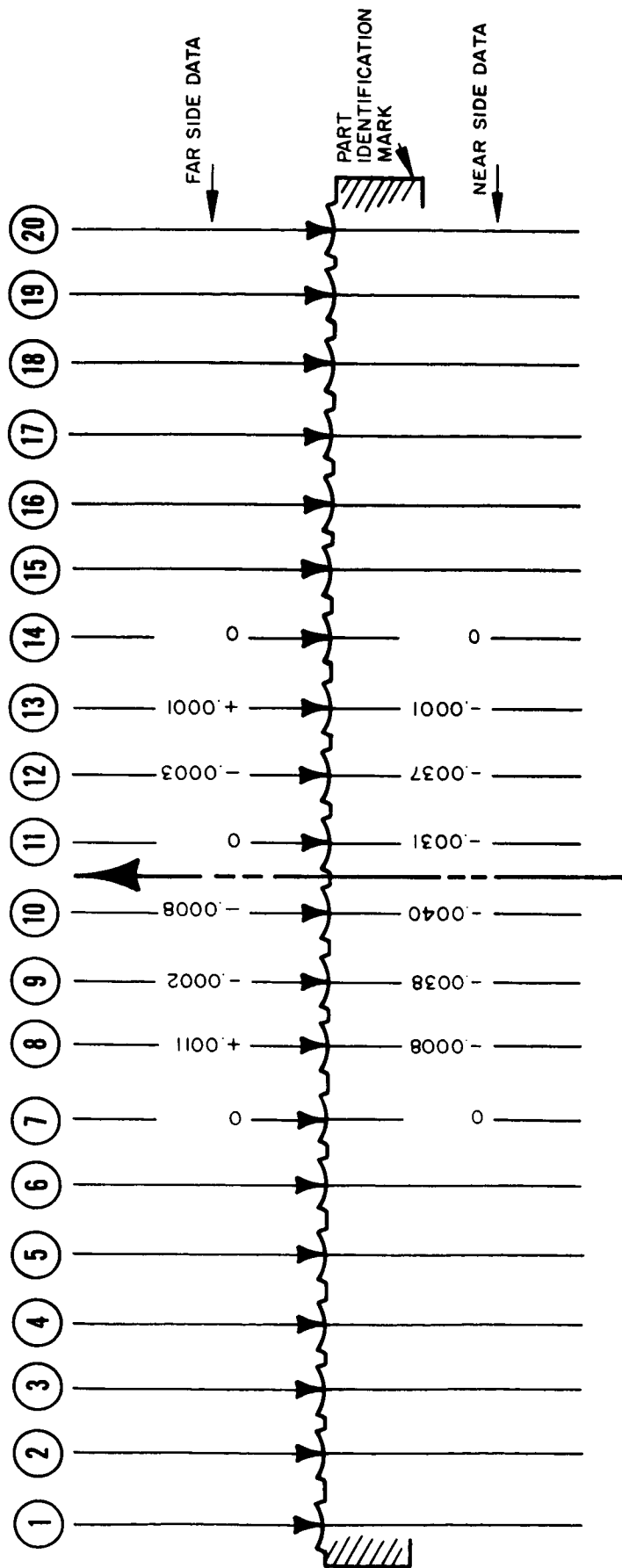
S/N	RECEIVING INSPECTION		WET HYDROGEN FIRE, 1 hr AT 1100 °C, HARPER FURNACE			WASH, EBW		GENERAL (VACUUM, 1 hr MUST BE 1 hr)	
	DIMENSIONS	FLOW TEST	FIRE	DATE	GROUP	DATE	GROUP	DATE	FURNACE
506	✓	—	—	—	—	✓	A	9-7-64 (APPROX)	HARPER
507	✓	—	—	—	—	✓	A	"	"
509	✓	—	—	—	—	✓	C	10-6-64	"
510	✓	—	—	—	—	✓	C	"	"
511	✓	—	—	—	—	✓	C	"	"
512	✓	✓	✓	10-5-64	D	10-5-64	E	10-8-64	VACUUM ELECT. TANTALUM
513	✓	✓	✓	"	D	"	E	"	"
514	✓	✓	✓	"	D	"	E	"	"
517	✓	✓	✓	"	D	10-7-64	G	10-9-64	"
519	✓	✓	✓	"	D	"	G	"	"

NOTE: GROUP INDICATES PARTS PROCESSED AT THE SAME TIME

RAL FLATTENING 1400 °C, 1 hr IF POSSIBLE) MASKED WITH TUNGSTEN)			EDGE FLATTENING (VACUUM, 1400 °C, 1 hr IF POSSIBLE) (MUST BE MASKED WITH TUNGSTEN)				INSPE	
TIME, TEMP, CONDITIONS	GROUP	REMARKS	DATE	FURNACE	TIME, TEMP, CONDITIONS	GROUP	REMARKS	DIMENSIONS
1 hr-1400 °C DRY HYDROGEN	A		9-8-64 (APPROX)	HARPER	1 hr-1400 °C DRY HYDROGEN	B		✓
"	A							✓
17 min-1650 °C DRY HYDROGEN	F	WET H ₂ 1100 °C J	10-8-64	ELECT- VACUUM TANTALUM	1/2 hr-1400 °C	K		✓
"	F	"	10-10-64	"	"	R		✓
"	F	"	"	"	"	R		✓
30 min-1400 °C	L		10-9-64	"	20 min-1400°C	N		✓
"	L	FLOW TESTED	"	"	"	N	FLOW TESTED	✓
"	L		"	"	"	N		✓
30 min-1450 °C	M			"	1/2 hr-1400 °C	O	TOOLS TURNED YELLOWISH	✓
"	M	FLOW TESTED		"	"	O	FLOW TESTED	✓

Fig. IV-9. Twenty-strip ionizer doublet process — flow chart.

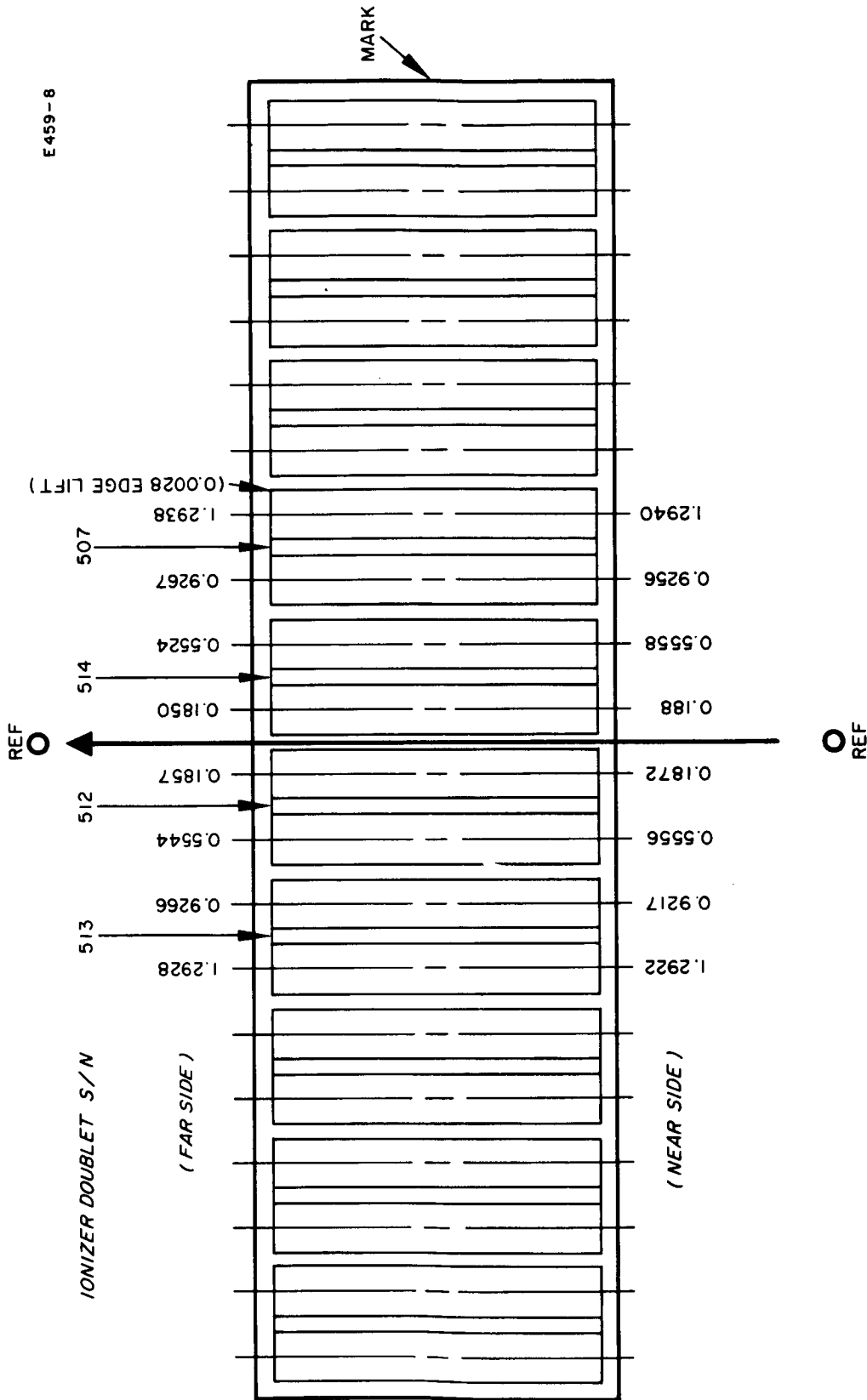
ACTION	WET HYDROGEN FIRE, 1hr AT 1100 °C, HARPER FURNACE			WELDED TO MANIFOLD S/N	REMARKS
	FLOW TEST	FIRED	DATE	GROUP	
	✓	✓	10-5-64	D	
	✓			A	
	✓				
	✓				
	✓				
	✓			A	
	✓			A	
	✓			A	
	✓				
	✓				



Manifold: "A"

Process Status: Post end welds, 512 and 514 and
post stress relieve, 1400°C,
1/2 hr. vacuum and edge flatten
(2nd) firing 1400°C, 1/2 hr.

Fig. IV-10. Records of inspections performed on 20-strip engine ionizers after welding some of the ionizer segments to the manifold. The data presented is the deviation in inches of the lens ends from an arbitrary reference plane through lenses 7 and 14.



Manifold: "A"

Process Status: Post end welds, 512 and 514 and
post stress relieve, 1400°C,
1/2 hr. vacuum and (2nd) firing
1400°C, 1/2 hr. edge flatten.

Fig. IV-11. Records of inspections performed on 20-strip engine ionizers after welding some of the ionizer segments to the manifold. The data presented are the distances in inches of the lens ends from a reference line through the middle of the ionizer.



Fig. IV-12. Photomicrograph of typical electric discharge machined tungsten surface (100x).

M 3022

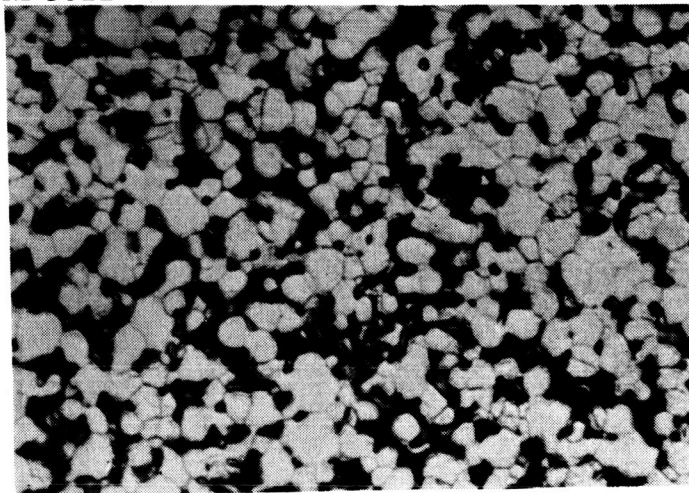


Fig. IV-13.
Grain and pore characteristics of a metallographically polished and copper evaporated sample of porous tungsten (500x).

A part of the comparison between ionizer materials is based on data obtained from photomicrographs. The surfaces studied are usually polished, but the actual engine ionizer surface is not; it is either machined with a single point tool or ground. The grinding or machining processes smear tungsten and copper over the surface and thus probably change the ionizing characteristics of the material.

A technique has been developed at Philips Metalonics to remove the smeared copper and tungsten. The following photomicrographs (Figs. IV-13 through IV-20) show the evolution of the process.

Figure IV-13 shows the grain and pore characteristics of a metallographically polished and copper evaporated sample of porous tungsten. Figure IV-14 shows the smeared surface, prior to copper evaporation, of a 50% HNO_3 etched surface of a ground ionizer. Figure IV-15 shows the smeared surface, prior to copper evaporation, of a 50% HNO_3 etched surface of a machined ionizer. Figures IV-16 and IV-17 show the same material shown in Fig. IV-14 and IV-15, respectively, except that the copper has been evaporated.

Various techniques were used in attempts to remove the smeared copper and tungsten. Figures IV-18, IV-19, and IV-20 show the effects of a concentrated HF-HNO_3 etch, a dilute HF-HNO_3 etch, and a Murakami etch, respectively. The first etch (Fig. IV-18) opened the pores to 160% of original size; the etching time was 10 sec. The second etch (Fig. IV-19) opened the pores to 100% and etching time was 90 sec. The third etch (Fig. IV-20) opened the pores to 100%; the etching time was 5 min.

The ionizers (Philips Mod E) used in the 20-strip engine are etched prior to evaporation of the copper as follows:

- a. the part is degreased with trichlorethylene
- b. it is etched with a solution (10 g $\text{K}_3\text{Fe}(\text{CN})_6$, 10 g NaOH , 100 ml H_2O) for 8 min
- c. it is then rinsed with distilled water for 1/2 hour

M 3015



Fig. IV-14.
Smeared surface, prior to copper
evaporation, of a 50% HNO_3 etched
surface of a ground ionizer (500x).

M 3016

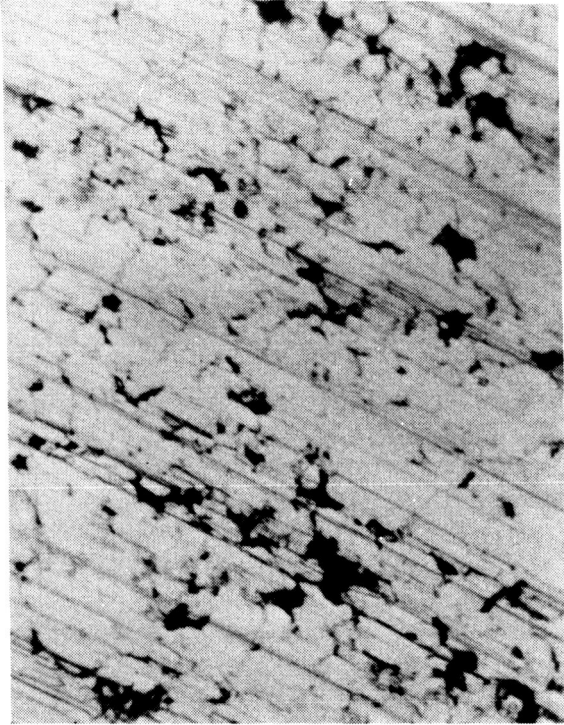


Fig. IV-15.
Smeared surface, prior to
copper evaporation, of a 50%
HNO₃ etched surface of a
machined ionizer (500x).

M 3017

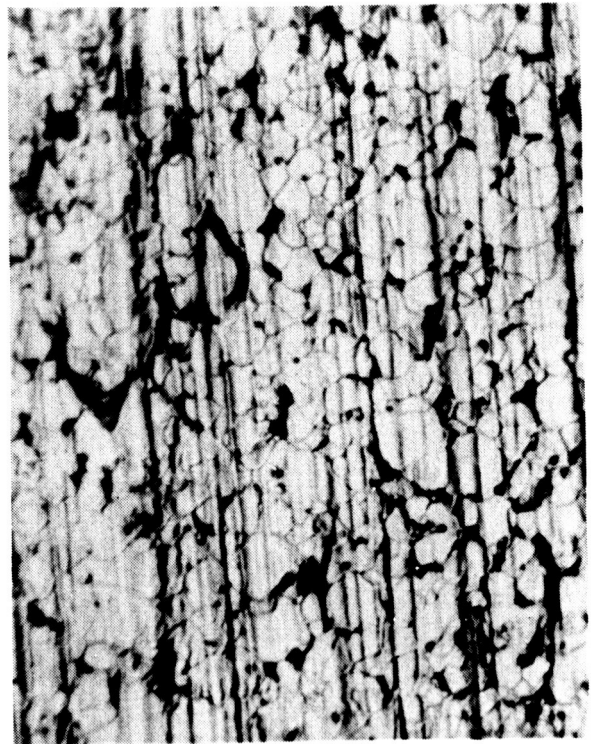


Fig. IV-16.
Fifty percent HNO₃ etched
surface of a ground ionizer
after evaporation (500x).

M 3018

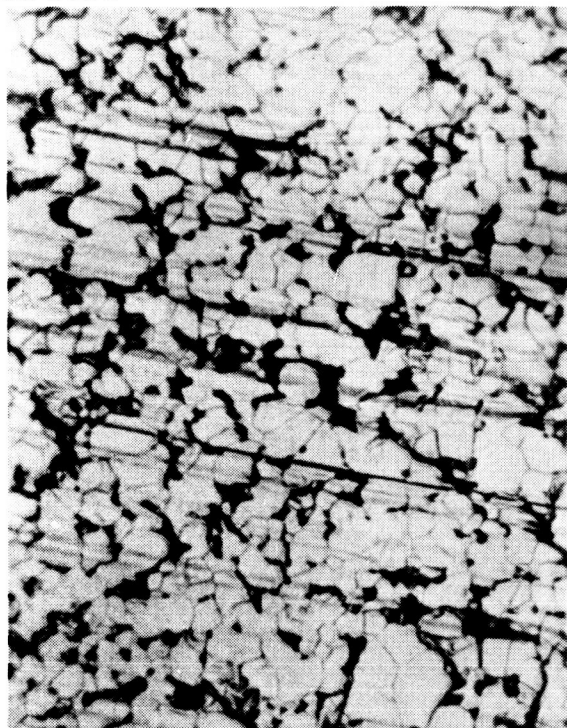


Fig. IV-17.
Fifty percent HNO_3 etched surface of a machined ionizer after evaporation (500x).

M 3021

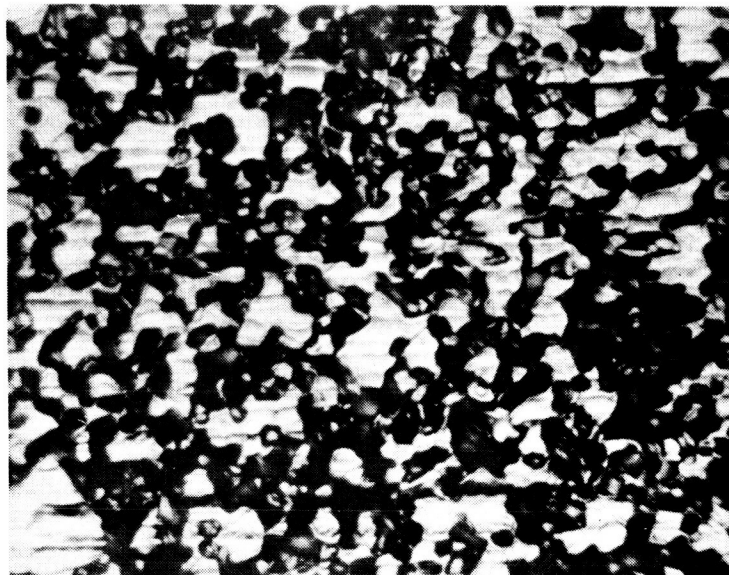


Fig. IV-18.
Effects of concentrated HF-HNO_3 etch on ground surface of ionizer. Etch time, 10 sec (500x).

M 3019

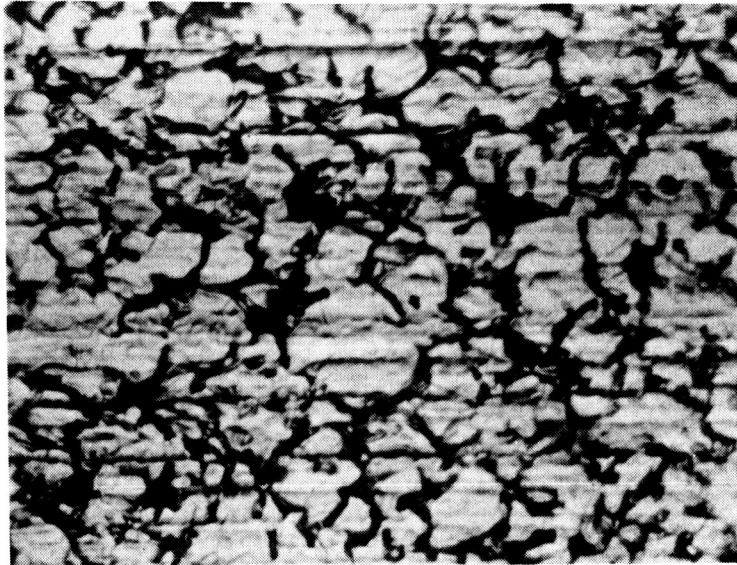


Fig. IV-19.
Effect of dilute HF-HNO₃ etch on ground
surface of ionizer. Etch time, 90 sec
(500x).

M 3020

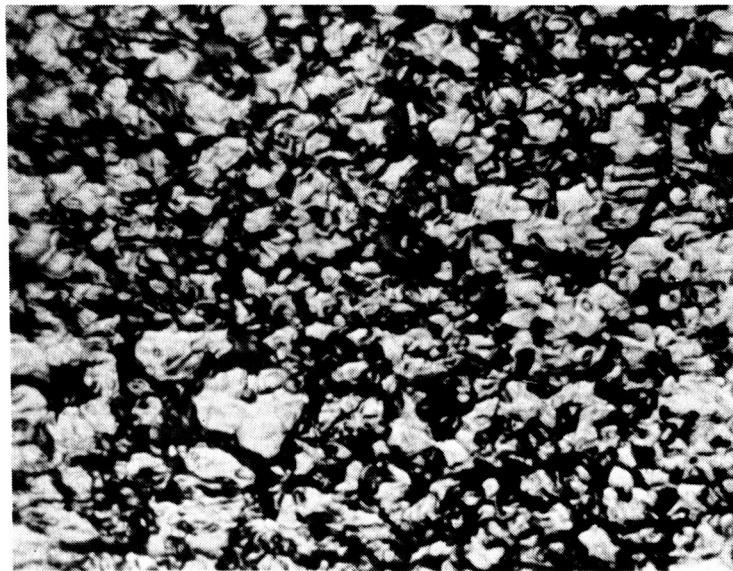


Fig. IV-20.
Effect of Murakami etch on ground sur-
face of ionizer. Etch time, 90 sec
(500x).

- d. the residue is removed with a 50 vol % solution of HNO_3 applied for 1 min
- e. it is rerinsed with distilled water.

4. Electron Beam Welding

Electron beam welding techniques for joining ion engine components have been used for almost three years at HRL. The ability of the techniques developed to produce reliable and consistent weld assemblies was proved early in 1964 when an operational engine (32-40-8) was randomly chosen for metallurgical sectioning and evaluation. Photo-micrographs of each weld joint in the assembly are presented as follows:

- Figure IV-21 — manifold to emitter, left side (20x)
- Figure IV-22 — manifold to emitter, right side (20x)
- Figure IV-23 — tungsten tube to manifold nipple (20x)
- Figure IV-24 — 98% tungsten-2% molybdenum sleeve to tungsten tube (20x)
- Figure IV-25 — 98% tungsten-2% molybdenum sleeve to molybdenum tube (20x)
- Figure IV-26 — nickel bellows to nickel sleeve (60x).

The most ambitious weld assembly concept arose during 1964 with the advent of the 20-strip ionizer in place of the 14-strip ionizer. The number of emitters and the nonemitting area were increased; a weld between the emitter and manifold was desired in alternate nonemitting areas to provide better thermal conductance to the emitter.

In order to determine the procedures required for minimizing assembly warpage, a preliminary welding study was conducted using obsolete 14-strip emitters. While it was realized that there was not a direct relationship between the obsolete ionizer and the 20-strip ionizer, it was believed that much basic data would be obtained concerning weld settings, stress relieving, and hot straightening procedures. Such a

M 3097

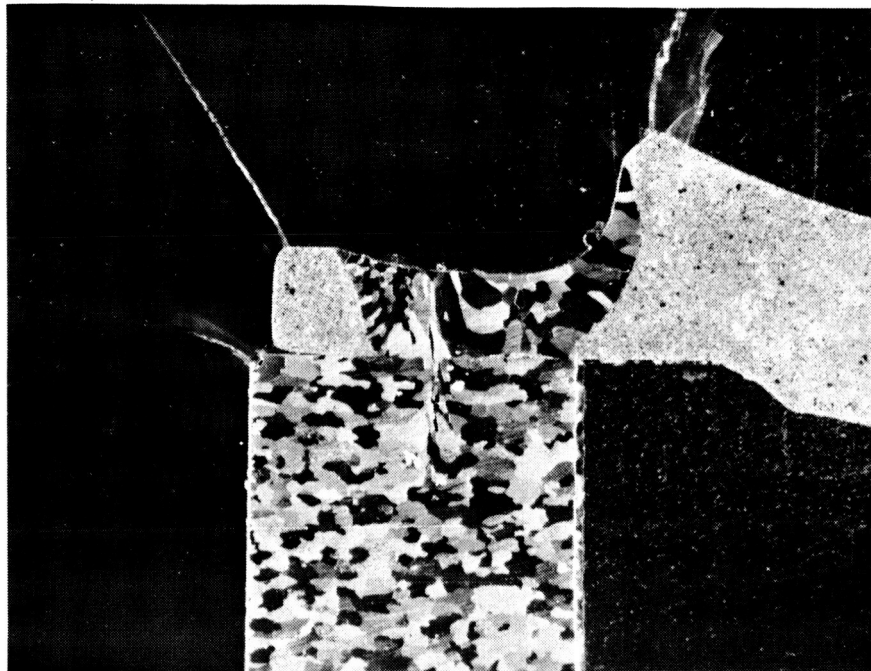


Fig. IV-21. Photomicrograph of electron beam weld — manifold to emitter, left side (20x).

M 3098

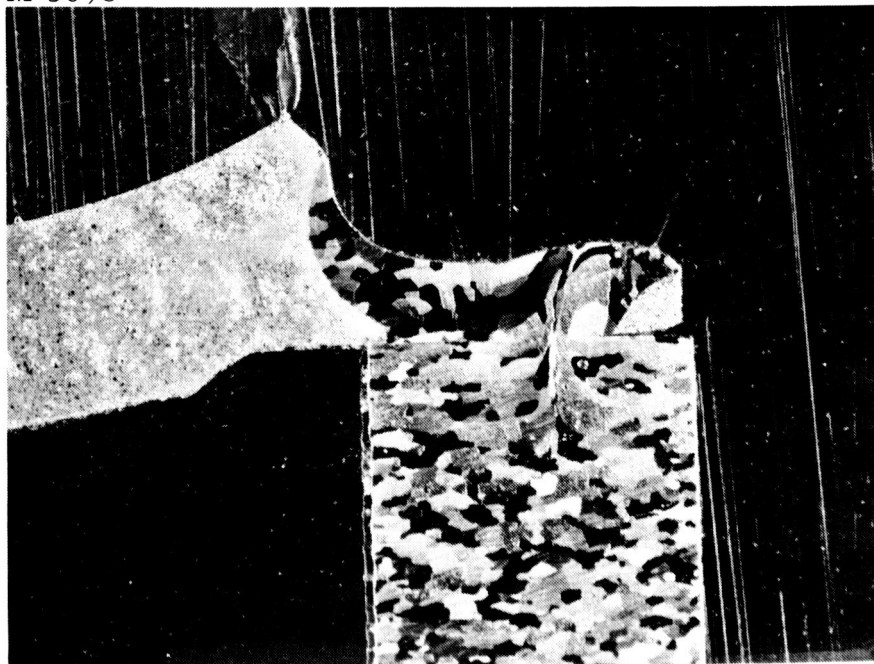


Fig. IV-22. Photomicrograph of electron beam weld — manifold to emitter, right side (20x).

M 3099

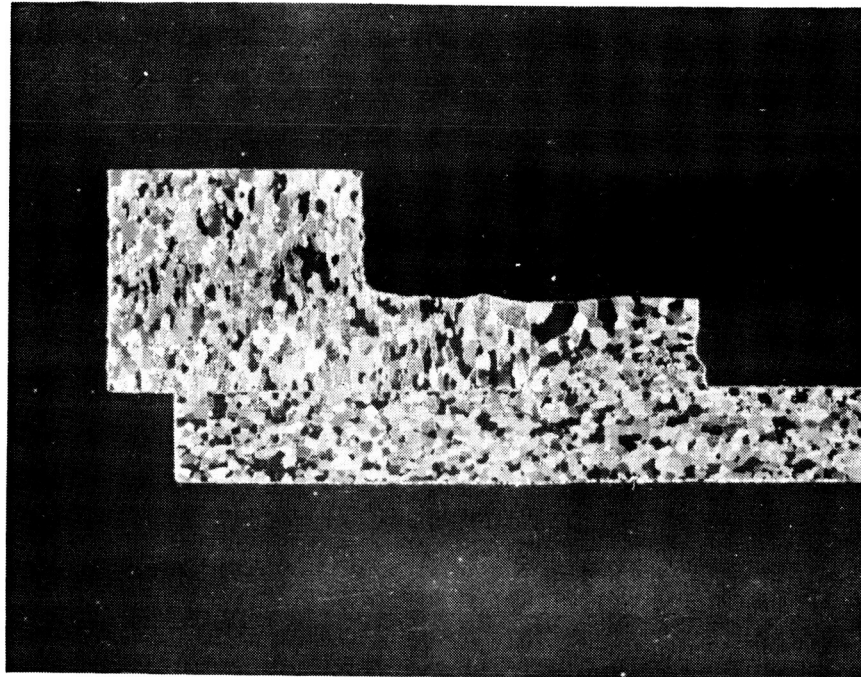


Fig. IV-23. Photomicrograph of electron beam weld — tungsten tube to manifold nipple (20x).

M 3100

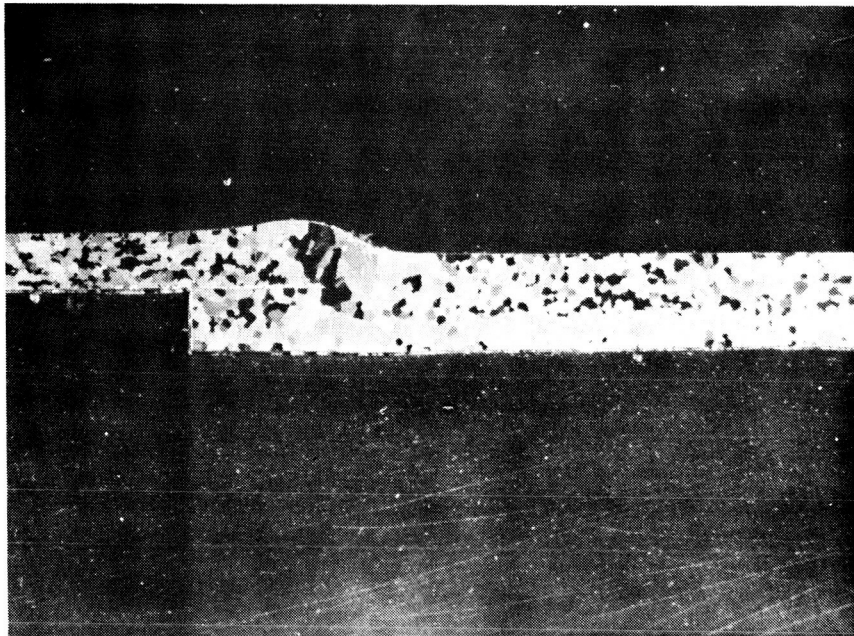


Fig. IV-24. Photomicrograph of electron beam weld — 98% tungsten-2% molybdenum sleeve to tungsten tube (20x).

M 3101

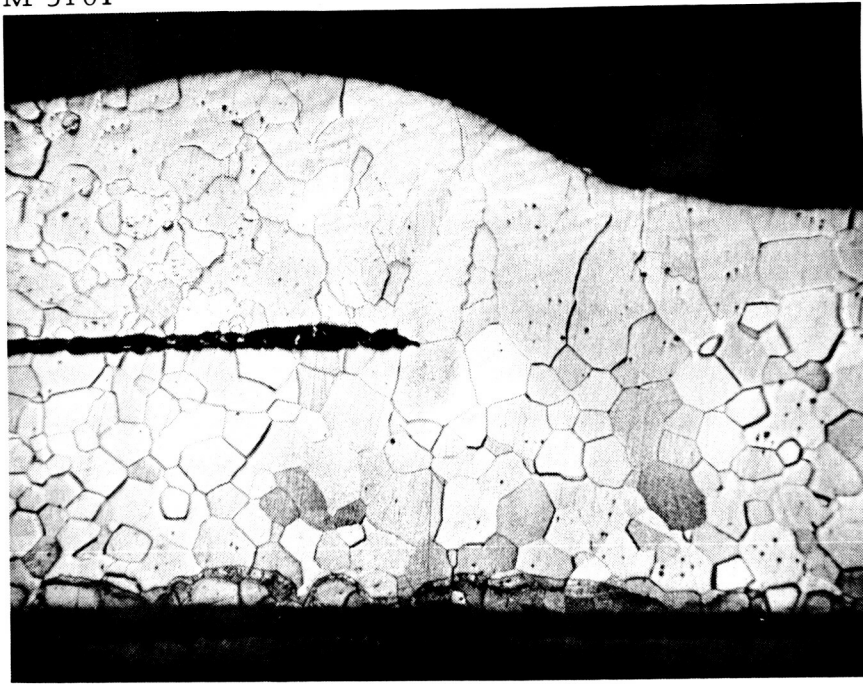


Fig. IV-25. Photomicrograph of electron beam weld — 98% tungsten-2% molybdenum sleeve to molybdenum tube (60x).

M 3102

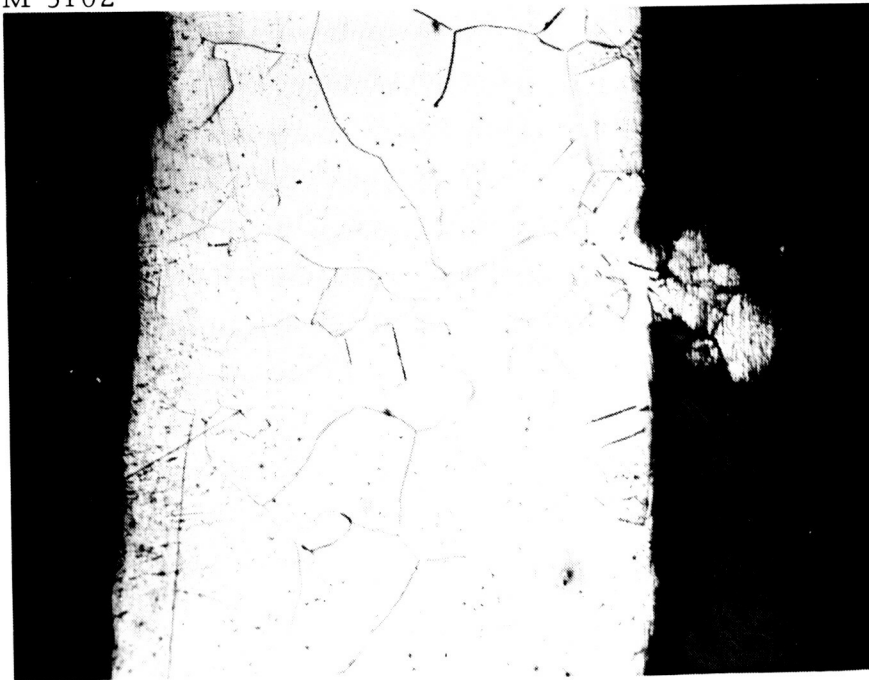


Fig. IV-26. Photomicrograph of electron beam weld — nickel bellows to nickel sleeve, 60x magnification.

study improved the probability of success on the first 20-strip assemblies and, because the 14-strip ionizers were on hand, a minimum cost was incurred.

Two obsolete Philips Mod B, 82% dense, 14-strip emitters with 0.040 in. grooves were chosen for this study. Emitter 14-255-1x was used for an intermittent weld study, and emitter 14-255-2x was used for a continuous weld study. The two emitters were identical in shape and dimensions.

The solid tungsten manifolds were machined by the electric discharge process. The manifolds differed from each other in the design of the cesium access slot locations on the support legs. Ionizer assembly 14-255-1x had 1/4 in. long cesium access slots located at three intervals along each support leg and adjacent to each other. These slots ran from top to bottom of the conductance legs and necessitated the use of an intermittent weld. Ionizer assembly 14-255-2x had the same slot alignment but the slots did not extend the full height of the legs. There was no interruption of the surface of the conductance leg; therefore, a continuous weld was applicable. Also, this manifold had a grooved back to receive the operational engine heater.

The first process in the fabrication of the porous tungsten ionizer assembly was the surface sealing of all nonemitting surfaces of the porous emitter by the electron beam process. Figure IV-27 illustrates a typical setup showing the emitter placed on the surface plate of a pre-heater, the spring loaded fingers for applying a positive force against the emitter, and a tungsten "picture frame" around the emitter which served several purposes. The first and most important function of the picture frame was to protect the edges of the emitter during the surface sealing process. The frame accomplished this by a machined recess which allowed the frame to protrude over the emitter edge and which prevented the beam from striking the edge. The frame also provided a runoff and runoff tab to eliminate start and stop marks on the critical emitter face. It provided a means of protecting the emitter from the

M 2704

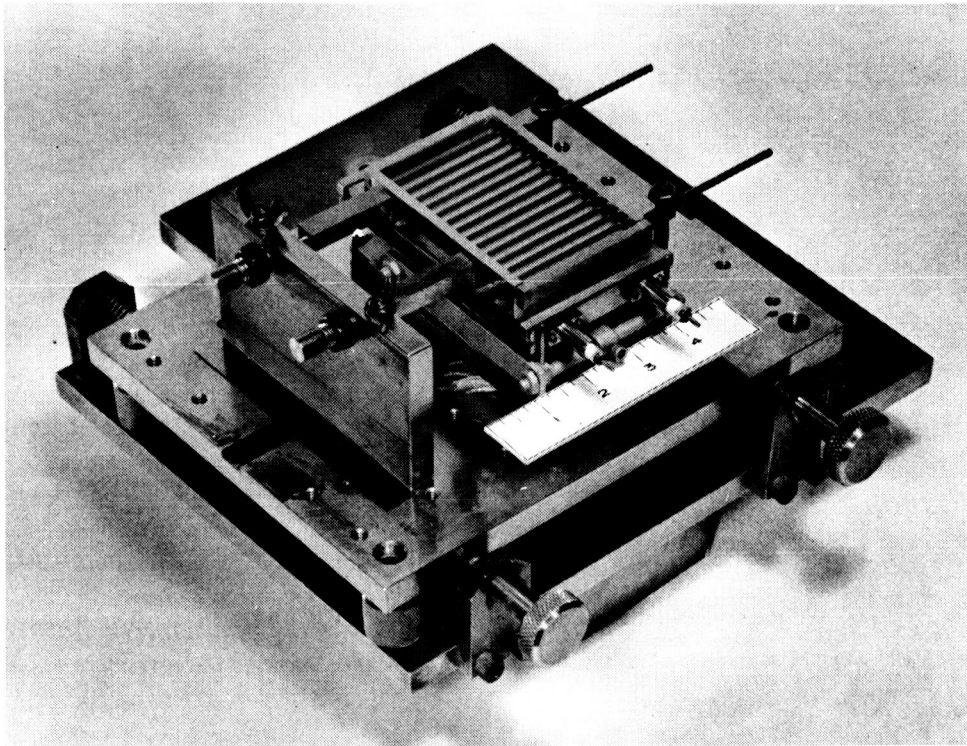


Fig. IV-27. Tooling used for sealing the porous material between each emitting strip of the multistrip ionizer.

preset spring tension of the holding fingers, and a means of positive unrestrained emitter positioning for accurate tracking under the beam. This fixturing allowed tracking accuracies to within 0.002 in.

Cross sections of emitters previously surface sealed with an identical power setting of 85 kV at 9 mA, 0.038 in. beam diameter at 20 in./min travel speed showed a penetration of 0.004 to 0.006 in. The preheat temperature for this schedule was 750°C to 800°C. The appearance of the sealed surface was bright and shiny and free of porosity.

The most important operation before welding the surface sealed emitter into a manifold is the mating of the emitter to the manifold. This operation was accomplished by fitting the parts together as an assembly between flat tungsten plates. The assembly was then fired in a furnace at 1600°C for 1 hour. The tungsten plates also acted as flattening weights. Thus, the assembly was flattened as well as stress relieved. This operation assured intimate contact between all surfaces to be welded. This step was extremely important in order to minimize distortion and cracking tendencies.

Up to this point, both emitters were processed in an identical manner; their welding procedures differed, however. The welding of assembly 14-255-1x will be discussed first (intermittent weld). Figure IV-28 illustrates the tooling for holding the emitter in contact with the manifold over its entire face. The holddown rods were 3/16 in. diameter tungsten. The three rectangular strips were also tungsten, and they were positioned directly over the cesium access slots to protect the emitter as the electron beam passes over them. This was a simple and positive way of making an intermittent weld under these conditions.

The ionizer assembly was then ready for a series of weld passes which included a stress relieving and flattening operation between each sequence of welds. The assembly was preheated in the welding chamber to 750 to 800°C. The first three weld passes were made using 115 kV at 11 mA, an 0.018 in. beam diameter, and 38 in./min travel speed. Examination of cross sections from previously welded parts utilizing this schedule indicated weld penetration through 0.045 in. porous tungsten and

M 3201

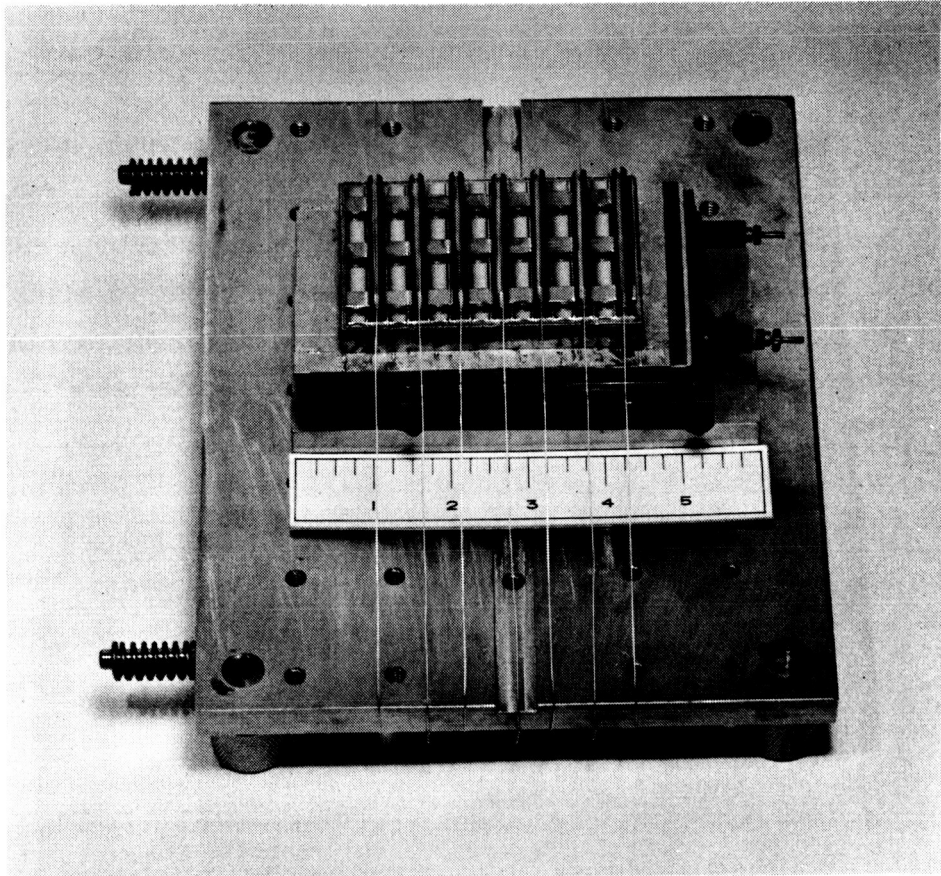


Fig. IV-28. Fixtures for welding 14-strip emitter to manifold thermal conductance legs (intermittent weld path).

0.015 in. into the support leg, and a weld width at the interface of 0.025 in. This condition was ideal because excessive penetration was not desirable from the distortion standpoint. The sequence of the weld passes was also very important, as indicated by previous development studies to prevent cracking of the porous tungsten emitter. The center weld passes were made first, followed by one weld pass on each side of center. The ionizer assembly was allowed to cool to 250°C in the chamber at 10^{-4} Torr. The assembly was then cooled to room temperature outside the chamber.

Before stress relieving, distortion measurements were recorded to analyze the distortion effect from the previous weld series. The ionizer assembly was next stress relieved (1600°C for 1 hour) and again distortion measurements were recorded for comparison. In this manner, not only a final distortion picture was obtained, but the intermediate steps could be analyzed as well.

Two more series of welds were made with two weld passes each, following the above procedure of stress relieving and recording. This completed the welding of the emitter to the seven support legs; Fig. IV-29(A-1) illustrates the amount of distortion in three planes of the ionizer assembly. It should be noted that the distortion increases along the direction in which the weld is made.

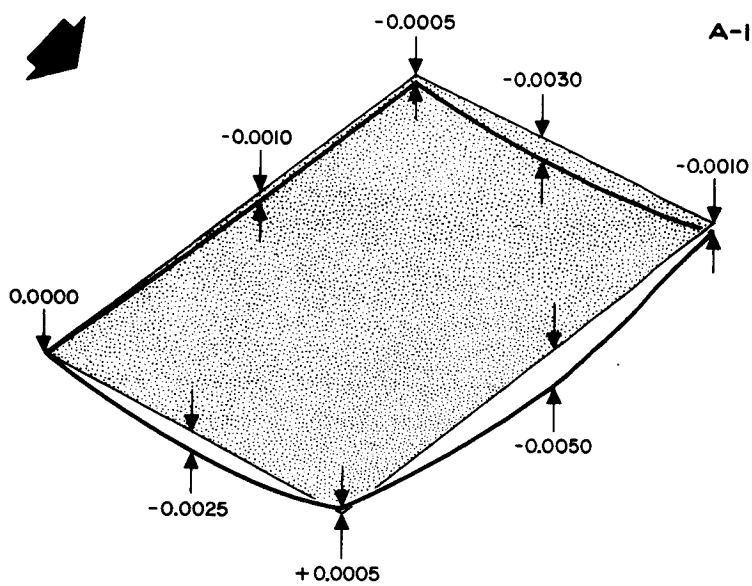
In the last stress relieving operation, prior to making the close out (periphery) welds, special attention was given to the placement of the flattening weights. They were placed on the periphery of the emitter to insure contact between the two surfaces to be welded. The four periphery welds were made in one pumpdown cycle of the electron beam welder. The schedule and procedure was the same as for the support leg welds except that the travel speed was increased to 55 in./min. The thickness of the emitter at this point is 0.030 in. compared with 0.045 in. at the support legs. Weld cross sections show penetration to be 0.015 in. and the width of the weld at the interface to be 0.030 in. Figure IV-29(A-2) shows distortion data after all welding operations and the final stress

relieving operation. The maximum distortion of 0.008 in. (trail edge of box) shown in Fig. IV-29(A-2) is more a relative than an absolute figure. The measurement method used, i.e., using only one reference point, did not provide sufficient information. From these initial data, it was considered advisable to continue the distortion study with improved measuring techniques.

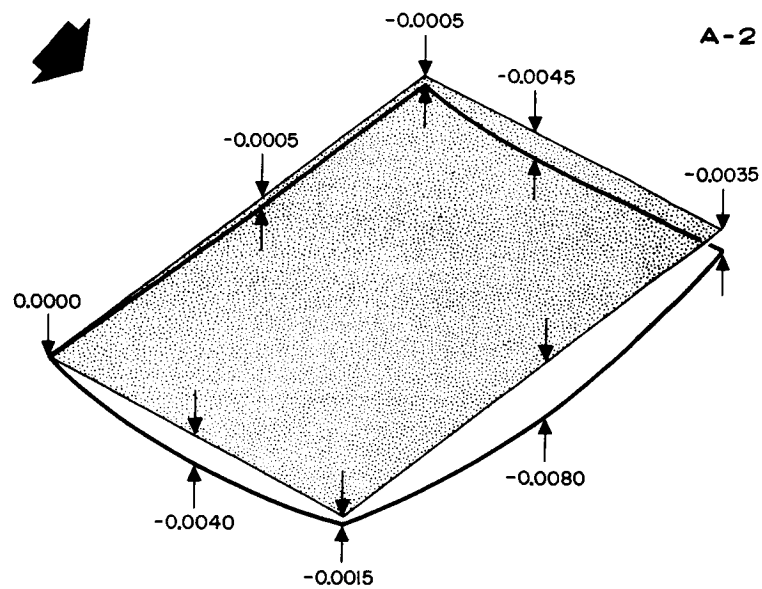
The welding procedure and schedule for fabricating ionizer 14-225-2x was the same as ionizer 14-225-1x with one exception — the weld was continuous rather than interrupted. Figures IV-29(B-1) through (B-7) indicate the distortion measurements taken during that particular sequence of the fabricating procedure. The measurement method used was to establish a reference plane using three predetermined points; in this case, the corners. Weld passes one and two were made and then, in order to determine the effectiveness of the stress relieving operation, measurements were again made after the stress relieving. It can be seen from this data (see Figs. IV-29(B-4) and (B-5), that the stress relieving operation was most effective prior to making the periphery welds. The desired flatness of the ionizer assembly should be secured at this time, as Fig. IV-29(B-6) indicates that the periphery welds added very little distortion to the assembly. After the periphery welds, the assembly was quite rigid and although low in distortion, it was high in residual stresses. Therefore, the stress relieving time and temperature was increased (1650°C in H_2 for 5 hours). Figure IV-29(B-7) indicates the final distortion after all welding operations and subsequent stress relieving. It can readily be seen that, even with the increased time and temperature, the final stress relieving and flattening operation was not as effective as the prior stress relieving operations.

After the final stress relieving, both welded assemblies were visually inspected with magnifications up to 200x. During this inspection, several small 1/8 in. to 3/16 in. long check marks were observed on the sides of each solid tungsten manifold. A nitrogen bubble check in alcohol revealed that two of these check marks leaked on each manifold.

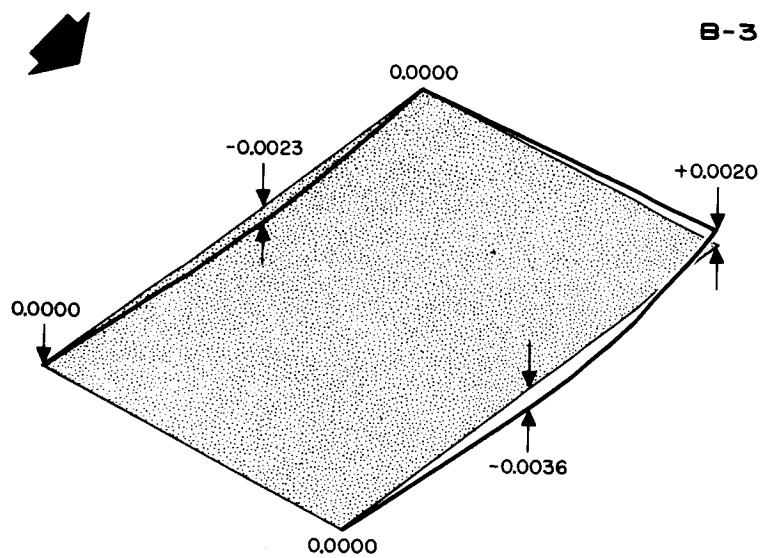
IONIZER ASSEMBLY NO. 14-225-IX



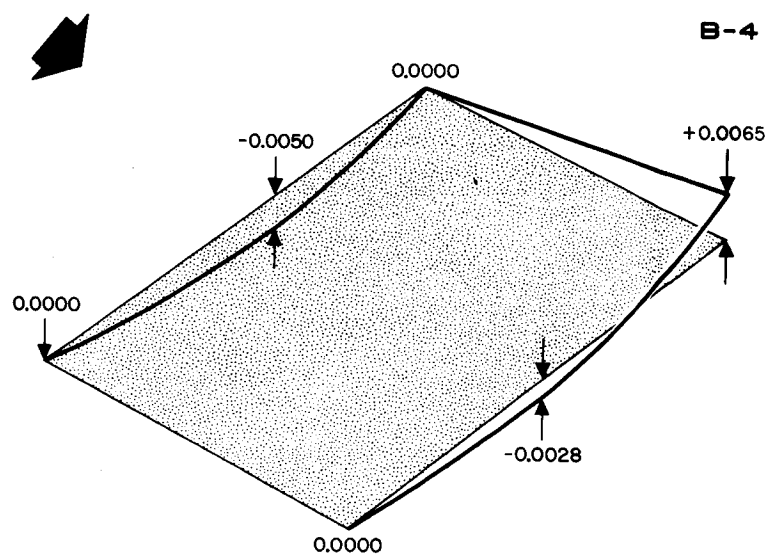
IONIZER, AFTER STRESS RELIEVING
AND SEVEN (7) LEG WELDS



IONIZER, AFTER STRESS RELIEVING
AND ALL WELDS



IONIZER, AFTER STRESS RELIEVING
1 HOUR AT 1600 °C
AND WELD PASSES 3 AND 4



IONIZER,
AFTER WELD PASSES 5 AND 6

Fig. IV-

DISTORTION STUDY • 14 STRIP IONIZER

LEGEND



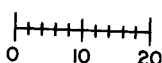
DIRECTION OF WELD



14 STRIP IONIZER,
BEFORE STRESS RELIEVING AND WELDING

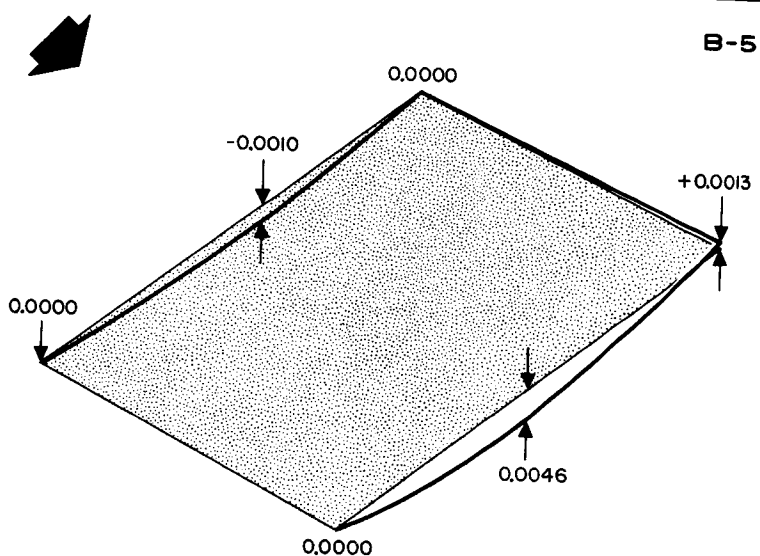


14 STRIP IONIZER,
AFTER STRESS RELIEVING AND WELDING



APPROXIMATE SCALE, 1/1000 INCH

IONIZER ASSEMBLY NO. 14-225-2X • CONT



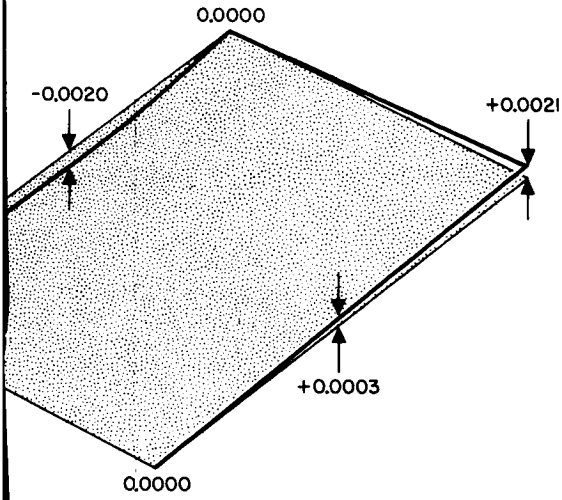
IONIZER, AFTER STRESS RELIEVING
1 HOUR AT 1600 °C
AND WELD PASSES 5 AND 6

AFTER

29. Ionizer (14-strip) electron beam weld distortion study.

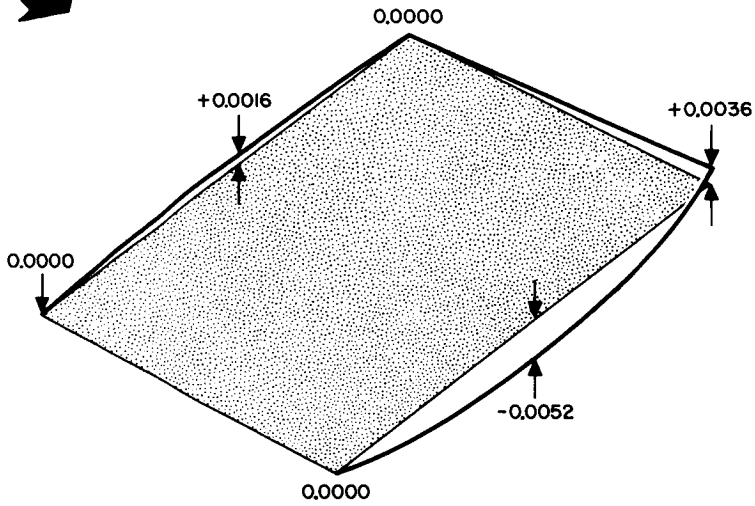
IONIZER ASSEMBLY NO. 14-225-2X

B-1



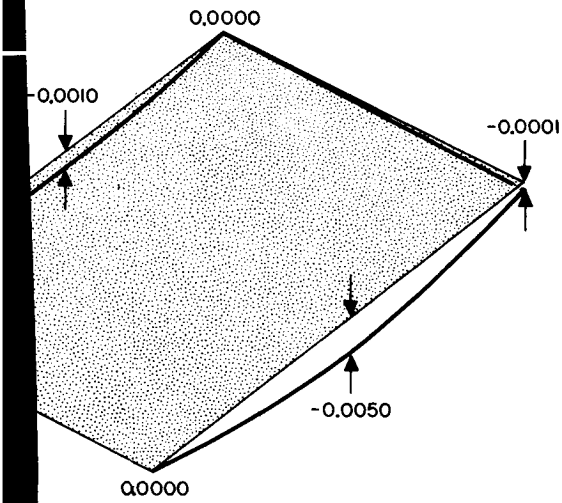
IONIZER, AFTER STRESS RELIEVING
1 HOUR AT 1600 °C
AND WELD PASSES 1 AND 2

B-2



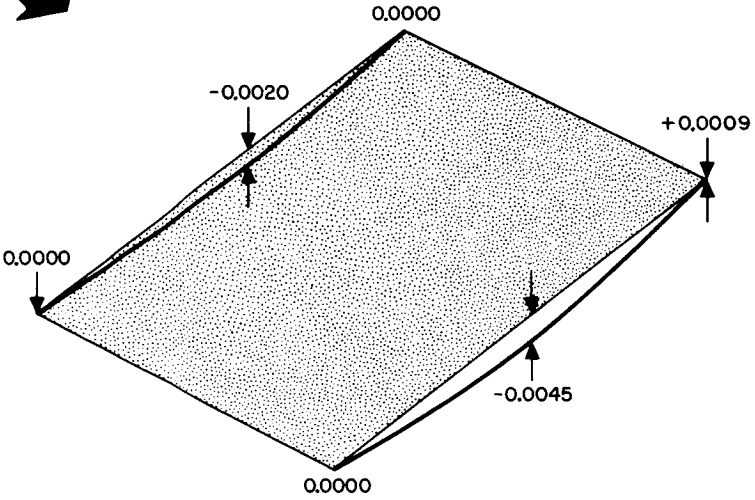
IONIZER,
AFTER WELD PASSES 3 AND 4

B-6



IONIZER,
FINAL WELD PASSES 7, 8, 9 AND 10

B-7



IONIZER, AFTER FINAL STRESS RELIEVING
5 HOURS AT 1650 °C IN H₂
AND ALL WELDS

It was determined by the appearance and location of these cracks that they were not a direct result of welding. From past experience and an analysis of these manifolds, it was suspected that the cracks were a result of the electric discharge machining process and that the cracks (which were microscopic in size and not completely through the wall) were present in the manifolds before welding. To substantiate this possibility, two as-machined manifolds were metallurgically polished and etched. Both manifolds showed signs of surface defects; see Fig. IV-30.

To complete the study, an emitter was welded to a small three-strip test manifold. The assembly was visually inspected after welding, and cracks were found in the same area as the surface defects. A cross section was made and analyzed. A Vickers hardness test was conducted on the cross section across the weld zone and manifold wall. The results of the test showed that there was no contamination in the weld zone or manifold wall. It was therefore concluded that the cracks were a result of the microcracks (due to electric discharge machining) propagating under the presence of welding stresses. Future manifolds will be fabricated by warm machining to avoid this problem.

During the preliminary study, the 20-strip ionizer concept was progressing. The original design of the 20-strip engine used two 10-strip ionizers to make up the ionizer-manifold assembly. A photograph of a 10-strip ionizer is shown in Fig. IV-31. The truncated wedge-shaped region between the cylindrical lens region is made nonemitting by controlled melting of the surface by bombarding it with a high energy electron beam. Beam-sealing the nonemitting portions of the ionizer, however, resulted in excessive shrinkage of these regions. The shrinkage, which was nonuniform, resulted in an over-all shift in dimension from 0.020 to 0.050 in. per side per 10-strip ionizer. These dimensional variations made it virtually impossible to attain nonintercepting engine optics. The shrinkage pattern for the 20-strip ionizer is shown in Fig. IV-32.

M 3254

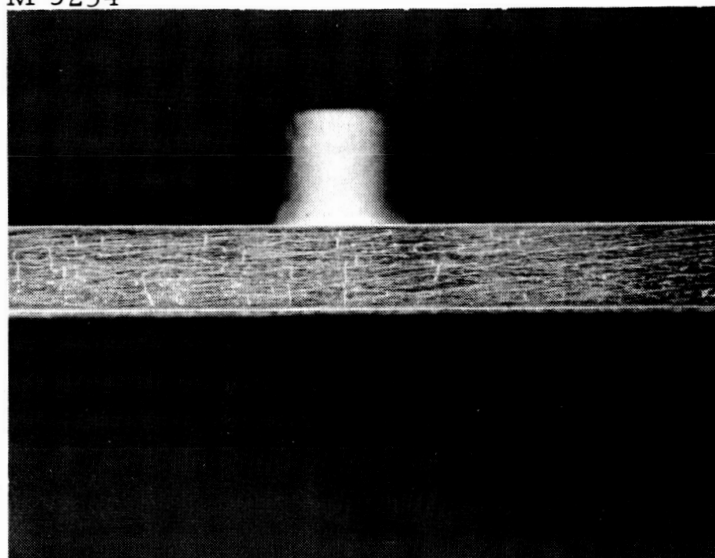


Fig. IV-30. Polished and etched tungsten manifold showing surface defects.

M 3591

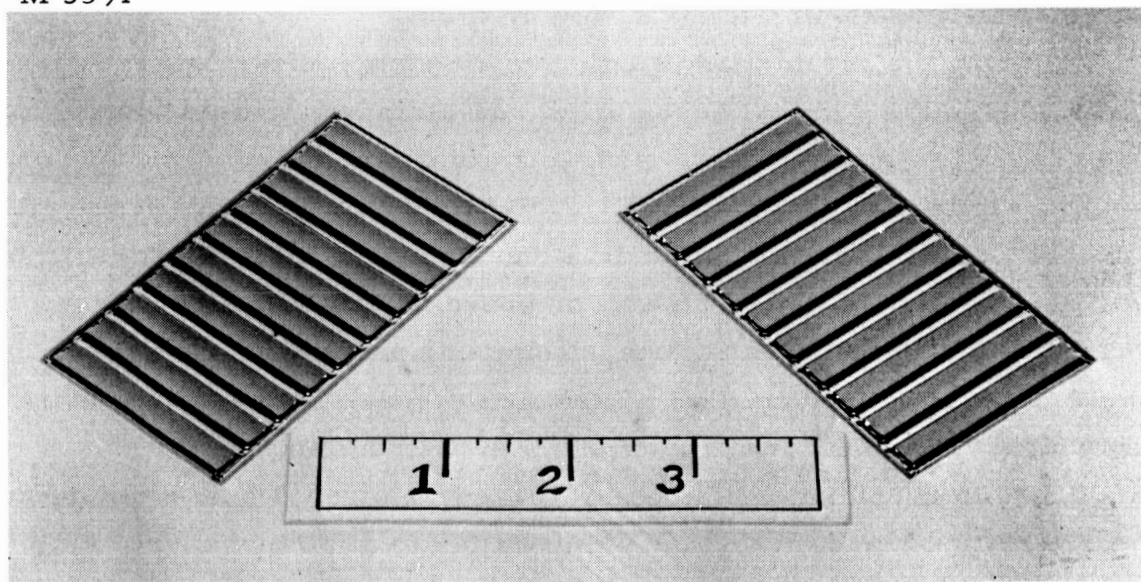


Fig. IV-31. Photograph of two 10-strip ionizers.

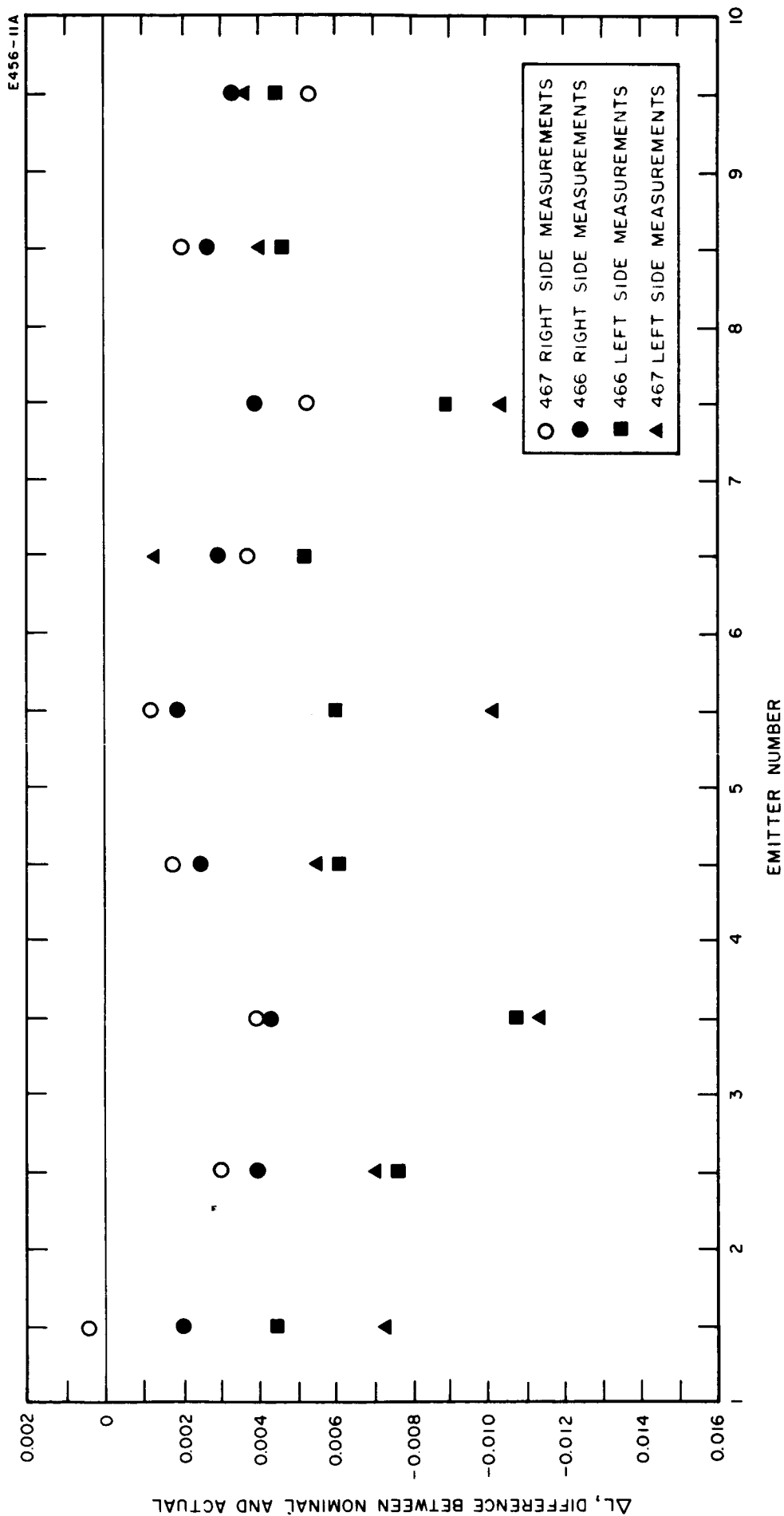


Fig. IV-32. Graph showing the variation in center to center spacing for two 10 strip ionizers.

Because of thermal considerations, the manifold was designed with interconnected compartments so that the ionizers could be welded between every two emitters. Thus, the two 10-strip ionizer elements could quite readily be reduced to 10 two-strip ionizer elements without changing the manifold. With two strips per ionizer element, each doublet could then be individually located on the manifold with respect to a reference position (the center line of the manifold parallel to the center line of the emitter) and thus could minimize the accumulative effect of shrinkage on the emitter-electrode optics.

Sealing of the wide groove was accomplished by utilizing a circle generator which rotates the beam in a circular fashion. The diameter of the circle can be varied. The tooling and preheating of the doublets was identical to the description given earlier in this report for the 0.040 in. grooves. The electron beam schedule was as follows:

Voltage	95 kV
Current	10 mA
Beam diameter	0.027 in.
Circle generated	0.148 in. in diameter
Travel speed	15 in./min.

Measurements of each ionizer were taken with the aid of an optical comparator before and after sealing so that an average shrinkage factor could be taken into consideration for future ionizers and to help in positioning the ionizers on the manifold. It was found that the average shrinkage per seal was 0.002 to 0.004 in.; the former occurred at the beginning and the latter at the end of seal (with respect to the direction of part motion). After sealing, each ionizer was flattened by vacuum firing at 1400°C with a suitable weight on the ionizer to ensure proper fit between the ionizer and the manifold.

The procedure for joining the ionizers to the manifold was similar to that developed with the aid of the obsolete 14-strip ionizers except that the doublets were used. The two center doublets (5 and 6) were the

first to be welded to the manifold. (Starting from one end of the manifold, the doublets are numbered from 1 to 10.) The initial weld was made at the two adjoining edges. The outer edges of the doublet lifted from the manifold as a result of stresses induced by the welding. The wedges were then made flush with the manifold by placing weights on the doublet and heating the assembly in a vacuum furnace at 1400°C for 1 hour. Inspection of the manifold after flattening the first pair of doublets showed that the manifold was flat to one-half mil. The second pair of doublets was placed on the manifold in positions 4 and 7. The unwelded edges of 5 and 6 and the adjoining edges of 4 and 7 were welded to the manifold. The outer edges of 4 and 7 had again lifted and were flattened. Inspection showed that the ends of the manifold had bowed nine mils. The height differences of the emitters with respect to each other deviated a maximum of 5.3 mils. The manifold was flattened with 14 lb of weight in the hydrogen furnace for 4 hours at 1650°C . The relative heights of the emitter did not change appreciably, but the bow at the ends was decreased to 4 mils.

The above process of weld, inspect edge, flatten, inspect, flatten, and inspect was repeated for doublets 3 and 8, 2 and 9, and 1 and 10. The maximum distortion reached 0.050 in. during some of the welds. Eventually the part was completed and, after flattening at 1650°C with loads to 26 lb, had a maximum over-all distortion of 0.0083 in. Pressure test of the first ionizer-manifold assembly showed (by bubble patterns) nonuniform flow through some of the ionizers. Although emission spectrographic analysis has not confirmed this, it is believed that sputtered metal from a newly developed and malfunctioning vacuum furnace had partially closed the pores on a few of the separately processed ionizer doublets. This special furnace has since been rebuilt and now performs very satisfactorily.

The large amount of weld distortion encountered with the first 20-strip manifold can be attributed to a number of factors. The fact that it was the first attempt at welding such a complex unit and even though

the preliminary study with the 14-strip ionizer contributed greatly to the successful joining of the assembly, it could not provide all the data required for assembling a distortion-free 20-strip ionizer. Also, in order to provide flexibility in locating the position of the ionizers on the manifold with respect to the electrodes, the widths of the doublets were such that there existed an 0.020 in. gap at the joint. This gap then required a minimum of two welds at each joint. A third factor which added to the distortion was that on three occasions the heater (used for preheating and slow cooling of the part) shorted out during welding and thus slow cooling could not be maintained.

During assembly of the first ionizer, these difficulties were identified and these additional important data were utilized in preparing the second assembly. New doublets were ordered which, with the aid of the data gathered on the first assembly of shrinkage factors for both sealing and welding of the doublets to the manifold, would provide a maximum gap of 0.006 in. between the doublet pairs. With this small gap, a single pass was sufficient to accomplish an excellent weld. The emitter to manifold thermal conductance leg welds were reduced by a factor of one-third. All transverse welds were completed; the ionizers were fastened to the ribs of the manifold. No flattening of the manifold was required. Only the lifted edges of the ionizer doublets, after welding one edge, were restored to the manifold surface by vacuum firing at 1400°C for 1/2 hour. In the previous ionizer, the distortion of the manifold from a single edge weld was as large as 0.050 in. The fastening of the 10 ionizer doublets to the manifold, for this second assembly, has resulted in a total distortion of only 0.0023 in.; it was not necessary to flatten the manifold.

In order to ensure proper preheating and uniform temperature of the ionizer and manifold, eliminate shorting of the heater, and provide slow uniform cooling of the assembly, the part was thoroughly heat shielded. A contributing factor in the essentially distortion-free welding of the second assembly is a result of the improved thermal control of both the ionizer and manifold before and during the weld cooling period.

It is believed that a temperature difference between the welded ionizer and heated manifold results in thermally induced stresses which cause the manifold to distort. The ionizer cools faster than the manifold which results in a bending moment and subsequent permanent deformation of this part.

The preheated ionizer-manifold assembly has been radiation shielded with thin tungsten sheets on both the top and bottom sides of the part. Only a gap in the weld region is made available for the electron beam. Subsequent to the weld and during the cooling process both the ionizer and manifold are maintained at the same temperature by the shielding, and the thermally induced stress is therefore greatly reduced.

The temperature difference between the ionizer and manifold required for the tungsten to exceed the yield strength has been computed as follows:

The bending moment applied to the manifold is

$$M = \frac{EI}{\rho}$$

where

$M \equiv$ moment

$E \equiv$ Young's modulus, 46×10^6 psi

$I \equiv$ moment of inertia of the section through the manifold

$\rho \equiv$ radius of curvature.

The bending stress is

$$\sigma = \frac{MC}{I}$$

where

$C \equiv$ distance from neutral axis, 0.2 in.

$\sigma \equiv$ stress (15,000 psi yield strength at 900°C for fully recrystallized tungsten).

Substituting the expression for I obtained from the bending moment equation, we get

$$\sigma = \frac{EC}{\rho} .$$

A sketch which describes the problem is shown in Fig. IV-33.

The radius of curvature from these relationships is 600 in. The computed change in length of the top surface of the manifold, considering two similar triangles with a difference in height of 0.2 in., a base width of the neutral axis of 0.740 in., and a radius of curvature to the neutral axis of 600 in., is 0.00025 in.

This 0.00025 in. change in length, which results in the tungsten exceeding its yield strength, can occur with a temperature difference of 80°C. The stress is applied to the manifold by the 80°C cooler ionizer.

B. Ionizer Heater Thermodynamics and Life Analysis

1. Ionizer Heater Thermodynamics

Ionizer heating for contact surface ion engines is accomplished by standard resistance heating elements. The element consists of a coil of tungsten wire through which current is passed; the physical size of the engine limits each element to a maximum diameter of about 1/2 cm. A voltage applied across the element produces I^2R heating which is radiated to the ionizer.

The success of ionizer heating by this method depends on the ability to transfer heat from the element to the ionizer. In other words, to maintain a constant ionizer temperature, a fixed amount of power from the heating element is required. If heat transfer is difficult between the heating element and the ionizer, a high heating element temperature is required. The only way to evaluate a heater is to calculate the temperature at which the element must operate for a fixed ionizer temperature. This is true because the limiting condition for a heater is

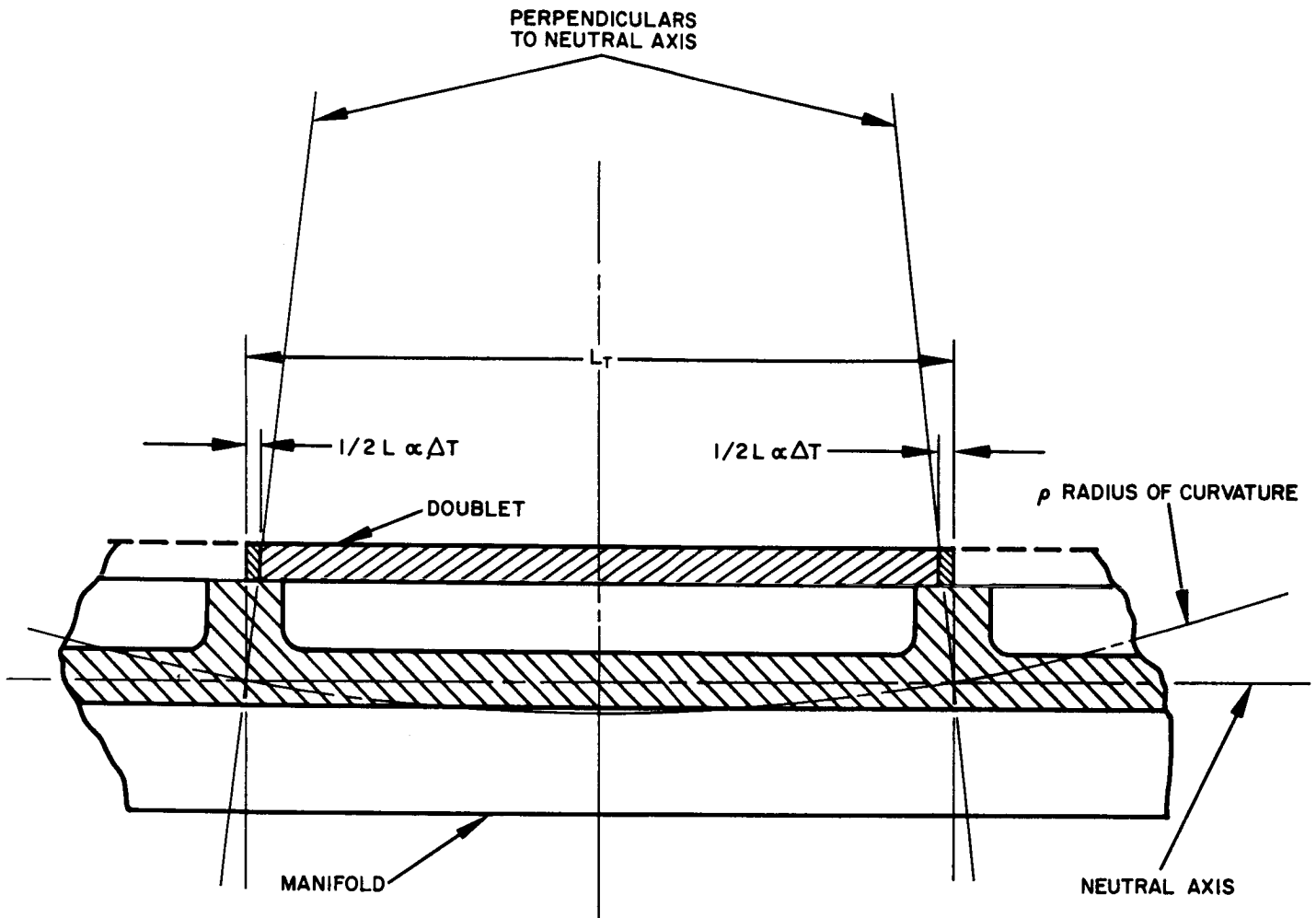


Fig. IV-33. Illustration of possible thermal stress if ionizer and manifold are not maintained at same temperature.

when the ceramic insulation between the element and the ionizer becomes so hot that it breaks down electrically, and later melts.

The relative heating abilities of various heater configurations can thus be evaluated. The only parameters really available for heater design are the following:

- a. The amount of ceramic required to insulate the heating element from the ionizer. The less ceramic required, the better the heater is. The ceramic acts as a radiation shield between the element and the ionizer and cuts down the heat transfer between them. Thus, a lower heater temperature is required for the minimum ceramic condition.
- b. The receiving area for radiation from the heating element. In other words, it is highly advantageous to bring tungsten ribs down from the ionizer structure to engulf the heating element. In this condition, there is more surface area for radiant interchange between element and ionizer. With more radiating area, the resulting heater temperature will be less. Conduction will readily take place from the ribs to the ionizer. It is the radiation mode which is chiefly limiting on a heater design.

We thus come to the ultimate conclusion that the best type of radiation heater consists of an element suspended within a receiving tungsten enclosure with a minimum of ceramic required to keep it in place. Then all of the surface area of the element will be utilized in the transferring of radiant energy from the element to the ionizer. There will also be no shielding effect due to the presence of ceramic in the intermittent region between the element and the ionizer.

There are 13 possible configurations for heating an ionizer by elements. The 13th is eight times better in the transferring of heat than the first crude heater configuration. When heat transfer is improved by a factor of eight, the resulting heater temperature is down by about 700°K (see Fig. IV-34).

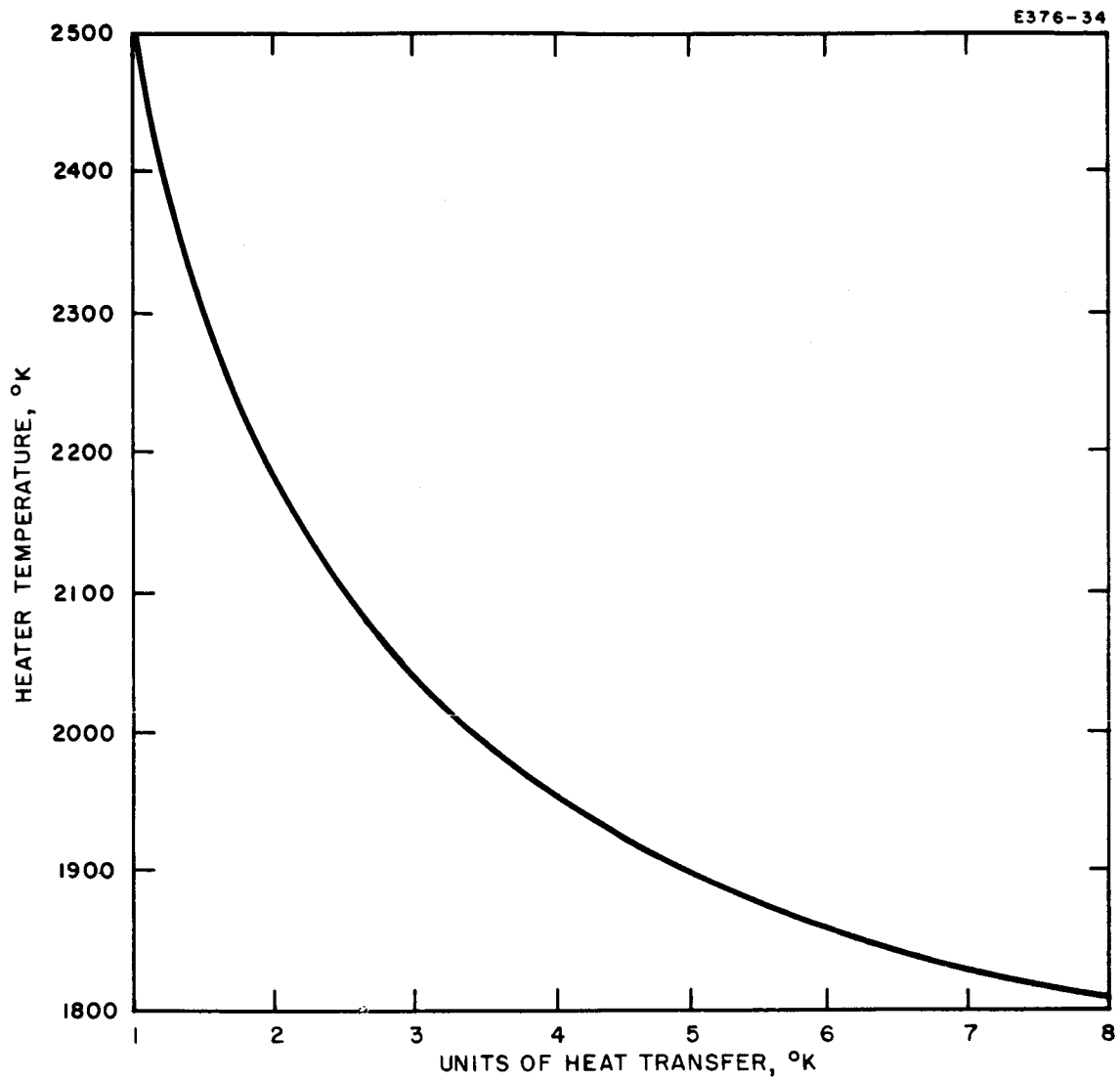


Fig. IV-34. Heater temperature versus units of heat transfer from heating element to ionizer manifold.

Since there are 13 possible configurations, but only eight modes of improvement, some of the configurations are not necessarily improvements in heater design but are merely alternative configurations. Whether one of the alternative configurations is preferable to another depends on such factors as implementation and heater interchangeability. Figure IV-35 shows all the various configurations.

A calculation will show that element to ionizer interchange through a ceramic slab is about half as effective as direct element to ionizer interchange. This makes an easy method of determining the relative value of the various heating arrangements. We shall assign one unit of heat transfer to an interchange through a ceramic slab; therefore, direct interchange has the value of two units of heat transfer.

The most elementary method of radiation heating is to enclose heating elements completely in ceramic and set them side by side directly under the ionizer (Fig. IV-35, heater No. 1). This first crude type of heating configuration can immediately be improved by adding a backplate over the rear of the ceramic insulation to receive radiation from a portion of the heating element which is not directed at the ionizer (heater No. 2B). Heat received by the backplate in this manner is subsequently conducted around the far edges of all the heating elements and up to the ionizer. Thus, we have gone from an initial one unit of heat transfer to an improvement where two units of heat transfer are accomplished for each heating element. The two end elements, in addition, accomplish three units of heat transfer, but this analysis is done for the general heating elements which are far inside an ionizer surface, so the end effects will be neglected for the two end elements. We may also have improved the heat transfer from one to two units by an alternative method — removal of the ceramic blocking direct interchange between the top of the element and the ionizer (heater No. 2).

The first type of heater discussed is designated No. 1 for the one unit of heat transfer. The second type, which has the backplate and two units of heat transfer, is designated No. 2B, and the last type of configuration is designated No. 2, since there are two units of heat transfer and no backplate.

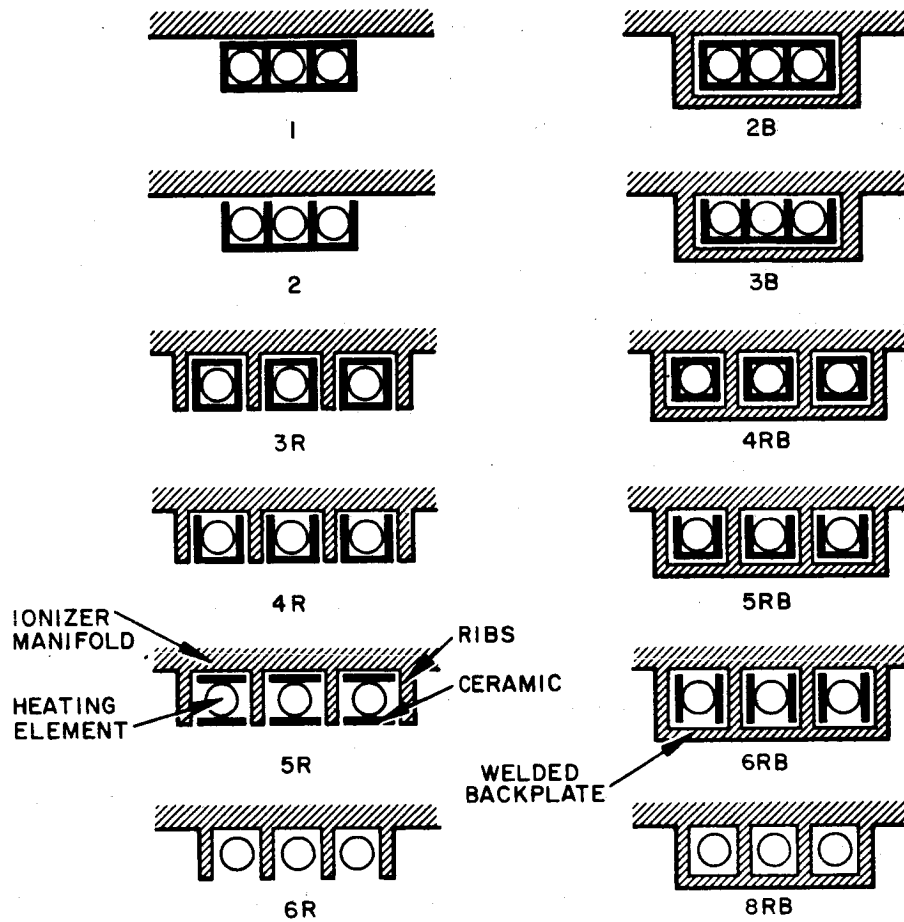


Fig. IV-35. Ionizer heating configurations.

The next improvement in heater design is to utilize a backplate with configuration No. 2 resulting in a No. 3B modification. Here there are two units of heat transfer because of direct radiation from the element to the manifold, and one additional unit of heat transfer through the ceramic at the bottom of the element and to the backplate. These four heater designs are the only ones which are available without utilization of ribs.

If we take the basic nonrib configuration No. 1 and separate the heating elements and their associated ceramic, inserting a rib down between two adjacent elements, we have configuration No. 3R. The R designates ribs and the 3 is used because (as one may observe from Fig. IV-35) there are three paths of radiant interchange available from the element to the manifold — one directly to the ionizer and two directly to adjacent ribs. We can now weld a backplate to configuration No. 3R, which results in configuration No. 4RB. In configuration No. 4RB, the heater element is still completely enclosed in ceramic which shields it on all sides. However, all surfaces of the element are utilized because there are receiving surfaces at the ionizer, backplate, and two side ribs. Four units of heat transfer can also be obtained without a backplate (with the rib configurations) by removal of that ceramic between the top of the element and the manifold (Fig. IV-35). This is heater No. 4R, which is similar to heater No. 2, except for the ribs from the ionizer placed between the heating elements. Heater No. 4R can further be improved by the addition of a backplate, to arrive at heater No. 5RB. In configuration No. 5RB, one of the heating surfaces radiates directly to the ionizer, contributing two units of heat transfer. The other three surfaces of the heating elements are utilized because there are receiving ribs and backplate on the other side of a ceramic shield.

We can also achieve five units of heat transfer without using a backplate by taking the No. 4R configuration, removing the bottom piece of ceramic, and rotating the remaining two long strips of ceramic 90° . This results in configuration No. 5R. In this configuration, the heating element is held in place by two long, grooved strips of ceramic. This

leaves two sides of the heating element free to radiate directly to the ribs, giving four units of heat transfer. An additional unit is picked up because the top of the element is radiating through a ceramic slab to the tungsten ionizer.

With the addition of a backplate, this configuration (with the ceramic strips rotated 90° or not) becomes heater No. 6RB. In this heater, two quarters of the element area radiate directly to receiving tungsten areas, and two radiate through a ceramic shield to tungsten ribs. The units of heat transfer thus total six. A configuration resulting in six units of heat transfer can also be obtained by utilization of heater No. 6R; the advantage of No. 6R is that no backplate is necessary. In this configuration, the elements are suspended completely, i.e., there is no ceramic between the element and the ribs-manifold structure. Thus, three sides of the heating element are utilized to their fullest because they can radiate directly to tungsten, giving a total of six units of heat transfer. This type of configuration can be facilitated, for example, by winding the tungsten heating wire around a ceramic rod and fastening it squarely on the center line of the rib's structure groove. In addition, ceramic spacers may be used every centimeter or so to insure that the heating coil does not short out on the tungsten manifold structure.

The ultimate in heating is thus obtained by welding a backplate to No. 6R. This results in heater configuration No. 8, where all four sides of the heating element are radiating directly to tungsten with no ceramic interference. In this condition, the heater will operate at the lowest possible temperature. With a radiation type heater, such as is used in ionizer heating, this is the best way of heating.

However, it is not necessary to go beyond a certain point in improving heater design since only small gains are made by doing so. For example, improving the design from heater No. 1 to heater No. 2 can lower the heater temperature as much as 400° . Continued improvement to heater No. 3 can reduce the temperature 200° more. We must then go to a No. 5 heater to produce an additional 200° temperature reduction.

Only 100° more reduction is produced in improving the design further to the No. 8RB heater. This effect is demonstrated in Fig. IV-34 where heater temperature is plotted versus units of heat transfer, starting with heater configuration No. 1 at a temperature of 2500°K. The curve is a decreasing exponential type, which rapidly approaches the assumed ionizer temperature of 1600°K. It appears that a configuration of the No. 6 type will be adequate for heater design, since improving No. 6 to No. 8RB will only bring about a 50° decrease in heater temperature.

The calculation will now be given to show that direct radiant interchange between heating element and tungsten manifold is twice as good as radiant interchange where a ceramic slab is acting as a shield between the emitting and receiving surfaces. Let a equal one quarter of the heating element area. Then the expression for the direct radiant interchange between a quarter of the surface of the heating element and a receiving area is given by

$$Q_d = \frac{\sigma a (T_H^4 - T_I^4)}{\frac{1}{\epsilon_H} + \frac{1}{\epsilon_I} - 1} \quad (IV-1)$$

The analogous equation for radiant interchange between a quarter of the heating element surface area and the ionizer, through a ceramic shield, is given by

$$Q_c = \frac{\sigma a (T_H^4 - T_I^4)}{\frac{1}{\epsilon_H} + \frac{1}{\epsilon_I} + 2 \frac{1}{\epsilon_c} - 1} \quad (IV-2)$$

For the above equations, we have the following nomenclature definitions:

- $\sigma \equiv$ Stefan-Boltzmann constant = $5.67 \times 10^{-12} \text{ W/cm}^2 \cdot \text{°K}^4$
- $T_H \equiv$ heater temperature
- $T_I \equiv$ ionizer manifold temperature

$\epsilon_H \equiv$ heater element emissivity

$\epsilon_I \equiv$ emissivity of tungsten ionizer

$\epsilon_c \equiv$ emissivity of ceramic.

There is much information on emissivities of both ceramics and tungsten as a function of temperature (see, for example, Ref. IV-1).

We find from the literature that $\epsilon_H = \epsilon_I = \epsilon_c = 0.25$. Evaluating expressions (IV-1) and (IV-2), we obtain

$$Q_d = \frac{\sigma a (T_H^4 - T_I^4)}{7}$$

and

$$Q_c = \frac{\sigma a (T_H^4 - T_I^4)}{14} .$$

Thus, direct interchange is twice as good as interchange through ceramic.

The next calculation important at this time shows how the resulting heater temperature depends on the various heater configurations. The result is a plot of T_H versus units of heat transfer available with the various heater configurations (Fig. IV-34). In order to perform this calculation, we must first choose a suitable ionizer temperature and the corresponding heater temperature for the No. 1 heater design T_{Ho} . To this end, assume that each element is required to heat a projected area on the ionizer surface. Thus, the required heat output for each heating element is

$$Q_{loss} = a\epsilon_I\sigma T_I^4 . \quad (IV-3)$$

This loss must be equal to the interchange between heater and ionizer (through ceramic Q_c).

$$Q_c = \frac{a\sigma (T_{Ho}^4 - T_I^4)}{14} \quad (IV-4)$$

Equating (IV-3) to (IV-4) yields the expression for T_{Ho} in terms of T_I ,

$$T_{Ho} = (1 + 14 \epsilon_I)^{1/4} T_I$$

Taking $T_I = 1600^\circ K$,

$$T_{Ho} = 2500^\circ K$$

With heater temperature established for the worst case (No. 1 design), we may calculate the improved heater temperatures which correspond to designs facilitating larger numbers of units of heat transfer q :

$$q (T_H^4 - T_I^4) = T_{Ho}^4 - T_I^4$$

Solve for T_H^4 in terms of T_I^4 and T_{Ho}^4 ,

$$T_H^4 = \frac{T_{Ho}^4 - T_I^4}{q} + T_I^4$$

Evaluate for $T_{Ho} = 2500^\circ K$ and $T_I = 1600^\circ K$:

$$T_H = \left(6.6 + \frac{32}{q}\right)^{1/4} 1000$$

Figure IV-34 is a plot of this relation.

2. Ionizer Heater Life

The life of the heater is primarily determined by the reaction of the heating element with the alumina insulators.

The Al_2O_3 -W vaporization data of Drowart, et al. (Ref. IV-2), concerning the evaporation of tungsten oxides, Al_2O , AlO , and oxygen from alumina contained in high temperature tungsten effusion cells have been utilized to help estimate heater life. Extrapolating this mass spectrographic data downward to our 1800°K operating temperature, it is estimated that the total pressure of WO , WO_2 , and WO_3 resulting from solid state reactions between Al_2O_3 and tungsten should be 10^{-9} mm or less. In the enclosed heater space with restricted efflux openings, this should cause only a very slow loss of tungsten. It is also probable that solid contact between tungsten and Al_2O_3 would be lost after the tungsten coil had been thermally set and the Al_2O_3 at the contact point had evaporated. The solid phase reaction should then cease.

Extrapolation of Drowart's data indicates that at 1900°K (somewhat higher than our case) the vapor pressure of oxygen, as atoms, from the dissociation of Al_2O_3 is about 10^{-8} mm. The data of Becker, et al. (Ref. IV-3), can be used to give an approximation of the rate at which WO_2 and WO_3 would evaporate from tungsten at this oxygen pressure. Rough calculations indicate a rate of about $4 \times 10^{-3} \mu\text{g}/\text{cm}^2\text{-min}$ as a maximum. This corresponds to a surface loss of about 1μ per year.

An allowable 10% reduction in heater diameter resulting from the reaction of tungsten with 10^{-8} Torr oxygen pressure would limit the heater life to 50 years. Jones and Langmuir data for 0.020 in. wire operating at 1800°K indicate a life very much greater than 50 years. The presently known failure modes indicate that the heater is very conservatively designed. Loss of heater cross section should thus be insignificant as long as the heater temperature remains below 1900°K . It is probable that more tungsten is lost from oxygen in the vacuum system environment or in the first period of insulator outgassing than in many hours of subsequent operation during which the reactions might take place.

The heater configuration which is presently used in both the three-strip as well as the 20-strip engines has a heat transfer coefficient between six and eight. A sketch of the ceramic installed into the ionizer-manifold assembly is shown in Fig. IV-36. Figure IV-37 is a photograph of the heater ceramics to be used in engine 2018-150-1. The heater configuration shown in the sketch and photograph was used in the 260-hour test of engine 32-150-4.

After the 260-hour test, there was no visible deterioration of the tungsten heater wire or alumina insulator. There was only slight discoloration of the pure white alumina where it was in contact with the tungsten. The discolored layer was too thin to measure readily, and any decrease in heater wire diameter was too small to be measured at 500x magnification. The tungsten wire was only partially recrystallized after this prolonged heating period. It had therefore never been heated even momentarily to as high as 2000°C.

A trace of dark material which had condensed on the cooler heavy molybdenum heater wire terminals was found by x-ray and spectrographic analysis to be mixed oxides of tungsten and molybdenum. No significant amount of alumina was found in this condensate. The same mixed oxides were found on the cooler exposed portions of alumina insulator. The spectrographic analysis of the terminal deposit showed 3% iron, 7% magnesium, 12% molybdenum, 17% silicon; the remaining metallic component was tungsten. The source of these deposits is not known. However, to eliminate the possibility of these materials originating from the ceramics or shields, these parts will be vacuum fired prior to installation in the engine.

C. Focus Electrode Heat Load and Temperature Distribution

Temperature control of the focus electrode has continued to be an important design consideration because of the need to reduce the number of ions formed on the electrode. Ions originating at the focus electrode do not go out with the beam, but instead impinge directly on the

E463-41

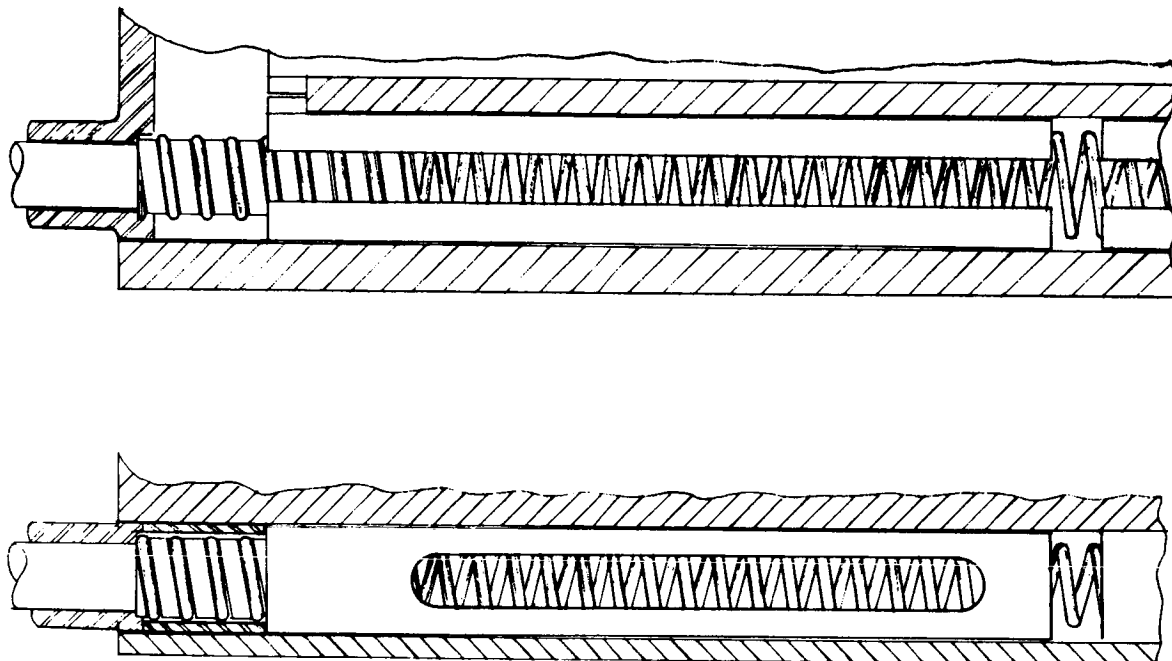


Fig. IV-36. Ceramic installation into the ionizer-manifold assembly.

M 3336

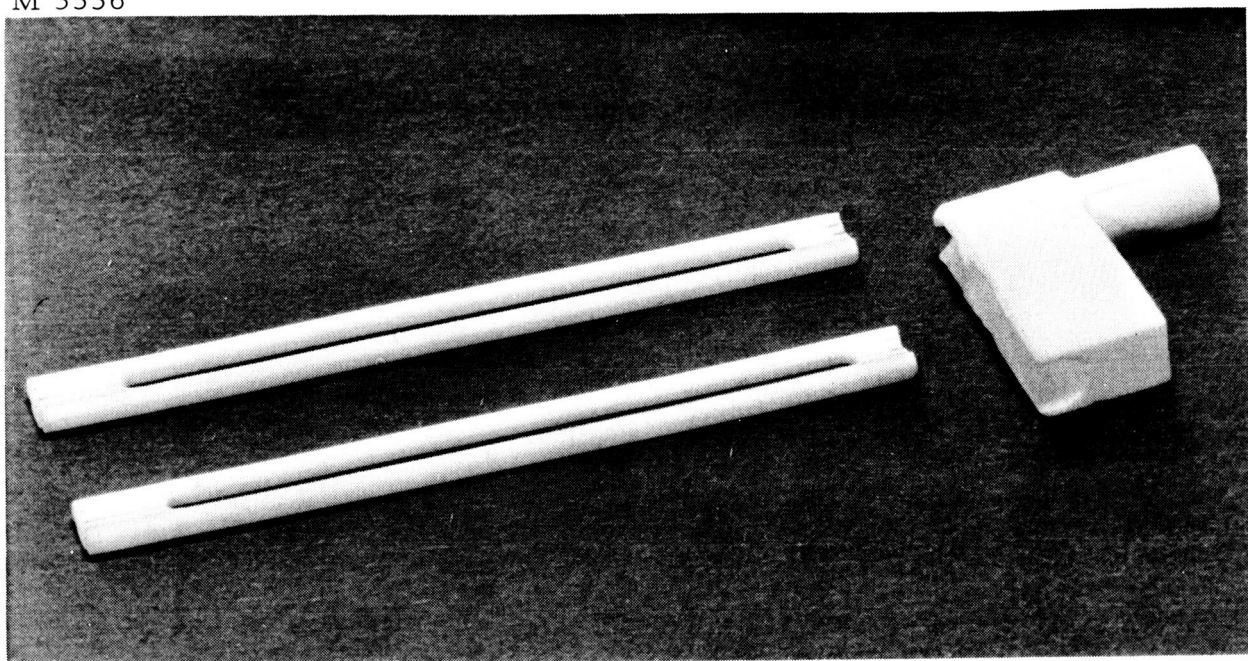


Fig. IV-37. Heater ceramics used in engine 2018-150-1.

accel electrode, and limit the operating lifetime. It has been attempted to keep the focus below 1000°K for this reason. When there has not been excessive electron bombardment, these attempts have been successful.

Considerable progress has been made in determining electrode heat loads and new designs to control temperature distribution. In the NAS 5-517 Phase III Summary Report, analytic methods for heat load and temperature determination were derived. Since then, experimental values have been obtained in the laboratory, and extensive comparisons have been made.

Heat drain structures to cool the focus electrode have been developed far beyond last year's status. Also, successful heat rejection has been achieved by pure radiation, eliminating the need for artificial cooling.

1. Analytic Results

In the NAS 5-517 Phase III Summary Report, it was shown that the temperature distribution along the focus electrode is given by the integral of:

$$kA_c \frac{d^2 T}{dx^2} + Q = 0 \quad (\text{IV-5})$$

where Q is the heat load per unit length. Values of Q were calculated for various ionizer temperatures and electrode cross sections. The results for zero electron bombardment power input are summarized in Table IV-1. From the various engine experiments run (32-40-8, 32-150-1, etc.) thermal data were compiled for comparison with these calculated numbers. It will be shown that for small cross sections the correlation is very good, but that more heat load than the calculated value exists for the larger sections.

TABLE IV-1

Calculated Focus Electrode Heat Loads

Electrode Width, in.	Ionizer Temperature, °K	Q_{\max} , W/cm
0.150	1600	1.3
0.040	1600	0.7
0.150	1400	0.75
0.040	1400	0.4

Returning to eq. (IV-5), there are three integrals of interest in calculating a temperature distribution on the focus electrode. The integral chosen depends on which are known inputs and which are unknown. The three categories are:

- both drain impedances known and heat load known
- both end temperatures and heat load known
- both end temperatures and center-line temperature known.

When both ends of the electrode are connected to the same heat sink at temperature T_s through different thermal impedances Z_1 and Z_2 , the desired expression is:

$$T(x) = T_s + Q \left[\frac{(Z_2 + Z_o/2)(Z_o x + Z_1 \ell)}{Z_o + Z_1 + Z_2} - \frac{Z_o}{2\ell} x^2 \right] \quad (\text{IV-6})$$

When the two end temperatures are known, the following equation describes temperatures at every point on the electrode:

$$T(x) = T_1 + (T_2 - T_1) \frac{x}{\ell} + \frac{QZ_o}{2} \left(x - \frac{x^2}{\ell} \right) \quad (\text{IV-7})$$

When the two end temperatures and center line temperatures are known, the equation to use is:

$$T(x) = T_1 + \left[3(T_{\text{CL}} - T_1) + (T_{\text{CL}} - T_2) \right] \left(\frac{x}{l} \right) - 2 \left[(T_{\text{CL}} - T_1) + (T_{\text{CL}} - T_2) \right] \left(\frac{x}{l} \right)^2 \quad (\text{IV-8})$$

In the foregoing equations:

$T_1 \equiv$ spring end temperature, $^{\circ}\text{K}$

$T_2 \equiv$ fixed end temperature, $^{\circ}\text{K}$

$l \equiv$ total electrode length = 5.5 cm

$Z_o \equiv$ total electrode impedance = l/kA_c , $^{\circ}\text{K}/\text{W}$

$k \equiv$ electrode thermal conductivity = $1.0 \text{ W}/\text{cm}-^{\circ}\text{K}$
(for molybdenum)

$x \equiv$ distance along the electrode, cm

$Q \equiv$ average heat load per unit length at surface of electrode, W/cm (consists of thermal ionizer radiation and accel electron bombardment, less some reradiation)

$A_c \equiv$ electrode cross-sectional area, cm^2

$T_{\text{CL}} \equiv$ center line temperature, $^{\circ}\text{K}$.

In the following discussion, the progress in thermal design of the electrode system is outlined. The experimentally determined heat loads and temperature distributions, as obtained from each successive engine test, were used to make the design improvements on subsequent engines. This has all been in an effort to cool the focus electrode not only as effectively as possible, but also in a way which would be practical for space flight.

2. Thermal Design

The first multistrip engine utilizing a radiator to reject the focus heat load (to maintain the focus temperature below the 1000°K range) was the 32-150-2 engine. The radiator successfully cooled the focus electrode under normal heat load conditions. However, the heat load eventually got so large (due to electron bombardment) that it was impossible to satisfy the temperature requirement with this heat rejection system.

Successful cooling under the nominal heat load conditions ($\sim 2.5 \text{ W/cm}$) is attributed chiefly to the much improved heat drain structure which has been developed and which was incorporated into the 32-150-2 and subsequent engine systems (see Fig. IV-38). The heart of the heat drain structure is a length of copper braid brazed to the tip of the electrode (as close to the ionizer as possible). The other end of the braid is fastened as closely as possible to the engine heat sink (radiator assembly). The braid consists of 800 copper wires, each 0.005 in. in diameter. They are 2.5 cm long, so that the thermal impedance of the braid is (thermal conductivity of copper = $3.8 \text{ W/^{\circ}K-cm}$)

$$Z_B = \frac{l_B}{k_C A_B} = \frac{2.5}{3.8 \pi/4 (0.005 \times 2.54)^2 (800)} = 6.5^{\circ}\text{K/W} \quad .$$

A certain amount of thermal resistance in the tip of the electrode is inherent in the electrode assembly. This amounts to (k of molybdenum is $1.0 \text{ W/^{\circ}K-cm}$)

$$Z_T = \frac{l_T}{k_M A_T} = \frac{(0.5)}{(1.0) (0.117 \times 0.8)} = 5.3^{\circ}\text{K/W} \quad .$$

There is also thermal resistance in the heat path from the downstream side of the braid to the sink. This path consists of a copper "finger" 3.0 cm long, 0.8 cm wide, and $1/16$ in. thick.

The finger impedance therefore is

$$Z_F = \frac{3.0}{(3.8)(0.8 \times 2.54/16)} = 6.2^\circ\text{K/W} \quad .$$

The total impedance of the heat drain structure (allowing 2°K/W for the interfaces) is only 20°K/W . This is a considerable improvement over previous heat drains, as is shown in this section.

3. Heat Load

Several methods have been used in the various engine tests to determine focus electrode heat load per unit length. The results agree quite well with each other. The most direct method is by measurement of the temperature differential (ΔT) across the tip of the electrode (see Fig. IV-38). We have determined this impedance (Z_T) to be 5.3°K/W . Hence, the heat load per unit length is obtained by:

$$Q = \left(\frac{2}{l}\right) \left(\frac{\Delta T}{Z_T}\right) \text{ W/cm} \quad . \quad (\text{IV-9})$$

The factor of two denotes that two ends of the electrode are rejecting heat symmetrically. The effective focus length l over which heat input occurs is 5.5 cm. Figure IV-39 shows the values of ΔT recorded during the 32-150-2 engine test at various ionizer temperatures from 1000 to 1700°K . The curve was taken on 16 March and the data corresponded to this line through 19 March. This method has been the one used on tests of engines 32-150-2, -3, and -4. The thermal load for a 1600°K ionizer was (obtaining ΔT from Fig. IV-39):

$$Q = \left(\frac{2}{5.5}\right) \frac{32}{5.3} = 2.2 \text{ W/cm} \quad .$$

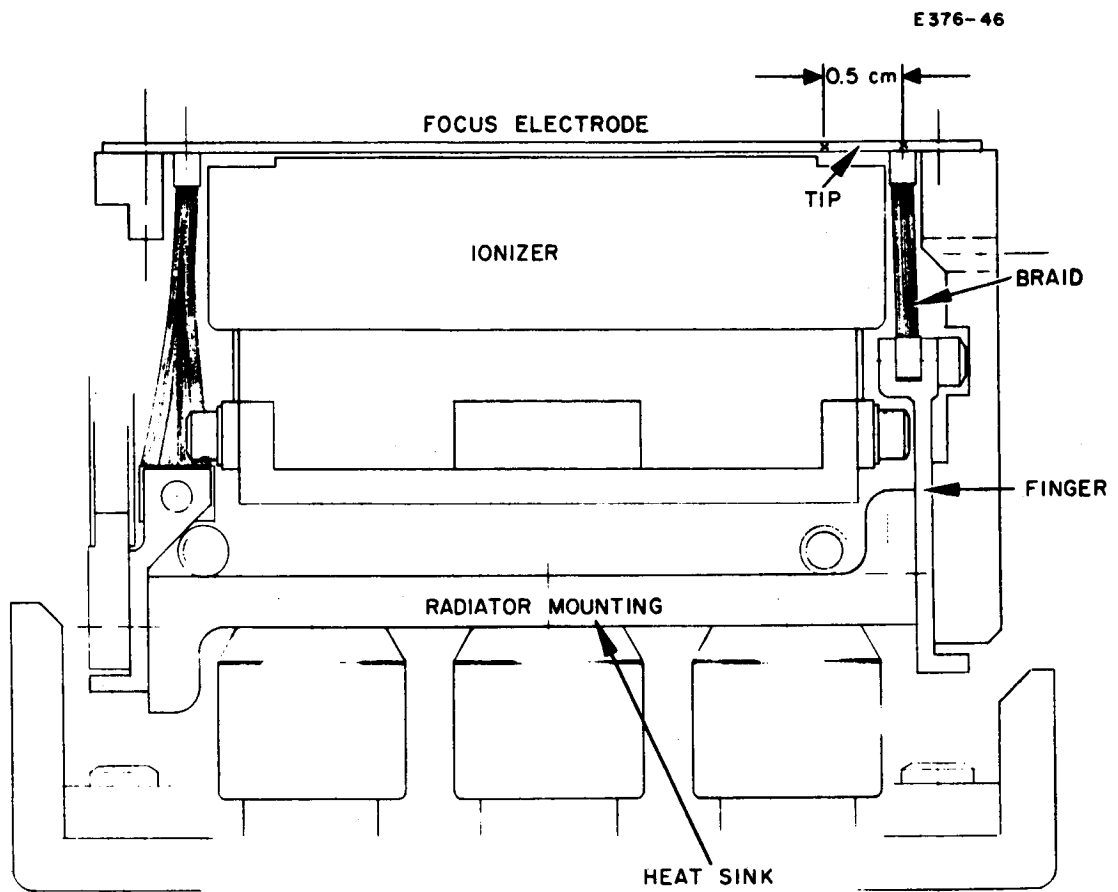


Fig. IV-38. Focus heat drain structure.

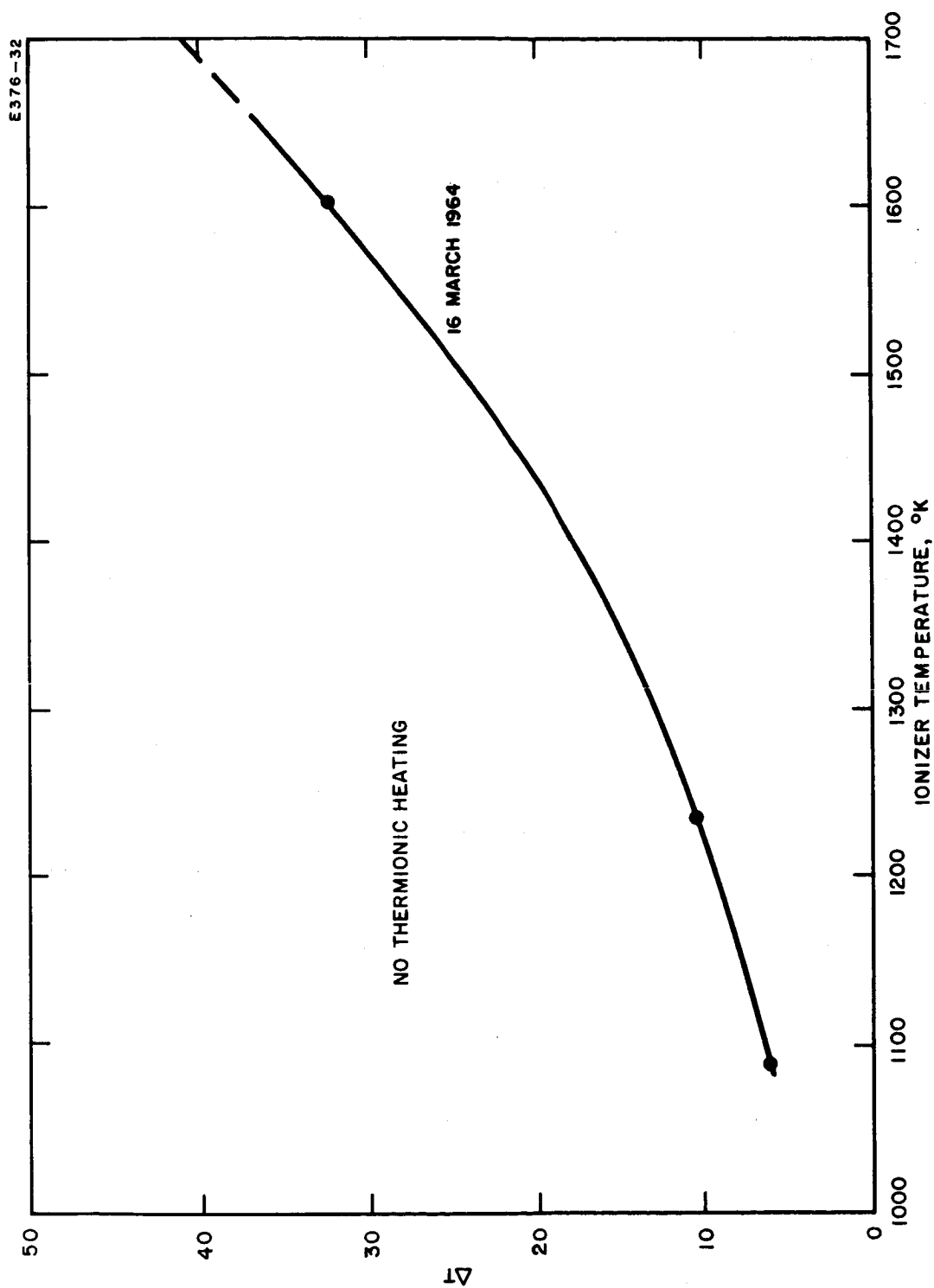


Fig. IV-39. Focus electrode temperature differential (across 0.5 cm of electrode length).

This value corresponds well with that obtained from the 32-150-1 thermal analysis, as will be shown. Comparison with the calculated value in Table IV-2 shows the measured heat load to be almost 1 W/cm larger.

The heat load on the focus electrode of engine 32-150-1 was obtained in a different manner. The heat load per unit length is known as a function of the temperature of the electrode center and the two ends by the equation:

$$Q = \frac{4}{Z_{ol}} (T_{\text{center}} - T_1) + (T_{\text{center}} - T_2) \text{ W/cm}$$

$$Z_o = 128^\circ\text{K/W (for 150 type engines)} \quad . \quad (\text{IV-10})$$

A separate thermal test was performed to establish the thermal characteristics of this engine, since a center thermocouple on the focus electrode was not allowed during engine operation. The ionizer was brought to several different temperatures, producing several sets of electrode temperatures and corresponding heat load. The results are presented in Fig. IV-40 where center temperature and heat load are plotted versus spring end temperature. The corresponding ionizer temperatures which produced various spring end electrode temperatures during the test are reported in Fig. IV-41. Thus, by cross-plotting Figs. IV-40 and IV-41, the heat load versus ionizer temperature relationship for the test was established. The following data show the thermal heat load during the test versus ionizer temperature.

<u>Ionizer Temperature, °K</u>	<u>Thermal Heat Load, W/cm</u>
1400	1.3
1600	2.1

These values may be compared with the calculated values in Table IV-2, and the experimental value obtained by the other method.

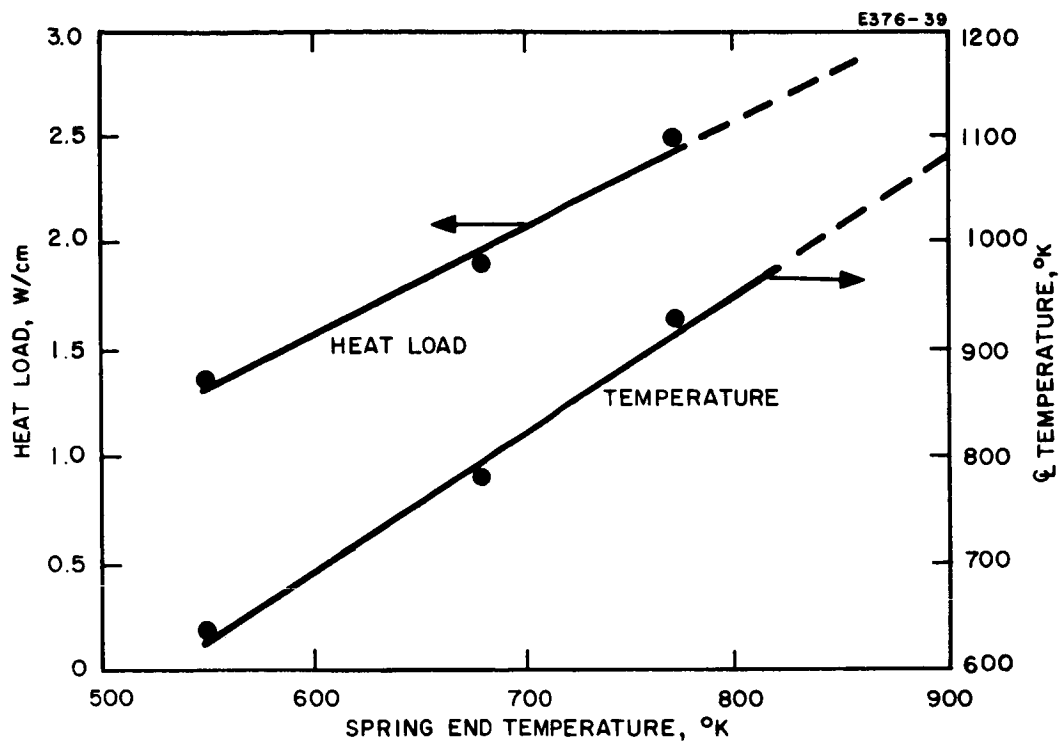


Fig. IV-40. Focus heat load per unit length versus spring end temperature. 32-150-1 engine test.

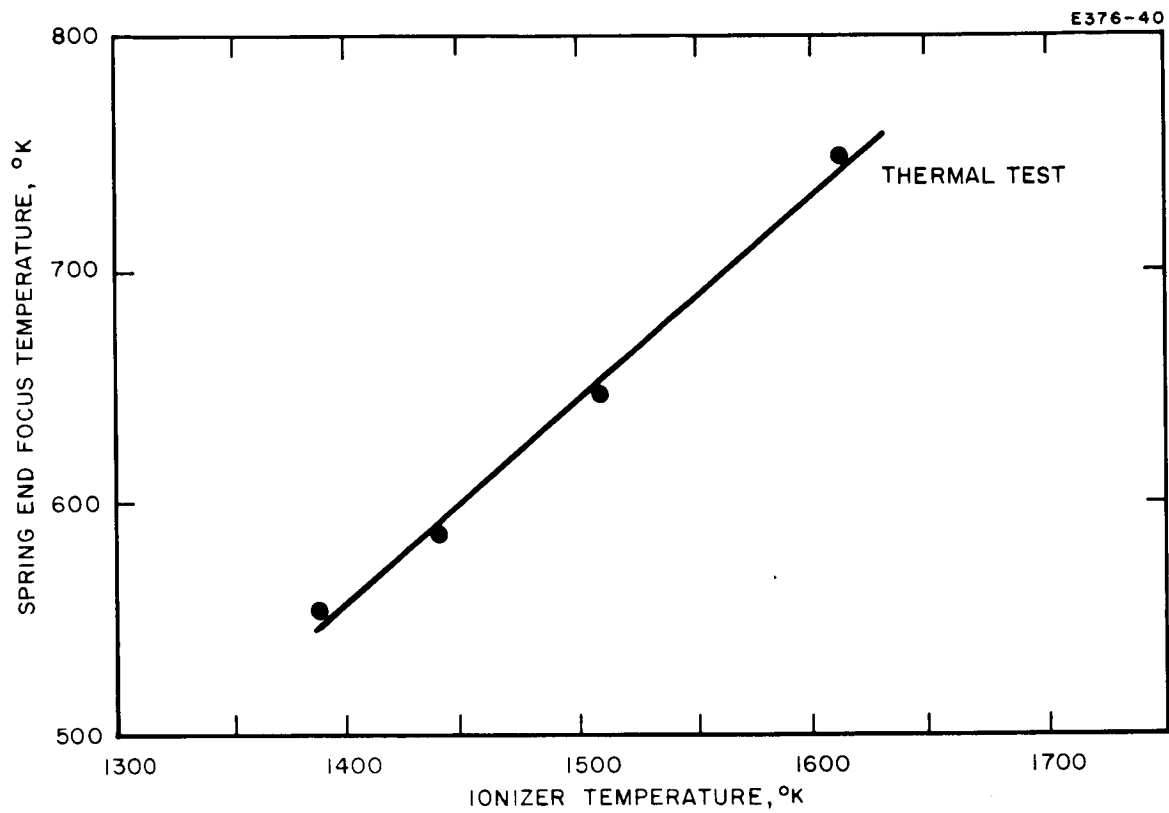


Fig. IV-41. Spring end focus temperature versus ionizer temperature.
32-150-1 engine test.

The oldest empirical method of heat load determination was that used on engine 32-40-8. The value of heat load (Q) was obtained empirically during the engine test, since it is simply the sum of the heat flow out both ends of the electrode divided by the electrode length:

$$Q = \frac{1}{l} \left(\frac{T_1 - T_s}{Z_1} + \frac{T_2 - T_s}{Z_2} \right) \text{ W/cm} \quad (\text{IV-11})$$

where

$Z_1 \equiv$ spring end thermal impedance, $^{\circ}\text{K/W}$ (from electrode end to sink)

$Z_2 \equiv$ fixed end thermal impedance, $^{\circ}\text{K/W}$

$T_s \equiv$ sink temperature, $^{\circ}\text{K}$.

The problem was to obtain Z_1 and Z_2 .

The impedance values Z_1 and Z_2 had to be determined by a slightly independent experiment with the 32-40-8 engine. Prior to actual operation, the ionizer was heated to the design temperature range with a thermocouple mounted at the center of the focus electrode. The usual thermocouples at the ends of the electrode (which remain during engine operation) were also mounted. With the end and center temperatures known, focus temperature is described by (IV-8), where, for the independent thermal experiment,

$$T_1 = 683^{\circ}\text{K}$$

$$T_2 = 477^{\circ}\text{K}$$

$$T_{\text{CL}} = 999^{\circ}\text{K}$$

$$T_s = 308^{\circ}\text{K}$$

$$Z_o = 550^{\circ}\text{K/W}.$$

The high value of T_{CL} occurred because there was no electrode shielding during the thermal test. (However, the shields were in place for the

operational test.) The impedances Z_1 and Z_2 were immediately obtained from the knowledge of the temperature distribution, as follows. Heat flow out the spring and fixed ends are given, respectively, by

$$q_1 = kA \left. \frac{dT}{dx} \right|_{x=0} = \frac{1}{Z_o} [3(T_{\text{f}} - T_1) + (T_{\text{f}} - T_2)] \quad (\text{IV-12a})$$

$$q_2 = -kA \left. \frac{dT}{dx} \right|_{x=l} = \frac{1}{Z_o} [(T_{\text{f}} - T_1) + 3(T_{\text{f}} - T_2)] \quad (\text{IV-12b})$$

The impedances are established by dividing the temperature differences between end and sink by the heat flows just determined. Thus,

$$Z_1 = \frac{(T_1 - T_s)}{3(T_{\text{f}} - T_1) + (T_{\text{f}} - T_2)} Z_o \quad (\text{IV-13a})$$

$$Z_2 = \frac{(T_2 - T_s)}{(T_{\text{f}} - T_1) + 3(T_{\text{f}} - T_2)} Z_o \quad (\text{IV-13b})$$

Evaluating for the 32-40-8 engine,

$$Z_1 = \frac{(683 - 308)(550)}{3(999 - 683) + (999 - 477)} = 140^\circ\text{K/W}$$

$$Z_2 = \frac{(477 - 308)(550)}{(999 - 683) + 3(999 - 477)} = 50^\circ\text{K/W} \quad .$$

As shown, these values have been considerably reduced in subsequent engines to a value of 20°K/W .

With the above impedance values thus established, eq. (IV-11) was used to calculate heat load. For a 1600°K ionizer, the focus spring end and fixed end temperatures were 600 and 400°K , respectively. Equation (IV-11) was used to determine the heat load per unit length:

$$Q = \frac{1}{5.5} \left(\frac{600 - 300}{140} + \frac{400 - 300}{50} \right) = 0.75 \text{ W/cm}.$$

This result compares well with the calculated value in Table IV-2.

4. Temperature Distribution

Methods have been developed to determine the complete temperature distribution along the length of the electrode during engine operation. The methods allowed temperature measurements to be made only at the extreme ends of the electrode, so that the thermocouples did not interfere with the engine optics or the beam.

The most accurate method of obtaining peak focus temperature during an engine test is to have previously calibrated the electrode. This is done by running a separate thermal test before the engine test and actually measuring center temperature versus end temperature. Then, during the engine test, the end temperature may be continually monitored, revealing the value of center temperature. This was the method used on engine 32-150-1 (see Fig. IV-40). If end temperature is then correlated with ionizer temperature, the complete picture is obtained. With the ionizer at 1600°K, for example, the focus center temperature was 880°K.

The above method was not always used since it required a separate thermal test. Other methods were available, however, once the heat load was established. For example, on the 32-40-8 engine test, with the determination of Q , all the required parameters had been obtained for (IV-7):

$$T(x) = 600 + (400 - 600) \frac{x}{5.5} + \frac{(0.75)(550)}{2} \left(x - \frac{x^2}{5.5} \right)$$

$$T(x) = 600 + (170x - 37.5x^2).$$

Figure IV-42 is a plot of this function, showing the focus electrode temperature profile during the 32-40-8 engine test.

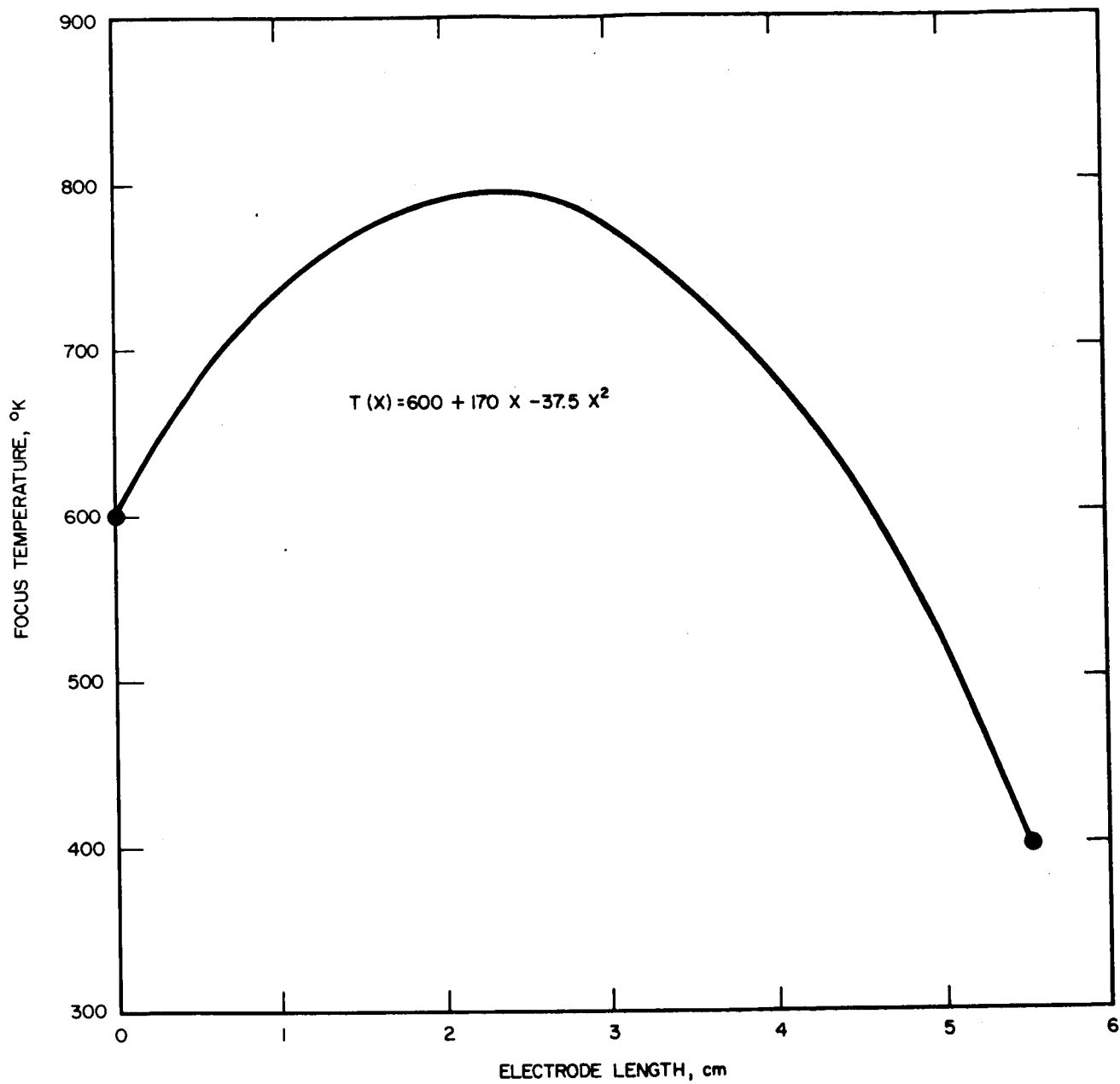


Fig. IV-42. Focus electrode temperature profile obtained during operational test of engine 32-40-8.

The focus temperature for the 32-150-2 engine test and all subsequent tests was obtained by a method enabling temperatures to be determined directly during a test, with no thermal test prior to engine test required. The peak focus temperature was obtained by the relation

$$T_p = T_1 + \frac{Q_l}{2} \left(\frac{Z_o}{4} \right) \quad (\text{IV-14})$$

where Z_o is the inherent electrode impedance ($Z_o = 128^\circ\text{K/W}$) and T_1 is the focus end temperature. The focus end temperature for the radiation cooled engine is recorded in Fig. IV-43 for a heat load consisting only of thermal radiation (32-150-2). The end temperature corresponding to a 1600°K ionizer is 720°K . Hence,

$$T_p = 720 + \frac{(2.2)(5.5)(32)}{2}$$

$$T_p = 720 + 190$$

$$T_p = 910^\circ\text{K}.$$

Figure IV-44 shows the heat flow, temperature differentials, and determined impedances for a typical engine run (32-150-1). The total impedance encountered in getting heat out of the tip of the electrode, across the interface at the electrode mounting, and through the copper loaded spring was 80°K/W for this engine. At the fixed end, heat travels through the molybdenum support to the sink. The fixed end impedance for engine 32-150-1 was 39°K/W .

A very probable cause for these high indicated impedance values was poor manifold shielding. Radiant interchange between the manifold and electrode support structure creates an additional load on the heat drains, requiring larger ΔT across the impedance. This phenomenon makes the apparent impedance larger than the actual impedance of the structure alone. The thermal impedances of both the spring and fixed ends of the focus electrode mounting structure were obtained from the

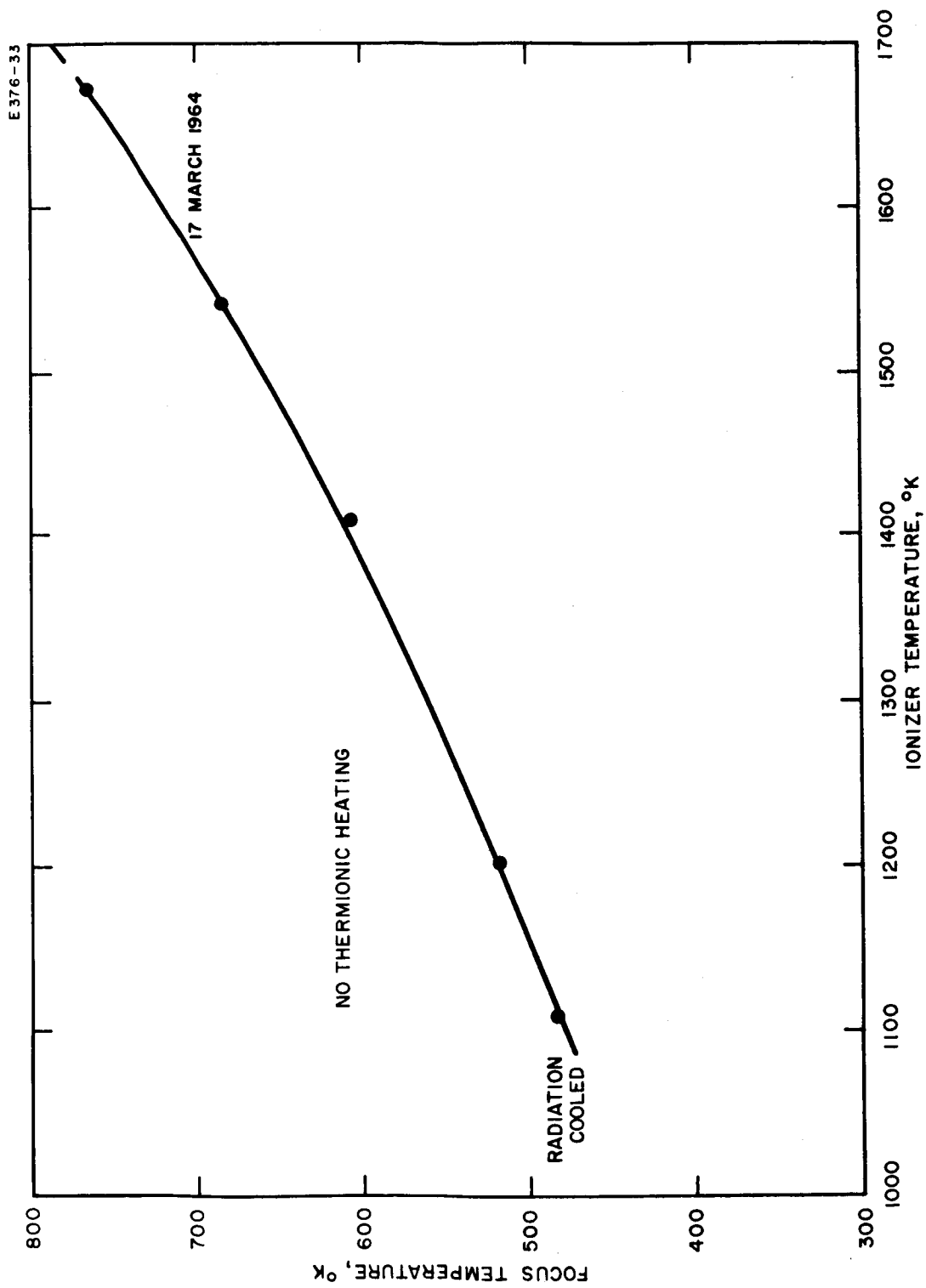


Fig. IV-43. Focus electrode end temperature versus ionizer temperature. 32-150-2 engine test.

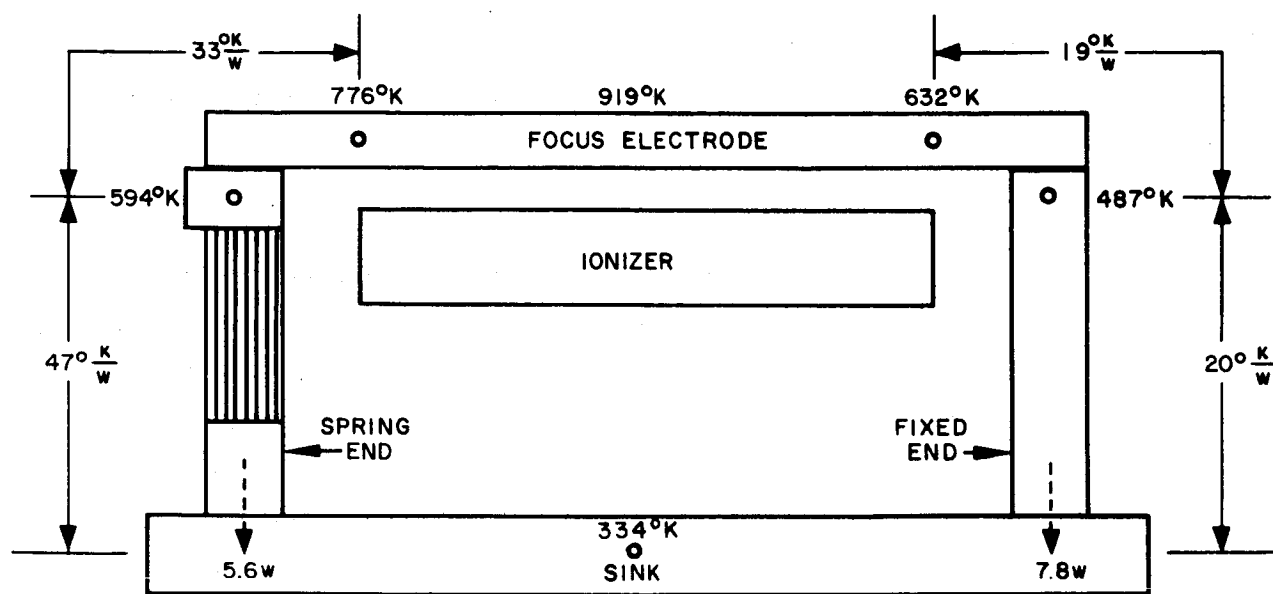


Fig. IV-44. Focus electrode and structure temperature distribution during an electrode heat load of 2.4 W/cm.

separate thermal test. With the electrode center and both end temperatures known, the heat flowing through the spring and fixed end structures is given by (IV-12a) and (IV-12b). The impedance value is obtained by measuring the temperature differential between the two end points of the heat path.

The 32-150-2 and subsequent engines exhibited improved heat drains and much better shielding between manifold and heat drain structure, as has been discussed.

5. Accel Drains and Focus Heat Load

During operation of an ion engine, there is generally more heat load on the focus electrode than that resulting from ionizer radiation alone. The increased heat load is due to electron bombardment from the accel electrode which shows up as accel drain current. Figure IV-45 shows the effect of this added heat load in increasing the focus temperature. An electron bombardment heat load of 0.6 W/cm increases the peak temperature by 150°. These profiles have been calculated for the 32-150-1 engine test, using (IV-6), where

$$Z_1 \equiv \text{spring end impedance} = 80^\circ\text{K/W}$$

$$Z_2 \equiv \text{fixed end impedance} = 39^\circ\text{K/W}$$

$$T_S \equiv \text{sink temperature} = 334^\circ\text{K}.$$

The degree of thermionic heating varied from engine to engine. The method of determining the thermionic power was to measure the focus heat load with beam on and off, the difference being the thermionic heating.

The focus electrode per unit length power increase due to electron bombardment is given by

$$Q_e = \frac{I_e V}{(2)(4)l} \text{ W/cm} \quad (\text{IV-15})$$

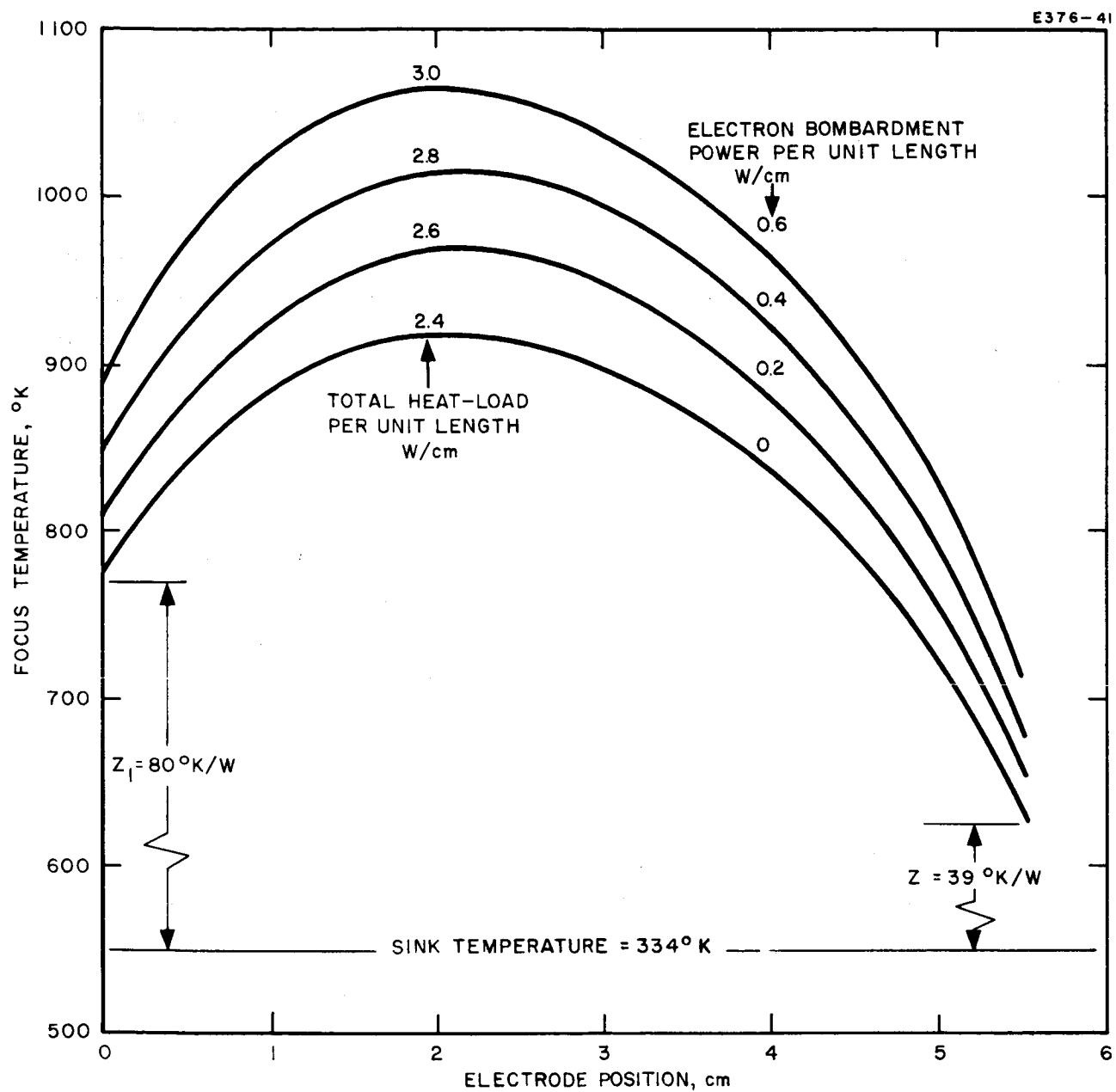


Fig. IV-45. Focus electrode temperature profile. 32-150-1 engine test.

where

$I_e \equiv$ total engine thermionic current, A

$V \equiv$ potential difference between focus and accel electrodes =
10 kV

$l \equiv$ electrode length = 5.5 cm.

The factor of four appears because there are four focus-accel electrode pairs in the three-strip engine. The factor of two takes into account the fraction of accel current that arrives at the focus electrode. When these values are inserted in (IV-15), the result is

$$Q_e = 0.23 \frac{W}{\text{cm} - \text{mA}} .$$

Thus each milliampere of accel drain produces an additional 1/4 W of focus electrode heating for the three-strip engine.

The accel electrode temperature has also been studied because of its relationship to thermionic emission. The data in Fig. IV-46 were taken during the 32-150-1 thermal test. Various ionizer temperatures have been considered.

D. Electrode Simulation Studies

It has been demonstrated that the materials used as focus and accel electrodes for cesium contact ion engines strongly influence the lifetime performance of the electric propulsion engines. The criteria involved in the selection were summarized in the report, "Electrode Materials for Contact Ion Engines" by H. L. Garvin and R. G. Wilson (Ref. IV-4). These criteria include the engineering properties of the materials such as their (1) structural strength at operating temperatures, (2) machinability, and (3) cesium compatibility; however, even more important are their basic physical properties such as sputtering characteristics and ion or electron emission characteristics when operated in a cesium vapor-filled region. During this past year an experimental

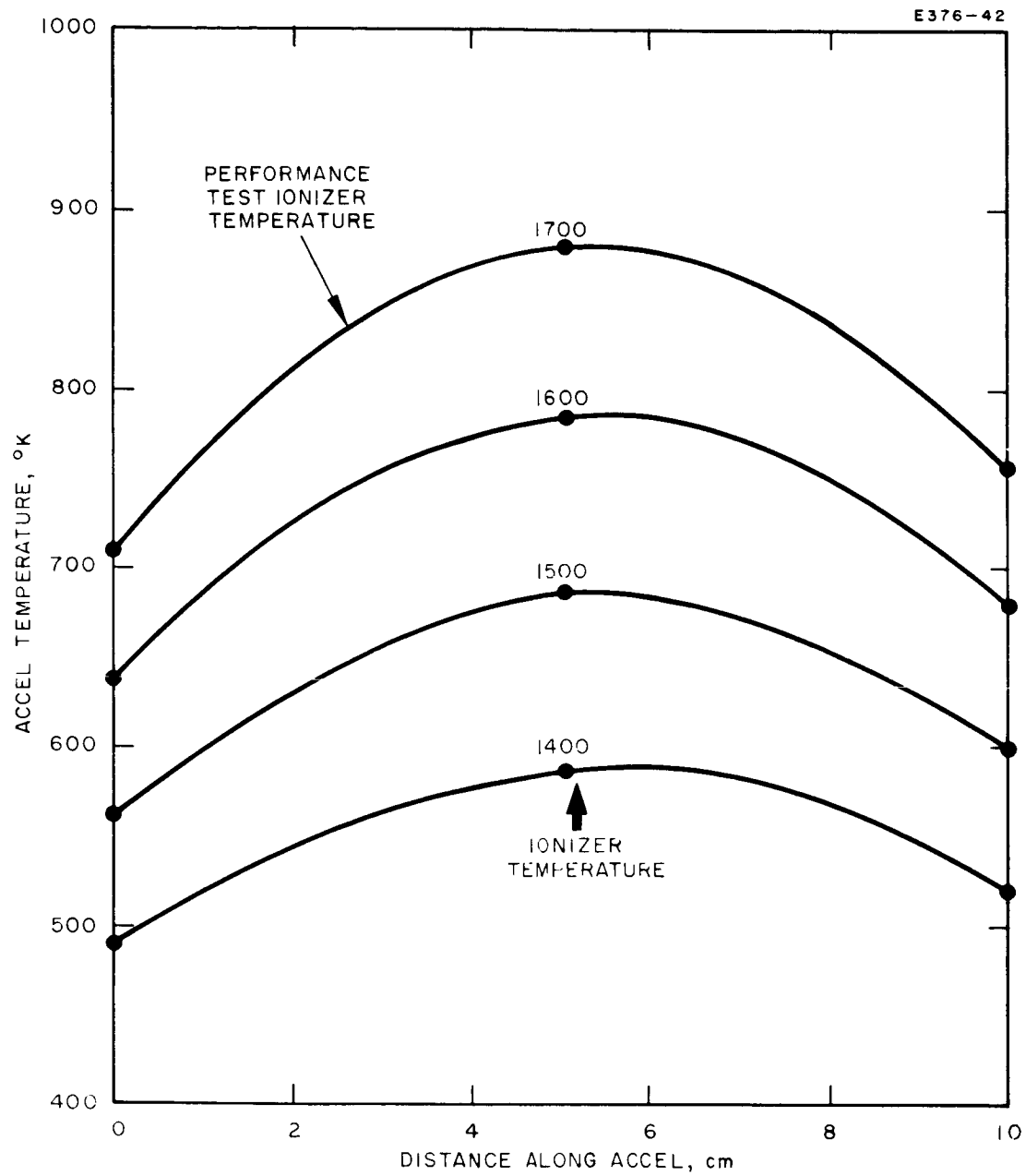


Fig. IV-4b. Accel temperature profiles for various ionizer temperatures. 32-150-1 thermal test.

program has been carried out to measure these characteristics for electrode materials, many of which have been used in vacuum tube applications and in thermionic energy converters although they have not been examined in detail. The experimental environment for evaluating materials was created in glass ESE (Electrode Simulation Experiment) tubes in which duplication of the operating conditions of the electrode region of an ion engine was attempted.

The schematic arrangement of the ESE tubes is shown in Fig. IV-47. The sample material to be examined is of approximately the same dimension as that used in the engine electrodes, and the cesium arrival rate is set to representative values of true engine conditions. The temperature varied from room temperature to its upper safe operating limit. The voltage gradients were capable of approximating those of the thruster accel system but tube lead-through proximity and the desire to reduce sputtering generally made it advantageous to operate only at high enough voltage to assure saturation of the ion or electron currents being observed.

The component structures of the ESE tubes changed slightly from one tube to the next, as the tests demanded, but the general concept remained the same. The sample material was heated directly (or by an attached resistance heater) and a portion of its surface was exposed to an electrostatically guarded collector surface. The application of negative or positive voltage to this collector determined the ion or electron species being measured. The ESE tubes were assembled, evacuated, and baked out in a 275°C oven to achieve a 10^{-7} Torr vacuum before sealoff. Following sealoff from the oil diffusion-pumped system, the tubes were evacuated to the low 10^{-8} Torr region (by means of a 0.2 liter/sec appendage ion pump) prior to distilling the cesium into the tube. The temperature of the sample was measured by attachment of a tungsten versus tungsten (26%)-rhenium thermocouple which was calibrated against optical pyrometric measurements. The neutral cesium arrival rate was determined by the vapor pressure of cesium vapor over the condensed phase maintained by the thermostatic bath.

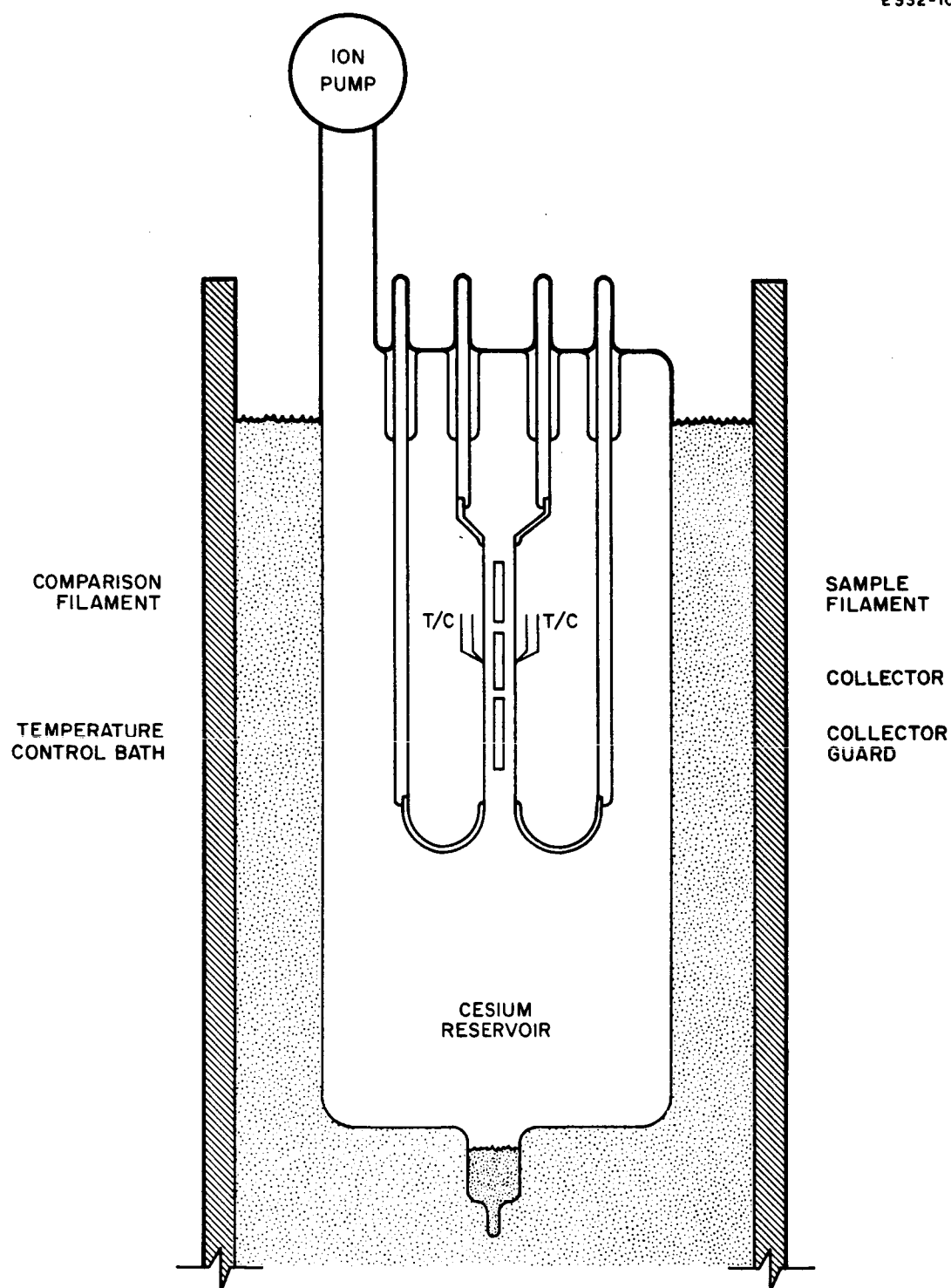


Fig. IV-47. Schematic of electrode simulation experiment tube arrangement.

1. Tungsten

In the first tube, the ion emission characteristics of tungsten were observed. This served to check the technique of the experimental system and also to observe the extent to which the ion emission fell off as cesium was adsorbed onto the surface. The characteristics are shown in Fig. IV-48. Clearly, the envelope of the sharp breaks in the curves corresponds closely with the critical temperature line published by Taylor and Langmuir (Ref. IV-5). The fall-off of ion emission at cesium arrival rate $\mu_a = 10^{16}$ atoms/cm²-sec indicates that an ion current of 10^{-6} A/cm² would be produced for an electrode temperature of 1100°K. The current density of 10^{-6} A/cm² is significant since this represents approximately one order of magnitude below the arrival rate of charge exchange ions at the accel electrodes. Thus, for ions originating at the focus electrode, the ion current must be this low or lower to be of secondary significance in engine life determination.

2. Molybdenum

An ESE tube containing a simulated molybdenum electrode was tested, and the results showed a marked similarity to tungsten (see Fig. IV-49). The critical temperature line is close to — but slightly crossing — the tungsten line, and the cesium adsorption is slightly greater; this indicates a lower operating temperature ($\sim 1050^\circ\text{K}$) to produce 10^{-6} A/cm². Thus, the selection of molybdenum as a focus electrode material for a cool focus electrode engine design is a reasonable one.

3. Platinum

In some recent theoretical analyses of cesium ion adsorption on refractory metal surfaces (Ref. IV-6), the materials with high vacuum thermionic emission work function (such as platinum, rhenium, and iridium) are expected to exhibit high binding energies for cesium and thus would result in a low cesiated thermionic work function, and consequently, in a low ionization efficiency. Measurements made in platinum

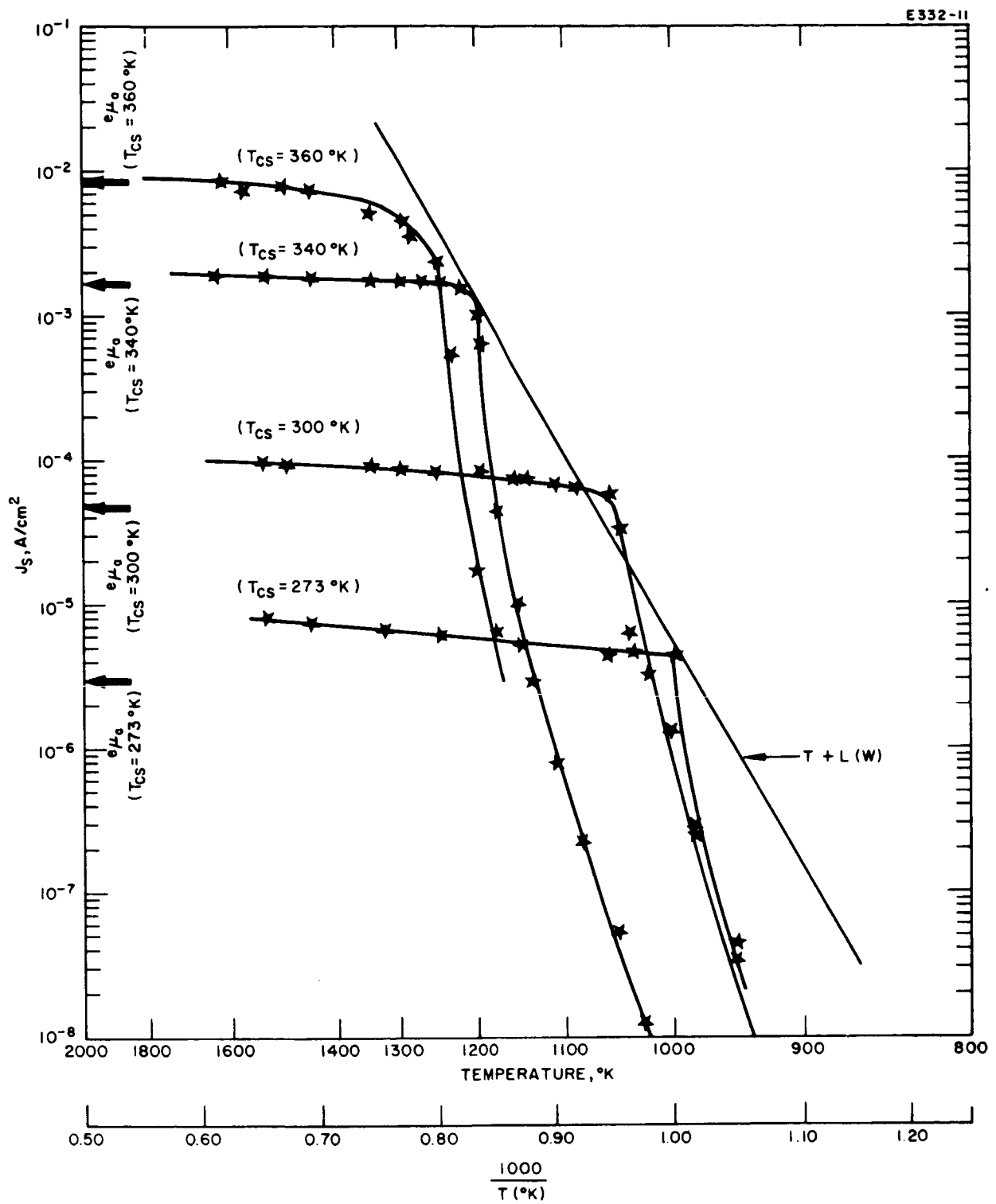


Fig. IV-48. Surface ionization characteristics for tungsten.

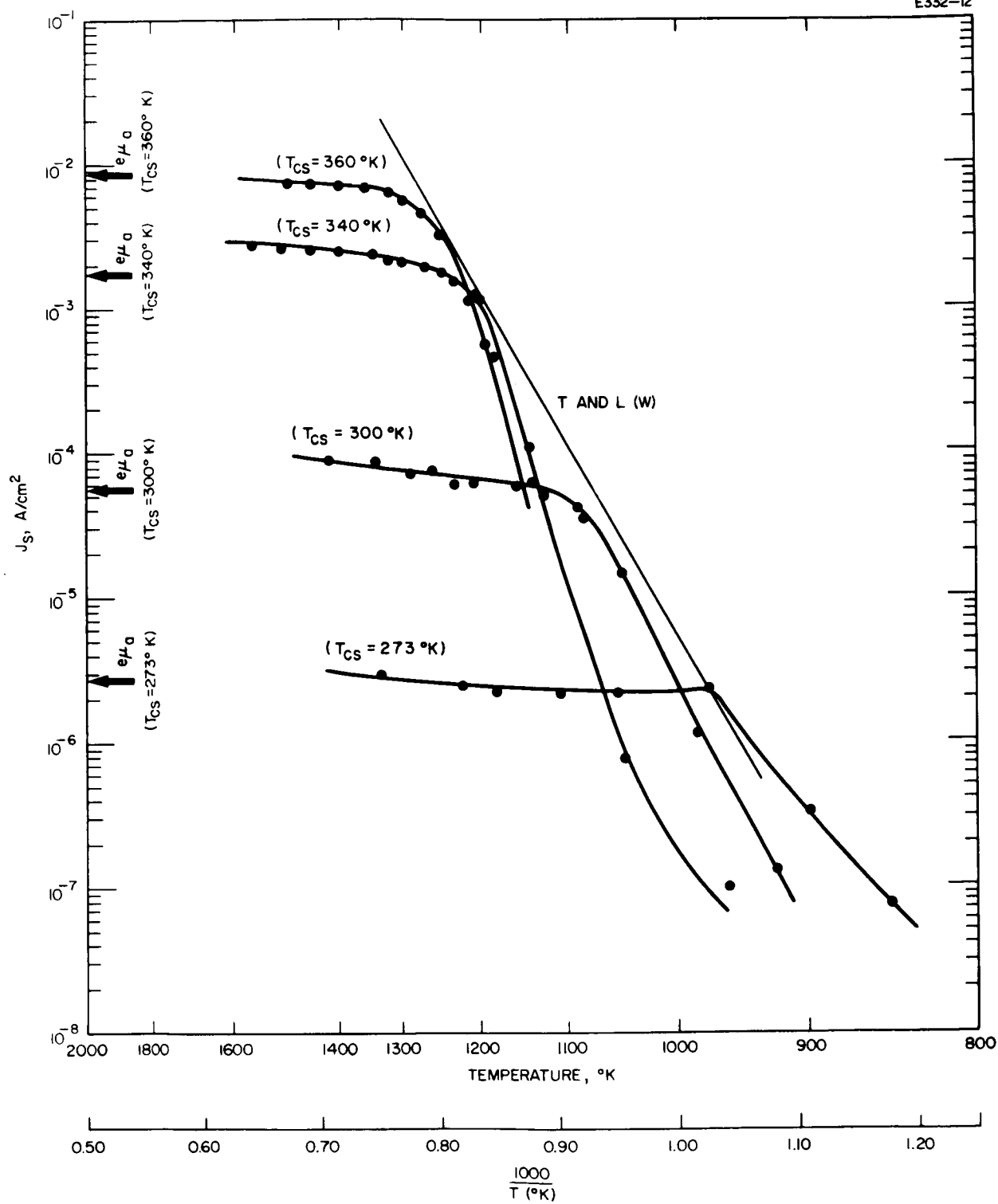


Fig. IV-49. Surface ionization characteristics for molybdenum.

and platinum-10% iridium samples (each with vacuum emission work functions greater than 5.0 V) showed this not to be the case (see Fig. IV-50). The critical temperature measurements indicated a lower critical temperature line than for tungsten, and the ionization falloff was not as steep. Thus, for $\mu_a = 10^{16}$ atoms/cm²-sec, a temperature below 920°K is required to reduce the ion current to below 10^{-6} A/cm². It cannot be generalized that the lower critical temperature would necessarily make platinum a better ionizer material. On the contrary, the critical temperature line appears to cross the tungsten critical temperature line at arrival rates of about 5×10^{16} atoms/cm²-sec, which is below the level of interest in ionizer operation. Thus, no gain in critical temperature is observed. Also, the ionization efficiency is seen to fall off sharply at these higher arrival rates. The cesium arrival rate would indicate a current of 2.6×10^{-3} A/cm² at 100% ionization, whereas the observed level is only of the order of 50% of this value. In general, platinum is found to be a poor choice for use in electrode structures despite the fact that it is a good vacuum material with a tendency to remain free of oxide films.

4. Molybdenum Disilicide

Surface ionization on the focus electrode is reduced by lowering the effective work function. In the materials described above, this is done by adsorption of a cesium layer. Materials having a low work function without being cesiated would operate in the same manner, if not better, because they would inhibit ionization even at the higher temperatures when refractories are uncoated with cesium. Materials which are candidates for such application include TaB₂, ZrC, MoSi₂, GdO₂, and thoriated tungsten. Two factors must be considered in this application: (1) the stability of the surface as a low work function non-ionizing medium, and (2) the compatibility of the material with the other components of the engine. Because the focus electrode reaches high temperatures and is close to the ionizer, it is possible that some of the material might vaporize or migrate to the porous tungsten ionizer.

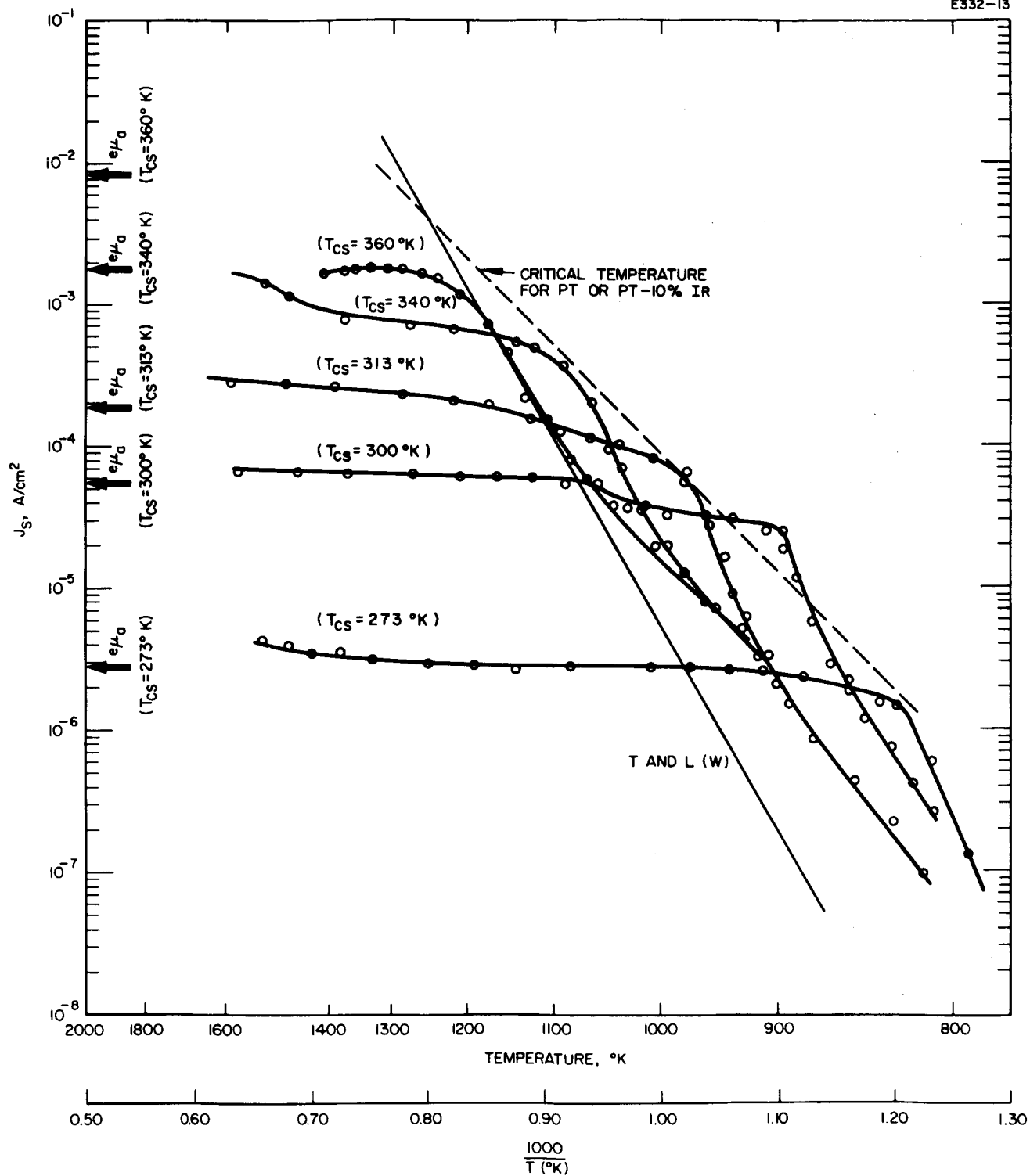


Fig. IV-50. Surface ionization characteristics for platinum or platinum-10% iridium.

Certain of the candidates (e.g., lanthanum and barium) are expected to be particularly harmful in that their tendency to lower the surface work function would drastically lower the efficiency of the ionizer. Other materials, such as iron or titanium, must be used with caution since their presence on the porous tungsten could cause it to sinter rapidly, thus gradually reducing the uniform transmission of the ionizer. Either of these effects would impair the performance of the engine.

The number of available choices of materials for electrodes is reduced when high temperature ($\sim 1500^{\circ}\text{K}$) operation is required. Of the materials with published low work function values, TaB_2 and MoSi_2 represent two reasonable choices (ϕ for TaB_2 is given as 2.9 eV and for MoSi_2 as 3.3 eV at 1400°K (Ref. IV-7)). Zirconium carbide is another possibility but its work function ($\phi = 3.5$ eV) is sufficiently high that it is doubtful that it can suppress the ionization to the level desired.

Techniques have been developed to prepare electrode surfaces of TaB_2 ; preliminary measurements indicate an electron emission work function of 4.5 eV, considerably higher than the published value of 2.9 eV (although the referenced work does not indicate that this was a stable value). The material has not been tested under cesiated conditions, but the work function indicates that it will probably show high ion emission characteristics.

Molybdenum disilicide electrodes were also prepared and have been tested extensively in cesium vapor. The electron and ion emission characteristics again show that the work function (4.9 eV) is higher than expected (see Fig. IV-51) and, correspondingly, the ion emission intolerably high.

5. Thoriated Tungsten

Although the use of thorium near an ionizer is hazardous, a sample of 2% thoriated tungsten was examined to see if a low work function would suppress the ionization characteristics. When the tube was first operated, the vacuum emission work function was seen to be approximately 3.1 eV and the ion production level (for a cesium arrival

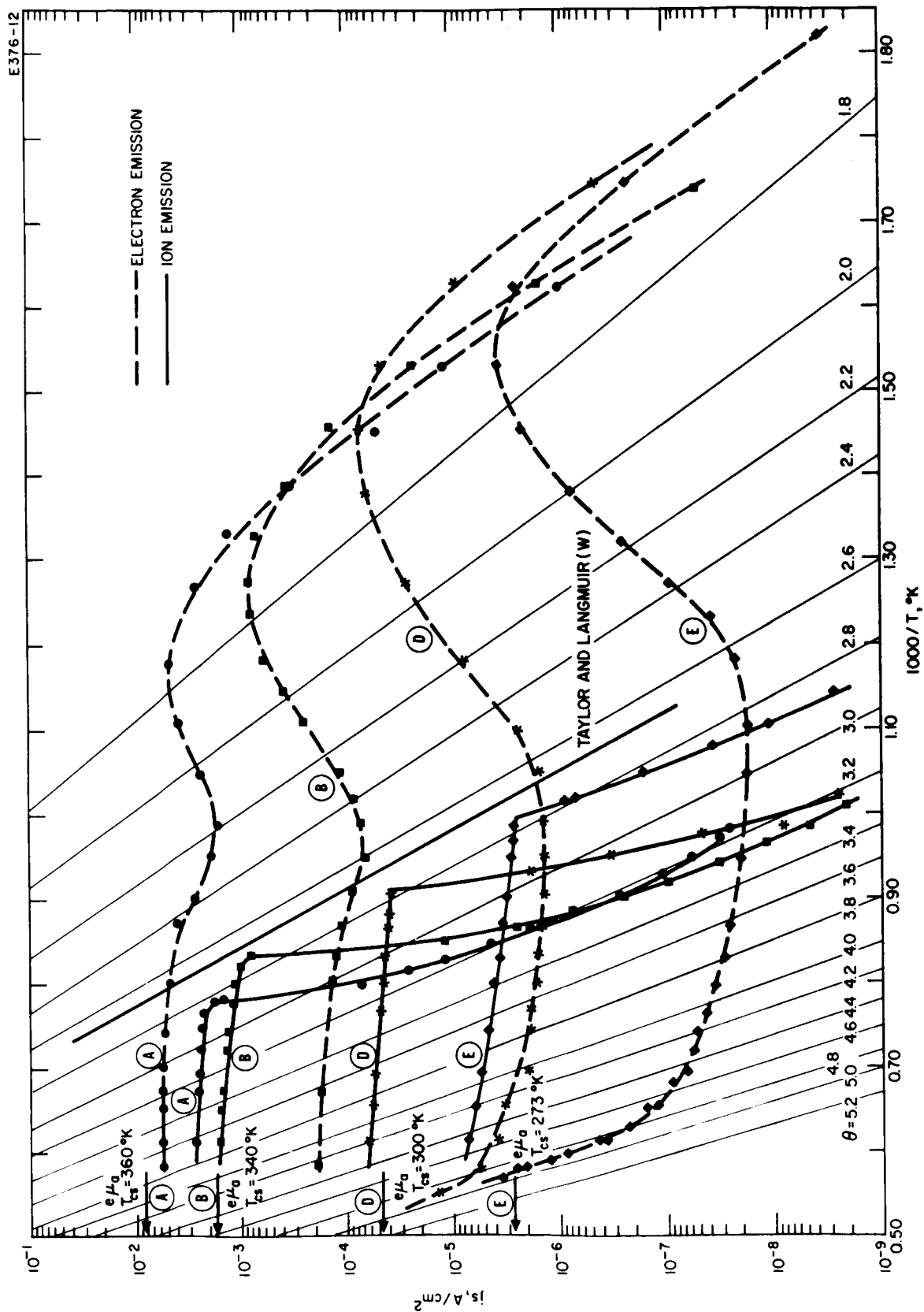


Fig. IV-51. Electron and ion emission characteristics for molybdenum disilicide.

rate of 10^{14} atoms/cm²-sec) was two orders of magnitude below the 100% ionization level. As tests were made at higher cesium arrival rates, the work function was seen to shift to approximately 3.4 eV, and this small change allowed the ion production to increase dramatically (see Fig. IV-52). By flashing the sample to high temperature, the low work function was seen to reappear (with a corresponding low ionization level); this was a transient effect, however, which wore off and indicated an instability of the surface for long term operation. Thus, the thoriated tungsten is not suitable for engine application, but it did provide proof of the principle that the low thermionic emission work function would suppress the ionization capabilities of the electrode surface. Although the Saha-Langmuir relationship would indicate that the surface ionization efficiency would decrease exponentially for $\phi < 3.89$ eV (the ionization potential of cesium), in this experiment the ionization did not decrease until the effective electron emission work function of 3.2 eV was reached. This may be attributed to the fact that the surface of the thoriated tungsten is complex, involving a thin, low work function layer of thorium on a patchy tungsten matrix rather than a uniform low work function surface.

6. Aluminum Oxide

Other materials which have been considered to be suppressors of surface ionization are insulator materials such as Al₂O₃. These contain few enough free electrons to make surface ionization improbable, yet are sufficiently good electrical conductors at operating temperatures to permit maintenance of the equipotential surfaces required for ion optics.

The first samples of Al₂O₃ which were tested were prepared as cylindrical sleeves on tungsten heater wires (see Fig. IV-53). Small wire probes were wrapped onto the sleeve to detect the buildup of voltage across the insulator. Attempts were made to attach thermocouples to the ceramic but the sample size was too small. As an alternative, optical pyrometric measurements were made and correlated with the heater power to define the sample temperature. Thus, from run to run and from

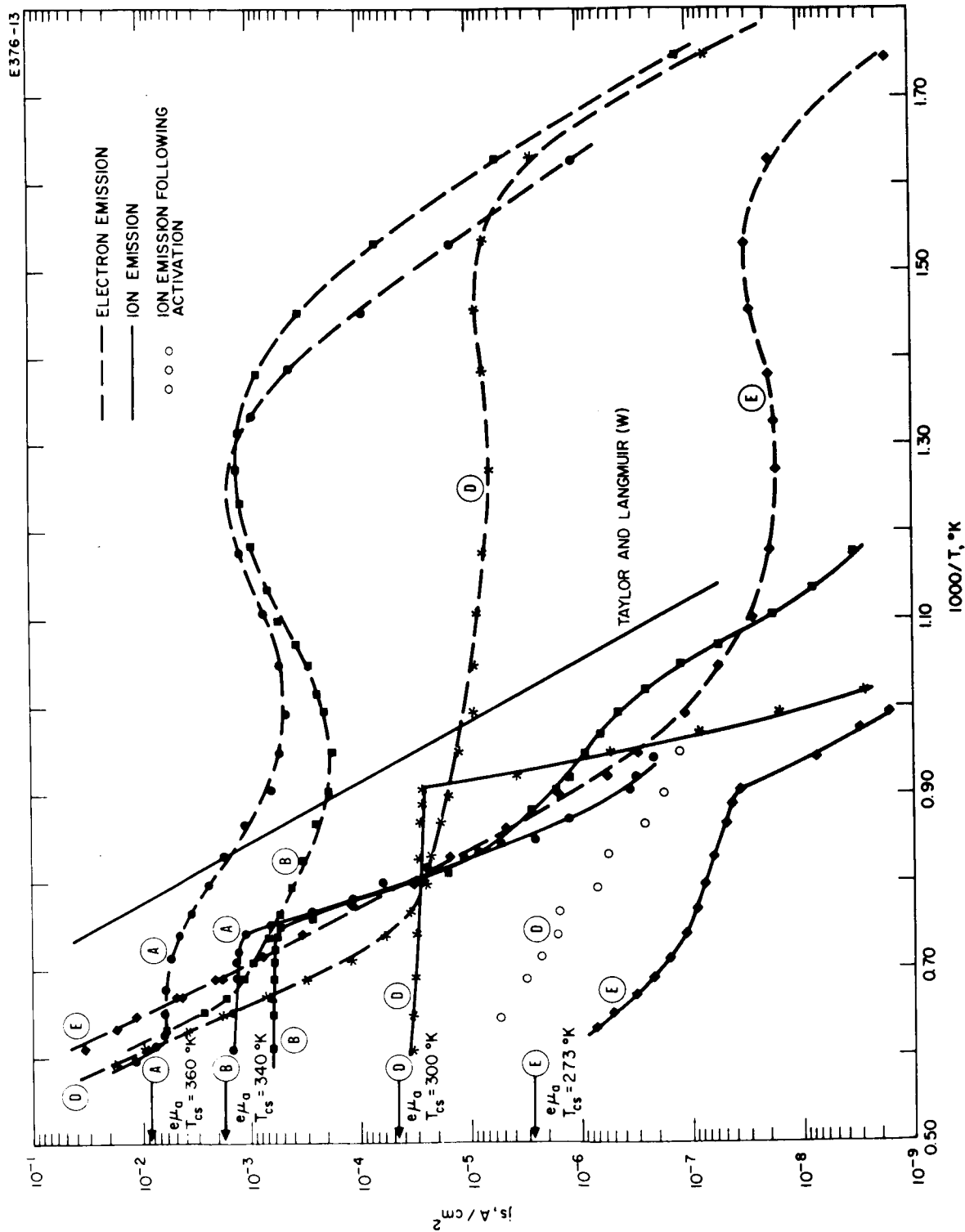


Fig. IV-52. Electron and ion emission characteristics for thoriated tungsten.

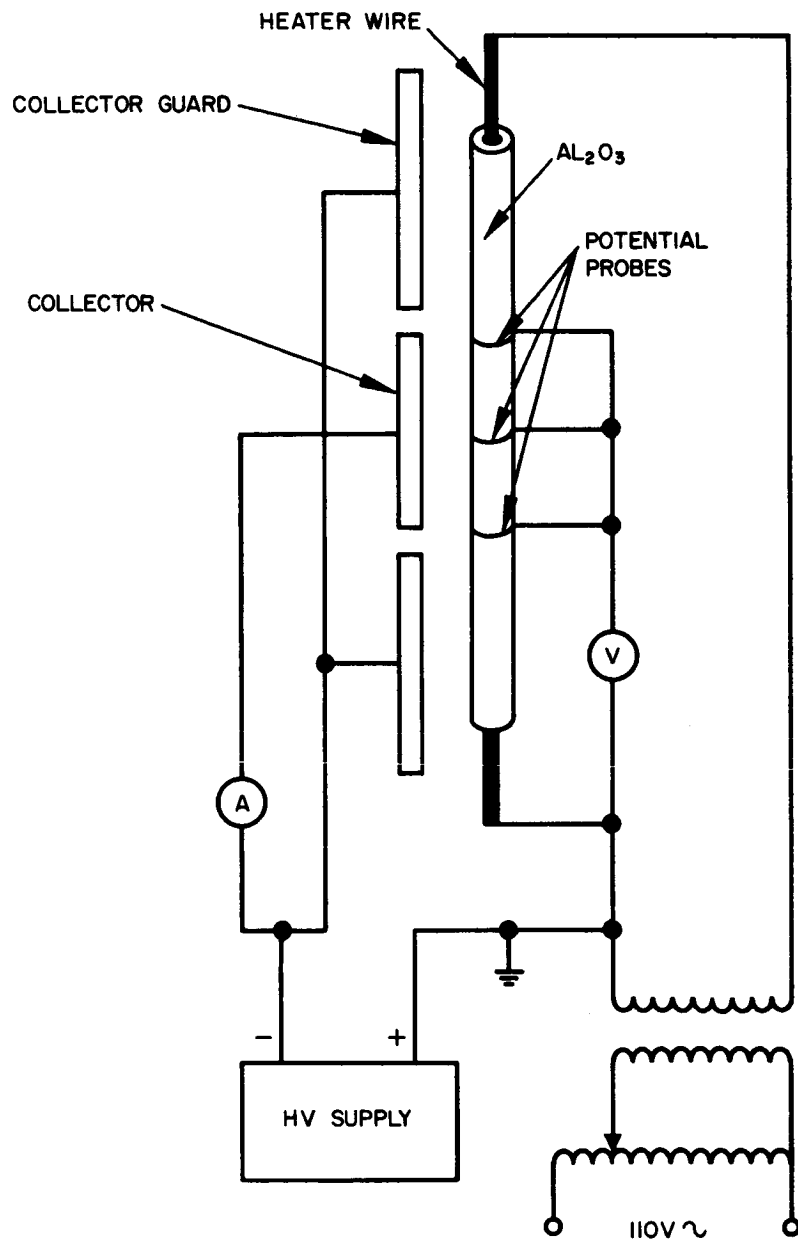


Fig. IV-53. Circuit for observing electron and ion emission characteristics of cylindrical Al_2O_3 sample.

sample to sample, the temperature conditions could be reproduced, but because of the illumination from the heater filament and the uncertainty in the spectral emissivity of the sample, the absolute temperature may be uncertain by as much as 200°K.

Figure IV-54 summarizes the observed ion emission characteristics from the Al_2O_3 sleeve. It is obvious that the ion production level is very much lower than that from the refractory surfaces. In addition, there is a reduced dependence on the cesium arrival rate. (The ion production level increases by only one order of magnitude, while the cesium level increases by three orders of magnitude.)

The electron emission is seen to follow an S curve, indicating that the surface of the insulator tends to coat with cesium; the bulk conductivity of the Al_2O_3 is low enough to provide approximately 1 mA/cm² across 0.010 in. thickness of Al_2O_3 without a significant voltage drop. At low temperatures (below 700°K), the cesium adsorption enhances the electron emission as the apparent work function decreases to approximately 1.7 eV.

Following these initial measurements on Al_2O_3 , Wilson (Ref. IV-8) made observations on a solid Al_2O_3 sample in an experimental tube using an aperture screen and a Faraday cup collector. His results indicated a marked enhancement in emission level over the results shown above (see Fig. IV-55 reproduced from his work). Again the temperature is somewhat questionable, although a thermocouple was inserted into the solid Al_2O_3 sample.

In hope of resolving the discrepancy, an ESE tube was constructed in which a 0.010 in. thick Al_2O_3 flat piece was brazed to a tungsten member, much as it would be done in an integral focus engine design. The tungsten was then heated by a radiation heater and the temperature was accurately measured by a tungsten versus tungsten (26%)-rhenium thermocouple. The results are shown in Fig. IV-56. It is interesting to note that the ion production falls off in the lower temperature region exactly as was demonstrated in Wilson's data. However, as the temperature was raised, the ion production did not proceed to a saturation level.

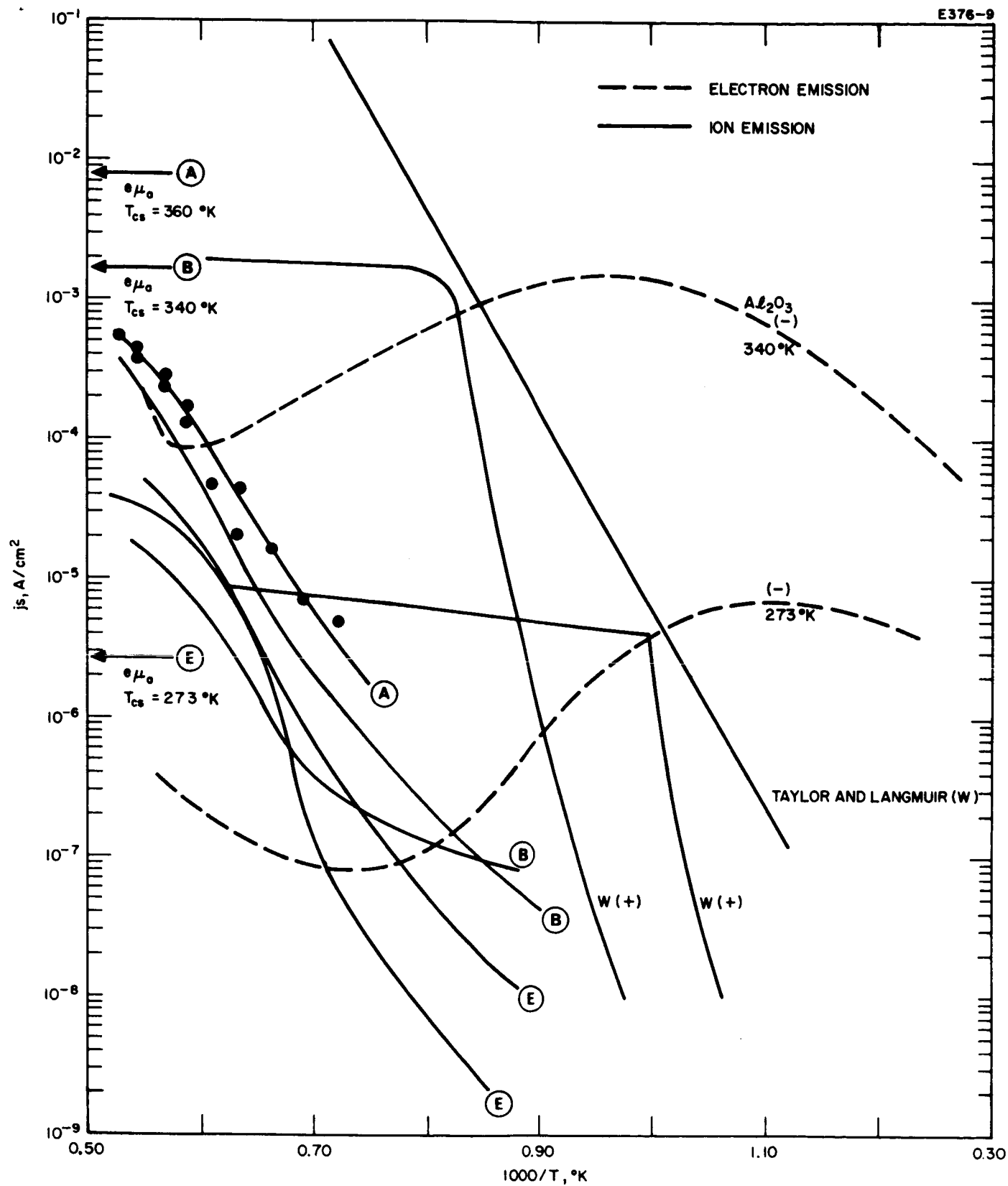


Fig. IV-54. Ion and electron emission characteristics of Al_2O_3 . Ionization characteristics of tungsten are shown for comparison.

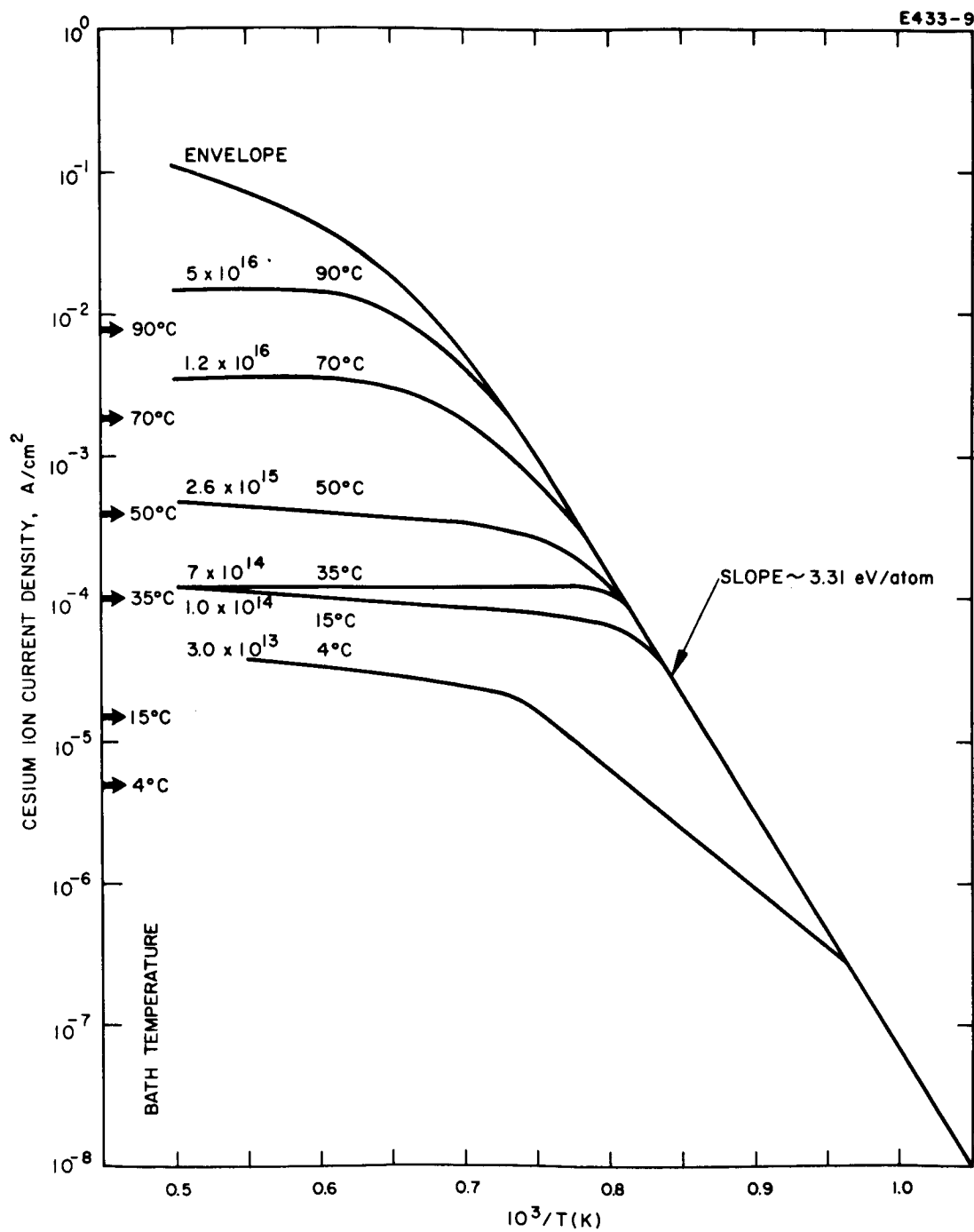


Fig. IV-55. Cesium ion emission data for aluminum oxide.

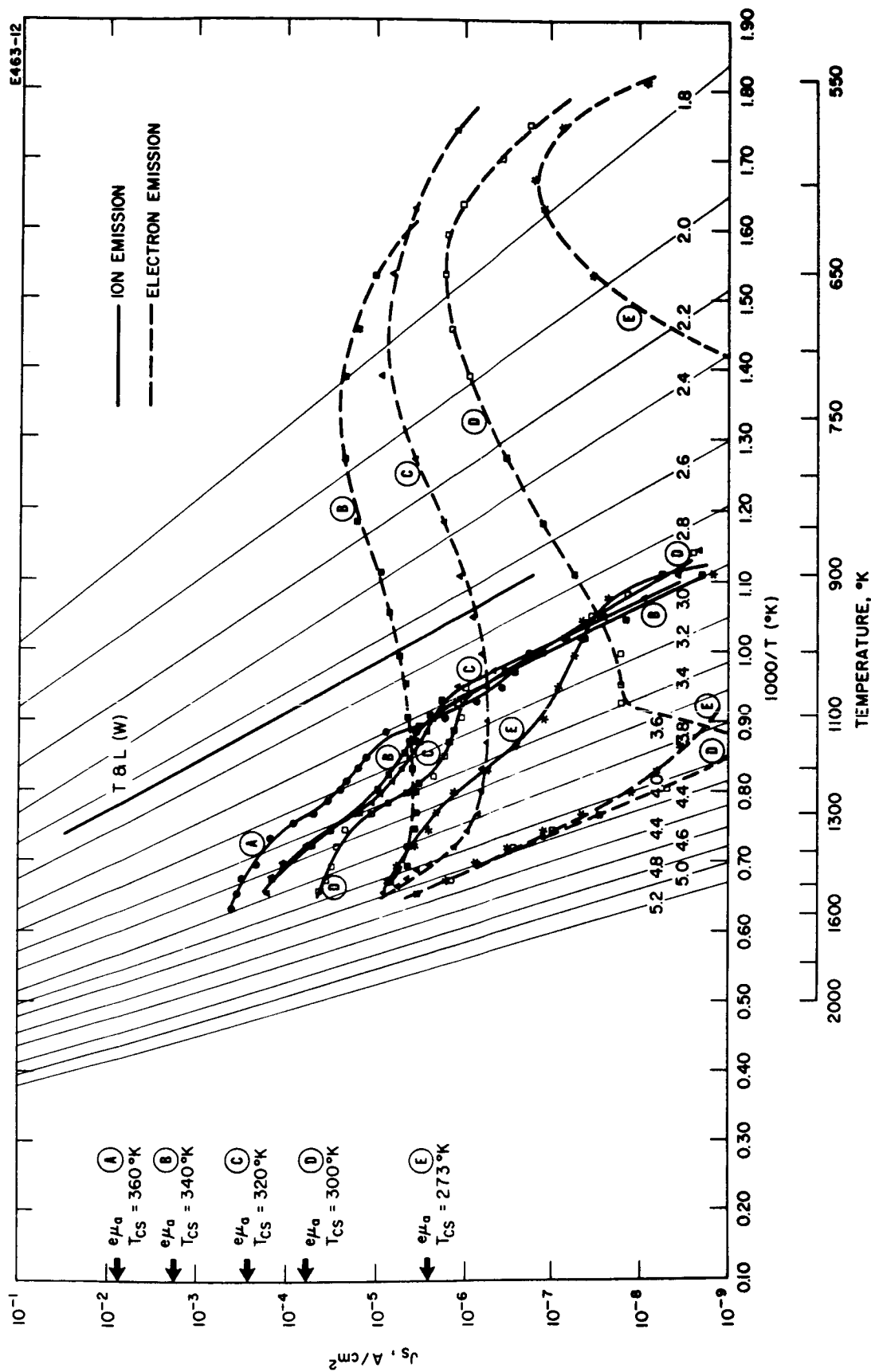


Fig. IV-56. Ion and electron emission characteristics of flat Al_2O_3 sample brazed to tungsten electrode.

The dependence on cesium arrival rate is greater than seen earlier but it is still not a direct dependence. The exact mechanism of this phenomenon is still under examination.

Other studies are being made on thin layers of Al_2O_3 for possible application to collector surfaces in thermionic energy converters (Ref. IV-9). In those cases, however, the films of oxide are very thin (30 to 2000 Å), the surfaces are operated at lower temperatures, and effective work functions are inferred from contact potential measurements (collecting electrons from a hot tungsten emitter). A motive diagram may be postulated in which the potential drop through the Al_2O_3 is strictly a resistance phenomenon which ties the cesium surface effects to the Fermi level of the substrate material. This would generally be the case only for films of Al_2O_3 thinner than the Debye length of electrons in the materials. The 0.010 in. thick samples which we have tested would be much thicker, and thus it must be expected that the behavior is primarily related to the surface dislocations and impurities of the polycrystalline Al_2O_3 material. The connection of surface charge (by ion or electron emission) to the Fermi level of the tungsten substrate is made through the bulk conductivity of the sample. This could contribute to some of the differences which have been observed between samples of differing geometry.

It is significant that the samples tested in the latter tube were made from integral focus electrodes prepared for an experimental ionizer and therefore represent the behavior expected in real engine conditions.

7. Copper

Copper has been widely used in the cooler electrodes of ion engines. Because of its high conductivity, it is used where thermal gradients are to be reduced; more important, however, copper is readily reevaporated without harmful effect to the porous structure in accel electrodes where sputtering may deposit it onto ionizer surfaces. On the other hand, since any accel electrode material can also be sputtered onto

the focus electrode (operating at a low enough temperature that it does not reevaporate), candidate accel materials (such as copper or beryllium) must be examined not only for their cesiated emission of electrons but also for their surface ionization capabilities.

An ESE tube was constructed using a copper tube as an emitter sample. A tungsten radiation heater was mounted in the tube, and a thermocouple was imbedded into the copper for temperature determination. In processing the tube, the copper sample was heated to 980°C to ensure that its surface would be clean and well outgassed. Figure IV-57 shows the ion and electron emission characteristics observed for cesium arrival rates from 10^{13} to 5×10^{16} atoms/cm²-sec. At the higher arrival rates, a blue discharge is evident in the tube when positive voltage is applied to the collector in order to draw electronic current.

The results indicate that copper deposited on a focus electrode surface could cause harmful ionization of scattered neutral atoms unless the temperature is maintained at less than 1010°K . Also, the cesiated electron emission from the accel electrode is of such a magnitude as to readily constitute the drain currents observed in engine operation. To reduce these drain currents to less than 0.1 mA/cm^2 , the accel temperature should be kept below 700°K or above 980°K . This effect has been confirmed in the operation of the 32-150-4 engine.

The extent to which copper or any accel material will adhere to and modify the surface of the porous tungsten ionizer is a subject of serious concern and should be investigated in ionizer material evaluation experiments. It would be most desirable if these experiments could simulate the ionizer operating conditions and the expected arrival rate of sputtered accel electrode material. The measurements must indicate, if possible, the effect on critical temperature and neutral fraction as the primary criteria for judgment of ionizer performance.

8. Titanium

Titanium should be considered for use in accel electrode structures because of its relatively low sputtering yield (0.8 for 5 kV

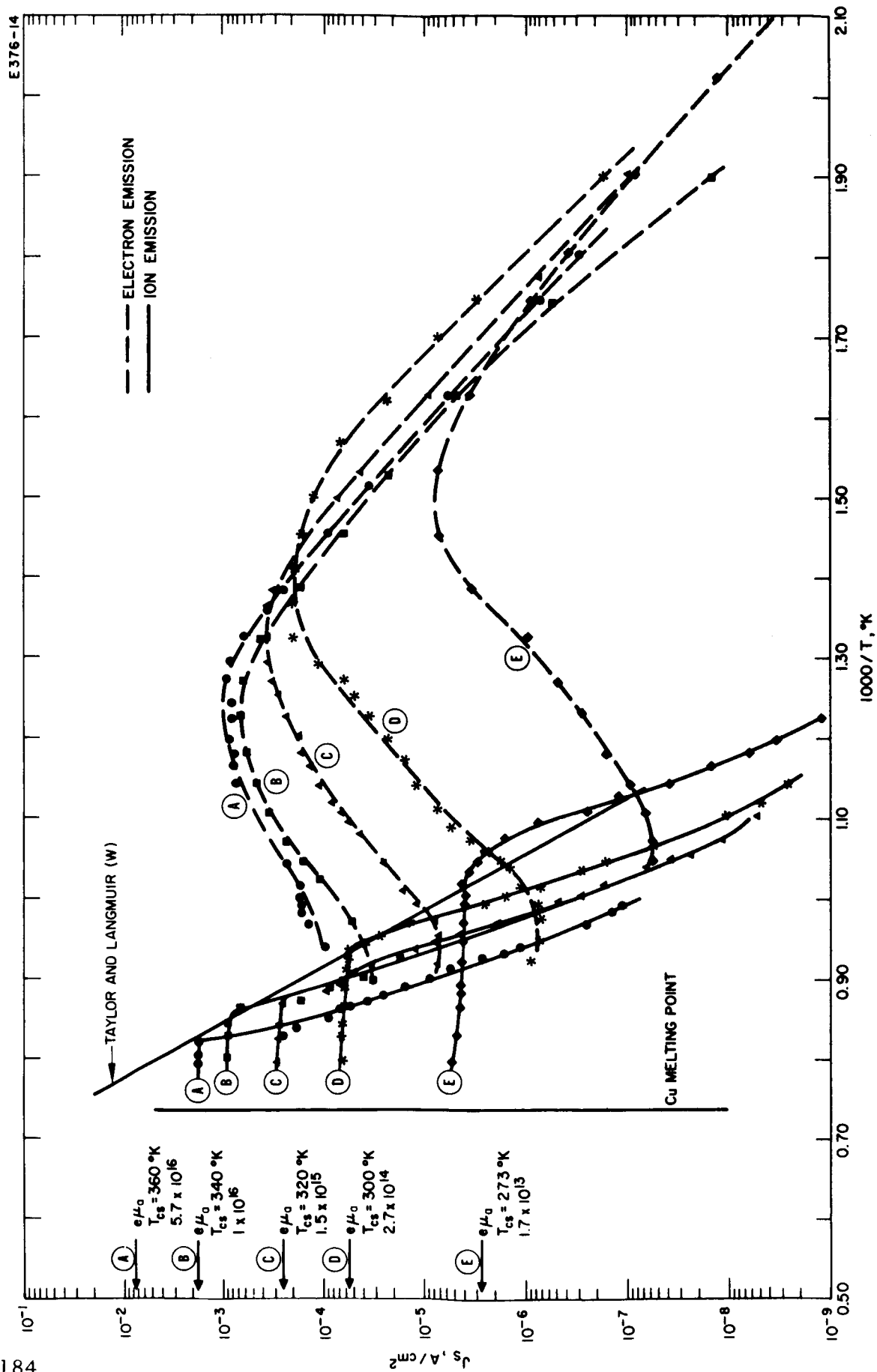


Fig. IV-57. Electron and ion emission characteristics for copper.

cesium ions) although little was previously known about its emission characteristics in a cesium environment. A ribbon of titanium metal was assembled into an ESE tube and directly heated to yield the results shown in Fig. IV-58. The vacuum emission work function is close to 4.1 eV, which differs only slightly from the published value of 3.95 eV. Most interesting, however, is its cesium ionization characteristics. It displays a lower critical temperature than all of the other materials tested, and its cesiated electron emission is nearly two orders of magnitude below copper for comparable operating conditions. On the other hand, at low temperatures, it reaches an effective work function below 1.5 eV. As a candidate accel electrode material, it would appear promising but, as mentioned above, it must be evaluated more thoroughly as to its influence on the ionization characteristics and sintering stability of porous tungsten ionizers.

9. Other Electrode Simulation Experiments

In addition to the material evaluations described above, the ESE tube experiments have been used to test additional aspects of engine operation. In one tube, the copper collector was equipped with a heater to permit simulation of drain currents expected with heated accel electrodes. The results did indeed show (as summarized in Fig. IV-59) that apparent drain currents can be dominated by the thermionic electron emission from the accel electrodes, hence the need for proper temperature of operation to suppress this emission. In the same experiment various potentials were applied to determine whether the ion emission level of a focus electrode surface was enhanced by the bombardment by electrons from the accel electrode and vice versa. To within the accuracy of our measurements, no enhancement was observed in the range from 40 to 4000 V ($\sim 10^4$ V/cm).

In one experimental tube an Al_2O_3 ionizing surface was subjected to sputtered copper material and its effect on ionization was observed. The surface never ionized to the level of metallic copper; however, its ionization was enhanced by a factor of two to five by prolonged sputtering

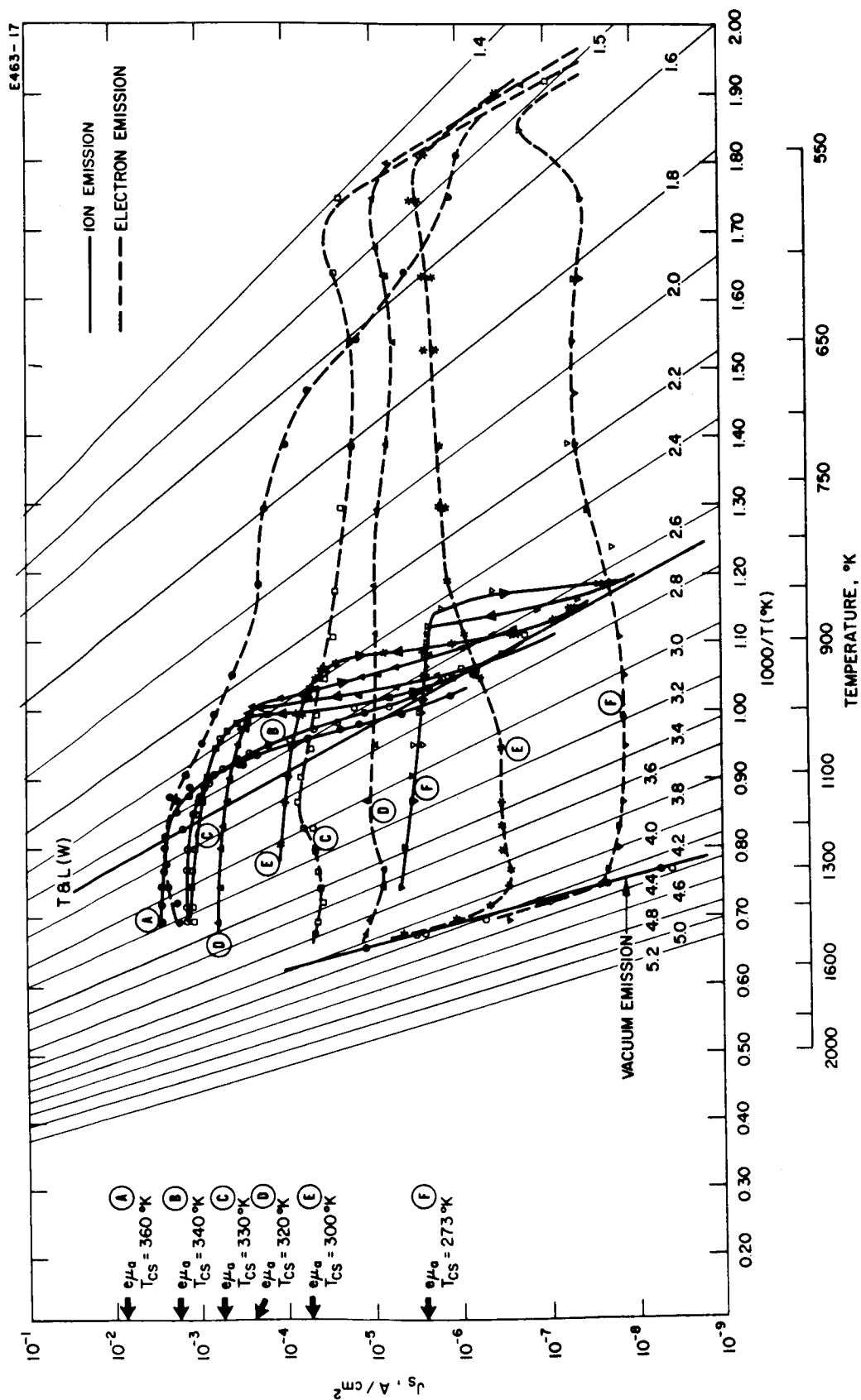


Fig. IV-58. Ion and electron emission characteristics of titanium.

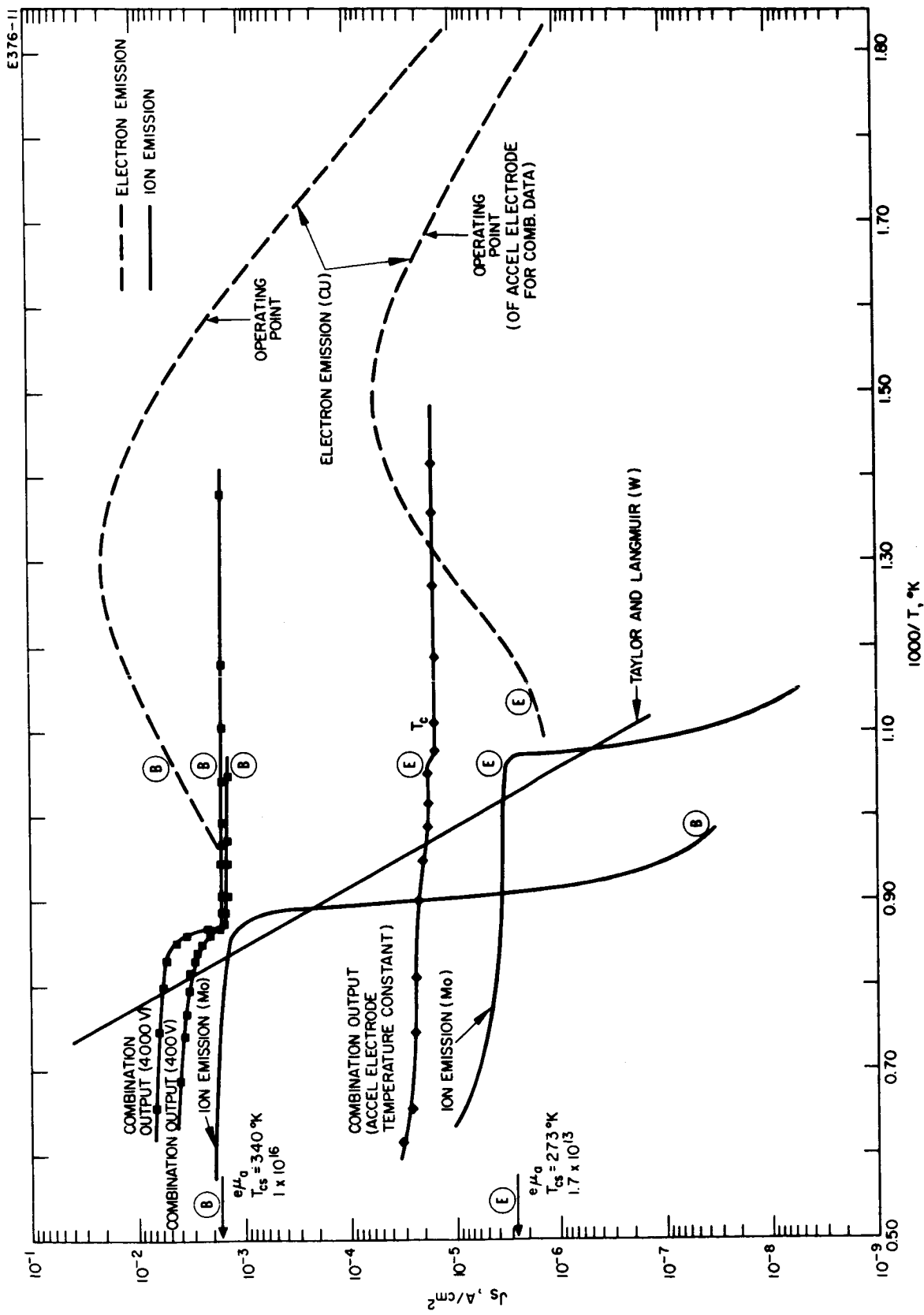


Fig. IV-59. Combination of electron and ion currents in heated accel electrode simulation. Accel biased negative with respect to focus for all curves.

(about 20 min at a copper arrival rate of approximately 10^{16} atoms/cm²-sec). This enhancement was seen to decay away at termination of the sputtering.

The technique of simulation of engine parts in a cesium vapor-filled tube has proven to be a useful tool in the understanding and analysis of ion engine operating characteristics.

E. Accel Drain Currents

The large drains observed in the first two test phases of engine 32-150-3, as well as those observed in the tests of the previous two engines, seem to originate from an accel electrode surface which greatly changes its characteristics with time. The most straightforward explanation is a time dependent decrease in the apparent surface work function of the accel electrode. Since accel temperature is constant with time, and the field at the accel surface does not change with time, a decreasing work function produces an increasing thermionic current. The time dependent surface changes could result from combinations of the following: buildup of a cesium dispenser type cathode on a roughened accel electrode, a cesium-oxygen-copper low work function surface, or field emission from a cesium-tungsten oxide coated accel electrode. The field has an important effect on determining the magnitude of the drains. Whatever the zero field value (determined by the condition of the surface), it may be increased almost an order of magnitude in the presence of a field.

Although field enhancement from a clean copper cesiated surface can account for the magnitude of the drain at the high accel temperatures, test data indicates a lack of correspondence between low accel temperature emission and the emission from a clean copper surface, even when the field is considered.

Analysis has shown that the electron current can be considerably reduced by the following:

1. reduction of the electric field in the region between the accel and focus electrode
2. reduction of the arrival rate of neutral cesium to the inter-accel-focus electrode region
3. reduction of the magnitude of the field enhancing effect on emission, of the surface of low work function contaminants, and of the surface coverage of cesium by increasing the accel electrode temperature.

One means of accomplishing the first two items is to remove the non-ion beam required portion of the accel electrode. The double optics accel configuration (NASA disclosure, November 1963) accomplishes this task. The third item is accomplished by operating the accel electrode at a high temperature. The opening in the accel electrode serves as a secondary optics system to eject unwanted ions originating from a high temperature focus electrode; in addition, the deletion of the central region of the accel electrode removes an unwanted collecting region for tungsten oxide, tungsten scales, cesium, and oxygen. These items enhance voltage breakdown between the focus and accel electrode. Figure IV-60 is an electrolytic tank trajectory plot of the accel system used in the last two phases of the test of engine 32-150-3. Figure IV-61 is the trajectory plot for the electrodes used in engine 32-150-4. These trajectories show only the ions and electron paths between electrodes. The main beam is not shown. The major difference in the trajectories lies in the reduction of the electron emitting area as well as in the ability of the optics to reject ions. The 32-150-4 system incorporates both factors. The sharp tips on the focus electrode of engine 32-150-4 reduce the ion density to the edge of the accel electrode by a factor of 15. The minimization of electron current to the focus, the ability to eject ions, and the reduced sensitivity to ions make the present version of the strip engine design more conservative. It is especially important to note that a controlled heat load to the focus electrode makes it feasible to control focus ions by temperature control. Recent tests have shown that the major heat

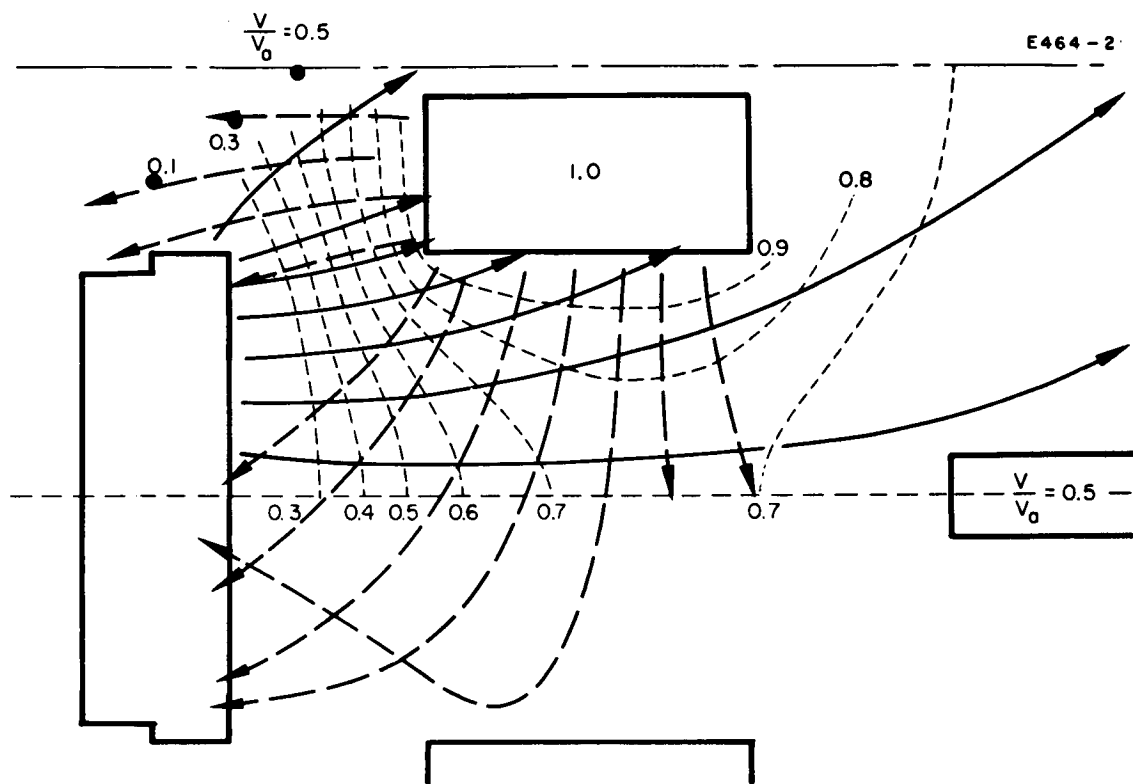


Fig. IV-60. Accel-focus electrode used in Phases 3 and 4 of engine 32-150-3. Ion and electron trajectories are shown for ions formed on the focus and electrons originating from the accel electrode.

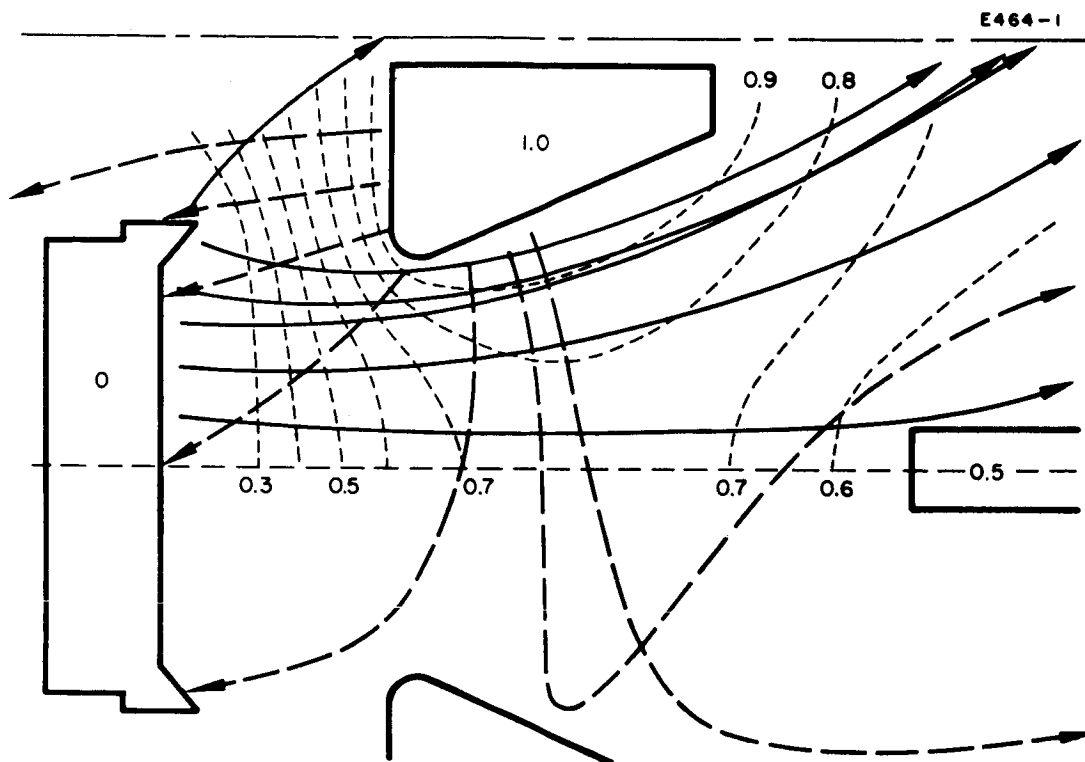


Fig. IV-61. Accel-focus electrode used in engine 32-150-4. Ion and electron trajectories are shown for ions formed on the focus and electrons originating from the accel electrodes.

load to the focus electrode is the electron component from the accel structure. Figure IV-62 shows the effect of accel drains and ionizer temperature on the method of heat rejection for the focus heat load. Low drains are important for this cooled focus type of engine in order to be able to reject the focus heat load without auxiliary heat transfer schemes. It is expected that the engines will operate with a drain factor between 0.3 and 1 mA/electrode.

A schematic of the double optics system is shown in Fig. IV-63. It may be observed that the accel area directly above the focus electrode no longer exists. Electron current is not completely eliminated from the region where the electrode is removed, since there is now emission from the inter-accel surface of the double optics electrodes. However, this inter-accel surface is exposed to an electric field which is considerably reduced from its value at the surface of a solid accel (see Fig. IV-64).

Thermionic emission from the accel surface is given by:

$$I = I_0 \exp\left(\frac{0.440 E^{1/2}}{T}\right) \text{ mA}$$

where

$I \equiv$ total thermionic current, mA

$I_0 \equiv$ zero field thermionic current, mA

$E \equiv$ field strength at the surface of emission, V/m

$T \equiv$ accel temperature.

(I/I_0) is plotted in Fig. IV-65 as a function of field from 0 to 10^5 V/cm, for various accel temperatures from 600 to 1000°K . The values of field for the two cases are:

$E = 10^5$ V/cm (normal field)

$E = 0.4 \times 10^5$ V/cm (reduced field at inter-accel surface).

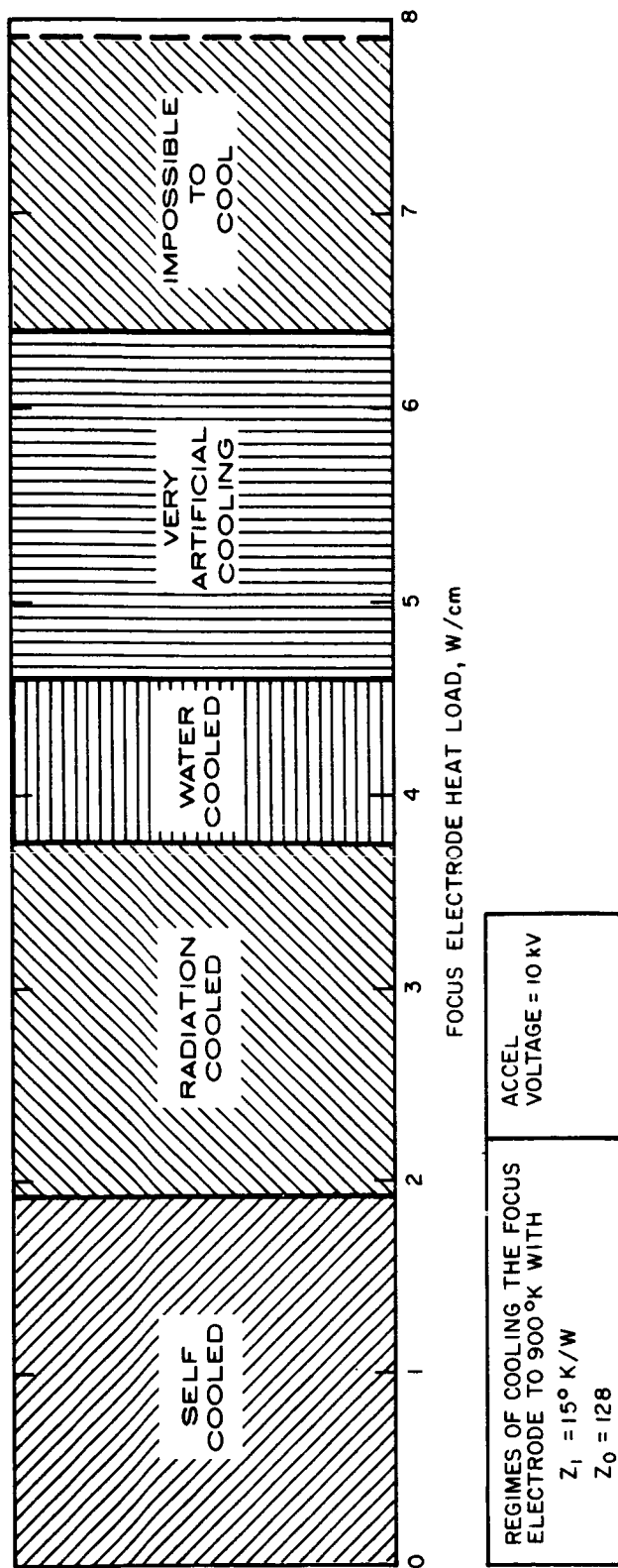
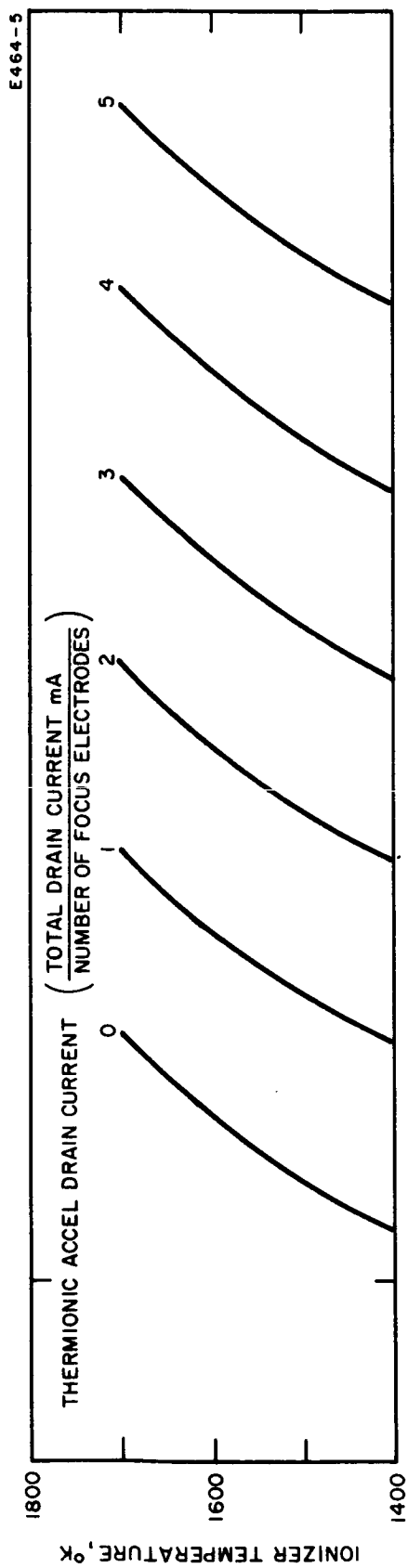


Fig. IV-62. Ionizer temperature-accel electron drain characteristic showing the methods of heat rejection required to maintain the focus electrode at 900 to 1000°K.

E410-8

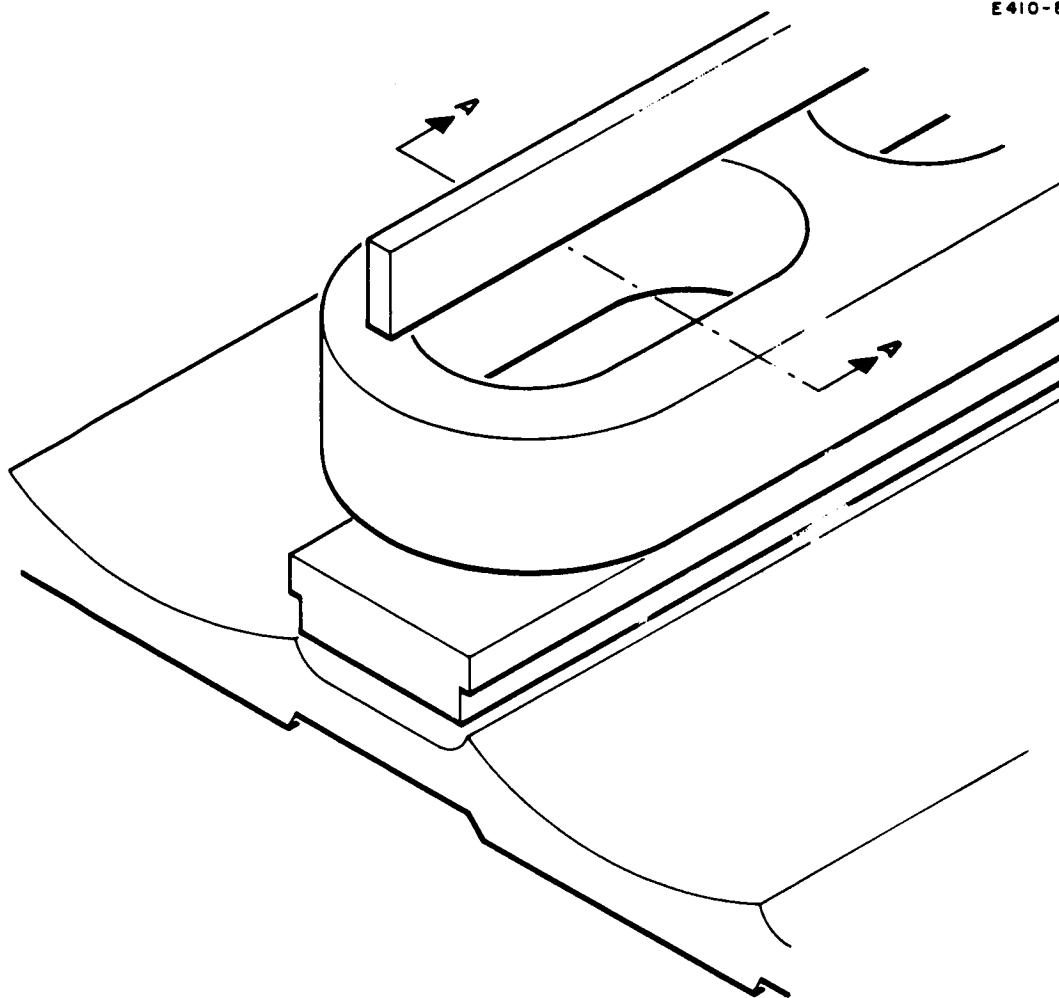
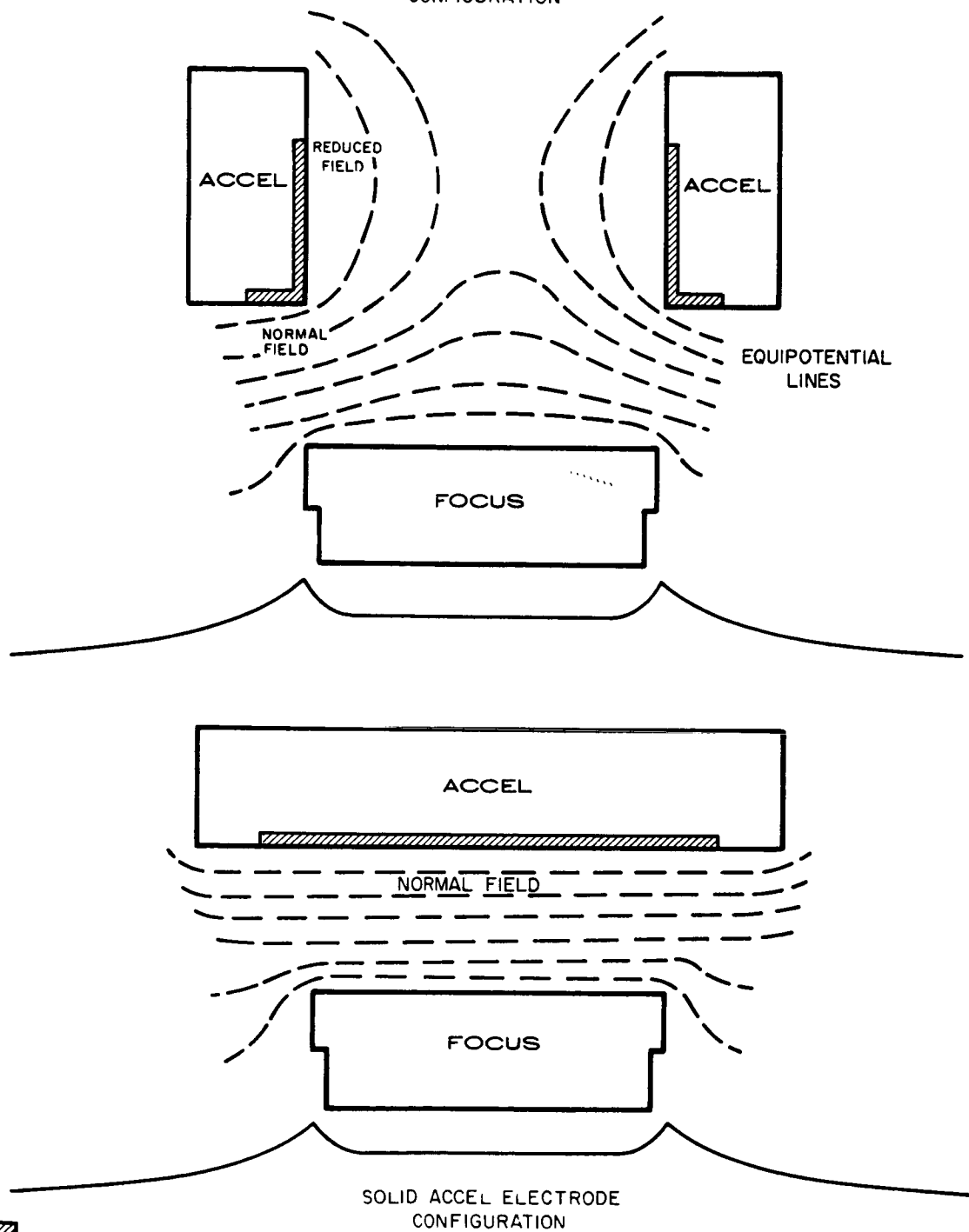


Fig. IV-63. Isometric view of double optics system.

DOUBLE OPTICS ELECTRODE CONFIGURATION

E464-8



INDICATES EMISSION REGION
OF ELECTRONS THAT ARRIVE AT FOCUS

Fig. IV-64. Conformal map showing the potential distribution between the accel and focus electrodes for both the conventional electrode shapes as well as for a form of the double optics system.

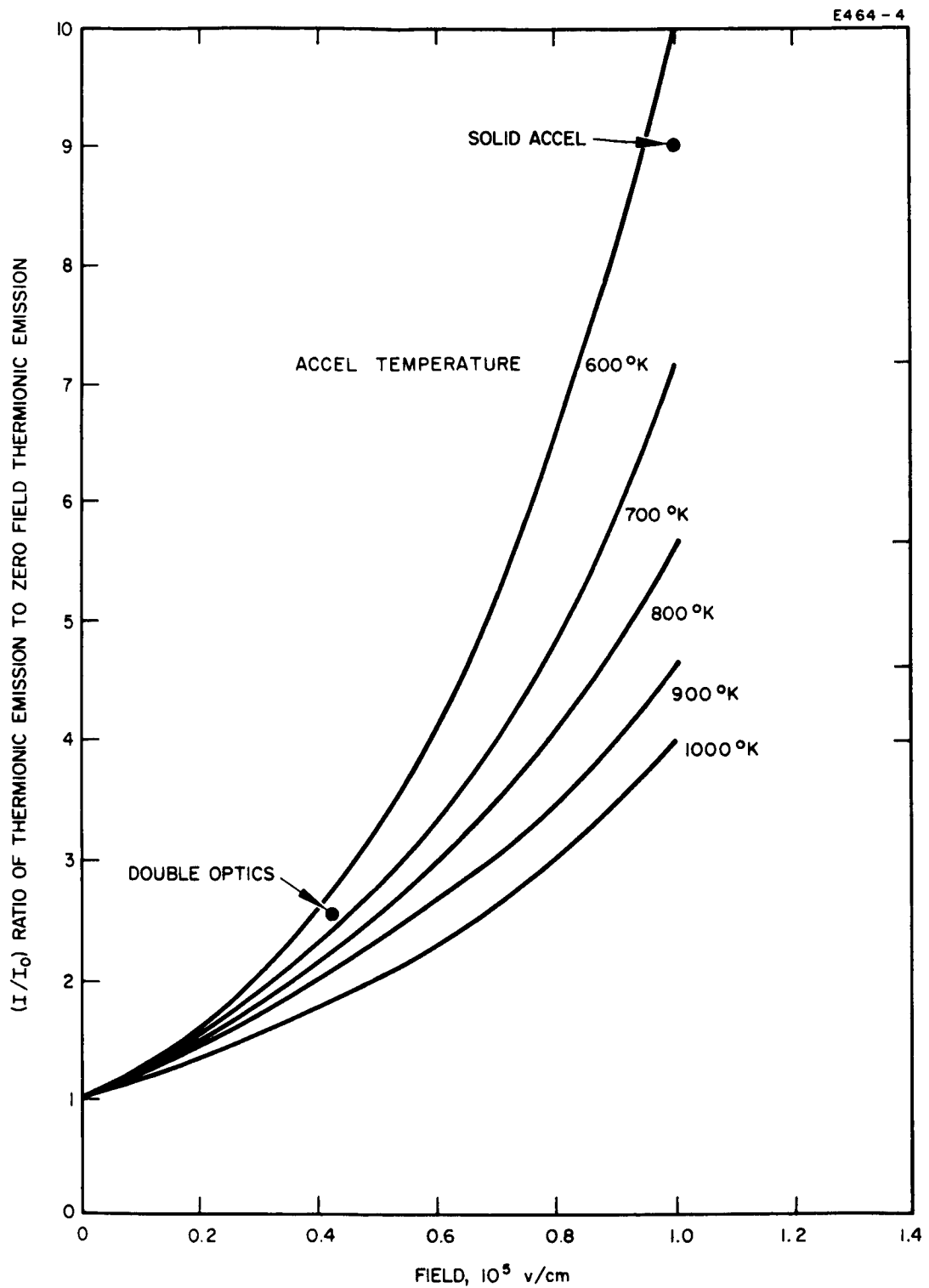


Fig. IV-65. Electric field effect on the thermionic emission for fields between zero and 10^5 V/cm. The curves also show the effect of temperature on the field enhanced emission.

These values are obtained from observation of the equipotential lines resulting from electrolytic tank studies (Model 70 optics and a voltage difference of 10^4 V between focus and accel electrodes). The accel temperature considered here corresponds to an ionizer temperature of 1450°K and is obtained from Fig. IV-46. These accel temperatures were measured on the 32-150-1 engine during thermal testing. Thus, $T = 625^\circ\text{K}$.

Using the above values of temperature and field, Fig. IV-65 gives the reduction in thermionic emission for the surface of reduced field:

$$I/I_0 = 9 \quad (\text{normal field})$$

$$I/I_0 = 2.5 \quad (\text{reduced field}).$$

The reduced-field portion of the double optics electrode has a thermionic current which is reduced by $2.5/9$ compared with the emission from a solid accel configuration. Of course, there is a portion of emitting area of the double optics accel which does not experience reduced field. In Fig. IV-64, it can be seen that three-quarters of the total accel surface emitting to the focus is subject to the reduced field. The over-all current reduction then is

$$\frac{I_{\text{double optics}}}{I_{\text{solid accel}}} = \frac{1}{4} + \left(\frac{2.5}{9}\right) \frac{3}{4} = 0.46 \quad .$$

Thus, the total accel current to the focus electrode is reduced by more than half, due to electric field effects alone.

The reduced neutral cesium arrival rate at the accel electrode (see Fig. IV-57) also reduces accel drain current. Cesium lowers the work function of the accel surface and produces higher thermionic current. The arrival rate of neutral cesium on the inter-accel surface has been calculated. The results (see Fig. IV-66) indicate that the neutral arrival rate is one-tenth the ionizer neutral evaporation rate. This is a factor of five less than the arrival rate for the center section of a solid accel structure (the value being one-half the ionizer evaporation rate).

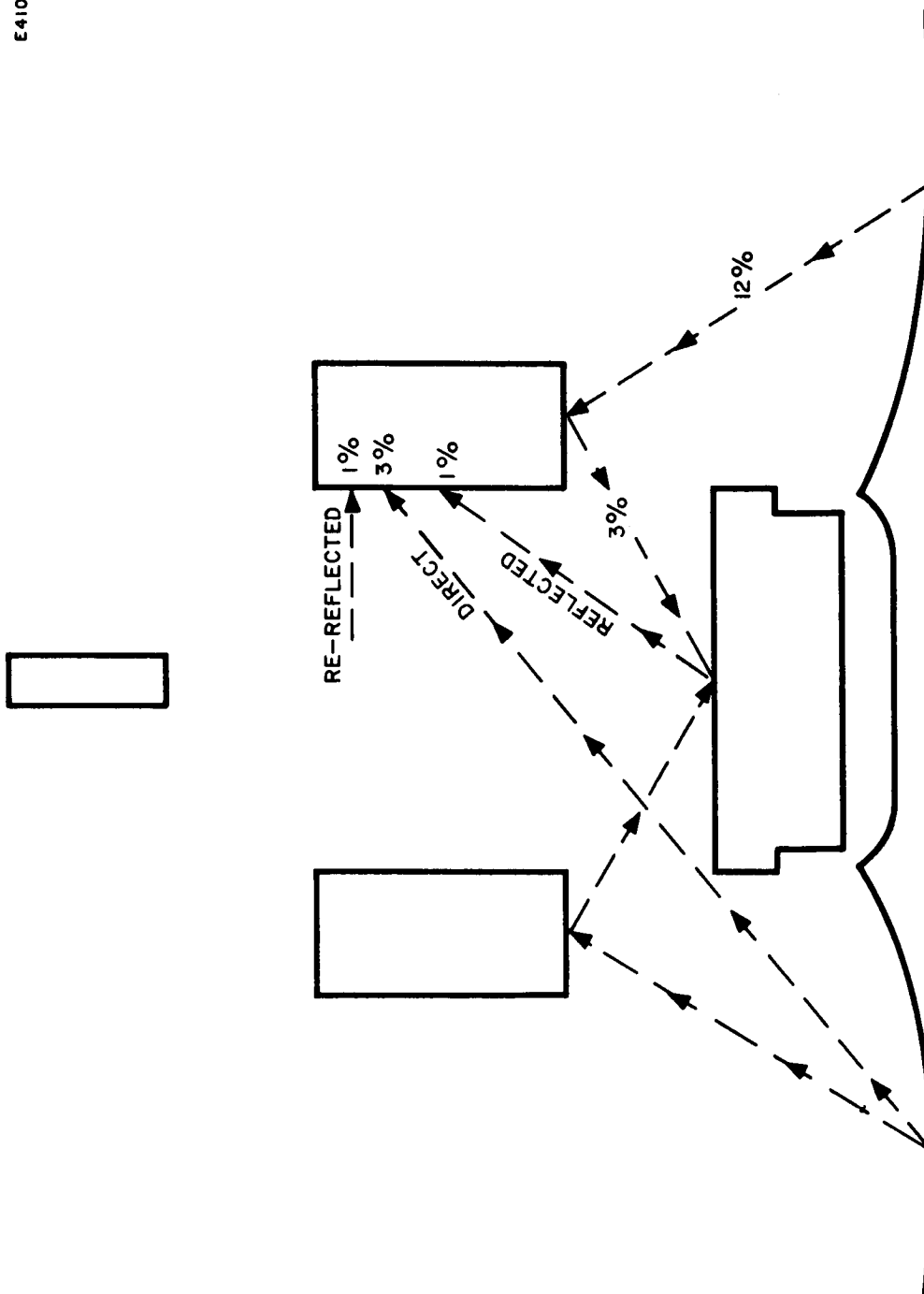


Fig. IV-66. Section A-A (see Fig. IV-63) of double optics system showing the arrival rate of particles from the ionizer surface to the focus and accel electrode.

A final effect which reduces accel drains is the reduction of tungsten deposits on the inter-accel surface of a double optics electrode, as opposed to the center section of a solid electrode. Tungsten depositing on the accel surface may cause spiked regions which create higher fields. A similar analysis for the cesium arrival rate shows that the tungsten deposition is also down by a factor of five.

The cesium arrival and tungsten deposition effects can only benefit the inter-accel area. This area represents three-quarters of the total area which emits electrons to the focus electrode. At higher accel temperatures (such as 1000°K), a factor of five reduction in arrival rate will result in a factor of 10 reduction in electron current from a clean surface (see Fig. IV-57). The emission from the inner accel region will thus be reduced essentially to zero. The 25% remaining current, with the accel operating at 1000°K instead of 625°K , will cause a further decrease by a factor of $4/9$. Thus the accel current will be approximately one tenth its value without both field and temperature effects.

The zero field electron emission data (Fig. IV-57) have been adjusted for an electric field of 10^5 V/cm and are presented with accel drain-accel temperature data for engine 32-150-4 in Fig. IV-67. The engine data show some correlation with field enhanced clean copper data at the higher accel temperature. The time dependent increase in drains was eliminated in the test of engine 32-150-4. Although the exact surface change which occurred is not understood, the increase in accel temperature in conjunction with the open accel structure seems to have had the effect of reducing the drain magnitude as well as the sensitivity of the system to the phenomenon which caused the time dependent apparent change in work function. Further information on the test of engine 32-150-4 is presented in Section III-C of this report.

F. Ionizer Manifold Pressure Distribution

The cesium pressure distribution in the manifold of ion engine 2018-150-1 has been studied. There should be little deviation in pressure from one point to another, since mass flow rate through the porous

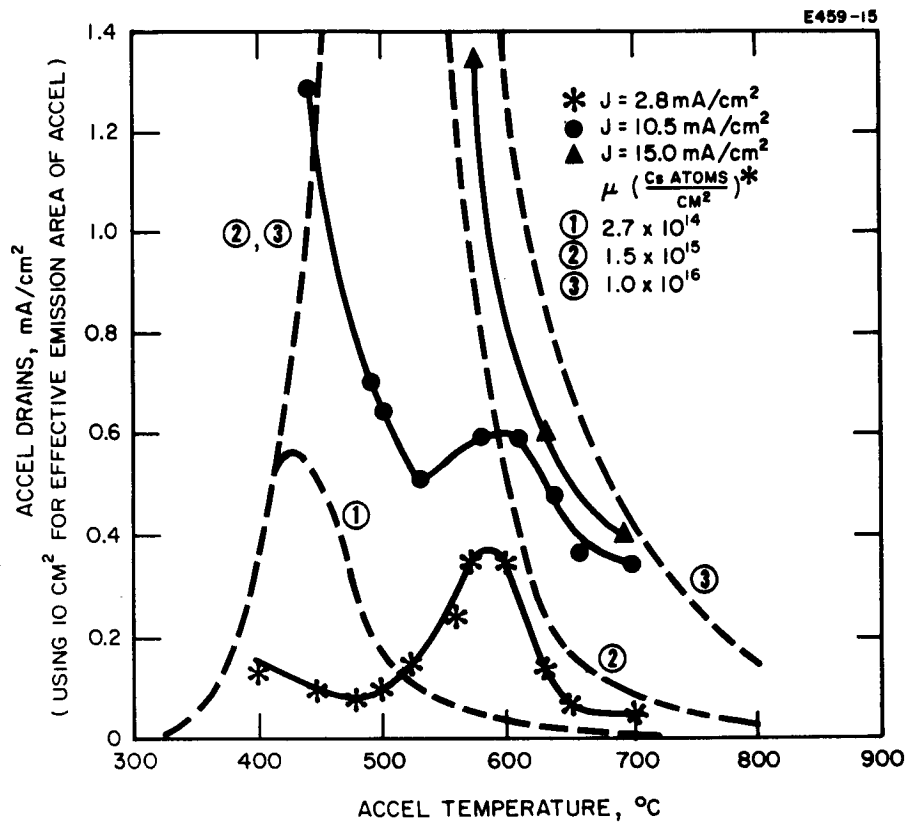


Fig. IV-67. Linear plot of clean copper current density versus temperature. Also presented is the experimental accel current density versus accel temperature for engine 32-150-4. The clean copper data have been corrected for Schottky effects for an electric field of 10^5 V/cm .

tungsten is directly proportional to the pressure behind it. Analytical results indicate that the transmission coefficient τ (ratio of atoms per square centimeter per second transmitted to those arriving) exhibits a critical effect in determining whether a large or small pressure deviation exists across the back of the ionizer. The nature of the flow is such that a low transmission coefficient ($\tau < 10^{-4}$) produces the desirable result of little pressure deviation. On the other hand, a high transmission coefficient ($\tau > 10^{-3}$) produces large differences in static pressure behind the ionizer. At $\tau = 10^{-4}$, the pressure deviation is almost undetectable. When increased transmission produces $\tau = 4 \times 10^{-4}$, the pressure deviation is up to 1%. Increasing transmission from this point on produces striking results. At $\tau = 6 \times 10^{-4}$, the deviation is 2% and at $\tau = 10^{-3}$, 5%. If the transmission becomes as high as 2.5×10^{-3} , the pressure deviation will be 25%. These figures correspond to a current density of 15 mA/cm^2 . At lower flow rates, the deviation is even worse (refer to Fig. IV-68).

The foregoing results may be obtained from Figs. IV-69 and IV-70. Figure IV-69 shows how the manifold pressure requirement decreases for increasing transmission coefficient. Figure IV-70 shows how the pressure deviation in the manifold increases as the pressure itself decreases. In this effect, a constant pressure differential is required to drive the cesium gas from the feed tube to the remote regions of the manifold. When the static pressure of the incoming gas is high, the driving differential represents a very small contribution, and the percentage pressure deviation is small. However, when the incoming gas pressure is low, the constant pressure differential begins to represent a considerable portion of the total pressure and hence produces a large percentage deviation.

Therefore, it is desirable (from the standpoint of producing even flow over the ionizer) to have a high static pressure in the ionizer manifold (at least 5 Torr) to keep the deviation below 0.5%. By definition, the requirement for high manifold pressure establishes a requirement for low transmission coefficient, since the cesium flow rate through the

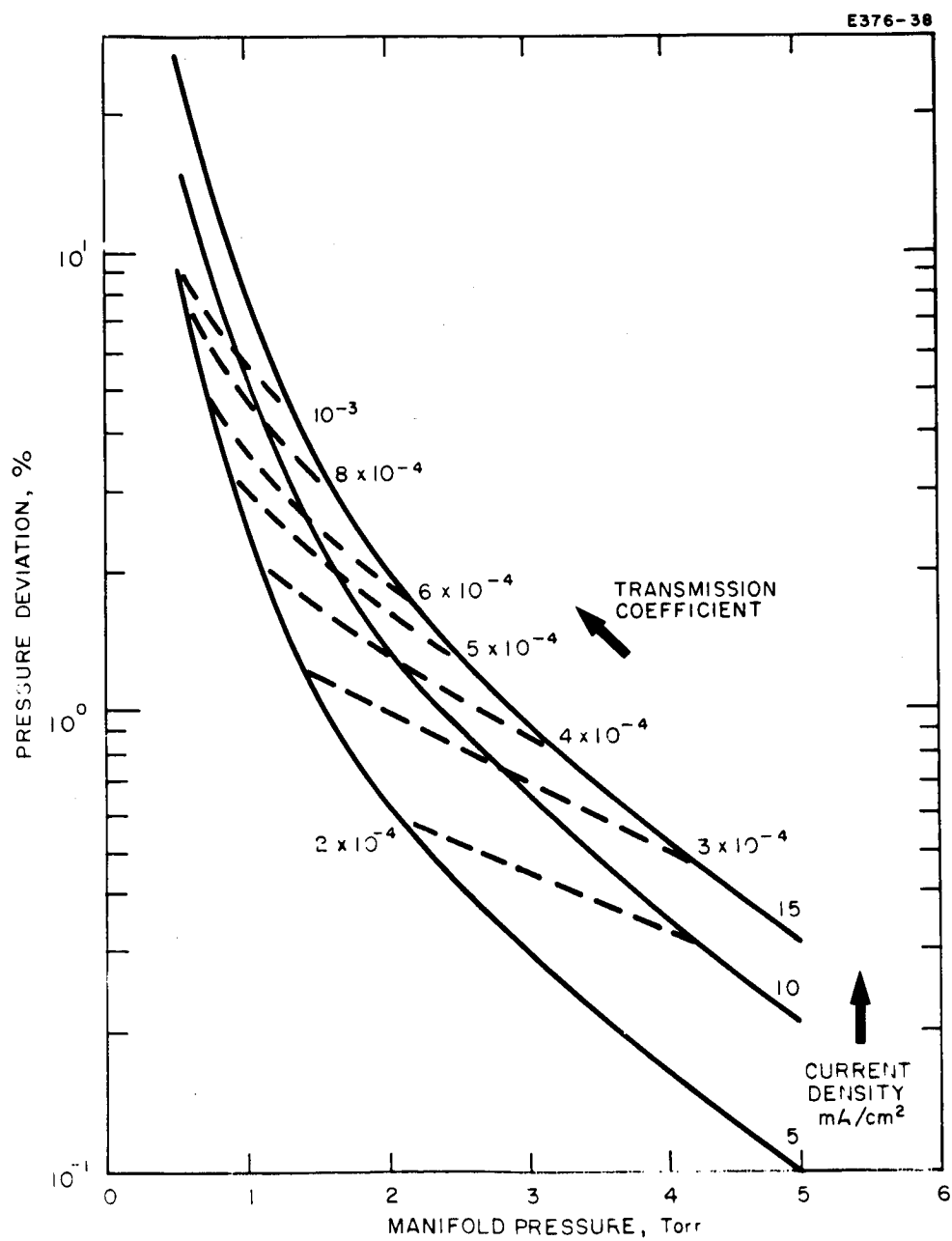


Fig. IV-68. Ionizer manifold pressure deviation as a function of transmission coefficient and current density. Engine No. 2018-150-1.

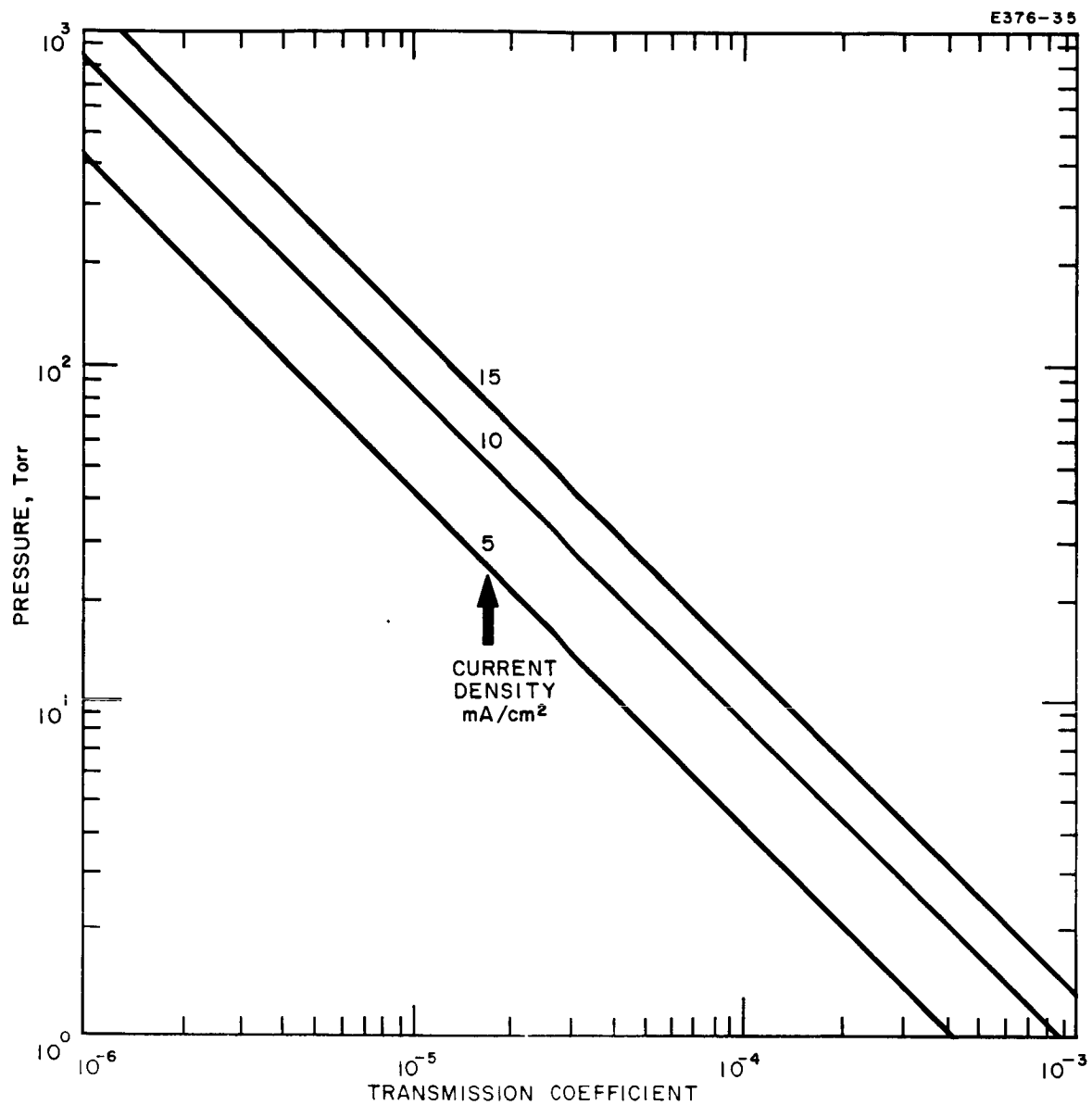


Fig. IV-69. Ionizer manifold pressure requirement for various current densities.

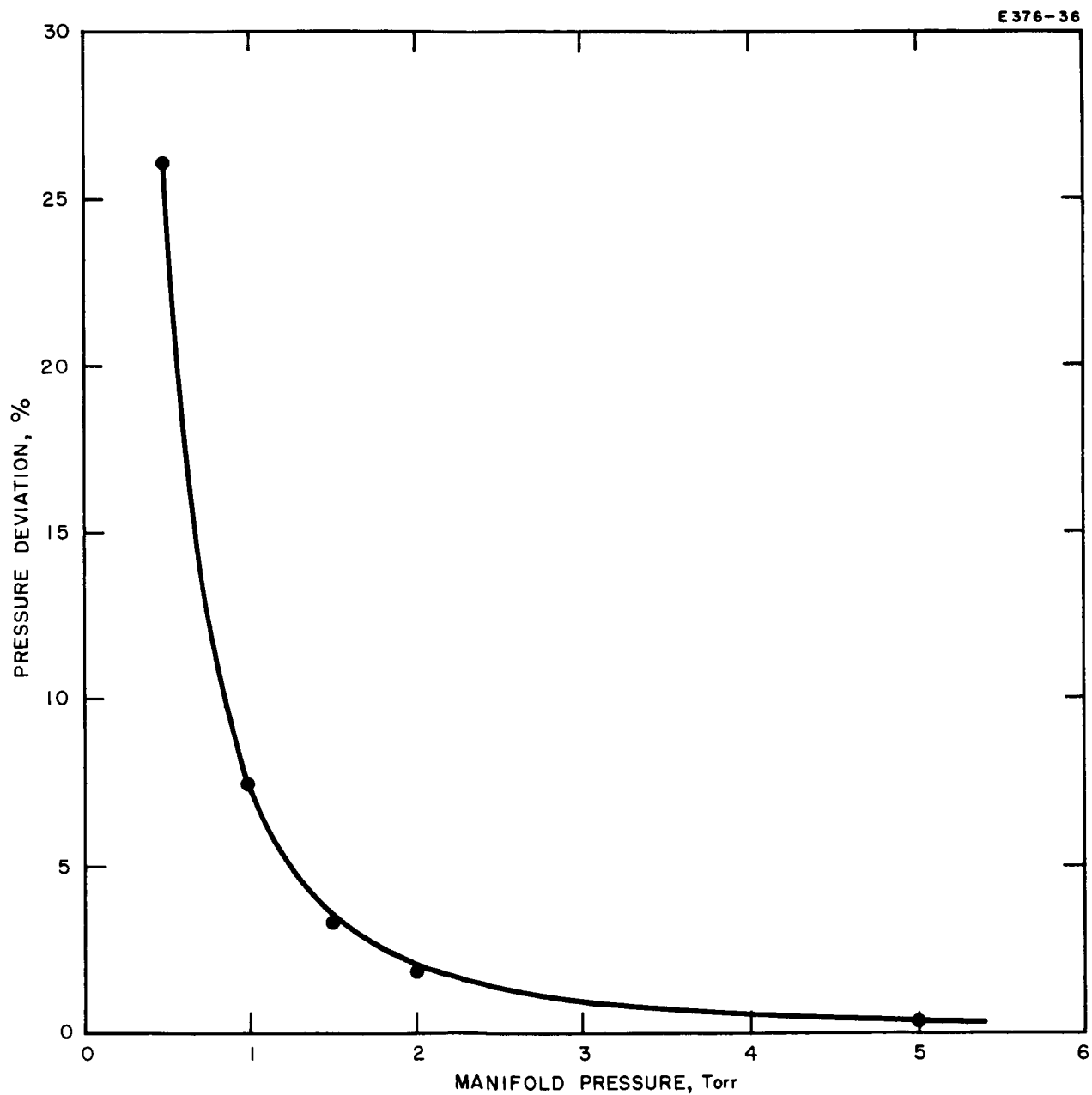


Fig. IV-70. Ionizer manifold pressure deviation for 2018-150-1 engine at design current density of 15 mA/cm^2 (or 10^{-3} g/sec).

ionizer must be the same in either case. These results are based on a cesium flow rate of 10^{-3} g/sec, which is that required to produce 15 mA/cm² ion current density over a total surface area of 54.6 cm². The ion flux for a 15 mA/cm² current density is 0.94×10^{17} ions/cm²-sec. The total mass flow rate of cesium is 10^{-3} g/sec.

The transmission coefficient and pressure are related by the expression

$$\phi = \left(\frac{1}{2\pi mkT} \right)^{1/2} \tau P \quad . \quad (IV-16)$$

$$\phi \equiv \text{ion flux} = 0.937 \times 10^{17} \text{ ions/cm}^2\text{-sec}$$

$$\tau \equiv \text{transmission coefficient}$$

$$m \equiv \text{mass of cesium atom} = 22.1 \times 10^{-23} \text{ g}$$

$$k \equiv \text{Boltzmann constant} = 1.38 \times 10^{-23} \text{ J/}^\circ\text{K}$$

$$T \equiv \text{manifold temperature} = 1700^\circ\text{K}$$

$$P \equiv \text{manifold pressure (average), dynes/cm}^2 \quad .$$

Evaluating (and converting P into Torr),

$$P = (1.27 \times 10^{-3}) \frac{1}{\tau} \text{ (Torr)} \quad . \quad (IV-17)$$

Figure IV-70 is a plot of this relationship (the 15 mA curve). For a transmission coefficient of 10^{-4} , the manifold pressure will be 13 Torr at the rated current density of 15 mA/cm. For a transmission coefficient of 10^{-3} , the pressure will only be 1.3 Torr.

We now calculate the manifold pressure drop. Figure IV-71 indicates how the flow distribution occurs in the 2018-150-1 manifold. The flow enters at the center from the feed tube and splits into equal halves. Two-tenths of the flow is immediately consumed by the initial ionizer strips which are adjacent to the feed tube entrance. The flow has conveniently been divided into tenths, since there are 10 separate gas

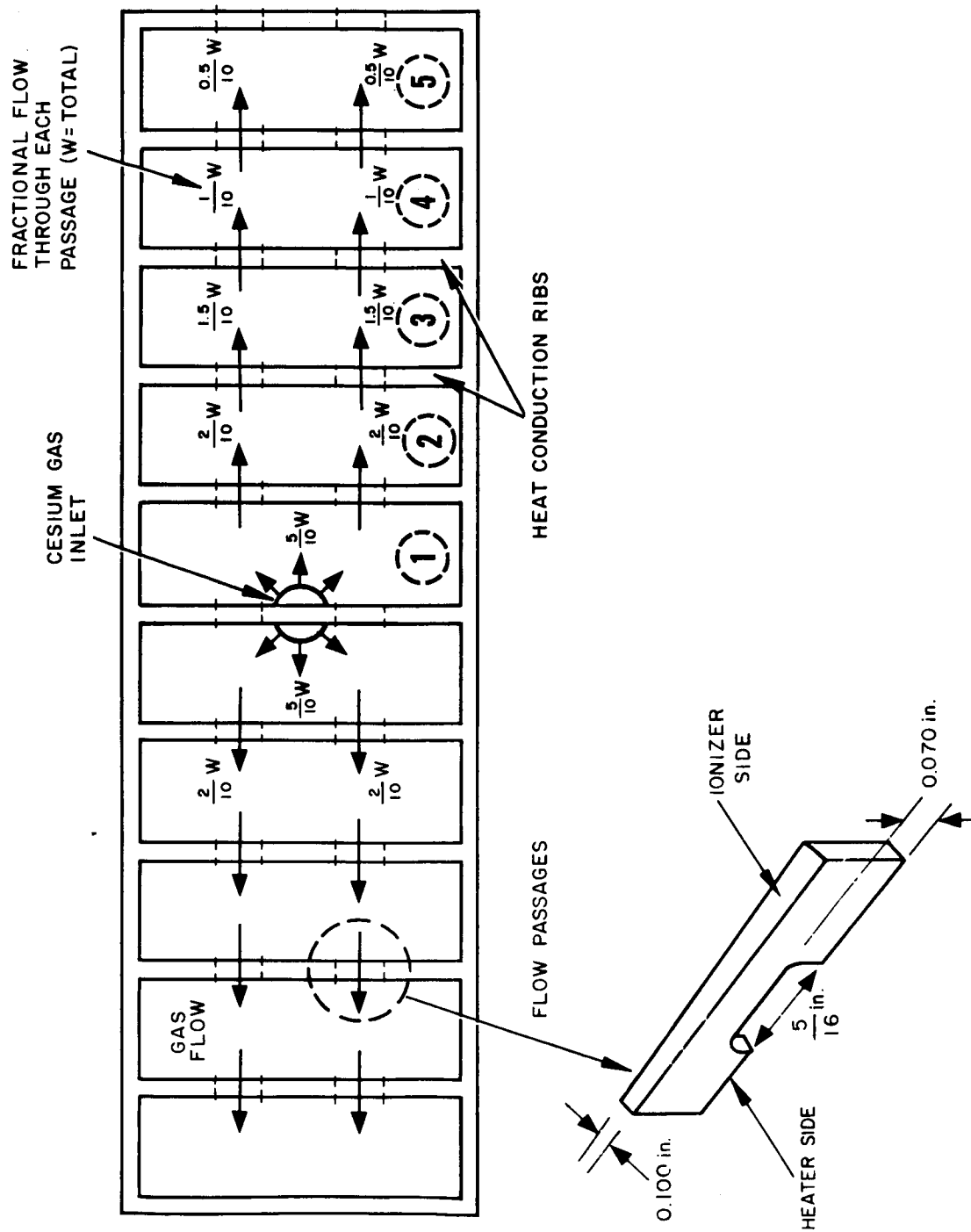


Fig. IV-71. Engine No. 2018-150-1 manifold.

plenums (each feeding two ionizer strips) connected by flow passages. The pressure drop occurs in these flow passages, which appear as restrictions to the gas movement. As the gas moves from the central plenum to the end plenum, the flow rate across each subsequent flow passage is diminished by half a tenth. The tenth is used because each plenum consumes a tenth the flow, and the half is used because there are two passages between each plenum.

Each passage is now treated as a short, rectangular duct.

$$W = \frac{1}{1 + \beta} \left(\frac{1}{64} \right) \left(\frac{D^2 A}{l} \right) \frac{P_u^2 - P_d^2}{\eta R T} \quad , \quad (IV-18)$$

where

$$\beta \equiv \text{short tube factor} = \frac{5620}{T^{1/2}} \frac{W}{l} \approx 0.14$$

$$\eta \equiv \text{viscosity of cesium vapor} = 0.807 \times 10^{-5} T^{1/2} \frac{\text{dyne-sec}}{\text{cm}^2}$$

$$D \equiv \text{hydraulic diameter} = \frac{4 \times \text{cross-sectional area}}{\text{circumference}}$$

$$A \equiv \text{cross-sectional area of duct, cm}^2$$

$$l \equiv \text{length of duct}$$

$$R \equiv \text{cesium gas constant} = 6.25 \times 10^5 \text{ ergs/cm}^2\text{K}$$

and P_u and P_d are the upstream and downstream pressures, respectively (dyne/cm²).

The dimensions of the duct are as follows:

$$a = 0.070 \text{ in.} = 0.178 \text{ cm}$$

$$b = 5/16 \text{ in.} = 0.795 \text{ cm}$$

$$l = 0.100 \text{ in.} = 0.254 \text{ cm} \quad .$$

The geometrical portion of eq. (IV-18) is readily evaluated:

$$A = ab = (0.178)(0.795) = 0.141 \text{ cm}^2$$

$$D = \frac{4A}{2(a+b)} = \frac{(2)(0.141)}{(0.973)} = 0.291 \text{ cm}$$

$$\frac{D^2 A}{l} = \frac{(0.291)^2 (0.141)}{(0.254)} = 0.0471 \text{ cm}^3$$

Equation (IV-18) becomes (also converting P into Torr),

$$W = \frac{(0.0471)(1333)^2}{(1.14)(64)(0.807 \times 10^{-5})(6.25 \times 10^5)} \frac{P_u^2 - P_d^2}{(1700)^{3/2}}$$

$$W = (3.25 \times 10^{-3})(P_u^2 - P_d^2) \text{ g/sec} \quad (\text{IV-19})$$

Equation (IV-19) thus gives the relationship between the upstream and downstream pressures across a restriction with known flow rate:

$$P_u^2 = P_d^2 + \frac{W}{3.25 \times 10^{-3}} \quad (\text{IV-20})$$

The total pressure deviation is obtained by using a relation between the incoming gas pressure and the gas pressure at the most remote regions of the manifold (four restrictions downstream). The flow schematic is demonstrated in Fig. IV-71. The plenums are numbered 1, 2, 3, 4, and 5. Then,

$$P_1^2 = P_2^2 + \frac{(2/10)W}{3.25 \times 10^{-3}} \quad (\text{IV-21a})$$

$$P_2^2 = P_3^2 + \frac{(1.5/10)W}{3.25 \times 10^{-3}} \quad (\text{IV-21b})$$

$$P_3^3 = P_4^2 + \frac{(1/10)W}{3.25 \times 10^{-3}} \quad (\text{IV-21c})$$

and

$$P_4^2 = P_5^2 + \frac{(0.5/10)W}{3.25 \times 10^{-3}} \quad (\text{IV-21d})$$

Solving the above set for P_1 in terms of P_5 results in the relation for total pressure deviation

$$P_1^2 = P_5^2 + \frac{1}{3.25 \times 10^{-3}} \left(\frac{2}{10} W + \frac{1.5}{10} W + \frac{1}{10} W + \frac{0.5}{10} W \right)$$

$$P_1^2 = P_5^2 + \frac{1}{3.25 \times 10^{-3}} \left(\frac{5}{10} W \right) \quad (\text{IV-22})$$

For a flow rate of 10^{-3} g/sec,

$$P_1^2 = P_5^2 + 0.154 \quad (\text{IV-23})$$

The ratio of the highest pressure in the system to the lowest pressure in the system is:

$$\left(\frac{P_1}{P_5} \right) = \left(1 + \frac{0.154}{P_5^2} \right)^{1/2} \quad (\text{IV-24})$$

The percent deviation is

$$\% = \frac{(P_1/P_5) - 1}{100} \quad (\text{IV-25})$$

Figure IV-70 is a plot of eq. (IV-19).

It was indicated earlier that a flow rate lower than that required for the 15 mA/cm^2 rated current density would produce a higher pressure deviation. This effect is shown by plotting on the same graph the curve in Fig. IV-70 together with curves for other flow rates. This is done in Fig. IV-68. The operational curve for an engine (i.e., the curve defining pressure deviation versus flow rate with all physical parameters fixed) is a line of constant transmission coefficient. Thus, lines of constant transmission coefficient have been superimposed on the constant flow rate plots. The intersection of a line of constant transmission coefficient with one of constant flow rate gives the pressure deviation for that condition, without reference to manifold pressure. Manifold pressure is eliminated as a variable in determining pressure deviation. This is desirable since manifold pressure is not controllable anyway, but is implicitly determined by transmission coefficient and flow rate. In Fig. IV-68, a line of constant τ intersects diminishingly lower flow rate curves at increasingly higher values of pressure deviation. Table IV-2 shows the low flow phenomena for typical values of transmission coefficient.

TABLE IV-2

Flow Rates for Typical Transmission Coefficient Values

τ	Current Density, mA		
	15	10	5
3×10^{-4}	0.5%	0.7%	1.2%
5×10^{-4}	1.2	1.9	3.5
8×10^{-4}	2.9	4.2	8.8
10^{-3}	4.3	6.6	12.0

G. Test Environment and Apparatus

1. Comparison of Pump Oils

In a continuing effort to prevent contamination of the ionizers by operating environments, a number of changes were made in the vacuum systems used for long duration tests. As a result, ionizer characteristics have significantly improved, indicating that the rate of contamination is now quite low. It is difficult, however, to determine the relative contribution to the improvement attributable to each change.

An important factor in reducing carbon contamination is undoubtedly the substitution of the silicone oil D.C. 705 for Convoil 20. At 25°C, the vapor pressure of D.C. 705 is 3×10^{-10} compared with Convoil 20's 2×10^{-7} Torr. Thermal breakdown products of the mineral oil type Convoil 20 produces a myriad of fragments up to 400 in molecular weight. The principal D.C. 705 breakdown product is a mass 77 phenyl group in much less abundance. Since the D.C. 705 has more thermal resistance, it does not load baffles and cryotrap with breakdown products as fast. The operating time until breakthrough is greatly extended. With a well trapped system, carbon fragments with masses less than 44 can be kept below 10^{-13} Torr for periods exceeding 28 days. After breakthrough, the lower amount of breakdown products of D.C. 705 and lower vapor pressure of D.C. 705 will cause less contamination in the vacuum chamber.

In kinetic vacuum systems, measurements of backstreaming and other contaminants are difficult to make quantitatively, but in the presence of bombarding electrons on surfaces, deposition of a polymerized organic layer as thick as $1700 \text{ \AA}/\text{sec}$ has been measured in the presence of rubber gaskets, vacuum grease, and diffusion pump oil (Ref. IV-10). By the use of a diffusion pump oil such as D.C. 705, proper greases, gaskets, and cryotrapping, this deposition can be reduced to as low as $10 \text{ \AA}/\text{sec}$.

Where it is necessary to use grease in the system, we are now using a new Apiezon Grease L as a replacement for the higher vapor pressure Apiezon M. Viton rubber was substituted for buna as rapidly as replacement O-rings are received.

Another major source of contamination is the system walls themselves. These are very difficult to clean or bake out because of the large areas and size of the tanks. Vacuum baking is also not readily performed. To compensate for this, extensive liquid nitrogen cryo-trapping is used over the tank walls. The engine mount is completely shielded from the diffusion pump inlet by a cold finger about 6 ft, 2 in. in area. A liquid nitrogen cooled coil protects the mounting and electrical components between the mounting flange (tank end) and the engine mount. To protect the system further, a liquid nitrogen baffle is operated over the diffusion pump at all times.

Ionizer contamination by engine components themselves is being minimized by the thorough decontamination and cleaning procedures carried out under the engine materials program.

2. Sputtered Material from Collector

a. Collector Configuration - A calculation has been performed to aid in evaluating the relative merits of various collector configurations. The type of collector considered here is a copper surface that intercepts the ion beam. Impingement of high energy particles produces sputtering of the collector material. Therefore, the criterion for evaluating various collector configurations is to select a configuration which returns the least sputtered material to the ionizer surface.

The sputtering is assumed to occur in a cosine distribution, in the same manner as thermal radiation. Hence, the two important variables in collector positioning are (see Fig. IV-73):

1. sine of the inclined angle α
2. inverse square of distance r .

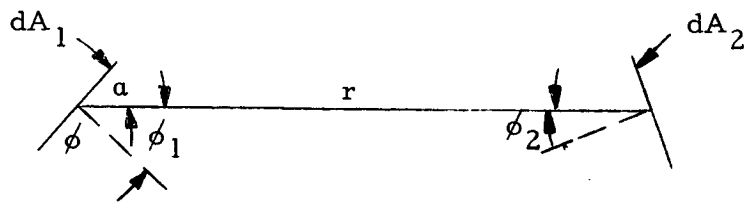


Fig. IV-72. Illustration of terms used in expression for view factor (see eq. (IV-26)).

The exact expression for the view factor F_{12} from an infinitesimal area dA_1 radiating to an infinitesimal area dA_2 at a distance r is:

$$F_{12} = \frac{\cos \phi_1 dA_2 \cos \phi_2}{\pi r^2} \quad (\text{IV-26})$$

where ϕ_1 and ϕ_2 are the angles between the normals of the surface and the line joining them. The view factor F_{12} is defined as the fraction of radiation (or particles) leaving dA_1 which is intercepted by dA_2 .

If the dimensions of a radiating and receiving area are small compared with the distance between them ($A_1, A_2 \ll r^2$) then (IV-26) may be used in its raw form, without integrating over the surfaces.

$$dA_2 \rightarrow A_2 \quad .$$

Taking A_2 as the ionizer surface,

$$\phi_2 = 0 \quad .$$

Since α is the inclined angle,

$$\alpha = (90 - \phi_1) \quad .$$

Equation (IV-26) becomes

$$F_{12} = \frac{A_2}{\pi r^2} \sin \alpha \quad . \quad (IV-27)$$

In the ionizer-collector problem, eq. (IV-27) is valid for the case where the beam spread over the collector surface is small compared with the distance between collector and ionizer. Within the geometrical constraints of a typical vacuum tank, this case is valid for:

1. A single surface which is not inclined ($\alpha \cong 90^\circ$), since the distribution of the beam over the collector surface does not become large compared with ionizer-collector distance.
2. A series of separate, closely spaced surfaces which may be inclined at very small angles without the distribution over any one surface becoming excessive. (This is later referred to as the multiple wedge case.)

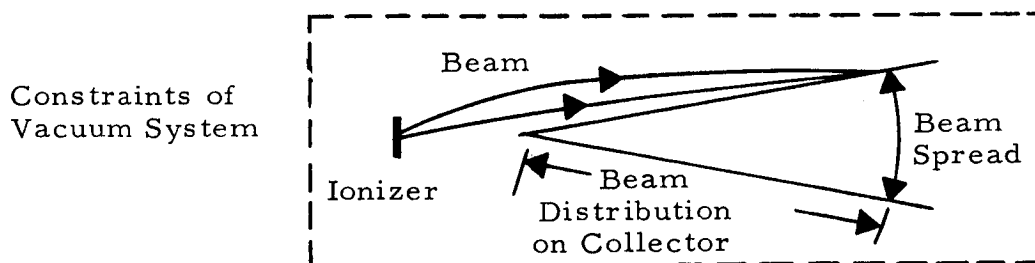


Fig. IV-73. Illustration of how beam is distributed on the collector due to beam spread.

However, the beam distribution will be large for a single surface collector at a small inclined angle (see Fig. IV-74). The equation describing this situation may be derived by integrating (IV-27) over the distributed area of the wedge:

$$F_{12} = \frac{\sin \alpha}{\pi} \left(\frac{A_2}{A_1} \right) \int_{r_1}^{r_2} \frac{dA_1}{r^2} \quad (\text{one side})$$

$$dA_1 = h \, dr \quad (h \equiv \text{dimension into paper})$$

$$A_1 = h(r_2 - r_1)$$

$$F_{12} = \left(\frac{\sin \alpha}{\pi} \right) \frac{A_2}{h(r_2 - r_1)} \int_{r_1}^{r_2} \frac{h \, dr}{r^2}$$

$$F_{12} = \left(\frac{\sin \alpha}{\pi} \right) \frac{A_2}{r_2 - r_1} \left[\frac{1}{r_2} - \frac{1}{r_1} \right] = \left(\frac{\sin \alpha}{\pi} \right) \frac{A_2}{r_1 r_2} \quad (\text{IV-28})$$

The resulting expression indicates that the distributed area problem is analogous to the infinitesimal area problem, with r^2 replaced by $r_1 r_2$, a "mean" distance between ionizer and collector.

Equations (IV-27) and (IV-28) may be put on a per unit area basis by dividing both sides by A_2 .

$$\frac{F_{12}}{A_2} = \frac{\sin \alpha}{\pi r^2} \quad (\text{IV-29})$$

This equation is plotted in Fig. IV-74. The result covers both cases, the infinitesimal and the distributed areas. In the case of the distributed area, r^2 is replaced by $r_1 r_2$.

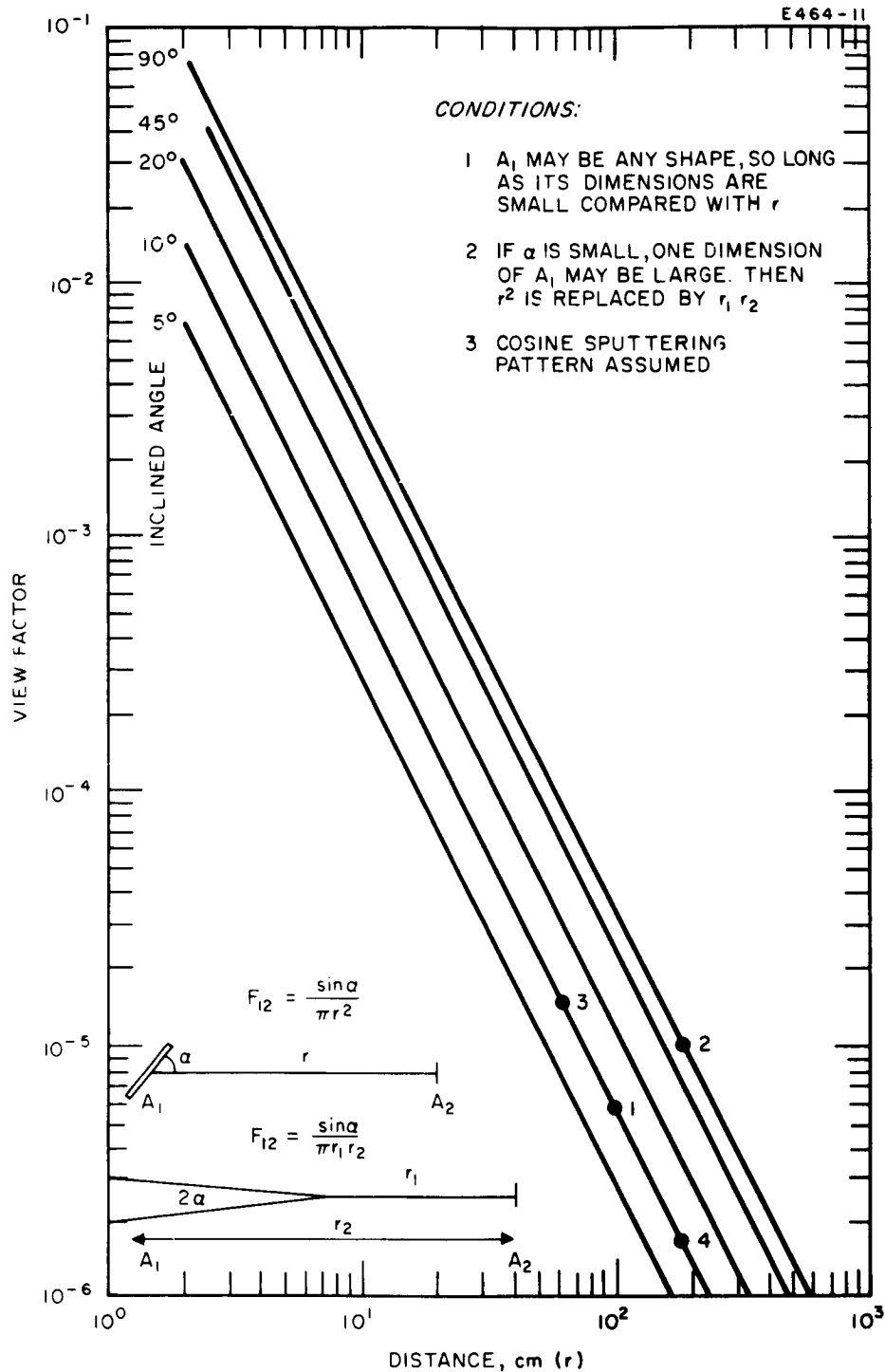


Fig. IV-74. View factors for various collector configurations showing the fraction of total sputtered atom which reaches the ionizer per square centimeter of ionizer surface.

Utilizing the dimensional constraints of the 4'A vacuum system, four possible configurations are given in Table IV-3 for comparison (see Fig. IV-75).

TABLE IV-3

Possible Collector Configurations for a 4 x 10 ft Vacuum Chamber

Case	α	r_1	r_2	r	F_{12}
1. A 4 ft wedge with apex angle (2α) equal to 20°	10°	2 ft	6 ft	3.3 ft (100 cm)	6×10^{-6}
2. A flat plate 6 ft from the ionizer	90°	6 ft	6 ft	6 ft (180 cm)	10^{-5}
3. Multiple 20° wedges 2 ft from ionizer	10°	2 ft	2 ft	2 ft (60 cm)	1.5×10^{-5}
4. Multiple 20° wedges 6 ft from ionizer	10°	6 ft	6 ft	6 ft (180 cm)	2×10^{-6}

The results for these configurations are shown in Fig. IV-74. They indicate that the multiple wedges at 6 ft show a significant advantage over the other configurations considered (at least a factor of three over the next closest). The reason is that both parameters — sine of inclined angle and inverse distance squared — have been optimized. This configuration has the added advantage of redepositing sputtered copper on itself, thus prolonging the life of the collector.

We now calculate the actual arrival rate of copper atoms at the ionizer, using the value $F_{12} = 2 \times 10^{-6}$.

Cesium current density	15 mA/cm ²
Ionizer area (3 strip engine)	9 cm ²
Total ion current	$9 \times 0.015 = 0.135 \text{ A}$
Number of cesium ions arriving at collector	$\frac{0.135}{1.6 \times 10^{-19}} = 0.85 \times 10^{18}$

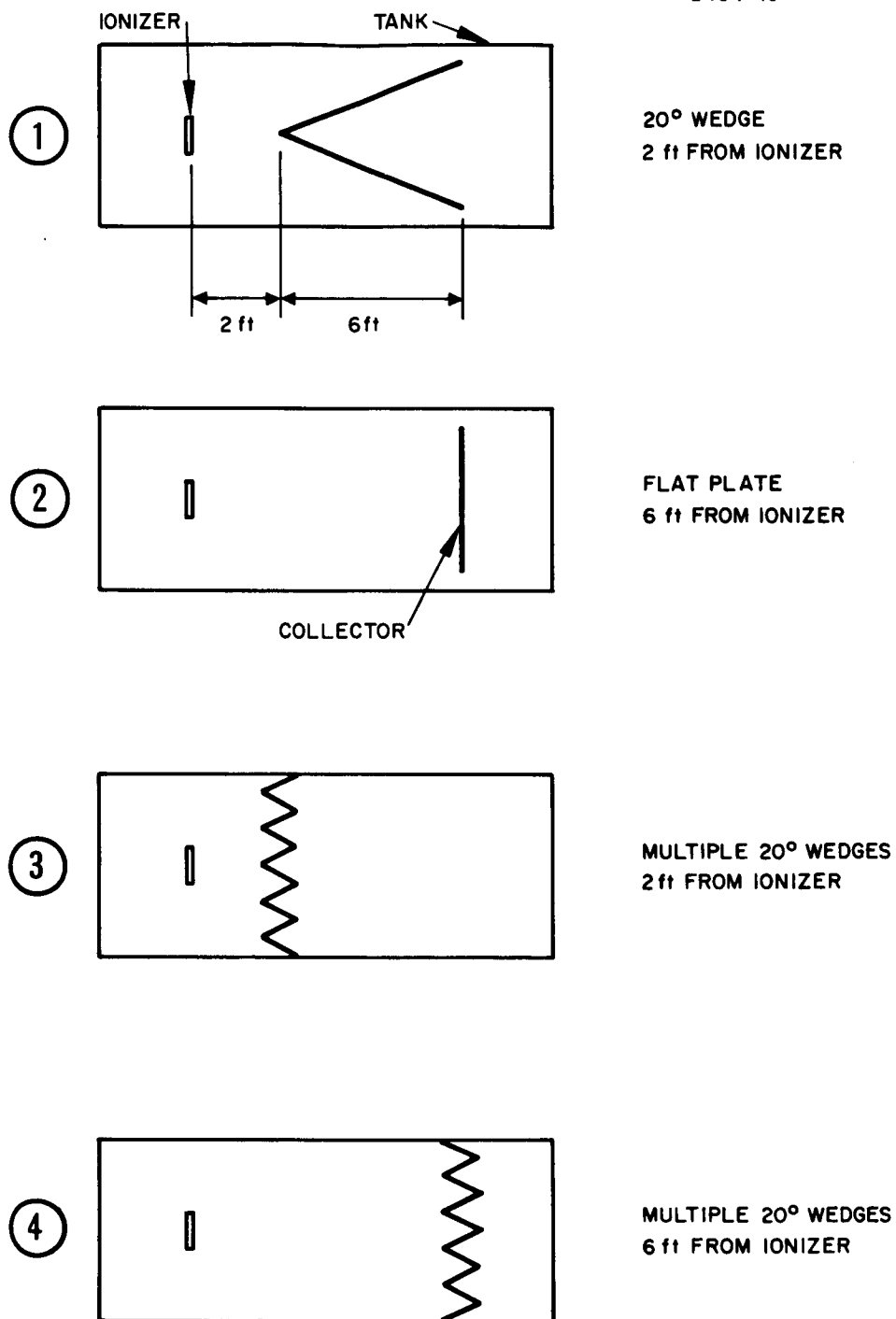


Fig. IV-75. Sketch of various collector geometries.

Copper sputtering yield	8
Copper atoms sputtered	$8 \times 0.85 \times 10^{18} = 6.8 \times 10^{18}$
Copper arrival rate at ionizer surface	$(6.8 \times 10^{18}) (2 \times 10^{-6}) = 1.4 \times 10^{13} \text{ atoms/cm}^2\text{-sec}$

Figure IV-76 shows that the present arrival rates of copper (1.4×10^{13} particles/cm²-sec) has a negligible effect on the ionizer work function. This arrival rate is based on a beam of 135 mA. Operation of the 20-strip engine, however, will increase the copper arrival rate by a factor of seven. The computed results of the work function depression as a function of copper arrival rate would probably show a slight work function depression.

b. Ion Beam Nondecelerating Collector - The collector used in the test of the three-strip engine used the case 4 design described in the analysis (see Fig. IV-75). The collector consisted of a row of 2-1/2 in. wide x 1/16 in. thick copper strips welded to a heavy water-cooled copper plate. The strips were fastened to the rear plate at a 30° angle with respect to normal. The strip spacing was adjusted to permit the beam to impinge only onto the angled surface. The collector-to-ionizer distance was 6 ft.

A contour map of the collector erosion, shown in Fig. IV-77, was made taking into account the angle of the louvers and assuming the erosion was over a flat surface. The major erosion, as expected, is along the axis perpendicular to the long dimension of the ionizer strips. A scale outline of the ionizer is superimposed onto the contour shown in Fig. IV-77.

The initial collector design for the 20-strip engine was established from the three-strip experiment. The data presented in the contour map were used to make a depth versus distance graph of the collector surface. An erosion pattern for the 20-strip engine was obtained by graphically adding the erosion from a series of seven properly displaced three-strip ionizer patterns. Figure IV-78 shows the expected erosion for a 260- and a 500-hour test. The current densities used are

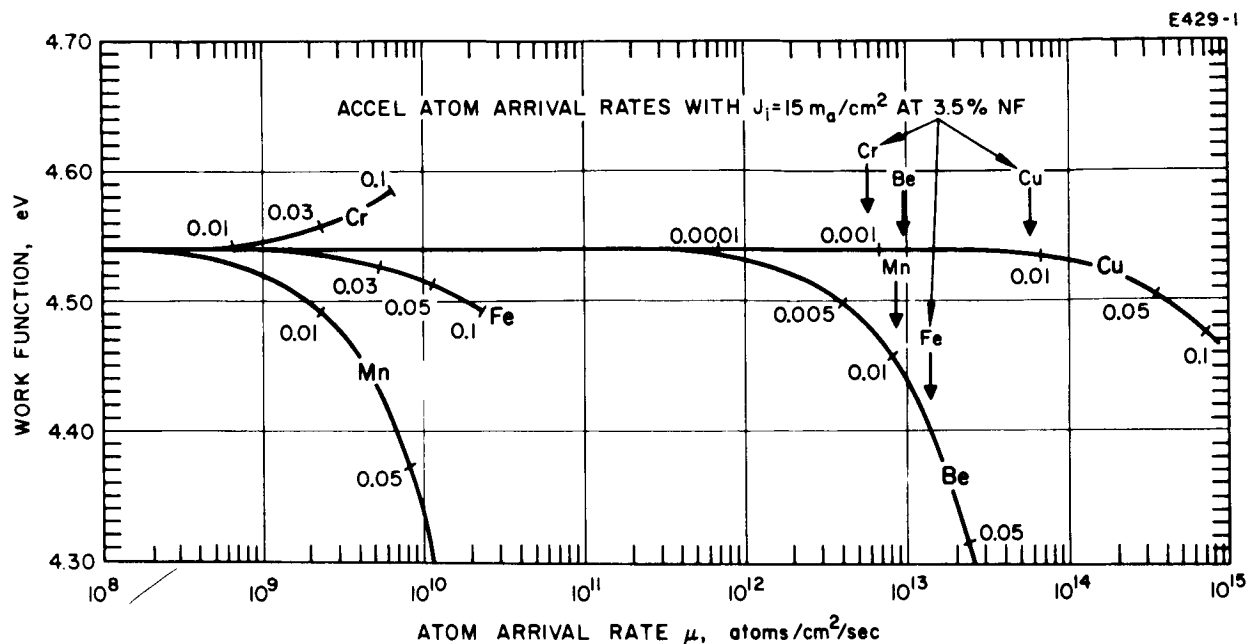


Fig. IV-76. Calculated depression of ionizer work function due to adsorbed film of material sputtered from the accel electrode (e.g., by charge exchange ions). The arrows indicate the calculated arrival rates of these materials due to charge exchange ion sputtering. The numbers on each curve denote the fractional monolayer coverage. It is seen that some materials could cause a serious work function depression at arrival rates of sputtered atoms even lower than the calculated level to be expected in engines.

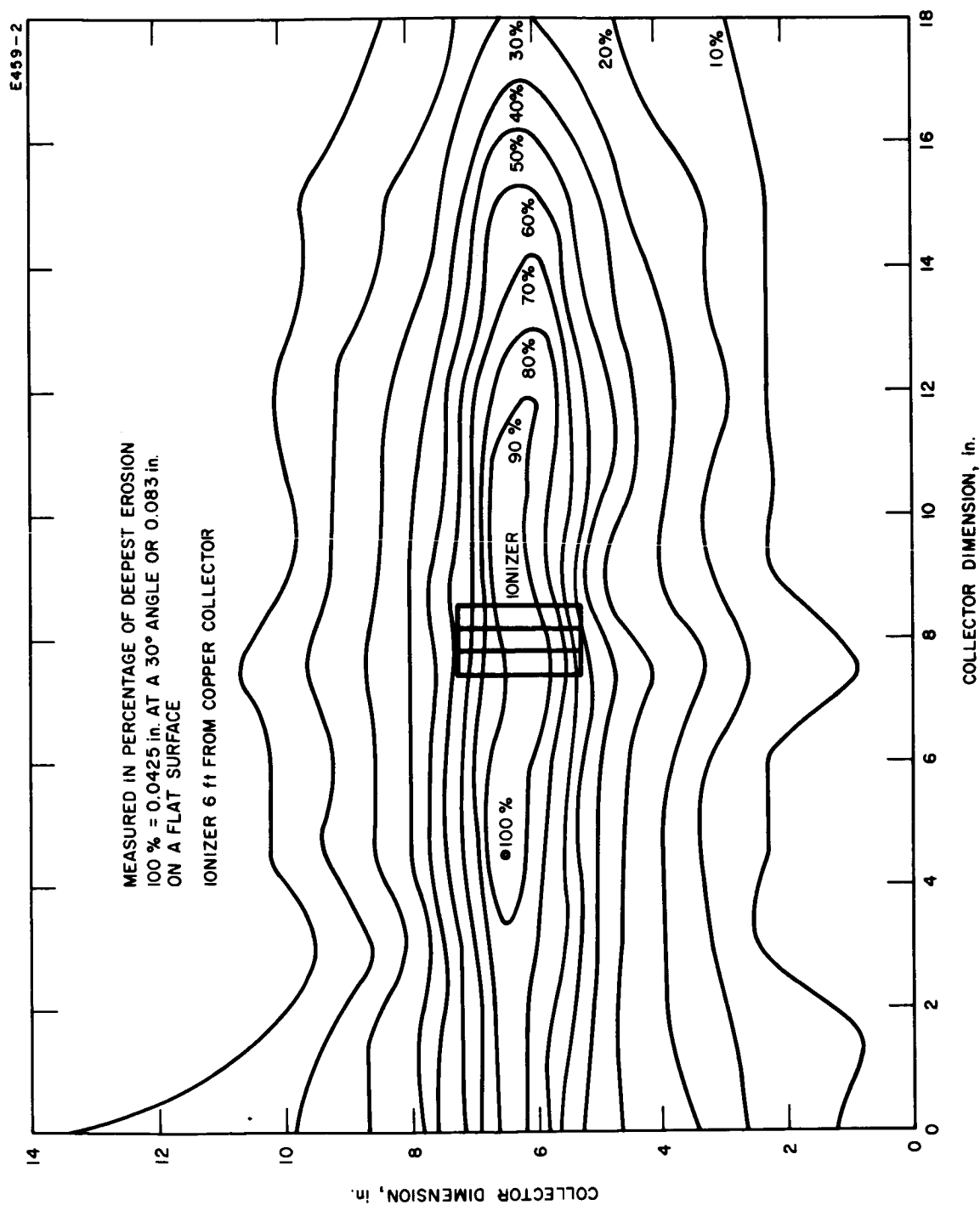


Fig. IV-77. Collector erosion pattern (with superimposed scale ionizer) resulting from the extended test of engine 32-150-4.

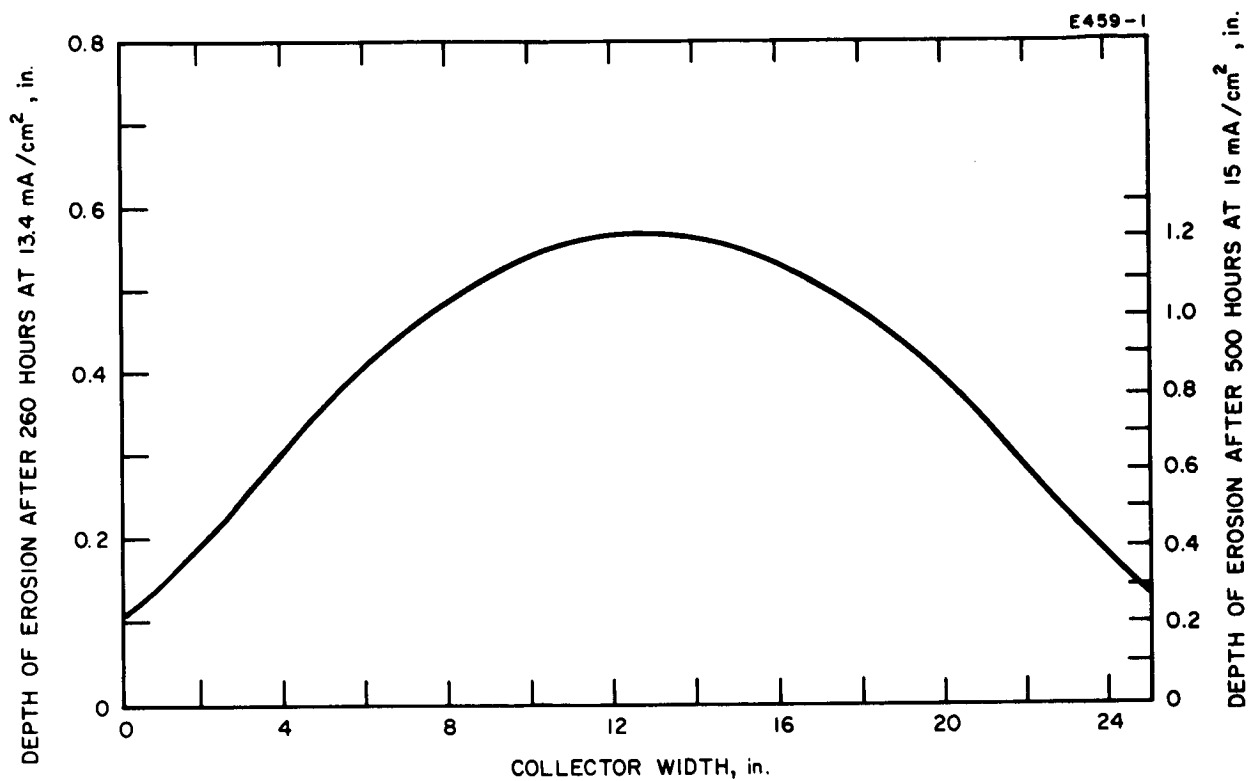


Fig. IV-78. Contour of collector erosion calculated for two operating conditions of a 20-strip engine.

13.4 and 15 mA/cm², respectively. The maximum depth of erosion was expected to be 1.2 in. The copper arrival rate to the ionizer has been shown to be 1×10^{14} atoms/cm²-sec. The reduction in the mass of the collector as well as the elimination of large quantities of copper from back sputtering onto engine parts can probably be reduced by using the decelerating collector system which was prepared for this large engine test.

c. Ion Beam Decelerating Collector — The laboratory testing of high-powered electrical thruster units for prolonged life tests presents two problems with regard to ion beam collection: (1) the normal "grounded" collector may be heavily eroded and eventually destroyed by sputtering of the impinging ion beam and (2) the sputtered material from the collector may fall onto the ionizer surface (in a contact ion engine) and interfere with the ionizer performance. In space applications, neither of these factors would be present; however, for ground testing both effects must be considered and, if possible, eliminated. Approaches to minimizing the back sputtering of collector material have consisted of using shallow angle collectors (vane-type) placed at as great a distance from the engine as vacuum chambers will permit. However, this technique is only a temporary solution since the eventual collector destruction is inevitable with longer, high-thrust tests.

An alternative approach is to decelerate the ion beam to an energy below its sputtering threshold (generally below 100 V) to permit its collection without destructive sputtering. Therefore, a decelerating collector structure has been designed and fabricated (see Fig. IV-79). The first grid maintains the ground potential of the ion beam in order that the decelerating potential of the collector will not feed back to the engine and interfere with the ion optics in the electrode region.

The second grid is biased 100 V negative to reflect the electrons in the neutralized beam. Without the establishment of this "electron trap" (between the engine and the collector) the electrons from the beam would be drawn to the decelerating collector chamber, causing beam de-neutralization and eventual beam dispersion.

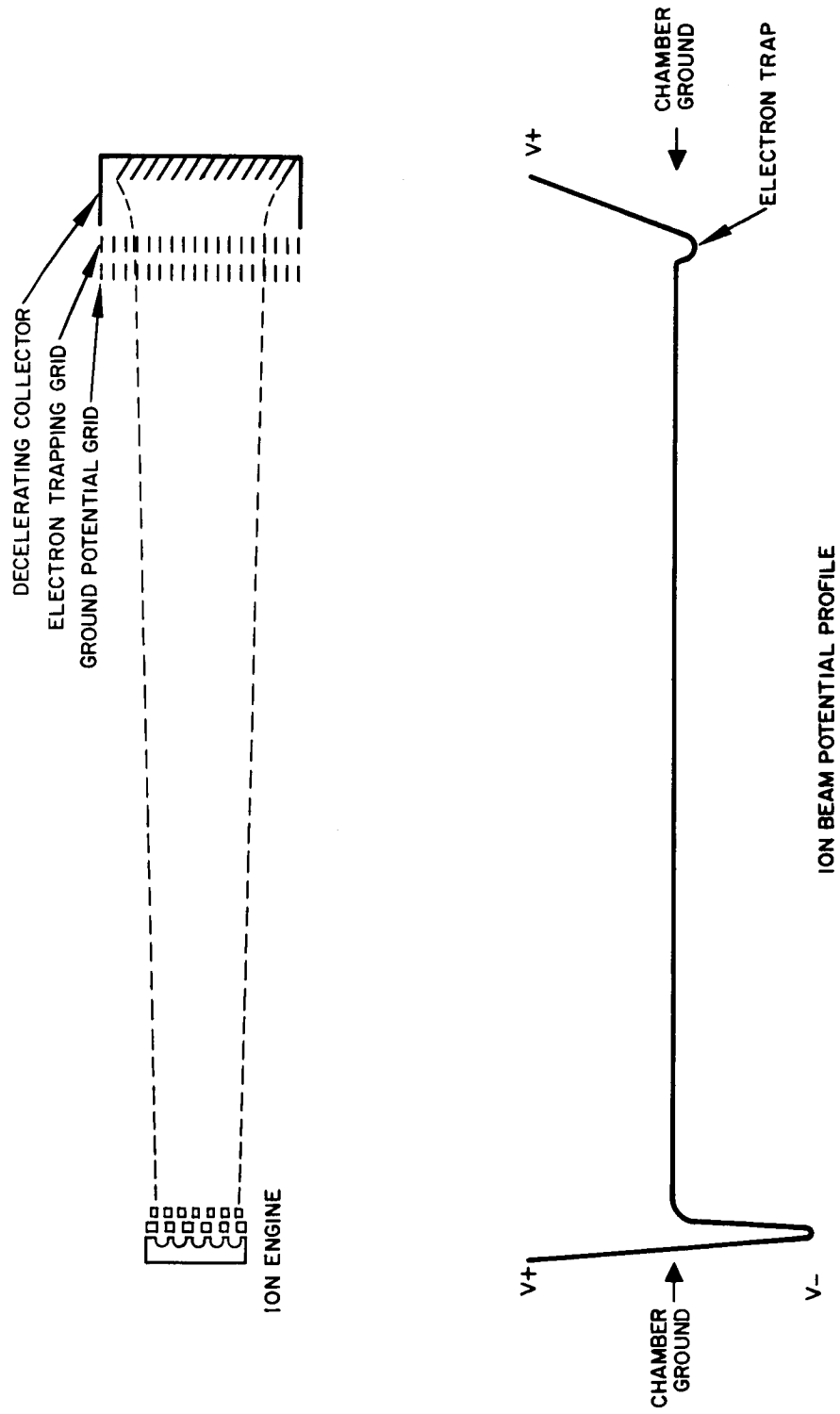


Fig. IV-79. Schematic of decelerating collector.

The collection chamber is biased to a voltage approximately 100 V below the voltage of the ionizer so that the ions will be collected without having the opportunity to establish a space charge sheath within the chamber.

The thin ribbon grids are intended to intercept only 1% of the ion beam, but slight variations in alignment plus beam dispersion will cause their eventual erosion. If this should occur and/or the decelerating structure were unable to hold the proper voltages, the entire collecting structure may be grounded to serve as a normal expendable collector. For this eventuality, an equivalent of 2 in. of copper plate has been included in the 4 ft vacuum chamber to assure continuous operation during a 500-hour engine life test.

3. Analytical Treatment of the Carbon Contaminated Ionizer

Means to deal with and/or eliminate carbon on the ionizing surface have been studied. Although carbon may be present in only a small amount, it has been assumed that there may be enough to appreciably harm the ionization properties of the tungsten ionizer (Ref. IV-11).

Analytical investigations of carbon effects with ionizers have been divided into two major areas of interest:

- a. Ionizers received in a carburized state, where decarburizing must take place prior to engine tests.
- b. Ionizers which are free of carbon initially, but which carburize during an engine run because of carbon carrying molecules in the environment.

In either of these areas of interest, the analysis depends heavily on the extent of diffusion between ionizer grains. If there is little communication from one grain to the next, the dimension of concern is very small (several microns). This is desirable from the standpoint of (a) above, since decarburization may then proceed with relative ease. On the other hand, contamination during operation becomes much more critical since the surface grains may fill with carbon before passing any on to the adjacent grains.

We first consider an ionizer which has a uniform carbon distribution throughout. In this case, we consider complete communication between adjacent grains and ways to make the surface carbon free for the duration of engine operation. This is certainly a much harder job than if there is no inter-grain diffusion; in that case, only surface grains would have to be cleaned out. With inter-grain diffusion, the surface grains are continually fed with carbon from the bulk ionizer regions. Since carbon diffusion in tungsten is extremely slow, the ionizer will be seen to behave as a semi-infinite slab.

In the decarburization process, the ionizer may conceivably behave in one of two modes, porous or solid. In the porous mode, the ionizer's tremendous internal surface area is utilized for the interaction of oxygen with carbon. If this mode exists, decarburization of the ionizer is considerably easier. In the solid mode, the difficulties in supplying oxygen to the internal porous structures and in removing the carbon dioxide are too great for the internal surface area to be of any value in removing carbon. Thus, only the outer surface of the ionizer is utilized, and it might as well be a solid slab as far as the decarburization process is concerned.

It is not known at this time to what extent the porous mode exists. Oxygen will not directly penetrate into the internal regions of the ionizer because of the oxygen reaction with tungsten, forming tungsten oxide within a small depth below the outer surface (Ref. IV-12). It may be possible to penetrate the ionizer with wet hydrogen (Ref. IV-13). With a wet hydrogen environment, oxygen could be made available to the internal area of the ionizer before it reacted with tungsten. The problem would then be the removal of the carbon oxide product from inside the porous structure. If too high a CO concentration is required to sustain the molecular flow of CO out of the porous structure, the formation of CO would be limited. However, it might be possible to create a viscous flow condition in which the CO would be swept out in a stream of wet hydrogen. This would require a large upstream pressure because the ionizer is a very restrictive flow passage.

At any rate, this case deals with a solid slab ionizer model, which represents the most difficult physical situation in which carbon may exist in an ionizer.

Theory predicts that a solid tungsten slab of ionizer dimensions (1 mm thick) would take unreasonable lengths of time to reduce a bulk initial carbon level down by an appreciable amount (the time constant for total bulk cleanup is 10^5 hours at 1900°K). The practical solution, then, involves reducing the surface concentration level to zero temporarily and sustaining it below some tolerable level for the engine life period. (In this case, "temporarily" could mean periods as long as a year.) The ionizer thus undergoes a cleanup period during which it is held at the highest tolerable temperature for a length of time determined by (1) the ionizer operating temperature, (2) the ionizer life requirement, (3) the maximum tolerable cleanup temperature, and (4) the ratio of tolerable carbon concentration at the surface to the initial carbon concentration.

The ionizer operating temperature need not exceed 1400°K , as has been verified in recent tests. The ionizer life requirement for immediate purposes has been 500 hours and eventually will be one year. The maximum tolerable temperature at which an ionizer can be held without damaging it is in the neighborhood of 1900°K . The ratio of tolerable carbon concentration to initial carbon concentration will arbitrarily be set at one order of magnitude.

The time constant for the cleanup of carbon from a tungsten slab is given in Ref. IV-14.

$$\tau = \frac{h^2}{\pi^2 D} \text{ sec} \quad (\text{IV-30})$$

where

$h \equiv$ slab thickness, cm

$D \equiv$ diffusion constant, cm^2/sec .

The time constant is the time required for the bulk concentration to drop to 37% of its initial value.

The diffusion constant is given by

$$D = 1.6 \times 10^{-6} \times 10^{\frac{-11,000}{T}} \text{ cm}^2/\text{sec} \quad , \quad (\text{IV-31})$$

where T is the slab temperature in degrees Kelvin. Figure IV-80 is a plot of (IV-30) using (IV-31) for the general case of any slab thickness and temperature. It is based on this plot that the value of 10^5 hours was quoted for the time constant of the ionizer at 1900°K . (It is also observed on this plot that particle sizes of the order of ionizer grain sizes (5μ) have a very small time constant.)

Since it is obvious that reduction of the bulk carbon content is almost impossible to achieve (by the mechanism of solid diffusion), we seek an equation to describe the diffusion of carbon within a very small distance from the surface of the ionizer. (Just such a relationship is shown in Ref. IV-15.)

$$\frac{C}{C_o} = \text{erf} \frac{x}{2\sqrt{Dt}} \quad (\text{IV-32})$$

where

$C \equiv$ carbon concentration at time t and distance x from the surface

$C_o \equiv$ initial concentration, constant with distance

$\text{erf} \equiv$ the error function.

The error function is defined by the equation:

$$\text{erf}(z) = \frac{2}{\sqrt{\pi}} \int_0^z \exp(-a^2) da \quad (\text{IV-33})$$

and is tabulated in such books as Ref. 16.

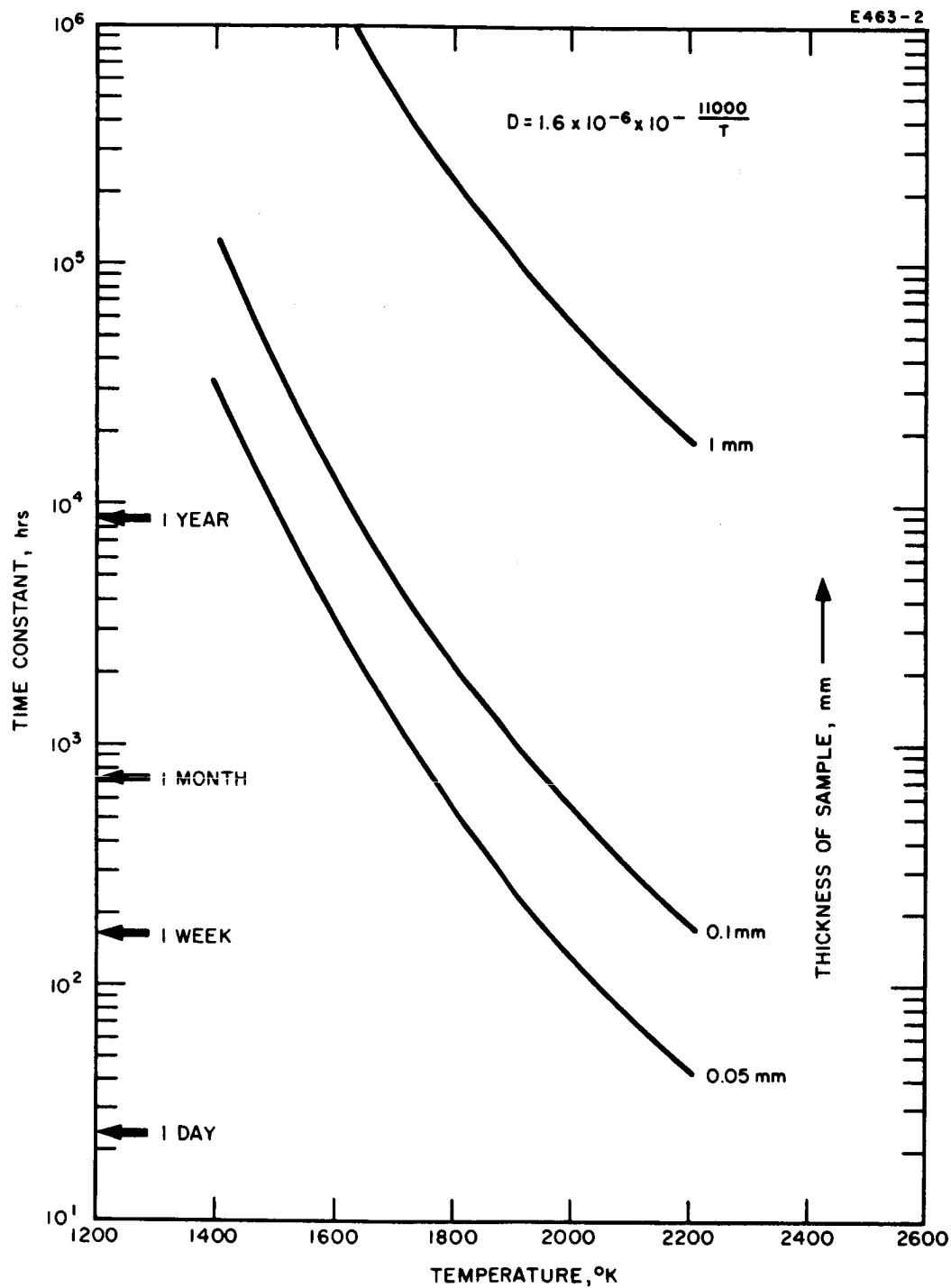


Fig. IV-80. Time constant for diffusion of carbon through solid tungsten. h = total thickness of a sample exposed to a decarburizing (or carburizing environment on both sides. A physical significance of the time constant is given in Fig. IV-86.

This solution requires that the distances x within the material be small compared to the total thickness of the material. Therefore, the bulk concentration is not affected by changing conditions near the surface and the solution corresponds to an infinite source. Actually, the solution is good up until the time that the concentration at $x = h/2$ is less than its initial value, for only then is it important that the ionizer is not infinite. Figure IV-81 is a plot of the concentration profile (normalized) at various times after the initiation of the cleanup period. The concentration at $x/h = 0.5$ is unaffected up until the time reaches one-tenth of a time constant. Since the ionizer time constant is on the order of 10^5 hours, the cleanup period will have to be a small fraction of a time constant (probably no greater than 0.001). Thus, the infinite source solution is valid for the ionizer cleanup problem.

The next step, of course, is to determine how long the ionizer will operate sustaining a carbon-clean surface. The surface concentration ceases to be zero the moment the ionizer slab is taken out of the decarburizing environment. However, the surface concentration takes a finite time interval to build up to a detrimental amount (one-tenth the bulk value). This interval can be hours, days, or weeks, depending on the shape of the concentration profile at the beginning of engine operation, and the operating temperature. We soon arrive at the conclusion that the key to sustaining a carbon-clean surface is to clean up the ionizer at a significantly higher temperature than that at which it will be operated. Otherwise, long cleanup periods are required, possibly even longer than actual engine life.

In order to calculate the surface recontamination time, it is necessary to determine the carbon concentration gradient at the surface at the end of the cleanup period. This is accomplished by taking the derivative of the right hand side of (IV-32) and setting $x = 0$:

$$\frac{d}{dx} \left(\frac{C}{C_o} \right)_{x=0} = \frac{1}{2\sqrt{D_{cu}t_{cu}}} \frac{d}{dx} [\text{erf}(0)] = \frac{0.564}{\sqrt{D_{cu}t_{cu}}} \quad (\text{IV-34})$$

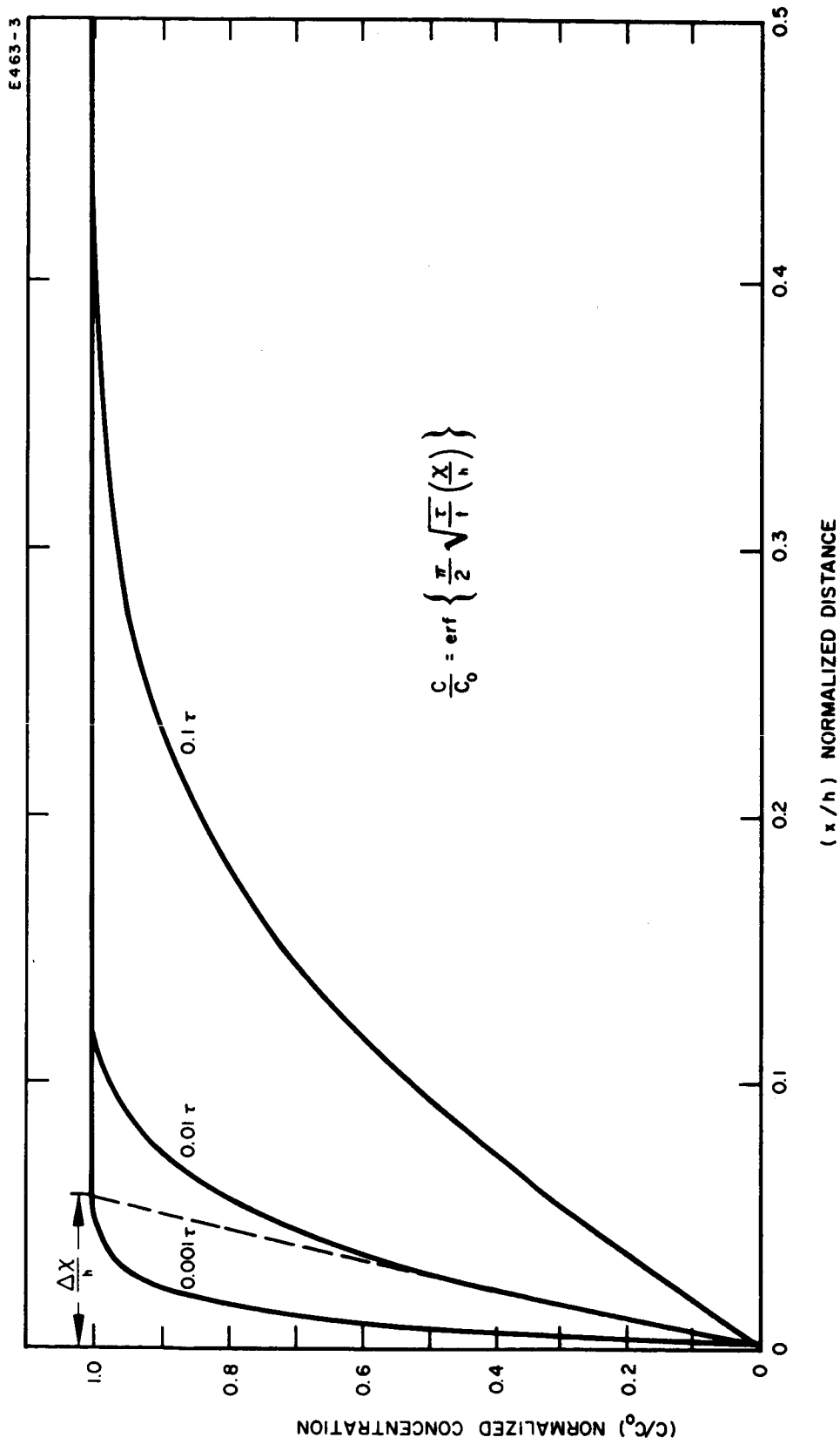


Fig. IV-81. Normalized carbon concentration profiles at various times after start of cleanup. Solid slab ionizer model. The profiles near the surface become successively flatter in time, as more carbon is removed. Concentration held always at zero at the surface by decarburizing environment.

where

$D_{cu} \equiv$ diffusion constant at cleanup temperature

$t_{cu} \equiv$ cleanup interval.

The rate of carbon flow per unit area to the ionizer surface at the beginning of the engine operating period is obtained by multiplying the right hand side of (IV-34) by the diffusion constant at operating temperature D_o . To obtain the time rate of change of concentration at the surface, we must divide this product by an incremental thickness Δx which represents the cleaned up region very close to the surface of the ionizer slab. This thickness is determined from a plot of normalized concentration versus x at $t = t_{cu}$ (see Fig. IV-82). Δx is the distance between the vertical line $x = 0$ and the intercept of the horizontal line $C/C_o = 1$ with the extrapolated slope at $x = 0$.

In Fig. IV-81, it is shown how Δx (normalized) is obtained for the particular case of $t_{cu} = 0.01 \tau$. The profile at $t = t_{cu}$ now becomes the initial distribution for the calculation of surface recontamination (see Fig. IV-82). Simple geometric reasoning indicates that Δx is the inverse of the slope at $x = 0$, but we have already obtained the slope at $x = 0$ (see eq. (IV-34)). Hence, Δx is the inverse of the right hand side of (IV-34)

$$\Delta x = \frac{\sqrt{D_{cu} t_{cu}}}{0.564} \quad (IV-35)$$

The time rate of change of normalized concentration at the surface of the slab is then:

$$\frac{d}{dt} \left(\frac{C}{C_o} \right)_{t=t_{cu}} = \frac{D_o}{\Delta x} \frac{d}{dx} \left(\frac{C}{C_o} \right)_{x=0} \quad (IV-36a)$$

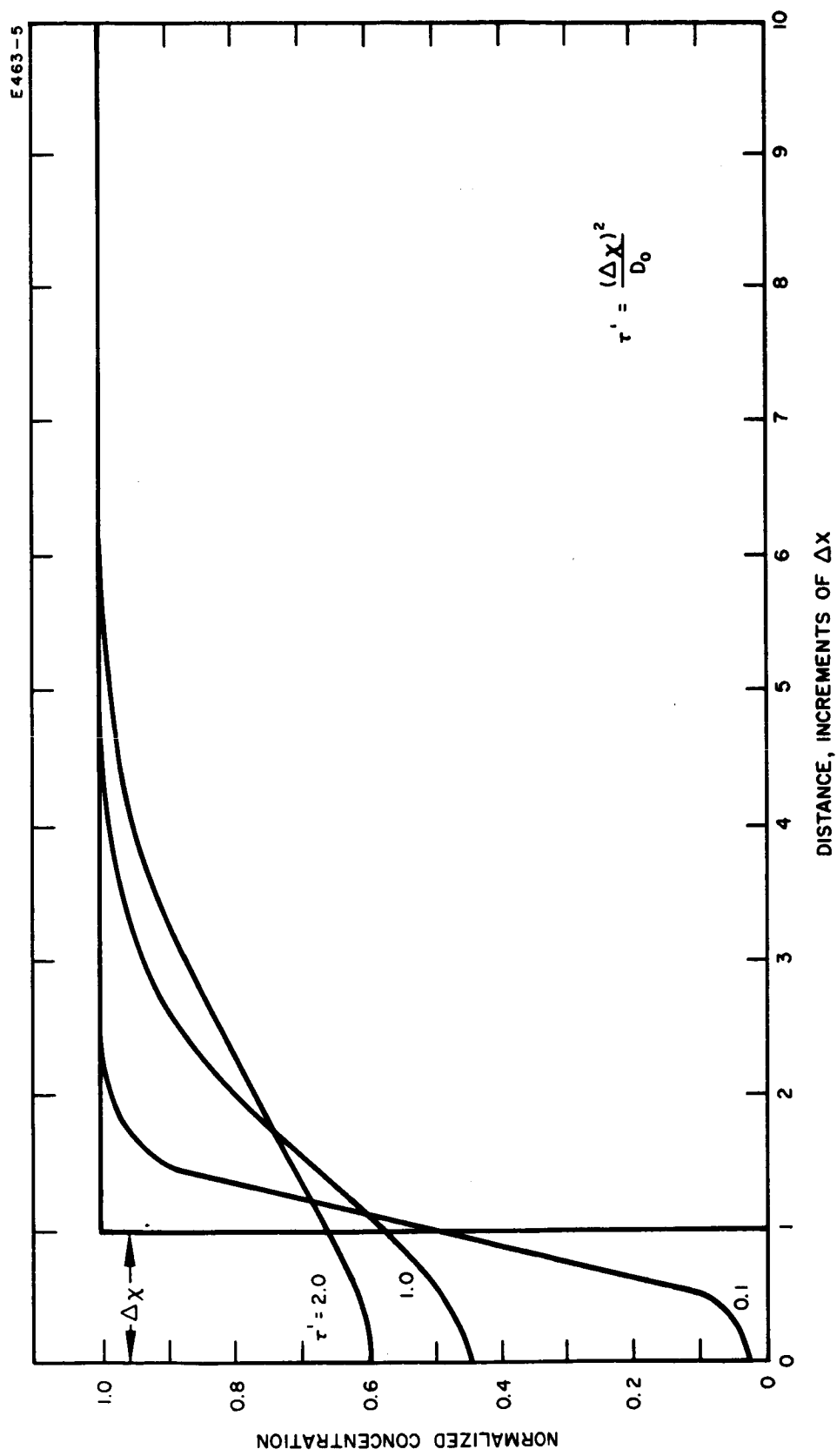


Fig. IV-82. Normalized carbon concentration profiles at various times after start of engine operation. Solid slab ionizer model.

When (IV-34) and (IV-35) are substituted into (IV-36a), the result is

$$\frac{d}{dt} \left(\frac{C}{C_o} \right)_{t=t_{cu}} = \frac{(0.564)^2}{D_{cu} t_{cu}} D_o \quad . \quad (IV-36b)$$

This result is good only for short time intervals ($t \ll \tau$) since the surface gradient is assumed constant for the duration of the interval. This assumption is valid for our work here. The time at which the concentration near the surface will return to one-tenth its initial (or bulk) level may be calculated by (IV-36b), since we are considering a small increase in (C/C_o) so that

$$\frac{d(C/C_o)}{dt} \rightarrow \frac{\Delta(C/C_o)}{\Delta t} \quad .$$

Hence, for the small increase in (C/C_o) of 0.1,

$$\frac{t_o}{t_{cu}} = 0.31 \left(\frac{D_{cu}}{D_o} \right) \quad . \quad (IV-37)$$

Equation (IV-37) is only a partial solution to the surface recarburization problem in that it only holds at the position $x = 0$ and for the first small increase in concentration level (0.1). The complete solution involves determining the carbon concentration at all positions in the slab and at any time after the start of the operating period (just as was done for the cleanup period). This solution has been carried out by numerical approximation. Only the results are presented here (Figs. IV-82 and IV-83). Figure IV-83 shows how the concentration near the surface builds up in time while concentrations at positions farther from the surface initially drop off as the carbon flows toward the surface. Eventually, the normalized concentrations at all positions approach unity.

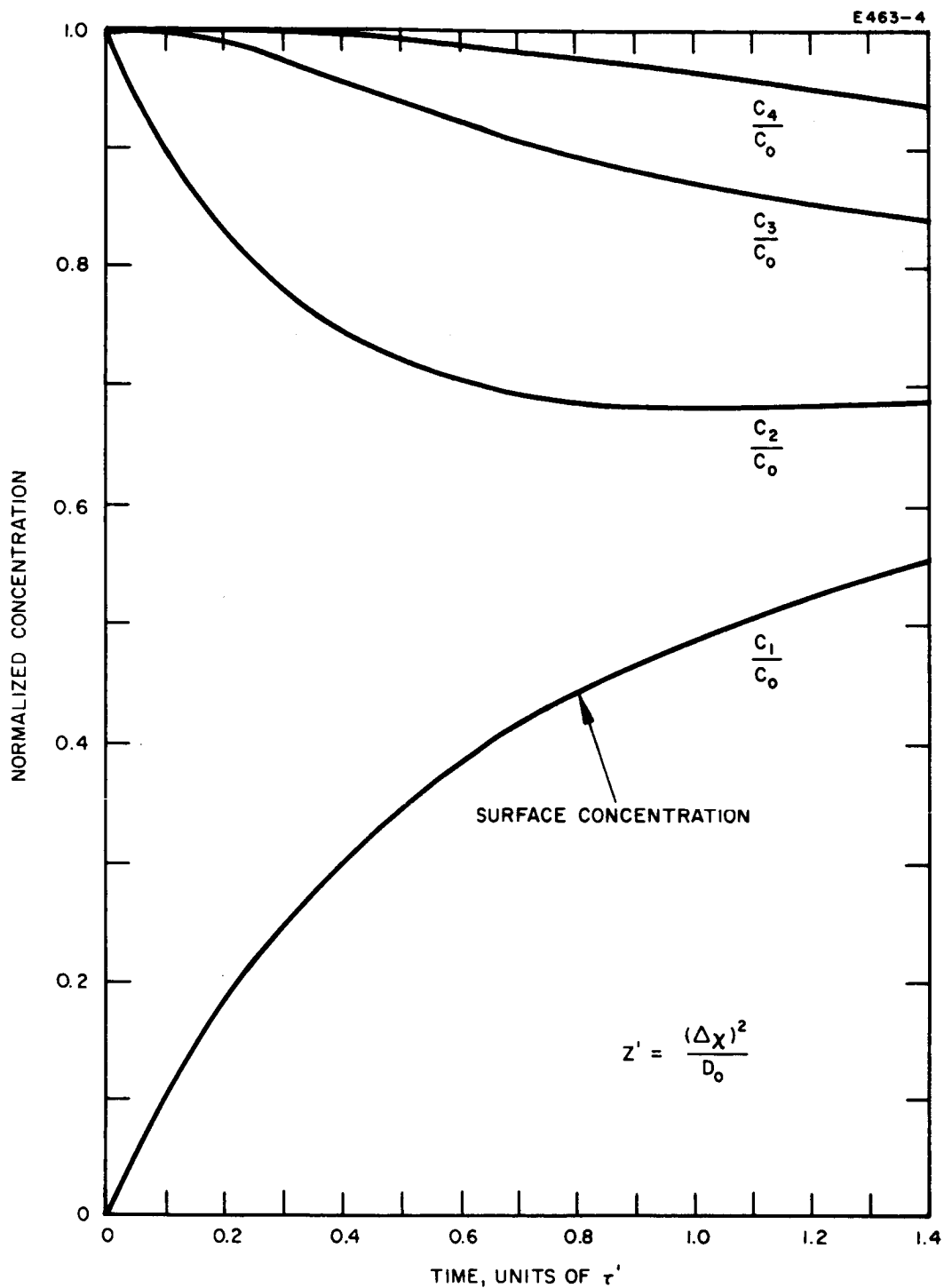


Fig. IV-83. Normalized carbon concentration versus time after start of engine operation. Surface value plus values at other positions (equal increments into ionizer solid slab model). When the decarburizing environment is removed, the region near the surface recontaminates, fed by adjacent regions deeper within the slab.

Figure IV-83 shows the carbon distribution at various times during the period of recarburization of the ionizer surface. The carbon diffuses out from the bulk region and eventually replaces the comparatively small amount removed during cleanup.

We now return to the result established in (IV-37). This relation gives the number of hours (or days, etc.) an ionizer may operate with a clean surface, for every hour (or day, etc.) of cleanup time. The solid diffusion decarburizing problem is strictly one of temperature — the temperature at which the ionizer is cleaned up relative to that at which it operates. The larger the difference created between these values, the more operating time is available per unit of cleanup time. Evaluating the right hand side of (IV-37) (using IV-31),

$$\frac{t_o}{t_{cu}} = 0.31 \times 10^{- \left\{ 11,000 \left(\frac{1}{T_o} - \frac{1}{T_{cu}} \right) \right\}} \quad . \quad (IV-38)$$

This relation is plotted in Fig. IV-84. For a cleanup at 1900°K and an operating temperature of 1400°K, 37 hours of carbon clean operation are bought with every hour of cleanup time. Thus, one year of operation is obtainable with a two-week cleanup period. However, if the operating temperature becomes higher, we rapidly lose carbon clean time. For example, at 1500°K, clean time is down by a factor of three and at 1600°K by a factor of 10. Thus, at 1600°K only four carbon-clean hours are available for each hour of cleanup. However, these high temperatures are unlikely. Also, should the cleanup process not be capable of 1900°K, the length of the carbon free period is again affected. Table IV-4 compares the effect for a 1900 and a 1700°K cleanup temperature.

It appears that solid diffusion alone is not a completely reliable mechanism to assure a carbon clean ionizer surface for extreme lengths of time. This is a result of (1) the critical nature of both cleanup and operating temperature, and (2) long time requirement for the cleanup

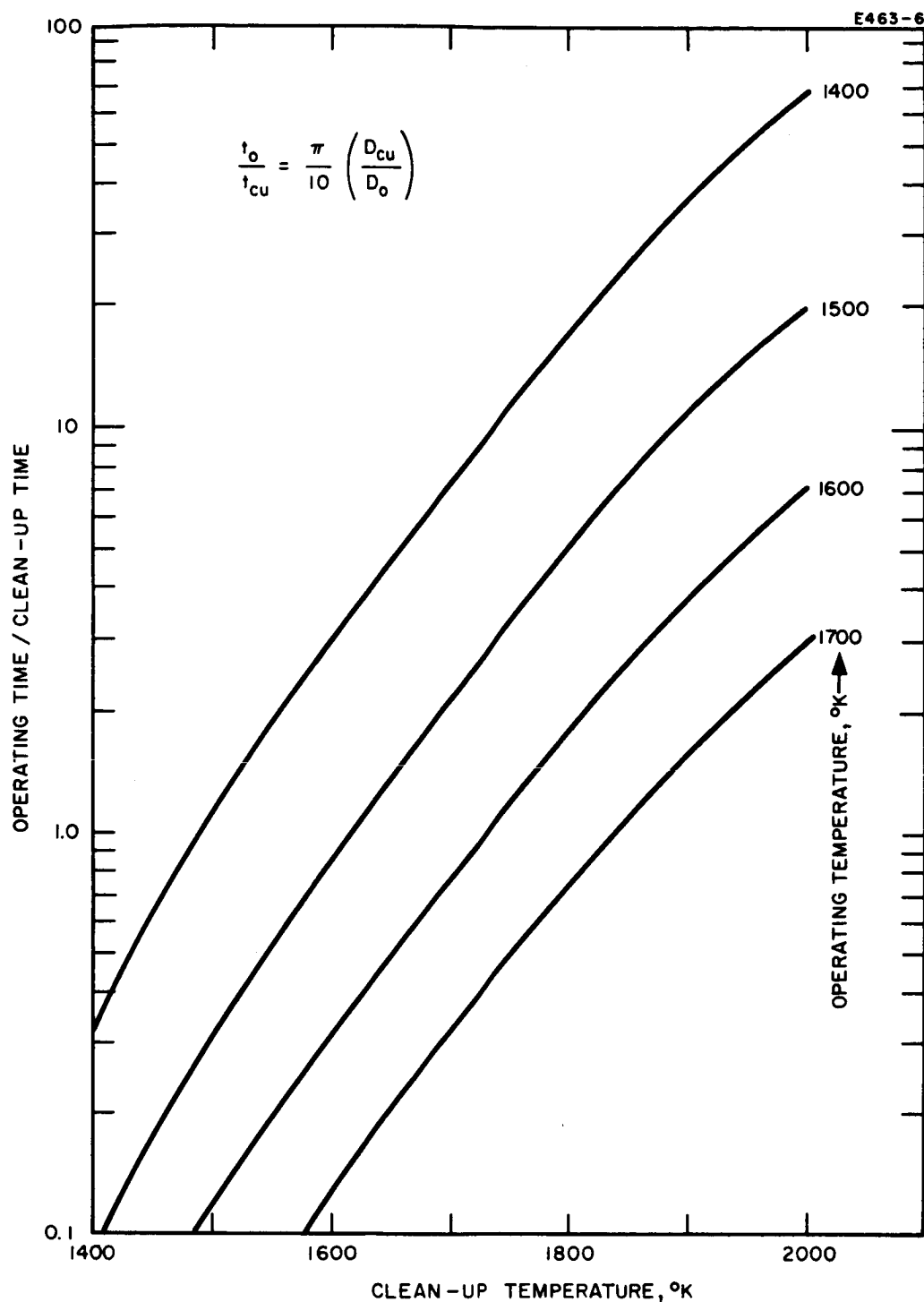


Fig. IV-84. Ratio of operating time (surface concentration does not exceed 0.1 initial or bulk level) to cleanup time (exposed to a decarburizing environment). The amount of operating time available per cleanup time depends on the temperature differential between cleanup temperature and operating temperature.

TABLE IV-4

Carbon Free Operating Hours per Cleanup Hour

Ionizer Operating Temperature, °K	Cleanup Temperature, °K	
	1900	1700
1300	270	32
1400	37	7
1500	11	2
1600	4	1

period. Therefore, continuing effort to utilize ionizer porosity in decarburizing processes is warranted.

It has been shown that the solid diffusion mechanism does offer an immediate and straightforward method of temporarily decarburizing ionizer surfaces long enough for laboratory engine tests (500-1000 hours).

We next consider ionizers which are initially free of carbon, but which carburize during an engine run. The first assumption made in this analysis was that there is no communication between ionizer grains. In other words, the resistivity to diffusion between grains is so great that the surface ionizer grains may completely contaminate before any significant carbon has passed off to the adjacent internal grains. This certainly represents the fastest possible way in which the surface coverage may reach a harmful value.

Work function of a tungsten surface partially covered with carbon has been analytically determined by R. G. Wilson (Ref. IV-11). The calculation performed here relates the surface coverage to the partial pressure of residual gases. This is accomplished by performing a mass balance between the carbon atoms which stick to the surface and those which volume diffuse into the bulk of an ionizer grain. The rate

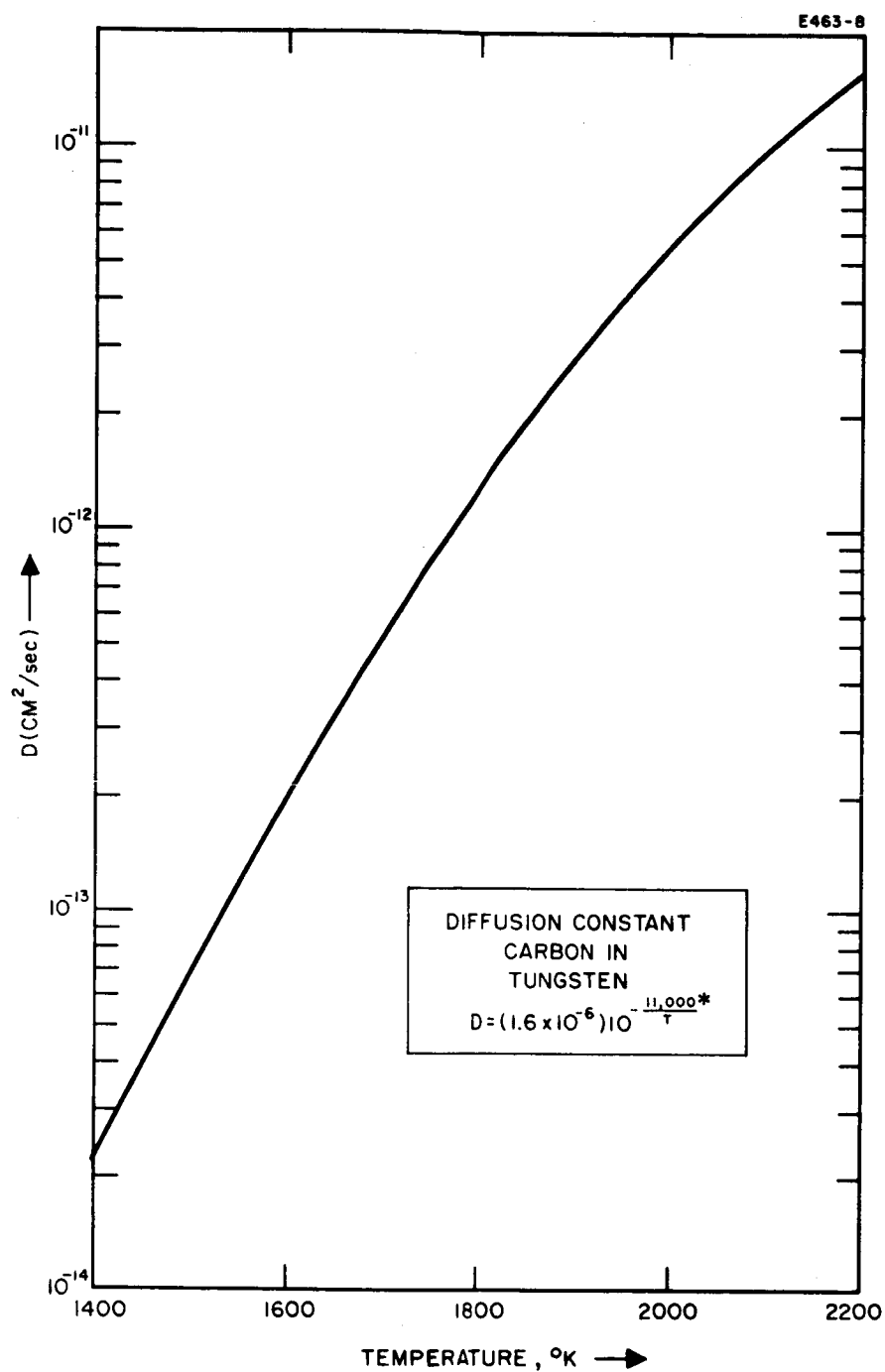


Fig. IV-85. Diffusion constant: carbon in tungsten. The diffusion constant is a key parameter in calculating the rate of build-up of carbon at the surface. For example, if diffusion with the grain is negligible, carbon will build up on the surface as fast as it arrives, and vice versa.

* Reference IV-12.

at which carbon diffuses into the bulk is proportional to the carbon concentration at the surface. Hence, a relationship exists between carbon sticking rate and surface coverage.

The characteristic time constant for carbon diffusion in an ionizer grain is given by

$$\tau = \frac{4a^2}{\pi^2 D}$$

where

$a \equiv$ grain size $= 5 \mu$

$D \equiv$ diffusion constant $= 2 \times 10^{-13} \text{ cm}^2/\text{sec}$ at 1600°K
(Ref. (IV-14) (Fig. IV-85).

Thus,

$$\tau = 140 \text{ hours.}$$

To realize the physical significance of the time constant, consider Fig. IV-86.

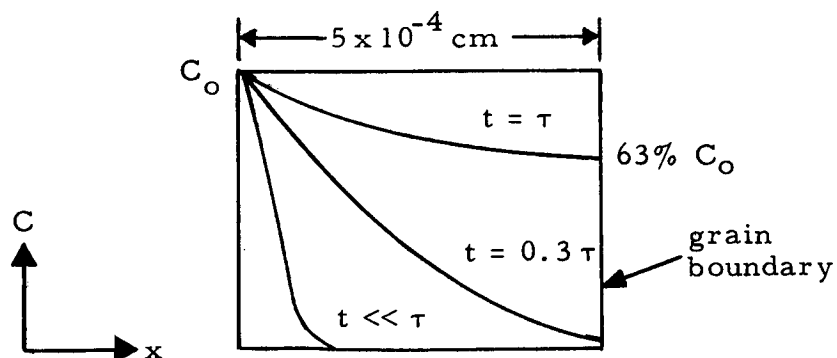


Fig. IV-86. Carbon concentration within a grain of tungsten as a function of time and distance from the surface.

With a constant carbon surface concentration C_o , the concentration versus distance across the grain appears at various times as shown. At t much less than τ , the carbon penetration into the grain is very small. At $t = 0.3 \tau$, the grain first begins to behave as a finite grain, as opposed to an infinite slab; i.e., carbon penetration has reached the far wall of the grain. At $t = \tau$, the carbon concentration at the far wall of the grain has reached 63% of the value at the contaminated surface. The exact expression for carbon concentration as a function of time and distance is given by

$$C(x, t) = C_o \left\{ 1 - \frac{4}{\pi} \sum_{v=0}^{\infty} \frac{1}{2v+1} \sin \frac{(2v+1)\pi x}{2a} \exp \left[- (2v+1)^2 \frac{t}{\tau} \right] \right\} \quad (IV-39)$$

This otherwise difficult equation is considerably simplified by considering two regimes of time: time less than 0.3τ and time greater than 0.3τ . Equation (IV-39) becomes:

$$C = \begin{cases} C_o \left[1 - \frac{4}{\pi} \sin \left(\frac{x\pi}{2a} \right) e^{-t/\tau} \right], & t > 0.3 \tau \quad (IV-40a) \\ C_o \left[1 - \operatorname{erf} \left(\frac{x}{2\sqrt{Dt}} \right) \right], & t < 0.3 \tau \quad (IV-40b) \end{cases}$$

Equation (IV-40a) is obtained in an analogous manner as given in Ref. IV-14 for diffusion out of a volume. Equation (IV-40b) is arrived at by considering the grain to be an infinite slab up to 42 hours (0.3τ), and using the infinite slab equations derived in Ref. IV-15.

The mass flow rate (per unit area) of carbon away from the surface and into the bulk of the grain is given by

$$\left(\frac{W}{A} \right) = D \left(\frac{\partial c}{\partial x} \right)_{x=0} \frac{\text{atoms}}{\text{cm}^2\text{-sec}} \quad (IV-41)$$

Taking the derivative of the right hand side of (IV-41) and multiplying by D results in

$$\left(\frac{W}{A}\right) = \begin{cases} \frac{2D}{a} C_o e^{-t/\tau}, & t > 42 \text{ hours} \\ \frac{0.564 C_o \sqrt{D}}{t^{1/2}}, & t < 42 \text{ hours.} \end{cases} \quad \begin{matrix} \text{(IV-42a)} \\ \text{(IV-42b)} \end{matrix}$$

Here 0.564 is the derivative of the error function of zero argument, and W/A is plotted as a function of time from (IV-42) in Fig. IV-87. The parameter is carbon surface concentration (atom/cm³), which is related to surface coverage θ by

$$\theta = \frac{C_o}{0.5 \times 10^{23}} \quad \text{(IV-43)}$$

where 0.5×10^{23} is the number of tungsten atoms/cm³ of pure tungsten. (It is assumed that a tungsten atom occupies the same amount of space as a carbon atom.)

The mass balance relationship appears as follows:

$$\sum_{i=1}^k n_i \epsilon_i \mu_i = \left(\frac{W}{A}\right) \quad \text{(IV-44)}$$

where

$n_i \equiv$ number of carbons in molecule i

$\mu_i \equiv$ arrival rate of molecules from gas i

$\epsilon_i \equiv$ sticking probability of a carbon atom in gas i

$\sum n_i \epsilon_i \mu_i \equiv$ total carbon sticking rate, atoms/cm²-sec.

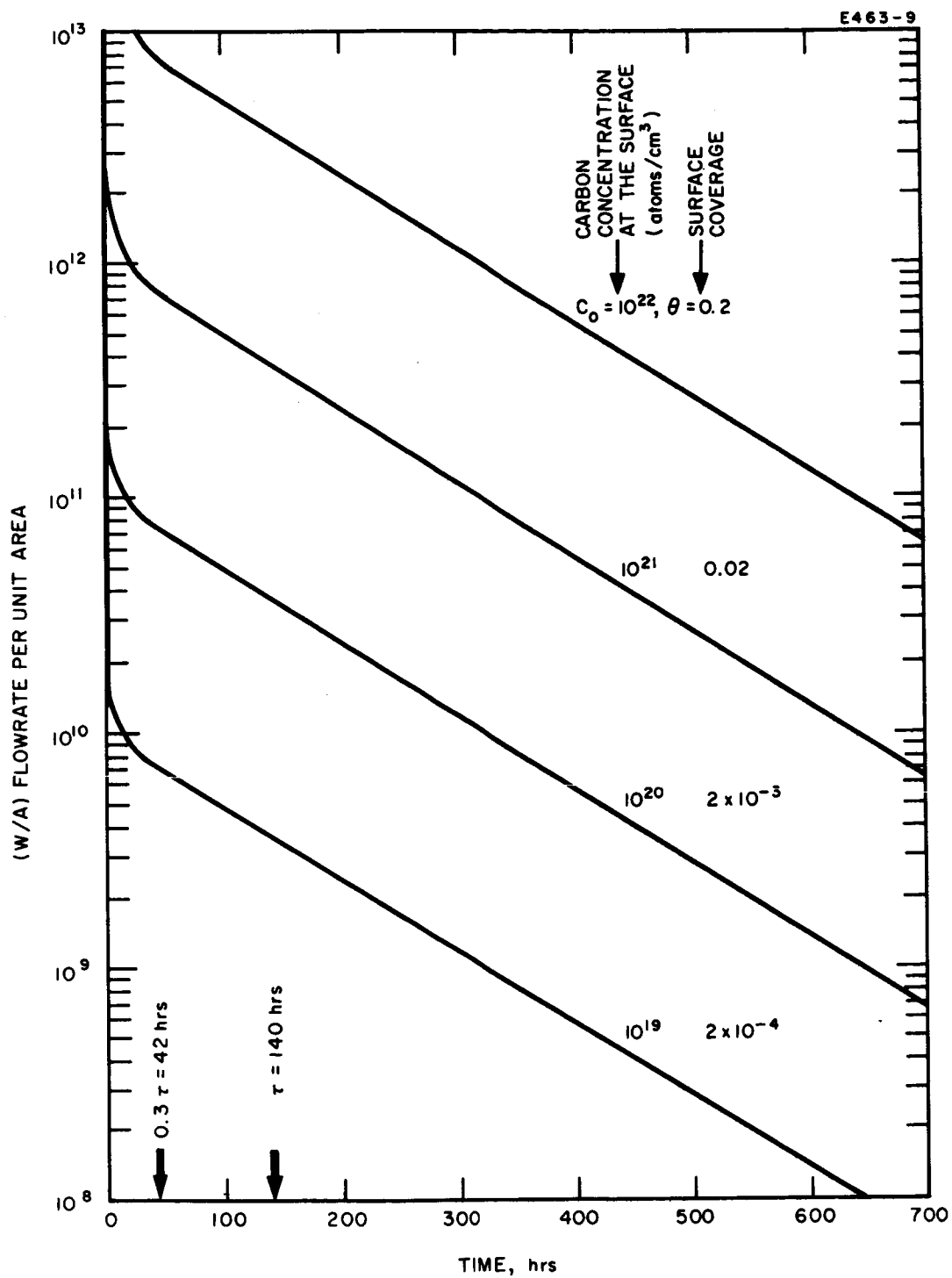


Fig. IV-87. Mass flow rate (atoms/cm²-sec) of carbon diffusing from the surface of a grain and into the bulk volume of the grain. Parameter is concentration (atoms/cm³) at the surface.

A cross plot of Fig. IV-87, utilizing (IV-43) and (IV-44) results in Fig. IV-88. Carbon surface coverage is plotted versus carbon sticking rate, with the parameter being various times that the grain surface is exposed to residual gases.

From the work of Denison (Ref. IV-17), we may relate the partial pressures of many of the carbon carrying molecules to a sticking rate of carbon atoms at the ionizer surface.

The molecular arrival rate for a particular gas is related to its partial pressure and molecular weight by

$$\mu = \frac{P}{(2\pi mkT)^{1/2}} \frac{\text{molecules}}{\text{cm}^2 - \text{sec}} \quad (\text{IV-45})$$

where

$$m = \frac{\text{M.W.}}{6.02 \times 10^{23}} \equiv \text{mass of molecule (g)}$$

$$T = 300^\circ\text{K} \equiv \text{ambient temperature}$$

$$k = 1.38 \times 10^{-16} \equiv \text{Boltzmann constant}$$

$$P \equiv \text{pressure (dynes/cm}^2\text{)}$$

$$\text{M.W.} \equiv \text{molecular weight.}$$

This becomes:

$$\mu = 2.03 \times 10^{21} \frac{P}{(\text{M.W.})^{1/2}}$$

where P is now in Torr.

The sticking rate of carbon atoms from a particular gas ($\text{C}_n\text{H}_x\text{O}_y$) is given by

$$n\epsilon\mu = \frac{2.03 \times 10^{21} P}{(\text{M.W.})^{1/2}} n\epsilon \quad .$$

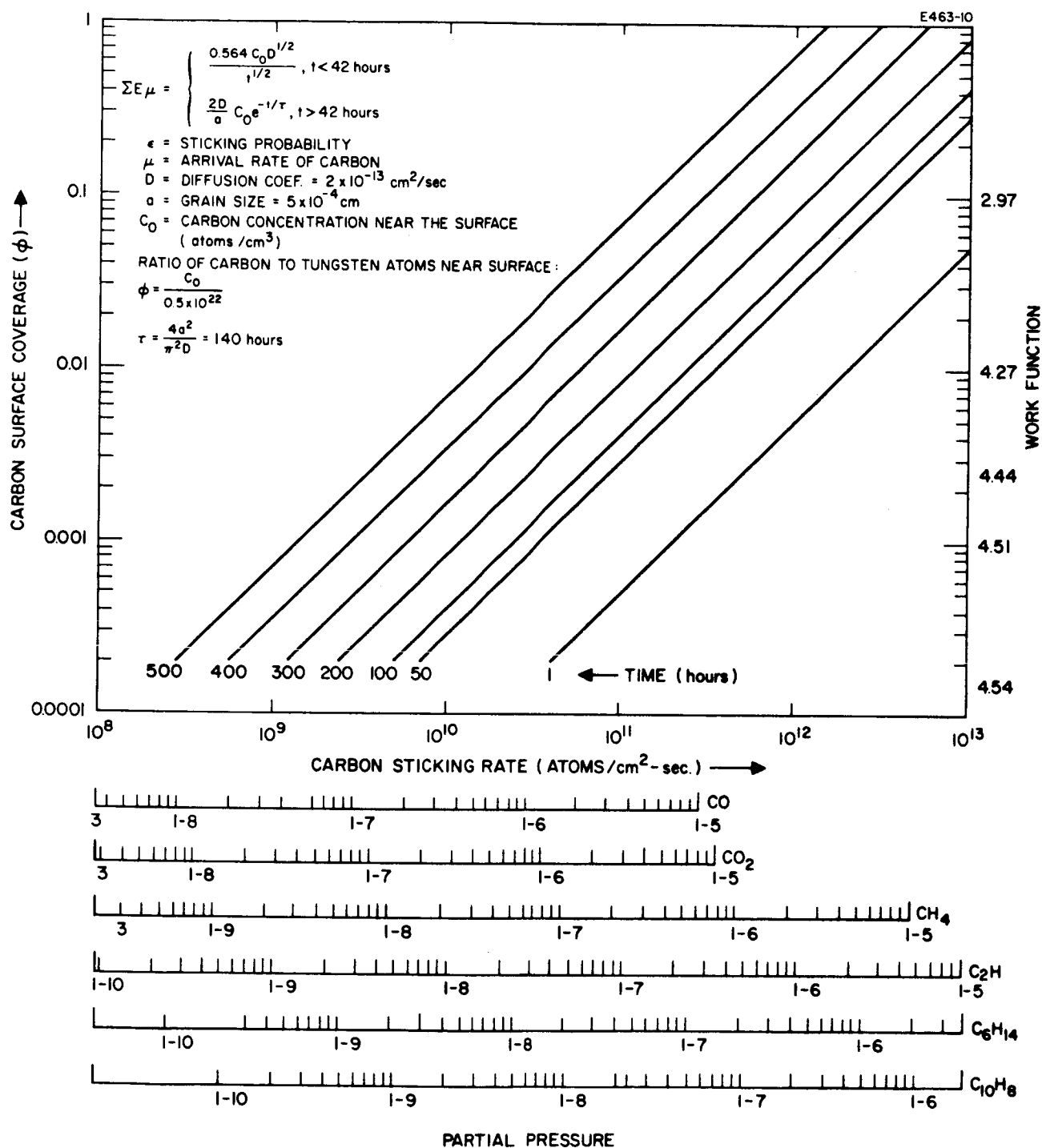


Fig. IV-88. Equilibrium surface coverage on tungsten versus carbon sticking rate for a 5 μ grain at 1600°K.

The following is a list of sticking probabilities given in Ref. IV-17.

TABLE IV-5
Sticking Probabilities of Carbon Atoms Contributed
by Various Gases

Chemical	Formula	Molecular Weight	Reaction Probability
Carbon Monoxide	CO	28	0.0001
Carbon Dioxide	CO ₂	44	CO ₂ → CO + O
Methane	CH ₄	16	0.0010
Ethylene	C ₂ H ₄	28	0.0015
Ethanol	C ₂ H ₆ O	46	0.0010
Acetone	C ₃ H ₆ O	58	0.0015
Benzene	C ₆ H ₆	78	0.0027
Hexane	C ₆ H ₁₄	86	0.0020
Xylene	C ₈ H ₁₀	106	0.0025
Naphthalene	C ₁₀ H ₈	128	0.0030

For a particular gas, the partial pressure is thus related to the carbon sticking rate by a constant factor, consisting of the molecular weight of the gas, the number of carbon atoms in the particular gas molecule, and the reaction probability. The relationship is illustrated by the superposition of the log scales of Fig. IV-89. For example, 10^{-8} mm of C₂H₄:

$$\underbrace{10^{-8}}_{\text{partial pressure}} \times \frac{2.03 \times 10^{21}}{(28)^{1/2}} \underbrace{(1.5 \times 10^{-3})}_{\text{sticking probability}} \underbrace{(2)}_{\text{carbon atoms}} = 1.1 \times 10^{10} \frac{\text{atoms}}{\text{cm}^2\text{-sec}}$$

Thus, the C_2H_4 scale at 10^{-8} mm lines up with a sticking rate of 1.1×10^{10} atoms/cm²-sec.

The work function versus surface coverage relationship from Ref. IV-11 appears as follows:

TABLE IV-6
Tungsten Work Function as a Function
of Surface Coverage of Carbon

θ	Work Function, eV
0.0001	4.54
0.001	4.51
0.0025	4.44
0.01	4.27
0.1	2.97

It can be seen that the work function does not significantly change until a surface coverage of ~ 0.0025 (corresponding to a change of 0.1 eV) is achieved. The length of time required for an ionizer grain to contaminate to a surface coverage of 0.0025 may be approximately known by considering the residual gas spectrum of carbon carrying molecules described in Ref. IV-18 (evaporator B with Meissner trap). The total pressure is 10^{-6} Torr.

Table IV-5 indicates that the sticking probability for carbon atoms in most molecules other than CO and CO₂ is about 0.002. For CO and CO₂ the value is 10^{-4} . Adding the arriving carbon from molecules 3 through 6 in Table IV-7 gives 3.5×10^{12} carbon atoms/cm²-sec. Multiplication by 0.002 results in a sticking rate of 0.7×10^{10} atoms/cm²-sec. To this we add the product of 2.1×10^{13} (arrival rate of carbon

TABLE IV-7

Typical Residual Gas Spectrum and Associated
Carbon Atom Arrival Rates

Molecule	Partial Pressure	Arrival Rate, μ	Number of Carbons, n	$n\mu$
1. CO	5×10^{-8}	2×10^{13}	1	2×10^{13}
2. CO ₂	3×10^{-9}	10^{12}	1	10^{12}
3. CH ₄	10^{-10}	6×10^{10}	1	6×10^{10}
4. C ₃ H ₈	2×10^{-9}	6×10^{11}	3	18×10^{11}
5. C ₄ H ₁₀	1×10^{-9}	3×10^{11}	4	12×10^{11}
6. C ₅ H ₁₂	4×10^{-10}	9×10^{10}	5	45×10^{10}

from CO and CO₂) times 0.0001 (sticking probability for CO and CO₂). Thus the total carbon sticking rate for a typical vacuum system of residual gases is

$$\sum \epsilon \mu n = 10^{10} \frac{\text{atoms}}{\text{cm}^2\text{-sec}} .$$

Location of a 10^{10} sticking rate on Fig. IV-88 indicates that the surface coverage reaches 0.0025 at about 350 hours. It must be emphasized that this result is an upper limit, i.e., it is only valid if the ionizer grain had no appreciable carbon level to begin with. Otherwise, the contamination time will be faster.

An interesting relationship results by holding partial pressure constant in Fig. 88 and plotting work function versus time. This cross plot is presented in Fig. IV-89 where the dashed line is directly from the 1600°K curves, while the solid lines are for 1400°K. It may be observed that for the same partial pressure (10^{-6}), the work function at

1400°K drops faster initially than at 1600°K, but eventually both approach the same low value. This is to be expected, since carbon diffuses away from the surface faster at the greater temperature. Eventually, however, the whole grain becomes contaminated.

The carburizing environment specified in Fig. 89 is:

$$\text{M.W.} = 28$$

$$\text{atom sticking probability/molecule} = 0.001.$$

These may be considered normalized conditions, so that any arbitrary conditions may be handled. For example, consider C_{10}H_8 at a partial pressure of 10^{-7} Torr. A carbon atom in this molecule has a sticking probability 10 times greater than for a single carbon carrying molecule (for which 0.001 applies). Thus the effective pressure is not 10^{-7} , but 10^{-6} , based on this consideration alone. Another consideration arises because of the difference in molecular weight. The arrival rate of C_{10}H_8 is a factor of $\sqrt{28/128}$ ($= 0.47$) less than the arrival rate for a molecule of molecular weight 28. Thus the effective partial pressure for C_{10}H_8 at 10^{-7} Torr is

$$(10^{-7})(10)(0.47) = 4.7 \times 10^{-7} \text{ Torr.}$$

The effective pressure is thus a factor of five over the apparent pressure.

When several carbon carrying gases are present simultaneously, the composite effective pressure will be the sum of the individual effective pressures. It is emphasized that CO and CO_2 have a reaction probability one tenth that of the other carbon carrying molecules. This must be considered when determining effective pressures of these gases.

Figure IV-89 indicates that for pressures greater than 10^{-6} Torr, drastic changes in work function occur within the first hour of operation ($> 1 \text{ eV}$ at 10^{-5}). With pressures less than 10^{-7} , it appears that 100 hours may be reached with little work function degradation ($1/10 \text{ eV}$).

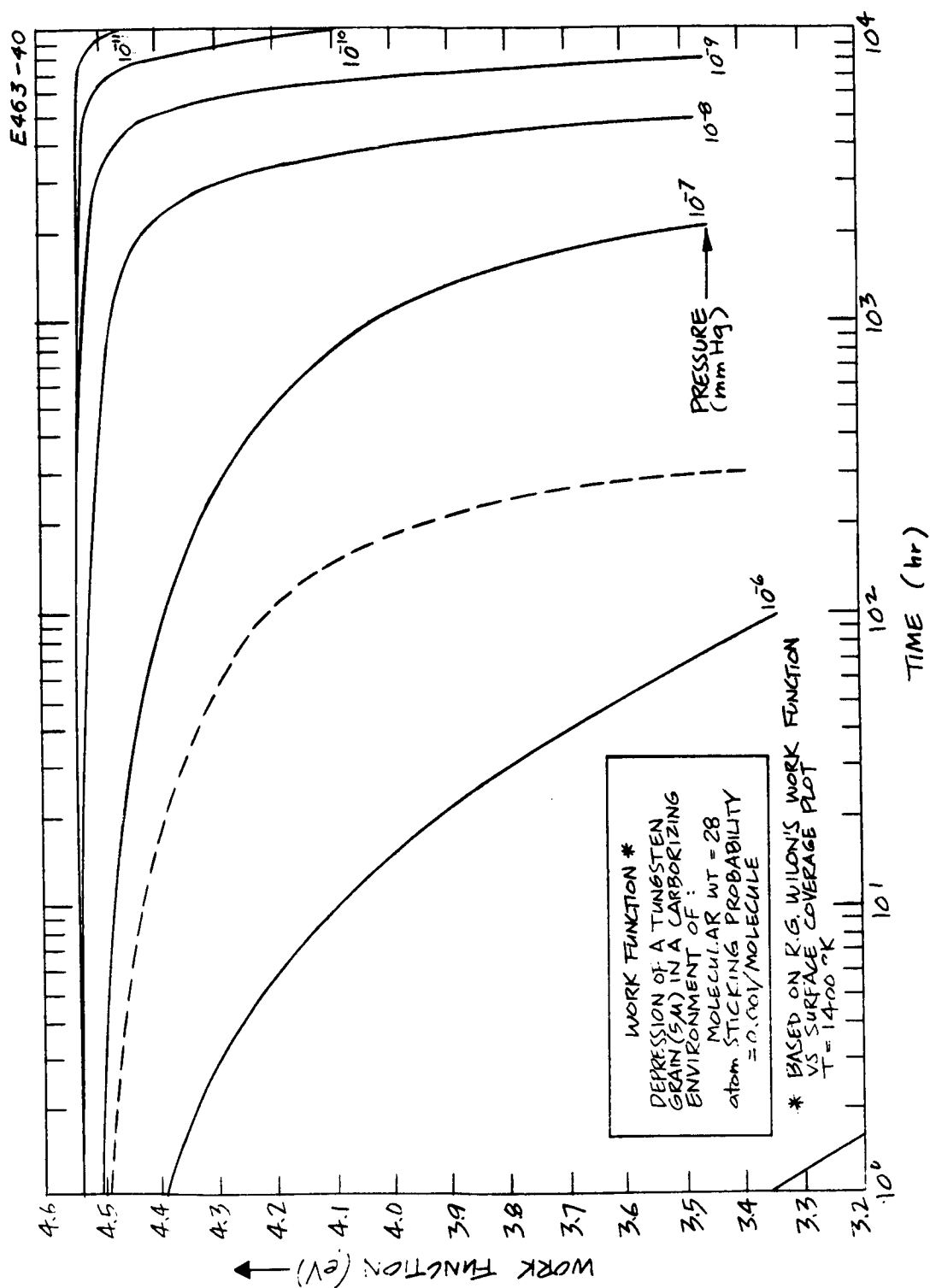


Fig. IV-89. Work function (based on Wilson's (Ref. IV-11) work function versus surface coverage plot). Depression of a tungsten grain (5 μ) in a carburizing environment of molecular weight 28. Atom sticking probability = 0.001/molecule. $T = 1400^{\circ}\text{K}$.

Similarly, for 1000 hours 10^{-8} Torr is required. Moreover, as the operating time approaches 10,000 hours, the effect becomes increasingly critical, requiring partial pressures as low as 10^{-11} .

4. Ion Engine Test Console

A test console was developed during the contract period. The console provides the various powers to the engine with overload protection and also serves as a central point for instrumentation of the engine parameters.

Power supplies include a variable high voltage ionizer supply, a variable high voltage accel supply, heater supplies which operate at the ionizer electrode potential, and a heater supply which operates at the accel electrode potential. A low voltage dc supply operating at the ionizer electrode potential provides power to the cesium solenoid valve.

Protection circuitry includes sensing of arcs and subsequent high voltage supply turn-off for arcs over 1 A for the ionizer supply and over 0.2 A for the accel supply. The solenoid power supply is off while the arc overload is in operation. The arc is allowed to clear before the high voltages are reapplied to the engine and the solenoid cesium supply valve is turned on, thus restarting the engine. Besides arc protection, the system will shut down completely when the average current overload for either the accel or ionizer supply is exceeded. With this type of shutdown, the operator must restart the console. The arc protection circuitry also shuts down the entire system in the event the total arc count exceeds the preset allowed count. The system is therefore not allowed to indefinitely start, shut down, restart, etc.

Instrumentation includes an eight-channel Sanborn recorder, two Varian strip chart recorders with a five-position switch on the negative and a 10-position switch on the positive recorder, four direct reading temperature indicator meters, meters to measure the accel supply voltage and current, the ionizer supply voltage and current, the sums of the accel and ionizer voltage (the accelerating voltage) and the net current in the beam.

A neutral particle detector is included as a part of the engine assembly. The console includes the filament power, collector voltage, deflector voltage, a micro-microammeter to measure the output from the detector, power to open and close the shutter on the neutral detector, and a timing switch to permit periodic operation of the detector.

The Sanborn recorder provides a permanent record of the accel supply current, accel supply voltage, ionizer supply current, ionizer supply voltage, and neutral detector output. This recorder is at ground potential and thus receives its input through voltage dividers to ground. The Varian recorders operate at the potential of the high voltage supplies. One recorder is used to make precision millivolt readings of the ionizer, focus electrode, flanges, radiator, and cesium boiler thermocouples. A 10-position switch permits the operator to select the function to be monitored on this recorder. The recorder is isolated from ground and connected to the ionizer supply. The second Varian recorder is used to measure the temperature of the accel electrode. The input to this instrument is through a five-position switch. A detailed description of functions that can be monitored on these recorders is presented in the summary specifications which appear later in this section.

Engine control by this console is provided by individual parameter control, i.e., the boiler temperature is controlled only as a function of its temperature, the ionizer temperature is controlled only as a function of their output voltage. Other engine parameters such as voltage with respect to engine perveance, beam current, neutral fraction, etc., are not included in this control system. Two on-off Honeywell units are used to regulate the boiler and ionizer temperature to the set point established by the operator. The high voltage supplies are regulated, in a convenient manner, by using a series tube, amplifier, and a variable reference which is coupled to a remotely controlled variac.

Figure IV-90 shows a front view of the console which contains the low voltage power supplies, direct reading meters, recorders, and neutral detector instruments. The high voltage supplies are housed in the console to the right of the control console.

M 3200

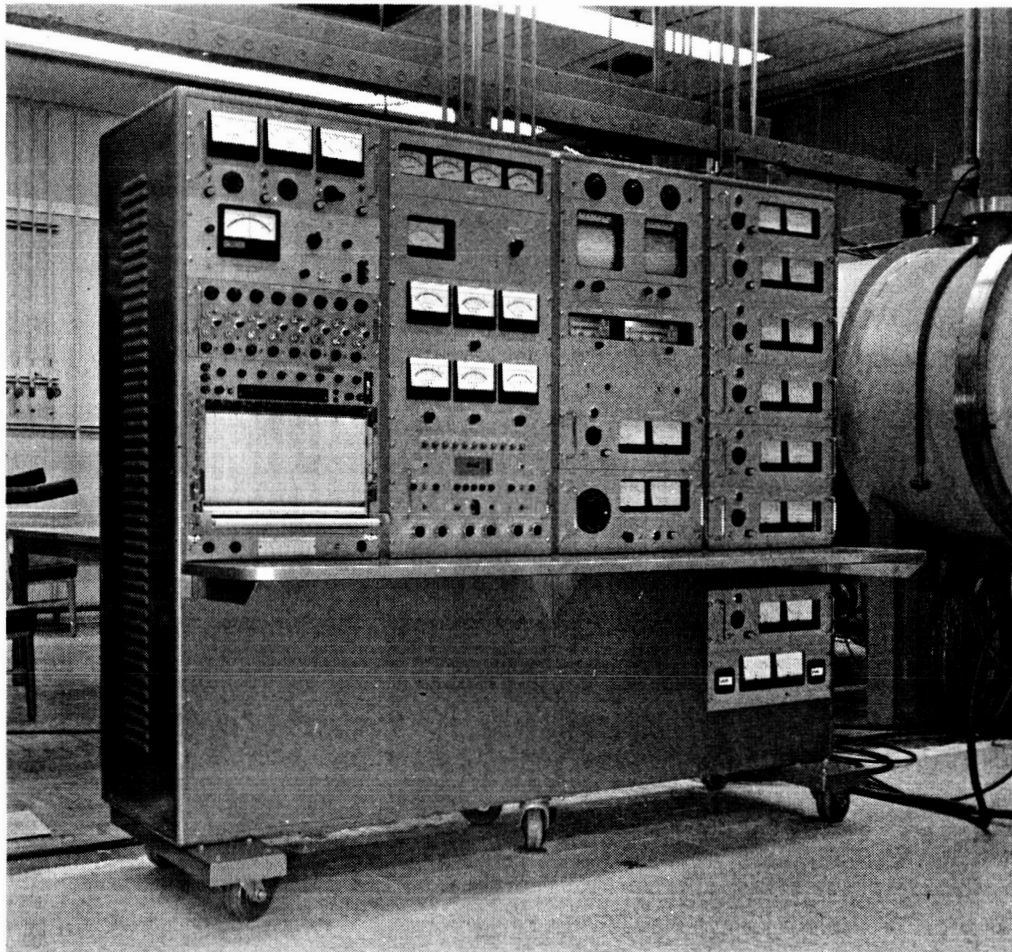
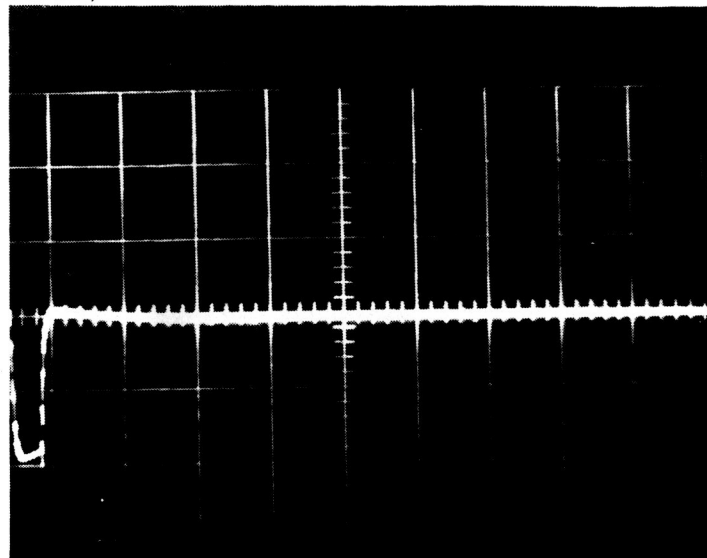


Fig. IV-90. Ion engine life test console.

The high voltage power supplies have been evaluated to obtain their steady state and transient characteristics. The ionizer high voltage power supply has a fundamental source impedance of $700\ \Omega$ as determined by application of a $10\ \mu\text{sec}$ shorting pulse load to the output terminals. The application of the narrow pulse load is used to simulate a momentary arc. Figure IV-91 shows oscilloscope photographs of the ionizer power supply (less a series inductor) transient response. It is interesting to note that the pulse load does not result in an overshoot in the output voltage of the power supply. The power supply used with an engine, however, has an inductor in the output circuit. The purpose of the inductor is to increase the response time of the output voltage after application of the equivalent arc load to the system. Figure IV-92 shows the ionizer power supply voltage drops from 4 kV to 2.8 kV after application of the arc load. The peak current increased during the pulse from a steady state level of 0.75 A to approximately 1 A. The peak current, with the series inductor, was thus limited for this $20\ \mu\text{sec}$ simulated arc. The response time for the voltage to stabilize increased from $10\ \mu\text{sec}$ to $100\ \mu\text{sec}$. It is believed that the latter condition is more desirable from the engine point of view since the drop in voltage permits the arc to be extinguished; the peak current thus has been limited. However, the recovery period is short when compared with the period between arcs, and therefore the amount of off-perveance engine operation becomes insignificant.

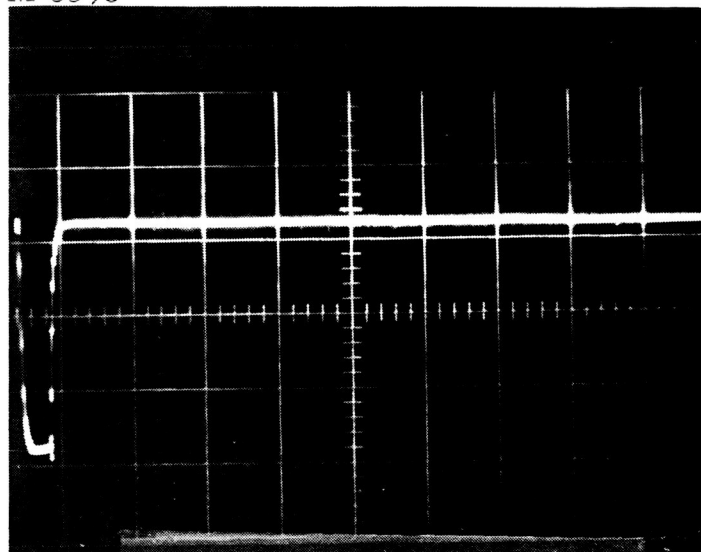
The accel supply has also been evaluated for its transient response to an equivalent arc load. In this case, the equivalent $10\ \mu\text{sec}$ arc load resulted in a voltage drop of 2.8 kV from 4 kV. The time required for the voltage to stabilize, after application of the pulse, was $140\ \mu\text{sec}$. No overshoot was observed. The peak current increased from a steady state level of 0.080 A to approximately 0.160 A. Figure IV-93 illustrates the transient characteristics of the accel power supply. Steady state regulation measurements have been made on both the ionizer and accel supplies. The ionizer supply output is regulated to better than

M 3595



(a)

M 3596

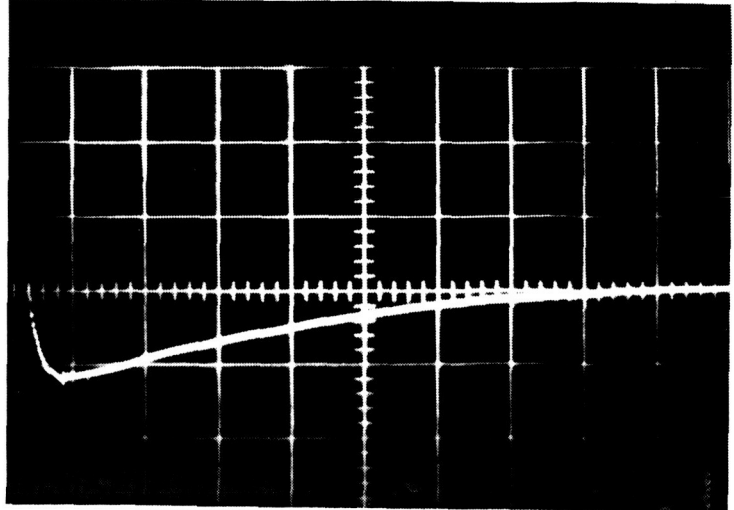


(b)

Fig. IV-91. Traces showing (a) voltage and (b) current response of ionizer supply to a 10 μ sec wide short circuit load (simulated arc). Measurements made without an inductor in output of supply.

M 3593

(a)



M 3594

(b)

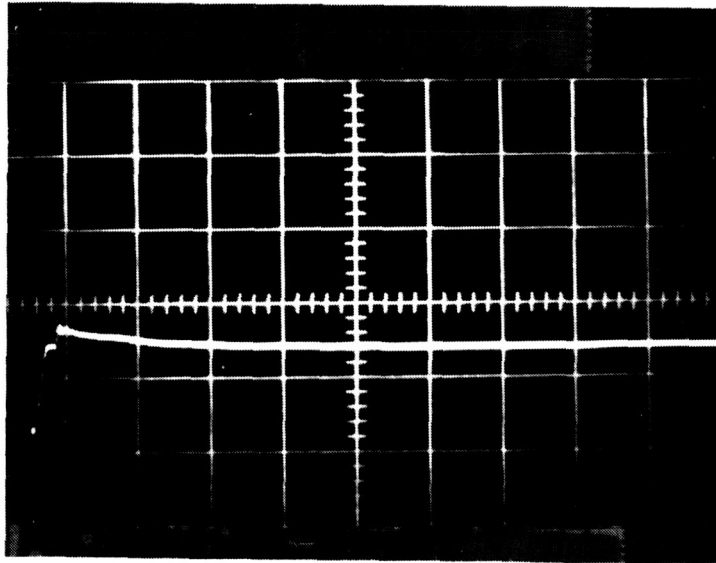
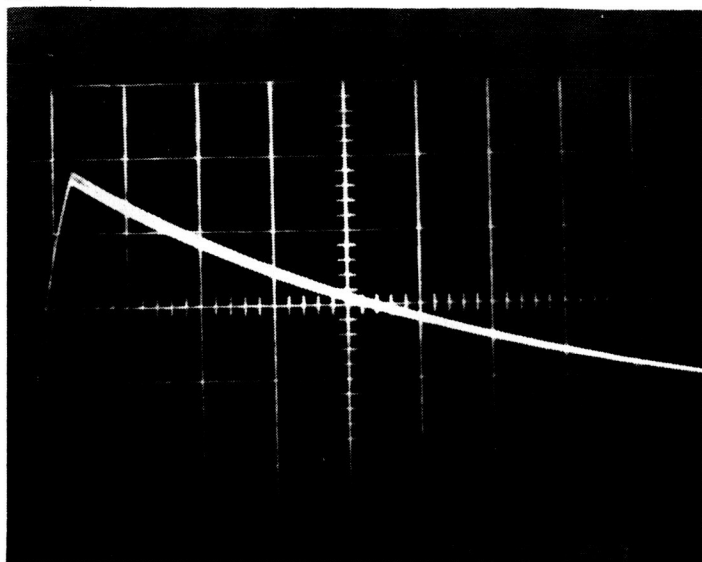


Fig. IV-92. Traces showing (a) voltage and (b) current response of the ionizer supply to a 10 μ sec wide short circuit load (simulated arc). Measurements made with a 10 H inductor in series with output of supply.

M 3598



(a)

M 3597

(b)

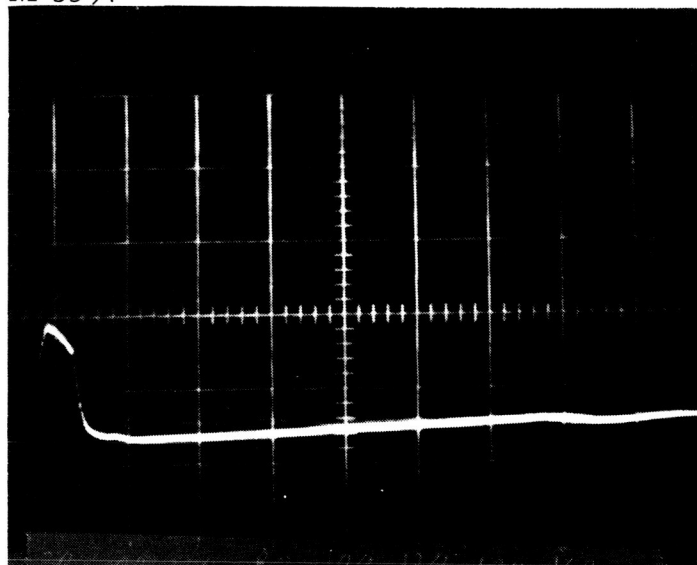


Fig. IV-93. Traces showing (a) voltage and (b) current response of the accel supply to a $10\ \mu\text{sec}$ wide short circuit load (simulated arc). Measurements made with a $10\ \text{H}$ inductor in series with output of supply.

$\pm 2\%$ for load variation to 1.1 A at 7.4 kV. A similar degree of regulation is attained by the accel supply for loads to 100 mA. Table IV-8 presents the load regulation data for both supplies.

TABLE IV-8

Ionizer Power Supply and Accel Power Supply Regulation Data

Ionizer		
Voltage, kV	Current, mA	Change, %
3.0	860	3.3
3.1	0	
5.4	980	
5.6	0	3.7
6.5	980	3.07
6.7	0	
6.9	1040	
7.0	0	1.40
7.4	1100	2.7
7.6	0	
Accel		
3.0	30	0.67
3.02	0	
5.0	50	
5.10	0	2.0
7.0	70	0.28
7.02	0	
9.0	90	
9.01	0	0.11
10.0	98	0.5
10.05	0	

SUMMARY SPECIFICATION OF THE CONSOLE

Input Power: 480 V $\pm 10\%$, 60 cycle, 3 phase
115 V $\pm 10\%$, 60 cps, 1 phase

I. Output Power

A. Miscellaneous (ac) power supplies (unregulated)

1.
 - a) 50 V at 5 A, ac output
 - b) Adjustment range 0-100%
 - c) Operates at ionizer potential and insulated for 10 kV. Four power supplies are available for functions such as the super heater, the flange heaters, and the cesium storage heater.
2.
 - a) 120 V at 20 A, ac output
 - b) Adjustment range 0-100%
 - c) Operates at ionizer potential and insulated for 15 kV. This power supply is for the ionizer heater and is controlled to maintain constant ionizer temperature by a Honeywell controller.
3.
 - a) 50 V at 5 A, ac output
 - b) Adjustment range 0-100%
 - c) Operates at ionizer potential and is insulated for 10 kV. This power supply is for the boiler heater and is controlled to maintain constant boiler temperature by a Honeywell controller.
4.
 - a) 50 V at 15 A, ac output
 - b) Adjustment range 0-100%
 - c) Operates at accel potential and is insulated for 10 kV. This power supply is for the accel electrode heater.

5.
 - a) 50 V at 1.0 A, dc output
 - b) Adjustment range 0-100%
 - c) Operates at ionizer potential and insulated for 10 kV. This power supply operates the cesium solenoid valve.
6.
 - a) 15 V at 60 A, ac output, center tapped
 - b) Adjustment range 0-100%
 - c) Operates at ground potential. This power supply is used to heat the neutralizer filaments.

B. Accel Power Supply

- a) 10 kV at 0.200 A, dc output
- b) Adjustable from 100 V to 10 kV
- c) Regulation (steady state) $\pm 2\%$ for a 0 to 100 mA load change
- d) Transient response (10 μ sec shorting pulse load); voltage drops to 25% of V_{ss} , current increases to $2 I_{ss}$. Voltage time constant 140 μ sec.
- e) Remote controlled from the main console.

C. Ionizer Power Supply

- a) 8 kV at 1.25 A, dc output
- b) Adjustable from 100 V to 8 kV
- c) Regulation (steady state) $\pm 2\%$ for a 0 to 1 A load change
- d) Transient response (10 μ sec shorting pulse load); voltage drop to 30% V_{ss} . Current increases to $1.25 I_{ss}$. Voltage time constant = 100 μ sec.
- e) Remote controlled from the main console.

D. Collector Power Supply

- a) 500 V at 1.5 A, dc output
- b) Adjustment range 0-100%
- c) Operates at ionizer potential and is insulated for 10 kV. This power supply provides the beam current when a decel collector system is used.

E. Electron Trap Power Supply

- a) 140 V at 1.0 A, dc output
- b) Adjustment range 0-100%
- c) Operates at ground potential. This power supply provides the electron trap voltage to prevent neutralizer electrons from entering the beam decel collector.

F. Diverter Electrode Power Supply

- a) 5000 V at 0.100 A
- b) Adjustment range 0-100%
- c) Operates at accel potential and is insulated for 15,000 V

II. Controls

A. Ionizer Temperature Control

- a) Type: on-off control of ac heater power
- b) Input: W26%Re-W5%Re T.C. 10 Ω resistance
- c) Range: 0°C to 1600°C direct readout
- d) Implemented with: Honeywell Pyro-Vane Model No. MH 105C204PS15
- e) Operates at ionizer potential and is insulated for 10 kV.

B. Boiler Temperature Control

- a) Type: On-off control of ac heater power
- b) Input: Iron-constantan T.C. $10\ \Omega$ resistance
- c) Range: 0°C to 400°C direct readout
- d) Implemented with: Honeywell Pyro-Vane Model No. MH105C204PS15
- e) Operates at ionizer potential and is insulated for 10 kV

III. Instruments

A. Eight Channel Strip Recorder - operates at ground potential

- a) Channel 6 input: 0-8 V dc equivalent to (0 to 8 kV) ionizer gain setting 2.0 V/cm
- b) Channel 8: 0-10 V dc equivalent to (0 to 10 kV) of accel voltage - gain setting 2.0 V/cm
- c) Channel 5 input: 0-10 V dc equivalent to (0 to 1) A ionizer current - gain setting 2.0 V/cm
- d) Channel 7 input: 0-10 V dc equivalent to (0 to 100) mA accel current - gain setting 2.0 V/cm
- e) Channel 3 input: 0-1.0 V dc equivalent to (0 to 10) μA of neutral detector readout - gain setting 0.2 V/cm
- f) Three spare channels

B. One Channel Strip Recorder, Varian Type G-11A - operates at ionizer potential

Input: 10-position, 2-pole switch

- a) Pos. 1 focus electrode T.C. F.S. output 50 mV
- b) Pos. 2 focus electrode T.C. F.S. output 50 mV
- c) Pos. 3 ionizer T.C. F.S. output 50 mV
- d) Pos. 4 ionizer T.C. F.S. output 50 mV
- e) Pos. 5 focus base plate T.C. F.S. output 50 mV
- f) Pos. (6 to 10) are spares

C. One Channel Strip Recorder, Varian Type G-11 — operates at accel potential

Input: five-position switch

- a) Pos. 1 accel T.C. F.S. output 50 mV
- b) Pos. 2 accel heater T.C. (fixed end)
F.S. output 50 mV
- c) Pos. 3 accel heater T.C. (spring end)
F.S. output 50 mV
- d) Pos. 4 and 5 are spares

D. Current and Voltmeters

These meters are at ground potential:

- | | |
|---|----------|
| 1. Accel Current Meter Range | 0-3 mA |
| | 0-10 |
| | 0-30 |
| | 0-100 |
| | 0-300 |
| | Off |
| 2. Ionizer and Net Current Meters Range | 0-3 mA |
| | 0-15 |
| | 0-30 |
| | 0-150 |
| | 0-300 |
| | 0-1500 |
| | Off |
| 3. Ionizer Voltage | 0-10 kV |
| 4. Accel Voltage | 0-150 kV |
| 5. Total Voltmeter | 0-7.5 kV |
| | 0-15 kV |
| | Off |

These meters are at ionizer potential:

- | | |
|-------------------------------------|-------------------------|
| 6. General heater supplies per IA.1 | 0-50 V ac
0-5 A ac |
| 7. Ionizer heater supply per IA.2 | 0-150 V ac
0-25 A ac |
| 8. Boiler heater supply per IA.3 | 0-50 V ac
0-5 A ac |

These meters are at accel potential:

- | | |
|---------------------------------|------------------------|
| 9. Accel heater supply per IA.4 | 0-50 V ac
0-25 A ac |
|---------------------------------|------------------------|

These meters are at ionizer potential:

- | | |
|------------------------------------|-----------------------|
| 10. Solenoid valve supply per IA.5 | 0-50 V dc
0-1 A dc |
|------------------------------------|-----------------------|

These meters are at ground potential:

- | | |
|--|-----------------------|
| 11. Neutralizer heater supply per IA.6 | 0-50 V ac
0-2 A ac |
| 12. Neutralizer electron output per IA.6 | 0-2 A dc |

These meters are at ionizer potential:

- | | |
|------------------------------------|--------------------------|
| 13. Collector power supply per I-D | 0-500 V dc
0-1.5 A dc |
|------------------------------------|--------------------------|

These meters are at ground potential:

- | | |
|--|------------------------|
| 14. Electron trap power supply per I-E | 0-200 V dc
0-1 A dc |
|--|------------------------|

These meters are at accel potential:

- | | |
|---|-----------------------------|
| 15. Diverter electrode power supply per I-F | 0-6000 V dc
0-0.030 A dc |
|---|-----------------------------|

E. Direct Reading Temperature Meters

1. 0-520°C iron constantan T.C. requires 10 Ω external resistance
2. 0-520°C iron constantan T.C. requires 10 Ω external resistance
3. 0-520°C iron constantan T.C. requires 10 Ω external resistance
4. 0-520°C iron constantan T.C. requires 10 Ω external resistance

(These meters are insulated above ground and are usually used to measure temperatures at the potential of the ionizer.)

F. Neutral Detector Instruments

Micromicroammeter: Hewlett-Packard type

425 A R

Ranges from 0-3 mA to 0-10 μ A

Heater filament supply 0-10 V at 10 A

Ion deflector voltage of 0-250 V dc

Collector voltage of 0-150 V dc

Shutter supplies (2) (momentary on) — 110 V ac-open solenoid, 110 V ac-closed solenoid

Shutter timer — open time 5 sec, close time 2 min
(solenoid power is off for 2 sec at the onset and trail edge of the 5-sec on signal)

IV. Overload Protection

A. Ionizer Supply

1. Steady state overload — adjustable from 100 mA to 1.0 A for the ionizer supply
2. Arc overload — adjustable from 2 to 10 A peak current pulse

B. Accel Supply

1. Steady state overload — adjustable from 10 to 100 mA for the accel supply
2. Arc overload — adjustable from 0.200 A to 10 A peak current pulse

C. Arc Count — adjustable from 10 to 50 arcs required to shut down all power to the console. The total number of arcs are read out on all electromechanical digital counter.

D. Arc Restart — the time required to reapply high voltages and power to the solenoid valve are separately adjustable from 2.0 sec to 120 sec.

V. ION OPTICS STUDIES

The Model 70 ion-optical system shown schematically in Fig. V-1 was developed in the previous phase of this program and has been used as the basic design in linear strip contact ion engines to date. This optical system provides high perveance (for cesium ions) with minimum accel electrode interception. The electrolytic tank trajectory tracer showed that the ion beam would be accelerated from the engine with less than 10^{-5} interception of beam ions with the accel electrodes. In addition, detailed digital computer studies of the optics showed that the current density profile from the center to the edge of a linear strip was uniform to within 20% and for 10 kV of accelerating voltage a minimum current density of 15 mA/cm^2 could be drawn from the ionizer.

Studies of the paths of ions created by charge exchange collisions showed that these ions intercepted the accel electrodes along the beam edges and caused a calculable erosion of the electrode. The rate of this erosion is directly related to the efflux of neutral cesium atoms from the ionizer and thus lifetime of the structure is strongly dependent on the ionizing capabilities of the porous ionizer.

Analysis of the paths of neutral cesium atoms which effuse from the ionizer indicates that a significant portion of the atoms scatter from the accel electrodes and fall onto the focus electrodes, which, due to their proximity to the ionizer, may be at sufficient temperature to cause surface ionization. Ions formed at the surface of the focus electrode are accelerated directly to the accel electrode and cause damaging sputtering erosion. Again, the reduction in arrival rate of neutral cesium atoms is desired and the improvement of ionizer characteristics is advantageous.

To reduce the accel erosion due to bombardment of ions from the focus electrode, it is required that the surface ionization of cesium atoms be inhibited. The methods for doing this require (a) the cooling

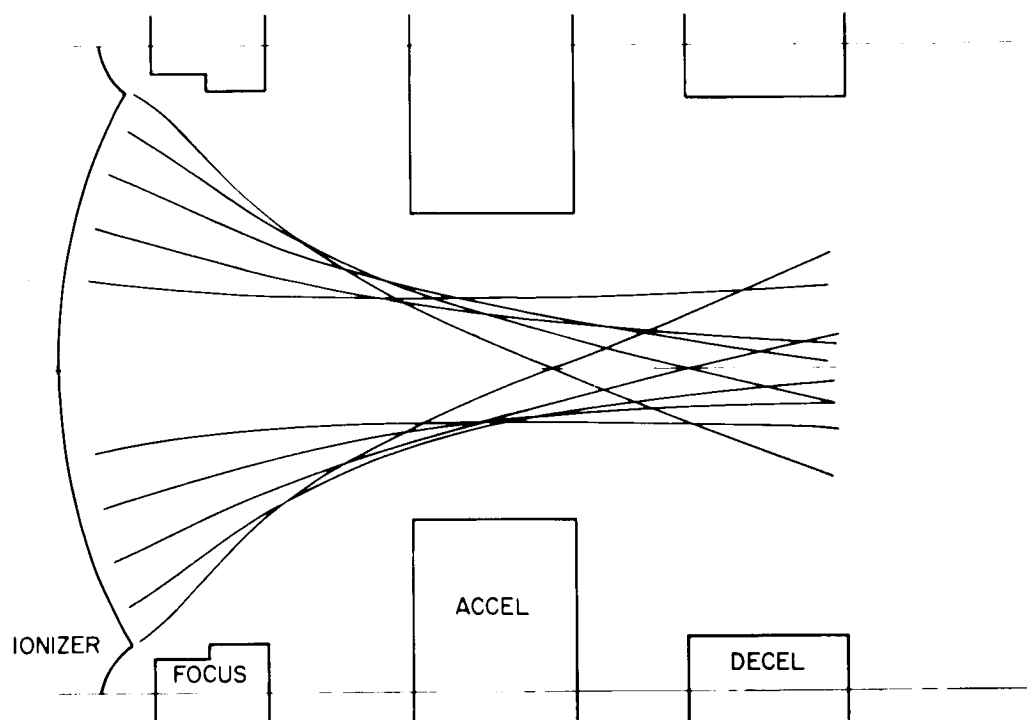


Fig. V-1. Model 70 ion optics shown with reduced space charge.

of the focus electrode to below 1000°K or (b) the selection of special electrode materials which are poor surface ionizing materials. Both the adoption of a cool focus approach and the low work function approach require the use of a precisely placed focus electrode which must operate in the high temperature region of the thruster. This presents mechanical complications, heat loss, and added weight in the engine. Thus, for engine simplicity and efficiency, it is desired to incorporate the focusing structure as an integrally mounted part of the ionizer. To this end an analytical and developmental program has been executed.

The first evaluations were made by use of the electrolytic tank trajectory plotter and digital computer calculations. The ion trajectories and ion current density profiles were examined for an ionizer whose surface was shaped to provide its own focusing protrusions. In the first configuration tested the porous ionizer was a surface of intersecting cylindrical surfaces; sharp cusps were formed to provide the focusing fields. As a starting point, the accel electrode placement and size was approximately that of the Model 70 optics. The results of digital computer analysis indicate that the majority of the beam ions clear the accel electrode (see Fig. V-2) but that ions emitted close to the knife edge do intercept the accel electrode and contribute to erosion. In addition, the current density profile shows (Fig. V-3) that the geometry is capable of extracting only a very small current density near the center of the radius but a very high density at the cusp. With such a characteristic, a uniform cesium flow through the ionizer would imply that the maximum tolerable flow density would be that of the lowest value. Shaping the thickness of the ionizer can accommodate the cesium flow to better utilize this profile but the inequality is severe and may be less desirable from a design standpoint.

Examination of an ionizer configuration in which a rectangular protrusion was attached (or machined as an integral part), between the ion emitting regions, showed more desirable characteristics (see Fig. V-4). The ion trajectories from the porous section and the edges of the

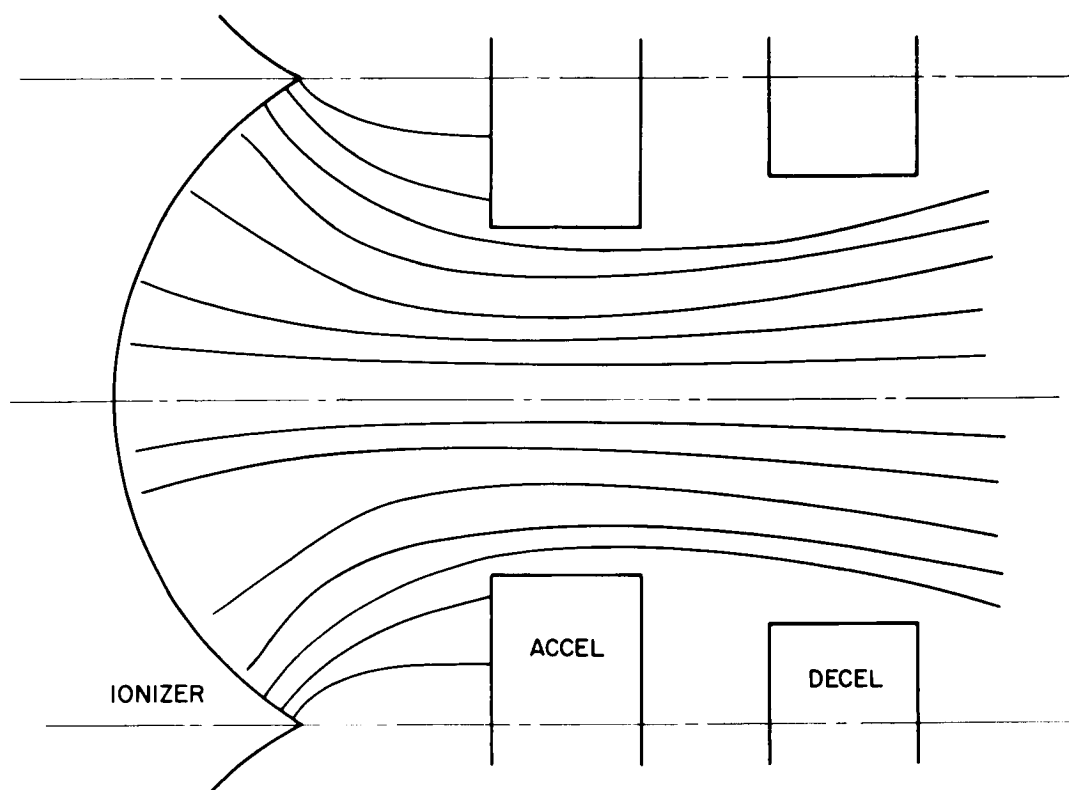


Fig. V-2. Ion trajectory plots for integral-focus optics (cusp type ionizer).

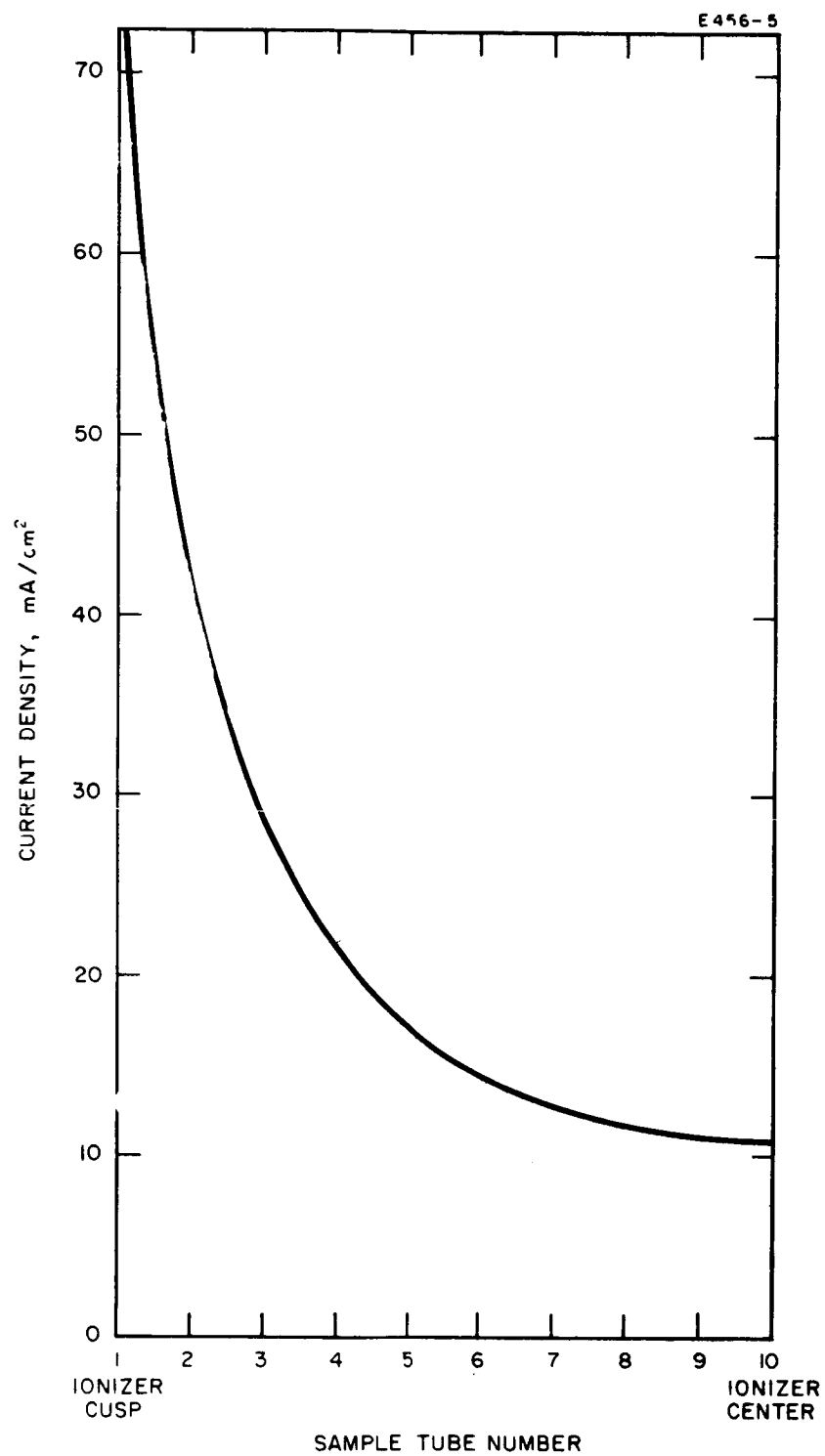


Fig. V-3. Current density distribution from cusp-type integral focus ionizer.

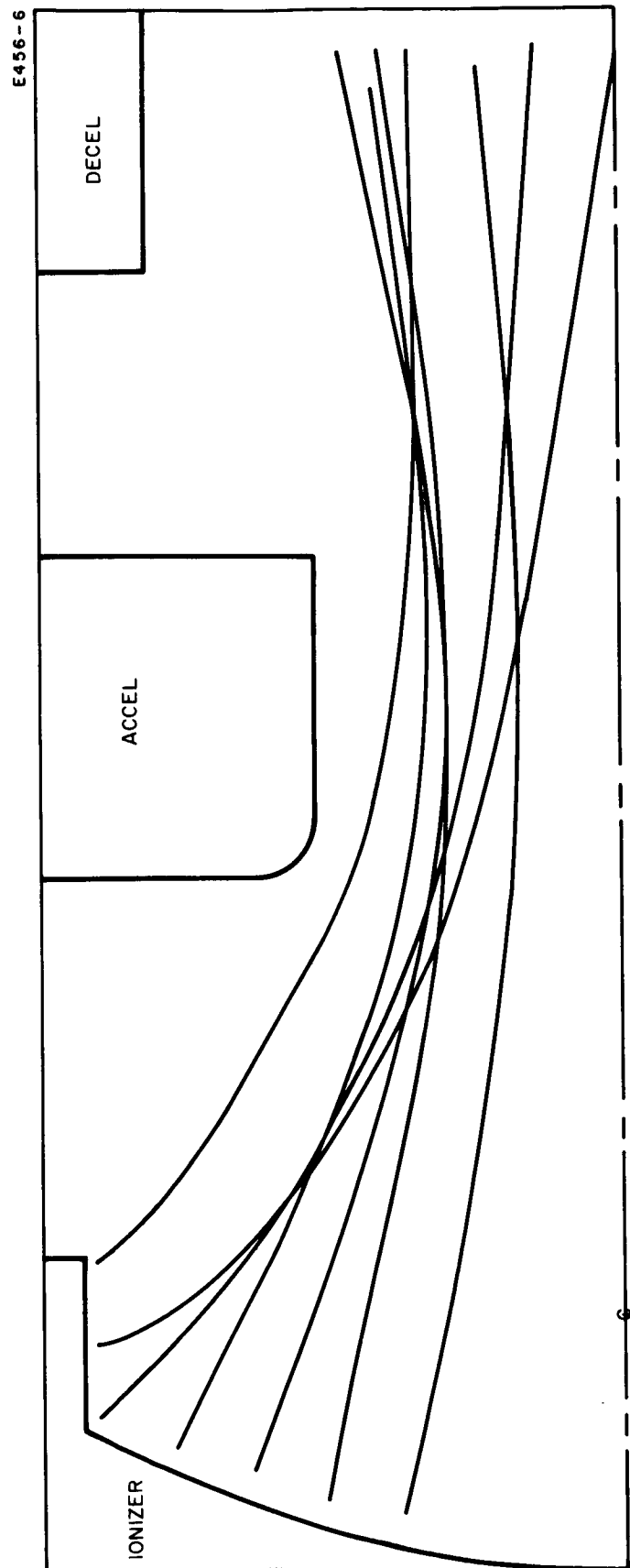


Fig. V-4. Ion trajectory plots (electrolytic tank) for integral focus optics with rectangular focusing structure.

projecting member were seen to clear the accel electrode and the current density profile was high and uniform (see Fig. V-5). Thus, the configuration is desirable except for the bad feature of the flat top on the projection which could cause ionization of scattered cesium atoms and consequent accel erosion.

A compromise between these two approaches (Fig. V-6) utilized a wedge rather than a rectangular attachment to yield a "knife-edge" focusing member. In one geometry tested, the ion trajectories cleared the accel electrode except for interception by those ions originating within approximately 0.005 in. of the edge. The spreading electric fields tend to reduce the depth of accel erosion and a system capable of 4000 hours of operation appears feasible.

A more refined test of this knife-edge configuration showed that the current density was quite high (over 15 mA/cm^2) and sufficiently uniform for high thrust engine operation. The sharp angle of this refined optics further reduces the density of accel erosion and extends the engine life. The use of a refractory focusing member, no matter how sharp, will provide the possibility of some ionization and eventual accel electrode erosion. Thus, the design which holds promise for the maximum engine lifetime might incorporate the non-ionizing properties of a material such as Al_2O_3 (or another surface ionization inhibitor) but shaped into the optimum focusing structure as illustrated by this last configuration.

In addition to the reduction of accel erosion by special ionizer design and by the use of ionization inhibiting coatings, the erosion due to charge-exchange ions may be reduced by the incorporation of a diverting electrode into the engine. The diverting electrode is placed between the accel and decel electrodes (or neutralizer in case decel electrode is eliminated) and, by operating at a more negative voltage than the accel, it tends to draw a large percentage of the charge exchange ions to it. Its location and shape are not as critical to the engine design and operation as the accelerating electrode. Thus, a greater total erosion is tolerated. Trajectory studies indicate that a factor of two to five gain in engine life may be realized by the use of such a system.

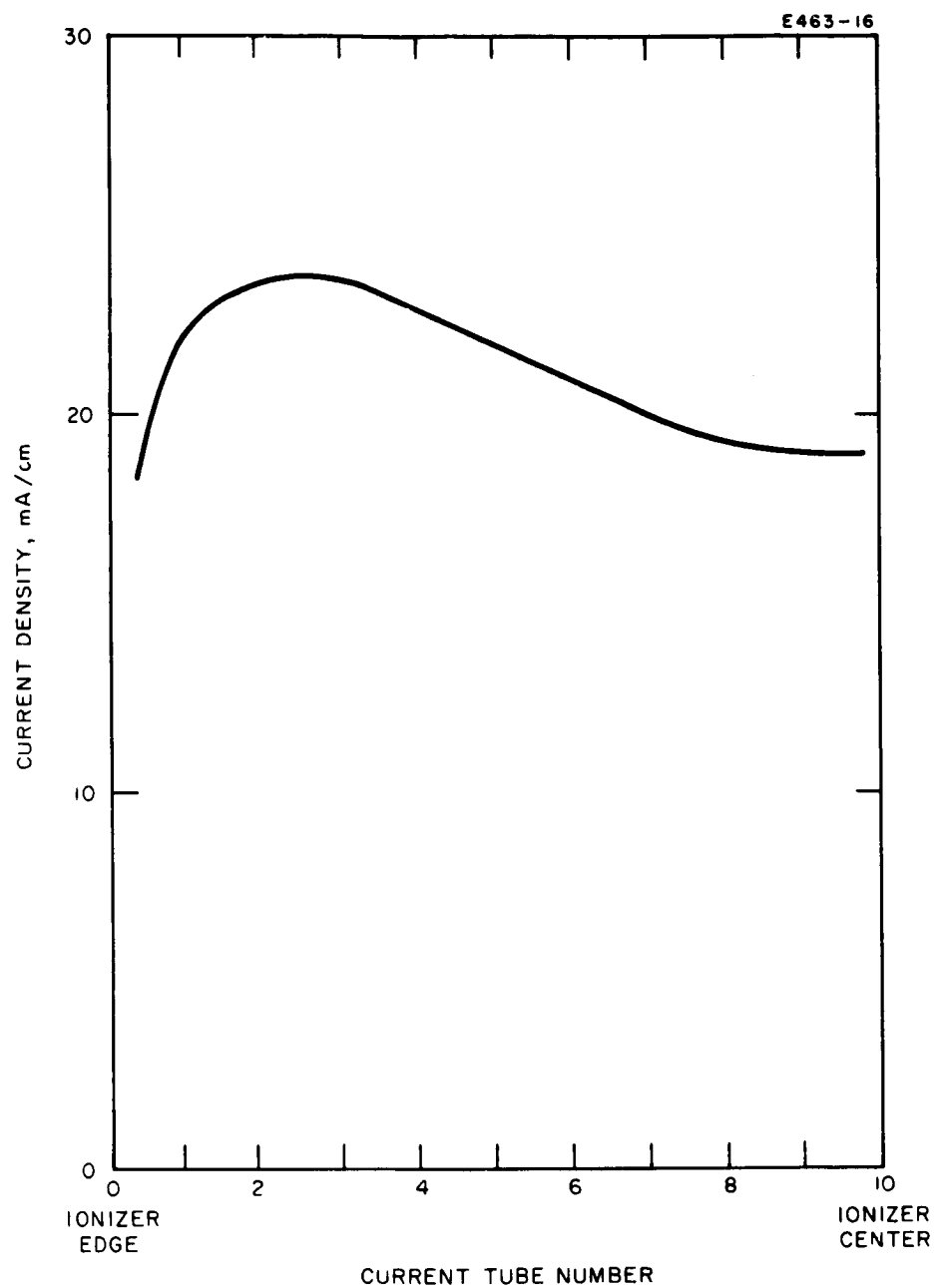


Fig. V-5. Current density plot (digital computer solution) for integral focus optics with rectangular focusing structure.

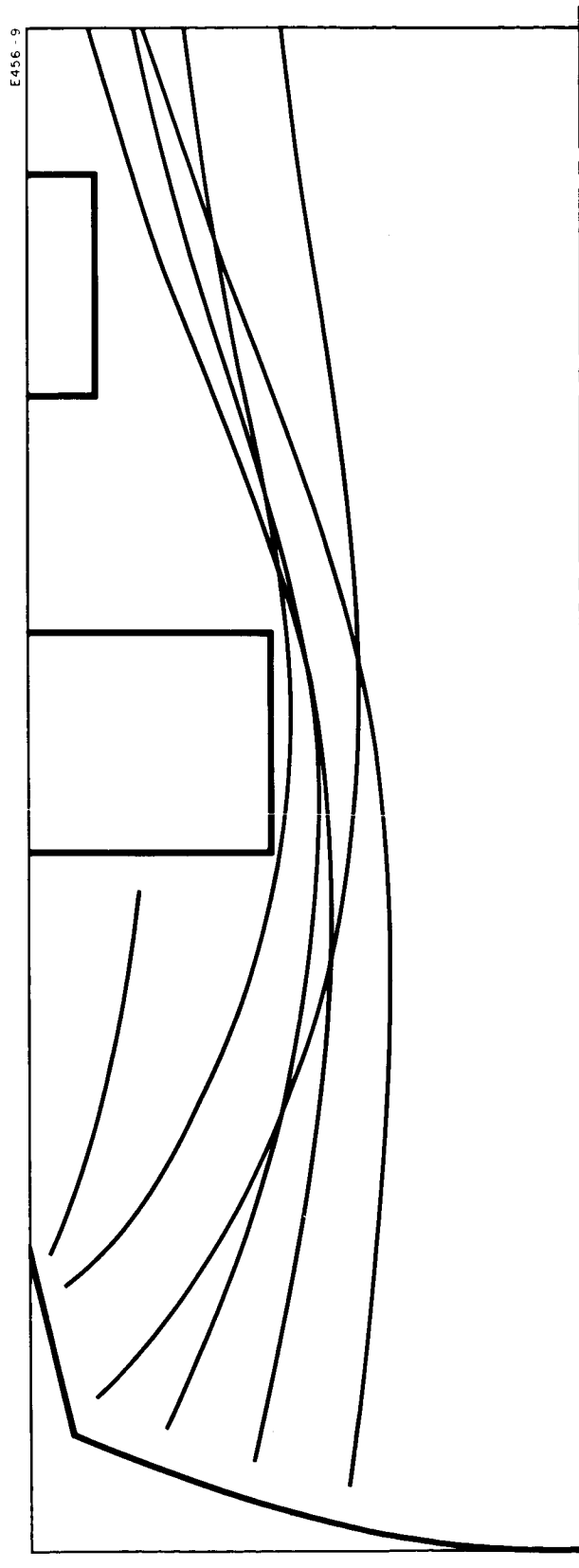


Fig. V-6. Ion trajectory plots (electrolytic tank) for integral focus optics with knife-edge focusing structure.

VI. CONTRIBUTORS

The work reported in the preceding sections has obviously been accomplished by a large group of people. These people have been working together as a closely coordinated team, making the separation of responsibilities for each phase of the program difficult. In the list below an attempt has been made to give credit to each contributor and to indicate his area of greatest participation in the program. Certainly the work reported herein could not have been accomplished without the untiring efforts and close cooperation of all of the following persons:

Mr. D. Berman	Multistrip Engine Thermal Analysis
Dr. G. R. Brewer	Department Manager
Mr. C. R. Collett	Report Preparation
Mr. R. B. Flaaten	Test Chamber Engineering
Dr. H. L. Garvin	Ion Optics and Materials Emission Characteristics Research
Mr. L. M. Hobrock	Multistrip Engine Tests
Mr. S. Kami	Multistrip Engine Mechanical Design
Mr. T. Killgrove	Multistrip Engine Mechanical Design
Mr. S. M. Robelotto	Electron Beam Welding Development
Mr. S. A. Thompson	Engine Life Tests
Mr. R. L. Zimmerman	Program Manager

REFERENCES

- IV- 1. W. H. Kohl, Materials and Techniques for Electron Tubes (Reinhold, New York, 1960).
- IV- 2. J. Drowart, G. DeMaria, R. P. Burns, and M. G. Inghram, J. Chem. Phys. 32, 1366 (1960).
- IV- 3. J. A. Becker, E. J. Becker, and R. A. Brandes, J. Appl. Phys. 32, 411 (1961).
- IV- 4. H. L. Garvin and R. G. Wilson, "Electrode Materials for Contact Ion Engines," AIAA Paper No. 64-684, August 1964.
- IV- 5. J. B. Taylor and I. Langmuir, Phys. Rev. 44, 423 (1933).
- IV- 6. A. J. Kennedy, Advanced Energy Conversion 3, 207-221 (1963); N. S. Rasor and C. Warner, J. Appl. Phys. 35, 2589 (1964).
- IV- 7. T. L. Matskevich, T. V. Krachino, and A. P. Kazantsev, Radiotekhn. i Elektron. 7, 1956 (1962); S. V. Yermakov and B. M. Tsarev, Radiotekhn. i Elektron. 7, 1956 (1962).
- IV- 8. R. G. Wilson, "Electrode Surface Physics Research," Quarterly Progress Report No. 2, Contract NAS 3-5249, pp. 27-34 (August 1964).
- IV- 9. R. A. Chapman, J. Appl. Phys. 35, 2832 (1964).
- IV-10. A. E. Ennos, Brit. J. Appl. Phys. 5, 27-31 (1954).
- IV-11. R. G. Wilson, "Electrode Surface Physics Research," Quarterly Progress Report No. 1, Contract NAS 3-5249 (May 1964).
- IV-12. D. Berman, "Production of WO_3 Within Porous Tungsten," Interdepartmental Correspondence HRL IPD 3-44 (September 1963).
- IV-13. H. J. Booss, Arch. Eisenhüttenw. 30, 761 (1964).
- IV-14. J. A. Becker, E. J. Becker, and R. G. Brandes, J. Appl. Phys. 32, 420 (1961).
- IV-15. P. G. Shewmon, Diffusion in Solids (McGraw-Hill, New York, 1963), p. 14.

- IV-16. Tables of the Error Function and Its Derivative,
National Bureau of Standards Applied Mathematics
Publications, 1954.
- IV-17. D. R. Denison, "The Effect of Carbon on the Surface
Ionization Of Cs on Tungsten," HRL Interdepartmental
Correspondence (July 1, 1964).
- IV-18. H. L. Caswell, IBM J. 4, 130-142 (1960).

DISTRIBUTION LIST FOR
SUMMARY REPORT
NAS 3-4109

Spacecraft Technology Procurement Section (1)
NASA-Lewis Research Center
21000 Brookpark Road
Cleveland, Ohio 44135

Technology Utilization Office (1)
NASA-Lewis Research Center
21000 Brookpark Road
Cleveland, Ohio 44135
Attn: Mr. John Weber

Office of Reliability & Quality Assurance (1)
NASA-Lewis Research Center
21000 Brookpark Road
Cleveland, Ohio 44135

Headquarters
National Aeronautics and Space Administration (2)
FOB-10B
600 Independence Avenue, S.W.
Washington, D.C. 20546
Attn: RNT/James Lazar

Commander
Aeronautical Systems Division (1)
Wright-Patterson Air Force Base, Ohio
Attn: AFAPL (APIE) Robert Supp

Jet Propulsion Laboratory (1)
4800 Oak Grove Drive
Pasadena, California
Attn: J. J. Paulson

NASA-Langley Research Center (1)
Technical Library
Langley Field, Virginia

Electro-Optical Systems, Inc. (1)
125 North Vinedo Avenue
Pasadena, California
Attn: Dr. A. T. Forrester

General Electric Company (1)
Flight Propulsion Lab
Cincinnati 15, Ohio
Attn: R. N. Edwards

Ion Physics Coporation (1)
Burlington, Massachusetts
Attn: Dr. S. V. Nablo

General Dynamics/Astronautics (1)
3302 Pacific Highway
San Diego, California 92112
Attn: Dr. A. E. S. Green

Thompson Ramo Wooldridge, Inc. (1)
New Products Research
7209 Platt Avenue
Cleveland, Ohio 44107
Attn: Dr. Park French

Space Technology Laboratories (1)
8433 Fallbrook Avenue
Canoga Park, California
Attn: Dr. D. Langmuir

North American Aviation, Inc. (1)
Rocketdyne Division
6633 Canoga Avenue
Canoga Park, California
Attn: Dr. Clayton McDole

The Marquardt Corporation (1)
Astro Division
16555 Saticoy Street
Van Nuys, California

NASA-Lewis Research Center (1)
21000 Brookpark Road
Cleveland, Ohio 44135
Attn: W. Rayle

Headquarters, USAF
Air Force Office of Scientific Research (2)
Washington 25, D. C.
Attn: Dr. M. Slawsky

United Aircraft Corporation (1)
Research Department
East Hartford, Connecticut
Attn: Dr. R. G. Meyerand, Jr.

Field Emission Corporation (1)
McMinnville, Oregon
Attn: Dr. F. Charbonnier

Lockheed Aircraft Corporation (1)
Missile and Space Company
Palo Alto, California
Attn: Dr. G. B. Shook

Oak Ridge National Laboratory (1)
Thermonuclear Project
Oak Ridge, Tennessee
Attn: Dr. A. Weinberg

Stanford University (1)
Hansen Microwave Laboratory
Stanford, California
Attn: Dr. G. S. Kino

General Electric Company (1)
General Engineering Laboratories
Schenectady, New York
Attn: Dr. Lynn Stauffer

Aerojet - General (1)
Nucleonics Division
San Ramon, California
Attn: Mr. J. S. Luce

Mashall Space Flight Center (1)
Huntsville, Alabama
Attn: Dr. E. Stuhlinger (M-RP-DIR)

MSA Research Corporation (1)
Callery, Pennsylvania
Attn: J. W. Mausteller

Aerospace Corporation (1)
P.O. Box 95085
Los Angeles 45, California
Attn: Technical Library Documents Group

U.S. Atomic Energy Commission (1)
Office of Technical Information Extension
P.O. Box 62
Oak Ridge, Tennessee

National Research Corporation (1)
70 Memorial Drive
Cambridge, Massachusetts 02142
Attn: R. W. Diehl

NASA-Lewis Research Center (2)
Spacecraft Technology Division
21000 Brookpark Road
Cleveland, Ohio 44135
Attn: J. H. Childs

NASA-Lewis Research Center (5)
Spacecraft Technology Division
21000 Brookpark Road
Cleveland, Ohio 44135
Attn: D. L. Lockwood

NASA-Lewis Research Center (1)
Spacecraft Technology Division
21000 Brookpark Road
Cleveland, Ohio 44135
Attn: R. J. Cybulski

AFPR, Hughes Aircraft Company (1)
Florence Avenue and Teale Street
Culver City, California
Attn: RWRAAC-2-D. Fisher

AFPR, Hughes Aircraft Company (1)
Florence Avenue and Teale Street
Culver City, California
Attn: RWRAPS-9-Mr. Weldon

NASA-Lewis Research Center (1)
Electromagnetic Propulsion Division
21000 Brookpark Road
Cleveland, Ohio 44135
Attn: W. R. Mickelsen

NASA-Lewis Research Center (1)
Electromagnetic Propulsion Division
21000 Brookpark Road
Cleveland, Ohio 44135
Attn: W. Moeckel

NASA-Lewis Research Center (1)
Electromagnetic Propulsion Division
21000 Brookpark Road
Cleveland, Ohio 44135
Attn: E. Richley

Litton Industries (1)
Electron Tube Division
960 Industrial Road
San Carlos, California
Attn: Dr. Rajindar Wadhwa

AFWL - Kirtland Air Force Base, New Mexico (1)
Attn: Capt. C. F. Ellis/WLPC

Westinghouse Astronuclear Laboratories (1)
Pittsburgh 35, Pennsylvania
Attn: Mr. H. W. Szymanowski, Mgr.
Electrical Propulsion Laboratory

NASA-Scientific and Technical Information Facility (6)
Box 5700
Bethesda 14, Maryland
Attn: NASA Representative RQT-2448

Library (2)
NASA-Lewis Research Center
21000 Brookpark Road
Cleveland, Ohio 44135

Reports Control Office (1)
NASA-Lewis Research Center
21000 Brookpark Road
Cleveland, Ohio 44135